Technische Universität Kaiserslautern
Fachbereich Mathematik

MATHEMATICAL MODELING AND SIMULATION OF TWO-PHASE FLOW IN POROUS MEDIA WITH APPLICATION TO THE PRESSING SECTION OF A PAPER MACHINE

Galina Printsypar

Vom Fachbereich Mathematik
der Technischen Universität Kaiserslautern
zur Verleihung des akademischen Grades
Doktor der Naturwissenschaften
(Doctor rerum naturalium, Dr. rer. nat.)
genehmigte Dissertation

1. Gutachter: Prof. Dr. Oleg Iliev

2. Gutachter: Prof. Dr. Yalchin Efendiev

Vollzug der Promotion: 25. April 2012

D 386

Acknowledgments

With deep gratitude I would like to acknowledge the support and help of my advisor Professor Oleg Iliev, whose guidance from very initial stages has been invaluable to me and enabled me to develop an interest and an understanding of the subject. Furthermore, I am very grateful to Dr. Stefan Rief for his continuous support during the entire time of writing this thesis and for the interesting discussions.

It was a pleasure working with Professor Ciegis. Our collaboration was very fruitful and resulted in a joint publication. Also, I would like to thank Professor Efendiev and Professor Lazarov for the valuable suggestions and the welcoming atmosphere at the Department of Mathematics at Texas A&M University during my internship. Additionally, I would like to acknowledge the Department of Flow and Material Simulation at the Fraunhofer ITWM for the financial support and the opportunity of working on this interesting topic. I also thank the industrial partner of the Fraunhofer ITWM, Voith Paper Fabric and Roll Systems GmbH at Heidenheim, for the provided experimental data and for the insight into the practical aspects of the issue.

Last but not least, I would like to thank my family for their everlasting support and encouragement.

Contents

List of Tables

List of Figures

Chapter 1

Introduction

The papermaking is a highly competitive and fast developing industry. Thus, paper machines have to be constantly improved. Current studies are concerned with the simulation of the processes occurring in the pressing section of a paper machine. In this industrial field the mathematical modeling is a powerful tool since laboratory experiments are a challenging and sometimes even impossible task. These studies aim at a development of an advanced mathematical model of the pressing section. It will help us to better understand the inside mechanisms of the process. The mathematical model will also allow us to perform different numerical experiments with various sets of parameters in a reasonable period of time. The achievement of the stated goal may lead to improvements of the papermaking industrial process.

1.1 Pressing section of a paper machine

The paper production is an industrial application, which attracts attention of many scientists. It is a challenging problem, investigated from different points of view by scientists from different fields. We are concerned with the mathematical modeling and simulation of the pressing section of a paper machine.

The paper machine is a huge piece of equipment which typically consists of four main parts (see Fig. 1.1): the headbox, the forming section, the pressing section and the drying section (see [39, 41]). Special woven plastic fabric meshes are used to transport the paper through all sections of the paper machine. During the production process, a wood pulp is transformed into a final paper product by performing different dewatering techniques. The headbox provides the suspension which consists of 99% of water and 1% of solid phase, wooden fibers. In the forming section, dewatering is performed by the natural filtration and sometimes with the help of suction boxes. After the forming section, the dry solid content of the paper increases to about 20%. In the next section, the dewatering is carried out by a mechanical pressing of the paper layer against properly selected fabrics, so-called

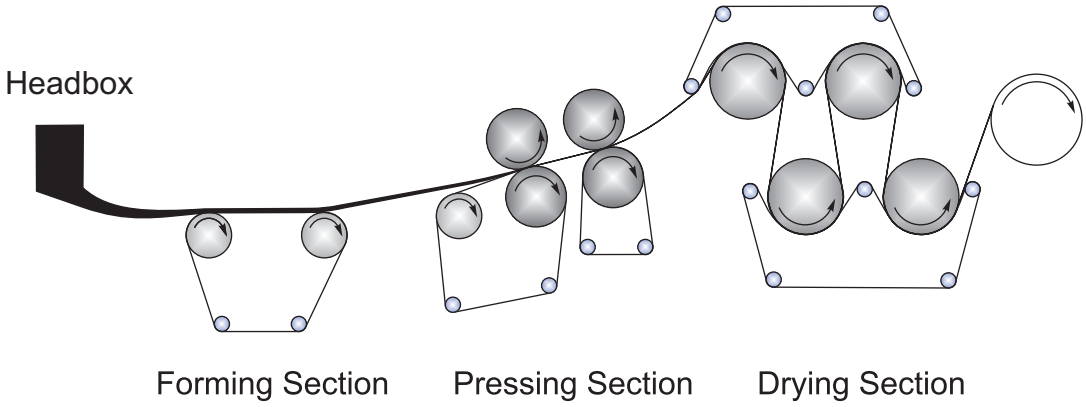

Fig. 1.1: Schematic representation of a paper machine

felts. The simplest construction of a pressing nip consists of two rotating rolls with the paper–felt sandwich transported between them at high speed up to $2000\ m/min$ as shown in Fig. 1.2 on the left. There exists also another type of a press nip which is called shoe press (see Fig. 1.2 on the right). The advantage of the shoe press is an extended pressing zone, which is about $300\ mm$ long in comparison to $40\ mm$ in the roll press case. In contrast, the thickness of the paper–felt sandwich is about $4\ mm$ and the thickness of the paper layer can go down to 100 micrometers. During the pressing of the paper layer against the felts, water is squeezed out of the paper and enters the felts. So, the water content of the paper decreases to about 50% after the pressing section. The last section is the drying section where the remaining water is removed by evaporation. Paper is transported over steam-heated cylinders and comes out of the drying section with a water content of 5%.

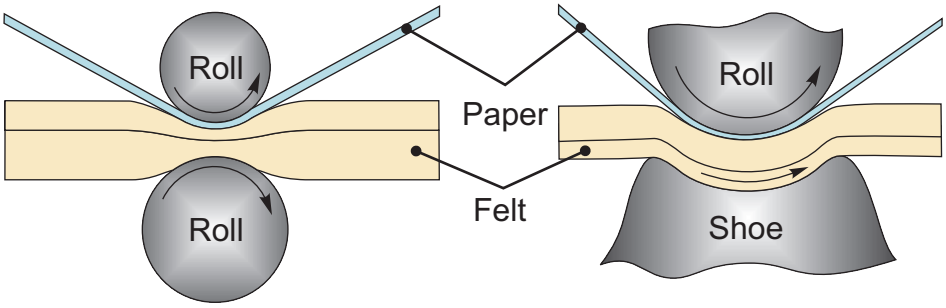

Fig. 1.2: Press nips: roll press (on the left), shoe press (on the right)

The pressing is a more economic way to remove the water from the paper than the drying. Therefore, the industry is actively working on improving the dewatering in the pressing section.

The laboratory experiments for the paper machine are very expensive and difficult to carry out. The simulation approach allows to reduce time and money needed for improving the design of the pressing section.

The pressing section is composed of a sequence of rolls and typically one shoe. Their positioning may vary depending on the paper machine. Fig. 1.3 shows a sketch of the pressing section. The paper web is usually transported either on one felt in the top or bottom position or between two felts as a sandwich. In some cases, when the paper web is strong enough compared to the applied load in machine direction, the web is transported towards the next press nip or to the dryer section without any felt support [41]. Thus, the paper layer sometimes is in contact with the felt and sometimes separated from it while passing the pressing section. Our mathematical model of the pressing section considers the layers to be transported all together. The separation is taken into account by specifying no-flow boundary conditions on the parts of the interfaces where the layers are not in contact in reality.

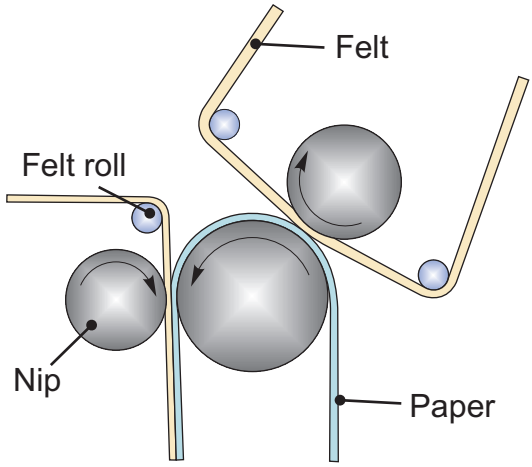

Fig. 1.3: Pressing section

The pressing process in a paper machine is very complex since such features as moving and deformable porous media, computational domain composed from different layers, multiphase flow, etc. have to be taken into account. There exist various approaches to model the pressing section of a paper machine [10, 12, 11, 28, 35]. The mass and momentum conservation equations are used together with a Lagrangian formulation along displacement characteristic lines (solid flow lines) in [28, 35]. In [10, 12, 11] the Lagrangian formulation of mass balance is used. In the last work by Bezanovic et al. [11] the compressible air is also considered. But all these models have a common feature, which is neglecting the capillary forces. Models which take into account the capillary

effect are presented in [9, 43, 44, 49]. The model described by Bermond in [9] uses a two-phase flow model including capillary pressure–saturation relations and introduces thermal aspects. In [43, 44, 49], the Richards' approach for flow in unsaturated porous media is adopted. None of the above mentioned models considers the dynamic capillary pressure effect, which is our main target. Further on, an advanced finite volume discretization, namely MPFA-O method, is employed here in order to provide more accurate discretizations. As a starting point, we have chosen the model realized in [43, 44].

1.2 Dynamic capillary effects

Typically, the capillary effect has a significant influence on the modeling of multiphase flow in porous media (see [5, 6, 7, 26]). The capillary pressure is defined as the difference in the phase pressures:

$$p_c = p_n - p_w,$$

where p_n and p_w are the pressures of non-wetting and wetting phases, respectively. To include this effect in numerical experiments, the capillary pressure can be presented as a function of the water saturation, and sometimes of other parameters of the filtration process. The typical approach to obtain this function is to construct the capillary pressure–saturation relation based on laboratory experiments. This process is carried out in the following way. To construct for example a drainage curve, at the beginning the sample of the porous medium is fully saturated with water. Then, air starts infiltrating the sample by increasing its pressure stepwise. When equilibrium is reached, the capillary pressure and the water saturation are measured. This measurement forms one point at the targeted capillary pressure–saturation curve. The time which is needed to reach equilibrium after changing the pressure can take from several hours to several days. Construction of the complete capillary pressure–saturation curve for the felt, which is used in the paper production process, may take several days.

Many scientists worked on parametrization of the measurement results (e.g. see [14, 37, 48]). This approach works quite accurately in case of slow infiltration processes. In our case, the drying process of the paper pulp takes much less time than the construction of the static capillary pressure–saturation curve. There also exist different studies which try to understand and parametrize a dynamic capillary pressure which is not based on the equilibrium condition (see [3, 4, 13, 34, 45, 23, 24, 25]). Detailed overview and analysis of these models was done by Manthey and can be found in [38]. We have chosen the approach proposed by Hassanizadeh and co-workers in [24]. Their method was derived based on the physical aspects of the porous media flow. Adaptation of this model to processes in the pressing section, as well as performing computational experiments for

evaluation of the influence of the dynamic capillary pressure, are the main topics of this paper.

Note, that in the above mentioned papers devoted to dynamic effects in the capillary pressure–saturation relation, the latter is accounted by including terms with time-derivative of the saturation. For the papermaking machine, we end up with a model including a space derivative of the saturation. This is due to the fact that the paper-felt sandwich is transported with about 1500–2000 m/min between the roles, and follows from the full model derived by Hassanizadeh and Gray in [24, 25]. For fixed porous media, the term with the space derivative of the saturation vanishes. We are not aware of any other paper where the dynamical effects are accounted by the space derivative of the saturation.

1.3 Discretization methods

The model of the pressing section has several specific features which have to be taken into account when we choose a discretization method. First of all, we would like to preserve boundaries between layers during discretization. Therefore, a grid which is based on the solid deformations is used. It means that we deal with a quadrilateral nonorthogonal grid. Moreover, the layered domain leads to discontinuities in permeability. In spite of it, the continuity of the pressure and the fluxes at local physical interfaces between grid cell has to be preserved. We also have to take into account that the permeability is presented by a full tensor and not by a diagonal one.

A number of schemes were proposed recently to discretize such kind of problems (see [1, 2, 18, 27] and references therein). Some of them were tested by Herbin and Hubert [27] for various types of test problems. They concluded that there does not exist the best scheme for any problem and that the method has to be chosen taking into account the specific features of the considered problem. Our choice is the MPFA-O method (see [1, 2, 19]). This method is intuitive. It is simply adopted for the complex boundary and interface conditions, which have to be preserved, and its usage for our problem has shown reliable results.

1.4 Main goals and structure of the thesis

Goals

- Extend the one-dimensional model for the pressing section of a paper machine obtained under the Richards' assumption and presented in [49] by accounting for the dynamic capillary pressure effects. The derived model has to be discretized and tested by performing some numerical experiments. The purpose of the extended one-dimensional model is to obtain the behavior of the fluid pressure and the saturation closer to real ones than behaviors that obtained by previously existing models.

- Theoretically investigate the one-dimensional model. Here the main objective is to prove the convergence of the discrete solution to the continuous one. The theoretical studies should be developed for both flow models, namely with the static and dynamic capillary pressure–saturation relations, with minimal restrictions on input data.

- Extend the one-dimensional model accounting for the dynamic capillary effects to two dimensions taking into account a multilayer computational domain and a possible formation of fully saturated regions.

- Appraise the admissibility of the Richards' approach for the considered problem. The objectives are to develop a two-dimensional mathematical model for the pressing section which will account for the air and water phases and to perform numerical experiments which will compare solutions of the models with and without the Richards' assumption.

Structure

Chapter 2: The objective of this chapter is to develop an advanced one-dimensional model of the pressing section of a paper machine. The mathematical model presented in [49] is extended by accounting for the dynamic capillary effects. At first, a two-dimensional model for a single-layer case is stated. Then, with the help of an averaging procedure in the vertical direction, the one-dimensional model is obtained. Discretization is performed with the help of the finite volume method. Numerical experiments are carried out for the model with the dynamic capillary pressure–saturation relation as well as with the static one to appraise the influence of the dynamic capillary effects. We also compare the simulation results with the existing laboratory experiments presented in [8].

The results of this chapter have been published in [29].

Chapter 3: To have a better understanding of the behavior of the obtained system of equations we carry out some theoretical studies. At first, we are concerned with the mathematical model with the static capillary pressure–saturation relation, which is presented by a nonlinear convection-diffusion equation. We prove the existence and the compactness of the solution of the discrete problem. The main result is presented by the final theorem which shows that the discrete solution converges to the solution of the continuous problem. Finally, we illustrate the obtained theoretical results with the help of a numerical test.

In the second part of this chapter we consider the mathematical model with the dynamic capillary pressure–saturation relation. The model is presented by a system of nonlinear equations, which makes the theoretical studies more complex in comparison with the static case. Here,

we start taking into account two possible flow regimes: the saturated and unsaturated water flow. At first, we propose a numerical algorithm of obtaining the solution of the discrete problem. Then, we prove the existence, compactness and the convergence of the solution of the discrete problem. Finally, the derived theoretical results and made assumptions are verified by numerical experiments.

The results of this chapter have been/will be published in [22, 42].

Chapter 4: The objective of this chapter is to develop a two-dimensional model accounting for the water flow within the pressing section. Richards' approach is used to describe the flow in the unsaturated zone. The dynamic capillary pressure–saturation relation is adopted for the paper production process. The mathematical model accounts for co-existence of saturated and unsaturated zones in a multilayer computational domain. The discretization is performed by the multipoint flux approximation O-method. Finally, different numerical experiments are carried out. At first, we consider single-layer cases to compare the results with the previously developed one-dimensional model and the laboratory experiments. Then, we use the sets of data provided by our industrial partner Voith Paper Fabric and Roll Systems GmbH at Heidenheim to evaluate the influence of the dynamic capillary pressure–saturation relation in the multilayer test cases.

The results of this chapter have been presented in [30].

Chapter 5: Validity range of the Richards' assumption, which has been used for our problem in all previous chapters, has to be investigated. A two-dimensional flow model of the pressing section is developed accounting for the water and air phases with the static capillary pressure–saturation relation. The boundary conditions are improved in a way that the water is allowed to escape from the computational domain through the upper and lower boundaries where the paper-felt sandwich is not in contact with the surface of the pressing roll.

The main focus of interest is to perform numerical experiments for the new flow model using the same input data as in the previous chapter and to compare the results obtained with the help of the Richards' model and the two-phase flow model.

Results of this chapter are being prepared for publication.

Chapter 2

One-Dimensional Model (Richards' Approach)

Mathematical modeling of the pressing section of a paper machine is a complex process, which consists of sequence of steps. At first, one decides how to account for the water infiltration processes within the pressing zone and for the solid deformations, occurring as a result of the transportation the paper-felt sandwich through the pressing nips. Secondly, some reasonable assumptions have to be made to obtain a model with solvable complexity. Thirdly, we properly choose a discretization method. Finally, we perform some numerical experiments and compare the obtained results with available laboratory experiments.

Some laboratory experiments were carried out by Beck in [8] in a single-layer case. Thus, to capture the main behavior of the fluid pressure and the fluid saturation and to compare them with the results from [8] as the first step we are going to develop a one-dimensional model. The model from [49] will be extended by taking into account the dynamic capillary pressure effects (see Section 1.2). Using this one-dimensional model we will go through all the development steps. The aim of the one-dimensional simulations is to state a basic mathematical model which can be improved and extended in the following studies.

In short, the objectives of this chapter are to present an accurate one-dimensional model and to study the influence of the dynamic capillary pressure–saturation relation on the solution of the problem describing the pressing section of a paper machine. The mathematical model, which describes the basic physical principles behind the pressing process, is developed in Section 2.1. In Section 2.2, the discretization by finite volumes is presented. Section 2.3 presents the numerical experiments. Finally, we discuss results in Section 2.4.

2.1 Mathematical model

In this section we state governing equations for the modeling of the water flow in the pressing section. At first, a two-dimensional model is considered. To develop a mathematical model for the pressing section in one dimension we have to consider a computational domain composed of only one layer. Therefore, the two-dimensional model is stated for the single-layer case. Then, the one-dimensional model is obtained with the help of an averaging procedure in the vertical direction. To conclude this section a model which is used to account for solid deformations in the single-layer case is briefly discussed. In short, Section 2.1 is constructed in the following way. At first, we state a two-dimensional model for single-layer case in Section 2.1.1. Then, in Section 2.1.2 we obtain from the two-dimensional model a one-dimensional model with the help of an averaging procedure. In Section 2.1.3 we present the elasticity model for the single-layer case, which accounts for the solid deformations.

2.1.1 Two-dimensional flow model in single-layer case

Concerning the modeling of the pressing section of a paper machine, the porous medium is composed of three phases: solid (denoted by index "s"), liquid (or water) (index "w") and air (index "a"). An *Eulerian approach* is used to describe our system. The computational domain $\Omega \subset \mathbb{R}^2$

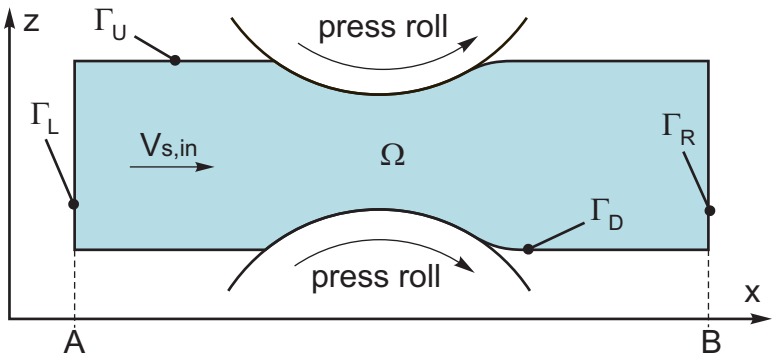

Fig. 2.1: Computational domain Ω

and its boundary $\partial\Omega = \Gamma_L \cup \Gamma_U \cup \Gamma_R \cup \Gamma_D$ are shown in Fig. 2.1. Let the boundaries of Ω be given in the following way:

$$\Gamma_L = \{(x,z) \in \mathbb{R}^2 : x = A,\ z \in [f_d(A), f_u(A)]\}, \quad \Gamma_U = \{(x,z) \in \mathbb{R}^2 : x \in [A,B],\ z = f_u(x)\},$$
$$\Gamma_R = \{(x,z) \in \mathbb{R}^2 : x = B,\ z \in [f_d(B), f_u(B)]\}, \quad \Gamma_L = \{(x,z) \in \mathbb{R}^2 : x \in [A,B],\ z = f_d(x)\}.$$

Then, $\overline{\Omega} = \{(x, z) \in \mathbb{R}^2 : x \in [A, B], z \in [f_d(x), f_u(x)]\}$, where $x = A$ and $x = B$ are fixed points and $A < B$.

As indicated in Fig. 2.1, let us assume that the paper–felt sandwich is transported through the press nips in horizontal direction from the left to the right with velocity $\mathbf{V}_{s,in}$ measured in $[m/s]$. The horizontal direction is designated as x-direction, while z-direction is the vertical component. The third direction is neglected since the length of the cylindrical roll is large, and lateral boundary effects are not considered.

Before we start formulating the mathematical model for the water flow in the pressing section let us make the following assumptions.

Assumption 2.1.1. (Richards' assumption) *Within the computational domain, the air remains at atmospheric pressure.*

Assumption 2.1.2. *Gravity is negligible.*

Assumption 2.1.3. *All phases are incompressible.*

Assumption 2.1.1 is made to simplify the mathematical model. But the admissibility of this statement still has to be shown and will be investigated in our future work. Assumption 2.1.2 is reasonable since the capillary and external forces are dominant in the pressing process. Therefore, the gravity does not significantly influence the movement of water inside the computational domain. Assumption 2.1.3 obviously makes sense for the water and solid phases. In case of the air phase, it still has to be confirmed.

The mass conservation equation in *Eulerian form* [5, 7, 26] for the water phase without source and sink in case of the two-phase flow is:

$$\frac{\partial (\phi S \rho_w)}{\partial t} + \operatorname{div} (\phi S \rho_w \mathbf{V}_w) = 0, \quad x \in \Omega, \tag{2.1}$$

where t is the time in $[s]$, S $([-])$ is the dimensionless saturation of the water phase, $\mathbf{V}_w$ denotes the velocity of the liquid phase in $[m/s]$, ϕ $([-])$ is the porosity and ρ_w is the density of the liquid phase, which is measured in $[kg/m^3]$. Let us remark that in the following all vectors and tensors will be written in bold type.

Assumption 2.1.1 states that the air is at atmospheric pressure. This assumption, in connection with paper dewatering, was earlier successfully employed in [43, 49]. Therefore, the air pressure is considered to be known and saturation of the air phase can be computed as $S_a = 1 - S$. Thus, only the mass conservation equation for the water (2.1) is considered.

To define the water velocity $\mathbf{V}_w$ in addition to the mass conservation equation, we have to consider a momentum conservation. The momentum equation for water phase can be represented

by the generalized Darcy's law (see e.g. [5, 7, 26]). Neglecting gravity (see Assumption 2.1.2) and taking into account a solid velocity, we have:

$$\phi S\left(\mathbf{V}_w - \mathbf{V}_s\right) = -\frac{k_{rw}}{\mu_w}\mathbf{K}\,\mathrm{grad}\,p_w, \quad x \in \Omega, \tag{2.2}$$

where k_{rw} $([-])$ is the relative permeability of the water phase, $\mathbf{V}_s$ is the velocity of solid in $[m/s]$, μ_w is the viscosity of the water in $[Pa \cdot s]$, $\mathbf{K}$ is the intrinsic permeability tensor in $[m^2]$, which we assume to be diagonal, p_w is the pressure of water in $[Pa]$. The solid velocity $\mathbf{V}_s$ appears as a result of the transportation and deformation processes.

According to Assumption 2.1.3, the liquid phase is incompressible ($\rho_w = const$). Thereby, the mass conservation equation for the liquid phase (2.1) together with (2.2) yields:

$$\frac{\partial(\phi S)}{\partial t} - \mathrm{div}\left(\frac{k_{rw}}{\mu_w}\mathbf{K}\,\mathrm{grad}\,p_w\right) + \mathrm{div}\left(\phi S\mathbf{V}_s\right) = 0, \quad x \in \Omega. \tag{2.3}$$

Eq. (2.3) has to be supplemented by a capillary pressure–saturation relation $p_c = p_c(S)$. In our case, when the paper–felt sandwich moves with about 2000 m/min between rolls, it is difficult to expect equilibrium conditions to be satisfied and including dynamic capillary pressure effect is very reasonable. We have chosen the dynamic capillary pressure–saturation relationship proposed by Hassanizadeh and Gray in [24, 25]:

$$\left(p_a - p_w\right) - p_c^{stat} = -\tau\frac{D^s S}{Dt}, \quad x \in \Omega, \tag{2.4}$$

where p_a is the air pressure in $[Pa]$, which is assumed to be zero in the following, τ is a so-called material coefficient in $[Pa \cdot s]$, p_c^{stat} is a empirical static capillary pressure–saturation relation, $\frac{D^s S_w}{Dt}$ is the material derivative with respect to a reference frame fixed to the solid phase:

$$\frac{D^s S}{Dt} = \frac{\partial S}{\partial t} + \mathbf{V}_s \cdot \mathrm{grad}\,S. \tag{2.5}$$

In general, τ may depend on saturation and other parameters, but in these studies we are concerned only with case when τ is a constant. We also remark that case when $\tau = 0$ leads to the standard model with the static capillary pressure.

A paper machine works in a non-stop regime during several days. Therefore, we are interested in a steady-state solution and the derivatives w.r.t. time in (2.3) and (2.4) are equal to zero. Remembering that the water is considered to be incompressible (see Assumption 2.1.3), we obtain:

$$-\mathrm{div}\left(\frac{k_{rw}}{\mu_w}\mathbf{K}\,\mathrm{grad}\,p_w\right) + \mathrm{div}\left(\phi S\mathbf{V}_s\right) = 0, \quad x \in \Omega, \tag{2.6}$$

$$p_w + p_c^{stat} = \tau \mathbf{V}_s \cdot \operatorname{grad} S, \quad x \in \Omega. \tag{2.7}$$

From now on to simplify the notations, we skip index "w" in the variables p_w, k_{rw} and μ_w.

Remark 2.1.1. *We should remark that the model (2.6), (2.7) is suitable only for unsaturated flow. Evaluation of the fully saturated regions is one of the issues of pressing section modeling. But in this section, we are not concerned with this side of the problem.*

2.1.2 One-dimensional flow model

In this section, we are concerned with the one-dimensional problem in machine direction with computational domain $\Omega = (A, B), B > A$ and boundary $\partial\Omega = \{x = A \cup x = B\}$ (see Fig. 2.1). To obtain the one-dimensional model, we employ an averaging procedure in vertical direction (see Appendix A.1).

Then, the one-dimensional mass conservation equation yields:

$$\frac{\partial}{\partial x}\left(\hat{S}(x)\hat{\phi}(x)\hat{V}_w^1(x)d(x)\right) = 0, \quad x \in \Omega; \tag{2.8}$$

where $\hat{\phi}(x)$, $\hat{S}(x)$ and $\hat{V}_w^1(x)$ are the vertically averaged quantities, $d(x) = f_u(x) - f_d(x) > 0$ is the thickness of the layer. We assume that in two dimensions the intrinsic permeability tensor $\mathbf{K}$ has a diagonal form:

$$\mathbf{K} = \begin{bmatrix} K(\phi) & 0 \\ 0 & \hat{K}(\phi) \end{bmatrix}.$$

Then, the xx-component of this tensor will present in the one-dimensional model. Taking into account Darcy's law (2.2) and omitting the hat sign over the averaged functions, Eq. (2.6) in one dimension reads:

$$-\frac{\partial}{\partial x}\left(d\frac{k_r(S)}{\mu}K(\phi)\frac{\partial p}{\partial x}\right) + \frac{\partial}{\partial x}\left(d\phi S V_s\right) = 0, \quad x \in \Omega, \tag{2.9}$$

where V_s denotes the x-component of averaged vector $\mathbf{V}_s$.

We consider the paper–felt sandwich to be transported horizontally with the constant speed $\mathbf{V}_{s,in}$. Therefore, the x-component of the solid velocity, V_s, does not depend on x and it is equal to $|\mathbf{V}_{s,in}|$. From now on, we consider V_s to be constant for our problem.

The dynamic capillary pressure–saturation relation (2.7) after the averaging procedure in the one-dimensional case yields (see Appendix A.2):

$$p + p_c^{stat}(S, \phi) = \tau V_s \frac{\partial S}{\partial x}, \quad x \in \Omega, \tag{2.10}$$

where all variables are the vertically averaged variables.

Boundary conditions

For the needs of the pressing section simulation, the boundary conditions have to be imposed. At first, let us make an assumption.

Assumption 2.1.4. *Boundaries Γ_L and Γ_R are far away from the pressing zone.*

We prescribe Dirichlet boundary conditions for saturation at $x = A$:

$$S(A) = C_0. \tag{2.11}$$

Since the boundary $x = A$ of the computational domain Ω is far enough from the pressing zone, there is no movement of water with respect to the solid skeleton. The stationary capillary pressure–saturation relation is satisfied and the following Dirichlet boundary condition is applied for pressure on the left boundary:

$$p(A) = -p_c^{stat}(C_0). \tag{2.12}$$

According to Assumption 2.1.4, on the right boundary the equilibrium with respect to the solid skeleton is reached as well. Therefore, on Γ_R we apply the zero-Neumann boundary condition:

$$\left.\frac{\partial p}{\partial x}\right|_B = 0. \tag{2.13}$$

2.1.3 Elasticity model in single-layer case

In addition to the flow, one has to account for the deformation of the porous media. In the current work we use developments from [43, 44]. In these studies the pressing section is simulated considering the elasticity model weakly coupled with the flow model supplemented by static capillary pressure–saturation relation. For the completeness of the stated model let us recall the elasticity model from [43, 44].

Since the pressing forces are very large (about $100\ kN/m$ in the roll press) they are the main reason of the solid deformations. Hence, we neglect the force of water acting on the solid phase. Thus, the flow and elasticity models can be weakly coupled. We assume that the solid phase is incompressible (see Assumption 2.1.3) and the porous medium gets deformed by a rearrangement of the solid skeleton in vertical direction. According to [31, 49], it is reasonable to assume that the felt and the paper behave viscoelastically. Then, to describe the behavior of the porous medium we

use the Kelvin-Voigt model for a single-layer case:

$$\mathrm{t}(x) = E(\varepsilon(x)) + \Lambda \left|\mathbf{V}_{s,in}\right| \frac{d}{dx} E(\varepsilon(x)) - k\mathrm{t}_{max}(x), \tag{2.14}$$

where t is the stress measured in $[Pa]$. The dimensionless strain is defined by:

$$\varepsilon(x) = \frac{l_0 - l(x)}{l_0}, \tag{2.15}$$

where l_0 is the undeformed thickness of the layer and $l(x)$ is the deformed thickness at coordinate x. In general, the nonlinear function E is related to the elastic part of the model. Λ ($[s]$) is the viscoelastic time constant which determines the speed of relaxation. In case of the paper layer, we have to take into account the permanent deformation, which is introduced in (2.14) by the third term on the right-hand side. This term depends linearly on the maximum stress to which the paper has been exposed multiplied by the constant k. The maximum stress has the form:

$$\mathrm{t}_{max}(x_0) = \max_{\substack{x \le x_0 \\ x_0 \in [A,B]}} \mathrm{t}(x). \tag{2.16}$$

In case when the minimum distance d_{min} between pressing rolls is given, the geometry of the computational domain is precisely defined. Then, the system of Eqs. (2.14), (2.16) is solved directly. Another possibility is that the pressing force is given, than this system is solved iteratively for different d_{min} while the correct geometry of the computational domain is not found.

Taking into account that the thickness of the layer is small, we consider porosity changes only in horizontal direction. Then, the porosity reads:

$$\phi(x) = \frac{\varepsilon(x) + \phi_0}{\varepsilon(x) + 1}, \tag{2.17}$$

where ϕ_0 is the porosity of undeformed layer. Using the computed stress, the flow mesh can be immediately obtained as well as the solid velocity.

This elasticity model, in connection with the flow model equipped with a standard (not dynamic) capillary pressure, is discussed in detail in the PhD thesis of Rief [43]. Following the approach from [43], we treat consecutively the porous media deformations and the water flow.

2.2 Discretization

To evaluate the influence of the dynamic capillary pressure model, we compare cases with the different material coefficients τ, including case when τ is equal to zero. Therefore, this section

consists of two parts. At first, we present the finite difference scheme for the model with the static capillary pressure ($\tau = 0\ Pa\ s$) (see Section 2.2.1). Then, assuming that τ is not equal to zero in Section 2.2.2 we discuss the numerical algorithm for the model with the dynamic capillary pressure–saturation relation. For discretization the finite volume method is used (see e.g.,[20, 46]).

Let N be the number of intervals into which our computational domain $\Omega = (A, B)$ is divided. Then, mesh on Ω is introduces in the following way.

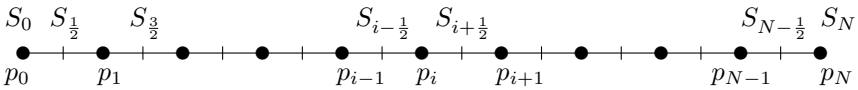

Fig. 2.2: One-dimensional mesh representation and numbering of variables

Definition 2.2.1. *The mesh on (A, B) denoted by $\mathcal{T}^{(A,B)}$ is given by a family $(\mathcal{K}_i^{(A,B)})_{i=\overline{0,N}}$, $N \in \mathbb{N}^+$ (see Fig. 2.2) such that:*

$$\mathcal{K}_0^{(A,B)} = (x_0, x_{\frac{1}{2}}], \quad \mathcal{K}_i^{(A,B)} = (x_{i-\frac{1}{2}}, x_{i+\frac{1}{2}}], \ \ i = \overline{1, N-1}, \quad \mathcal{K}_N^{(A,B)} = (x_{N-\frac{1}{2}}, x_N)$$

and families:

$$\mathcal{X}_1^{(A,B)} = \{x_i = A + ih,\ i = \overline{0, N}\}, \quad \mathcal{X}_2^{(A,B)} = \{x_{i+\frac{1}{2}} = A + \left(i + \frac{1}{2}\right) h,\ i = \overline{0, N-1}\},$$

where $h = (B - A)/N$ is the size of the mesh.

2.2.1 Problem with the static capillary pressure

When the coefficient τ in (2.10) is equal to zero the initial system of Eqs. (2.9), (2.10) becomes a nonlinear Eq. (2.9) with boundary conditions (2.12), (2.13), where the pressure p is considered as an unknown variable. Then, saturation is a dependent variable and expressed as an analytical function of the pressure.

We discretize (2.9) by a finite volume method. Then, the finite difference scheme for the model with the static capillary pressure (2.9), (2.12), (2.13) is presented by the following system:

$$p_0 = -p_c^{stat}(C_0), \tag{2.18}$$

$$\begin{aligned} -\hat{a}_{i+\frac{1}{2}} \frac{p_{i+1} - p_i}{h} + \hat{a}_{i-\frac{1}{2}} \frac{p_i - p_{i-1}}{h} \\ + V_s \left(d_{i+\frac{1}{2}} \phi_{i+\frac{1}{2}} S_{i+\frac{1}{2}} - d_{i-\frac{1}{2}} \phi_{i-\frac{1}{2}} S_{i-\frac{1}{2}} \right) = 0,\ i = \overline{1, N-1}, \end{aligned} \tag{2.19}$$

$$\hat{a}_{N-\frac{1}{2}} \frac{p_N - p_{N-1}}{h} + V_s \left(d_N \phi_N S_N - d_{N-\frac{1}{2}} \phi_{N-\frac{1}{2}} S_{N-\frac{1}{2}} \right) = 0, \tag{2.20}$$

$$\hat{a}_{i-\frac{1}{2}} = d_{i-\frac{1}{2}} \frac{k_{r,i-\frac{1}{2}} K\left(\phi_{i-\frac{1}{2}}\right)}{\mu},\ i = \overline{1,N}, \tag{2.21}$$

where

$$k_{r,i+\frac{1}{2}} = k_r(S_{i+\frac{1}{2}}), \quad d_{i+\frac{1}{2}} = d(x_{i+\frac{1}{2}}), \quad \phi_{i+\frac{1}{2}} = \phi(x_{i+\frac{1}{2}}).$$

Assumption 2.2.1. *Let $p_c^{stat}(S,\phi) \in C((S_r,1]\times(0,1))$ such that $p_c^{stat} : (S_r,1]\times(0,1) \leftrightarrow \mathbb{R}^+$, where $S_r > 0 \in \mathbb{R}$ is the residual saturation ([−]).*

According to Assumption 2.2.1, the function p_c^{stat} has an inverse with respect to S function $\left(p_c^{stat}\right)^{-1}(p,\phi)$. Therefore, an approximation for the saturation can be given in the following form:

$$S_0 = C_0, \tag{2.22}$$

$$S_{i+\frac{1}{2}} = \left(p_c^{stat}\right)^{-1}\left(-p_i, \phi_{i+\frac{1}{2}}\right),\ \ i = \overline{0,N-1}, \tag{2.23}$$

$$S_N = \left(p_c^{stat}\right)^{-1}(-p_N, \phi_N). \tag{2.24}$$

Remark 2.2.1. *In case of the standard capillary pressure–saturation relation, the saturation can also be approximated in the following way:*

$$S_0 = C_0, \tag{2.25}$$

$$S_{i+\frac{1}{2}} = \left(p_c^{stat}\right)^{-1}\left(-\frac{1}{2}(p_i + p_{i+1}), \phi_{i+\frac{1}{2}}\right),\ \ i = \overline{0,N-1}, \tag{2.26}$$

$$S_N = \left(p_c^{stat}\right)^{-1}(-p_N, \phi_N). \tag{2.27}$$

This approximation gives us a finite difference scheme with second order accuracy. But the numerical simulations result in nonphysical oscillations. It happens because of the approximation of the convective term in (2.9) by central differences. In the following, we choose to have first order accuracy and solution without oscillations.

The discretization (2.18)–(2.21) is a system of nonlinear algebraic equations. It is solved by Newton's method (for more details see [17, 36]).

2.2.2 Problem with the dynamic capillary pressure

When the material coefficient τ is not equal to zero we are concerned with the system of Eqs. (2.9)–(2.13), which accounts for the water flow including the dynamic capillary effect. The finite difference scheme for the mass conservation Eq. (2.9) with boundary conditions (2.12), (2.13) is presented by the system of Eqs. (2.18)–(2.21). Finite volume scheme for Eq. (2.10) with boundary condition

(2.11) is introduced using an intermediate value of saturation. For each spatial step i we split the discrete algorithm into two steps. In the first step, a prediction of water saturation value $\hat{S}_{i+\frac{1}{2}}$ for any $i = \overline{0, N-1}$ or $\hat{S}_N$ is computed by solving one of the following equations:

$$S_0 = C_0, \tag{2.28}$$

$$p_0 = \frac{2}{h}\tau V_s \left(\hat{S}_{\frac{1}{2}} - S_0\right) - \tilde{p}\left(\hat{S}_{\frac{1}{2}}, \phi_{\frac{1}{2}}\right), \tag{2.29}$$

$$p_i = \frac{1}{h}\tau V_s \left(\hat{S}_{i+\frac{1}{2}} - S_{i-\frac{1}{2}}\right) - \tilde{p}\left(\hat{S}_{i+\frac{1}{2}}, \phi_{i+\frac{1}{2}}\right), \quad i = \overline{1, N-1}, \tag{2.30}$$

$$p_N = \frac{2}{h}\tau V_s \left(\hat{S}_N - S_{N-\frac{1}{2}}\right) - \tilde{p}\left(\hat{S}_N, \phi_N\right). \tag{2.31}$$

where

$$\tilde{p}(S) = \begin{cases} p_c^{stat}(S_*) & \text{for } S < S_*, \\ p_c^{stat}(S) & \text{for } S_* \le S \le 1, \\ p_c^{stat}(1) & \text{for } S > 1; \end{cases} \tag{2.32}$$

and $S_* > S_r$.

At the second step, this value is corrected with the help of a simple restriction operator:

$$S_i = \begin{cases} S_* + \eta & \text{for } \hat{S}_i < S_* + \eta; \\ \hat{S}_i & \text{for } S_* + \eta \le \hat{S}_i \le 1 - \eta; \\ 1 - \eta & \text{for } \hat{S}_i > 1 - \eta; \end{cases} \tag{2.33}$$

for all $i = \{\overline{\frac{1}{2}, N - \frac{1}{2}}, N\}$. Here $\eta > 0$ is some small value which satisfies $\eta \to 0$ as $h \to 0$.

Remark 2.2.2. *S_* may be chosen as $S_r + \epsilon$, where ϵ is some small value. It is done to make sure that the function $\tilde{p}(S)$ is bounded. In this case it is possible to show that solution of this system exists and converges to solution of the continuous problem (see Section 3.2).*

Remark 2.2.3. *The restriction operator (2.33) is introduced to make sure that the saturation has a physical value from interval $(S_*, 1)$. As it is going to be discussed in Section 3.2 this operator may also be used to include into consideration the second flow regime, namely saturated water flow.*

The proposed finite difference scheme (2.28)–(2.33) also defines the numerical algorithm which is used to obtain the numerical solution.

Table 2.1: Experimental data for one-dimensional test case

Variable	Dimension	Value
k_r	$[-]$	$S^{3.5}$
K	$[m^2]$	$K_0 \frac{\phi^3}{(1-\phi)^2}$
K_0	$[m^2]$	$5e-12$
μ	$[Pa\ s]$	$8e-4$
V_s	$[m/min]$	100
p_c^{stat}	$[Pa]$	$a(\phi-1)\left(\frac{1}{S-S_r}-\frac{1}{1-S_r}\right)^{1/2}$
a	$[Pa]$	$\frac{P_0}{1-\phi_0}\left(\frac{1}{C_0-S_r}-\frac{1}{1-S_r}\right)^{-1/2}$
S_*	$[\%]$	10
S_r	$[\%]$	S_*-1e-3
P_0	$[Pa]$	-5000
C_0	$[\%]$	50
ϕ_0	$[\%]$	87.5
A	$[m]$	-0.05
B	$[m]$	0.05

2.3 Numerical experiments

The goal of this section is to study the influence of the dynamic capillary pressure on the behavior of the solution for different values of τ and to find out how accurate the obtained one-dimensional model is. Numerical experiments were carried out for parameters which are typical for a paper layer during a production process (see [43, 44]). The distribution of the porosity and the thickness of the layer are obtained from the elasticity model briefly discussed in Section 2.1.3, motivated and implemented in [43, 44] (see Figs. 2.3, 2.4). The remaining data, needed for computational experiments, is presented in Table 2.1 (see [43, 44]). Here we notice that the static capillary pressure–saturation relation satisfies Assumption 2.2.1 made during the development of the numerical algorithm.

2.3.1 Numerical experiment for the different values of the coefficient τ

Simulation results for the material coefficients between $\tau = 0$ and $10^4\ Pa\ s$ are presented. This range of the parameter τ was chosen, because for $\tau = 0\ Pa\ s$ we have the standard model with $p = -p_c^{stat}$, then we increase this value by a factor 10 for each new experiment until we observe the significant difference for both output functions, pressure and saturation. We should note that this range of τ does not contradict the real values of the material coefficient which were observed in different experiments [23, 38].

The distribution of porosity and the thickness of the layer, which are used as input data, are presented in Figs. 2.3 and 2.4. Results are shown in Fig. 2.5, where saturation S is plotted as a function of x. Five different curves are presented, they correspond to values of τ equal to 0, 10, 10^2, 10^3 and 10^4 $Pa\ s$. The case when τ is equal to zero represents the static capillary pressure curve. Fig. 2.5 shows that for this set of input parameters, there is no significant difference in saturation for all values except $\tau = 10^4$ $Pa\ s$. But for pressure (see Fig. 2.6 and 2.7) we observe that the changes start already from $\tau = 10$ $Pa\ s$. Thus, we conclude that the dynamic capillary pressure model included in the simulation of the pressing problems influences the solution.

It was experimentally verified in [8] that the pressure peak locates before the center of the pressing zone. The model with the standard capillary pressure–saturation relation ($\tau = 0$ $Pa\ s$) gives a symmetric distribution of the pressure with the maximum value occurring at the center of the pressing nip and values of the fluid pressure greater or equal to initial value. But when we include the dynamic effect in the capillary pressure a shift of the peak is observed. Moreover, the behavior of the pressure profile obtained by our model corresponds to the experimental data reported in [8]. It means that we observe the same decrease of the pressure below the initial value behind the center of the pressing zone and before the equilibrium w.r.t. the moving solid phase is reached (see Fig. 2.6 and [8]).

Hassanizadeh and co-workers have suggested that the value of τ is larger for larger domains (see [33] and references therein). Taking into account the thickness of the felt, small values of τ are expected. This conclusion is also in agreement with numerical and laboratory experiments. According to the behavior of pressure from the experimental data (see [8]) we expect that the material coefficient τ has an order $10 - 10^2$ $Pa\,s$ for the test case which is used in our numerical experiment. Nevertheless, results are presented for the range of τ from 0 to 10^4 $Pa\ s$ to observe the sensitivity of the model.

2.3.2 Comparison of our one-dimensional model with the two-dimensional model from [43]

To evaluate the quality of the one-dimensional model, we compare our numerical results for $\tau = 0$ $Pa\ s$ with results obtained in [43]. The model realized in [43] is two-dimensional and takes into account the geometry of the press rolls. The distribution of pressure obtained by the model from [43] for the set of parameters described above is presented in Fig. 2.8. Note that this experiment is possible only in the single-layer case. To be able to compare simulation results, we average the pressure obtained by the 2D model in vertical direction. Pressures are plotted in Fig. 2.9 and the difference between them in Fig. 2.10. From this experiment, we can see that the order of the error between the one-dimensional and the averaged two-dimensional models is about 1%. The error

consists of two parts. The first part arises from omitting the vertical direction. This part of the error is irreducible. The second part appears to be due to the different approximation schemes. The two-dimensional model is discretized by the finite element method. Our numerical scheme is obtained by the finite volume method and the upwind approximation is used to discretize the convective term. Due to this fact, in the Fig. 2.9, we observe a shift of the pressure curves, which can be reduced by refining the mesh. Hence, we can conclude that the obtained one-dimensional model is suitable for the simulation of the pressing section of a paper machine in the single-layer case and in the case of the diagonal intrinsic permeability tensor.

2.3.3 Convergence test

It is known that in the case of nonsmooth data, unphysical effects can be observed in the numerical solution. Therefore, we perform the numerical experiment for different types of input data to evaluate the rate of convergence of the approximate solution to the continuous one.

Since the analytical solution is unknown, we consider a reference solution for a very fine mesh $\mathcal{T}_*^{(A,B)}$. This approximation of the continuous solution is defined as $p_{\mathcal{T}_*}$. Then, we compute the error E_n between the discrete solution $p_{\mathcal{T}_n}$ for a given mesh $\mathcal{T}_n^{(A,B)}$ and the reference solution $p_{\mathcal{T}_*}$ in the L_2-norm using the following formula:

$$E_n = \frac{\|p_{\mathcal{T}_*} - p_{\mathcal{T}_n}\|_{L_2}}{\|p_{\mathcal{T}_*}\|_{L_2}}.$$

We should notice that $p_{\mathcal{T}_*}$ is not the exact solution therefore if we change the step size of the reference mesh h_* the dependence E_n can also change. But we assume that h_* is small enough so that these changes are not significant.

We consider three different cases for input data, the porosity $\phi(x)$ and the thickness of the layer $d(x)$. The first experiment is carried out for the data which is continuous, but not continuously differentiable, $\phi(x),\ d(x) \in C$. These curves have one point $\hat{x} \in (A, B)$ where first derivatives do not exist. Then, to obtain the second case when the input data is at least twice continuously differentiable, $\phi(x),\ d(x) \in C^2$, we apply the spline interpolation to intervals which contain $\hat{x}$ such that $(\hat{x} - l_i/2, \hat{x} + l_i/2)$ for $i = 1, 2, 3$. These intervals have lengths $l_1 = 2\ mm$, $l_2 = 5\ mm$ and $l_3 = 10\ mm$, respectively. For the third experiment, we use such functions for the porosity and the thickness of the layer that they are differentiable for all degrees of differentiation, $\phi(x),\ d(x) \in C^\infty$, and given by:

$$\phi(x) = \frac{\phi_0 - \epsilon(x)}{1 - \epsilon(x)}, \quad d(x) = d_0(1 - \epsilon(x)),$$

where $d_0 = 0.56\ mm$ and

$$\epsilon(x) = \frac{C_i}{\sqrt{2\pi 49}} e^{-\frac{x^2}{2 \cdot 49}},\ i = 1, 2,$$

with $C_1 = 4.9$ and $C_2 = 5.9$. Thus, we study the convergence for six different test cases.

Results for the model with the stationary capillary pressure–saturation relation ($\tau = 0\ Pa\ s$) are presented in Fig. 2.11. For dynamic capillary pressure with $\tau = 10\ Pa\ s$ the convergence results are shown in Fig. 2.12. In these figures we also show the order of convergence. The estimated order r is defined as:

$$r = \frac{1}{N_e - 2} \sum_{n=2}^{N_e - 1} \frac{\log |E_{n+1}/E_n|}{\log |E_n/E_{n-1}|},$$

where N_e is the number of experiments.

For the model with stationary capillary pressure ($\tau = 0\ Pa\ s$) (see Fig. 2.11), the rate of convergence is $O(h)$, but the convergence behavior is the same for all types of input data. In case $\tau = 10\ Pa\ s$ the convergence rate is also $O(h)$ for all data types.

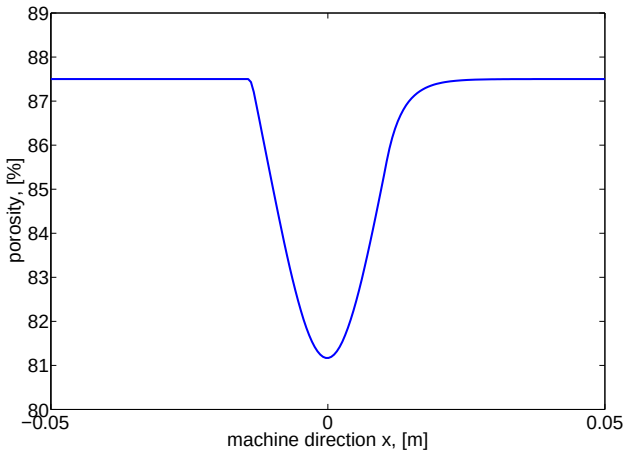

Fig. 2.3: Porosity

2.4 Results and discussions

The first objective of this chapter was to investigate the behavior of the capillary pressure–saturation relation proposed by Hassanizadeh and Gray in one dimension in application of the pressing section simulation. This relation has shown to have a significant influence on the results. The obtained profiles of pressure and saturation affected by the new description of the capillarity have agreed

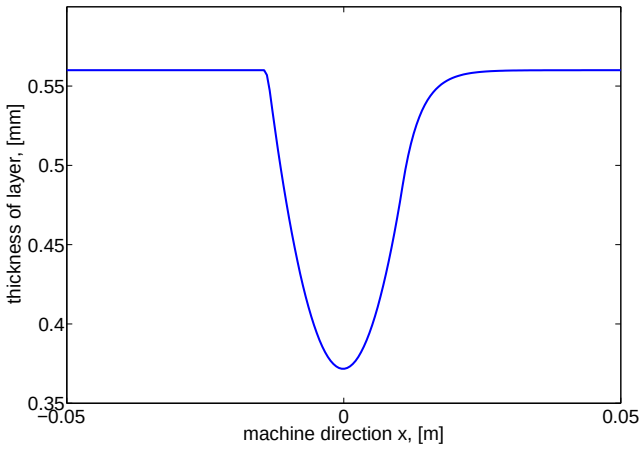

Fig. 2.4: Thickness of layer

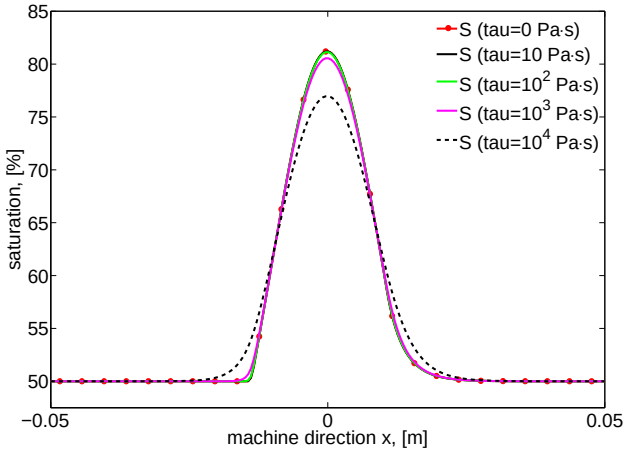

Fig. 2.5: Saturation for different values of τ

with the physical behavior of the pressing process which was observed in laboratory experiment [8].

The second objective was to develop an accurate one-dimensional model for modeling the pressing section of the paper machine. We have used an averaging procedure in vertical direction (see Section 2.1.2) to obtain the one-dimensional results which contains information about other directions. This model has given very good results, which are comparable with results obtained by the two-dimensional model in single-layer case.

The numerical experiments showed that the material coefficient τ has great influence on the

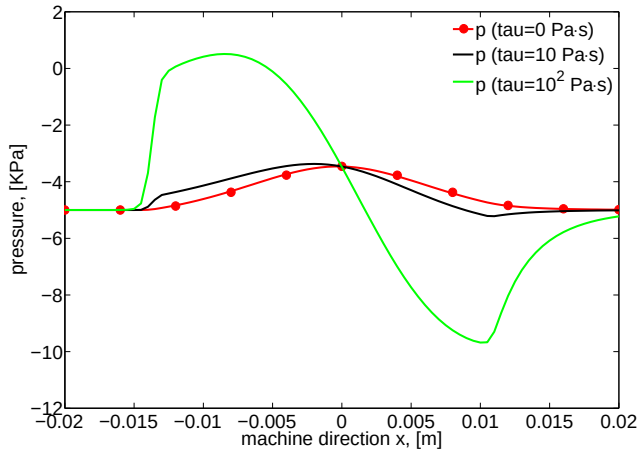

Fig. 2.6: Pressure for τ equal $0, 10, 100\ Pa\ s$

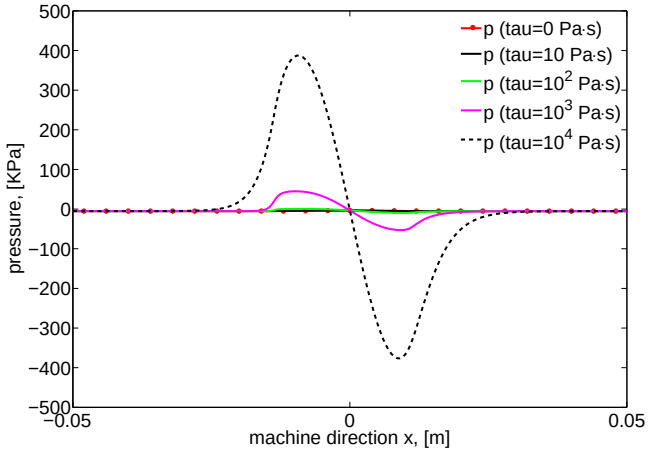

Fig. 2.7: Pressure for different values of τ

solution. According to the laboratory experiment presented in [8] we expect the order of the coefficient τ to be 10–100 $Pa\ s$. But there is no information about the range of the coefficient τ for the present problem and more work, including measurements, is needed.

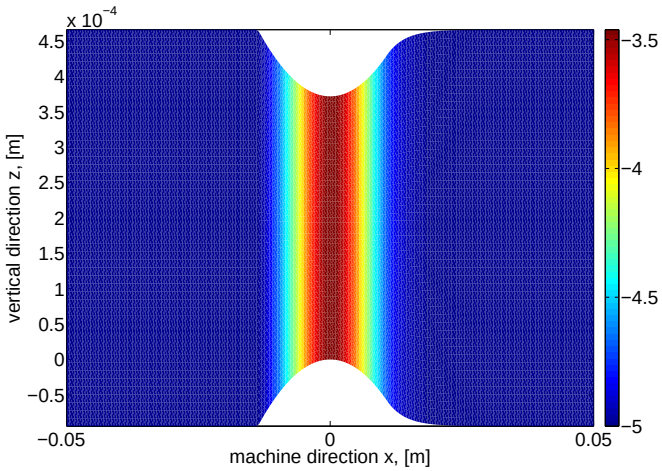

Fig. 2.8: Pressure obtained with the help of the two-dimensional model from [43]

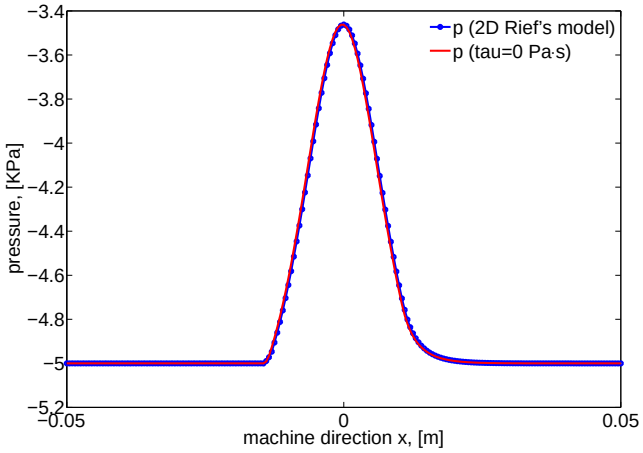

Fig. 2.9: Pressure obtained with the help of our one-dimensional model and the two-dimensional model from [43]

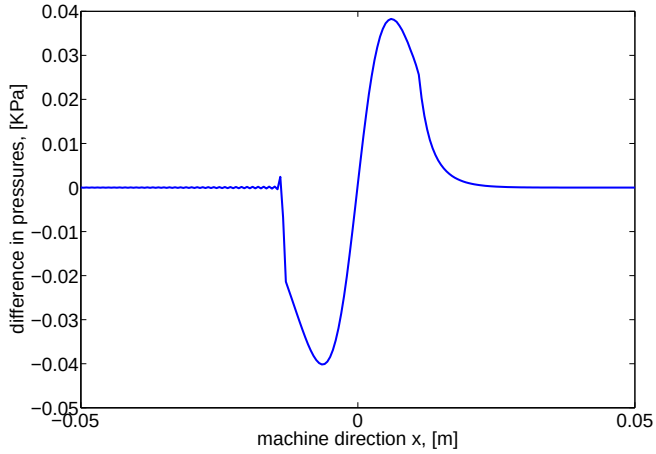

Fig. 2.10: Difference in the pressures obtained with the help of our one-dimensional model and the two-dimensional model from [43]

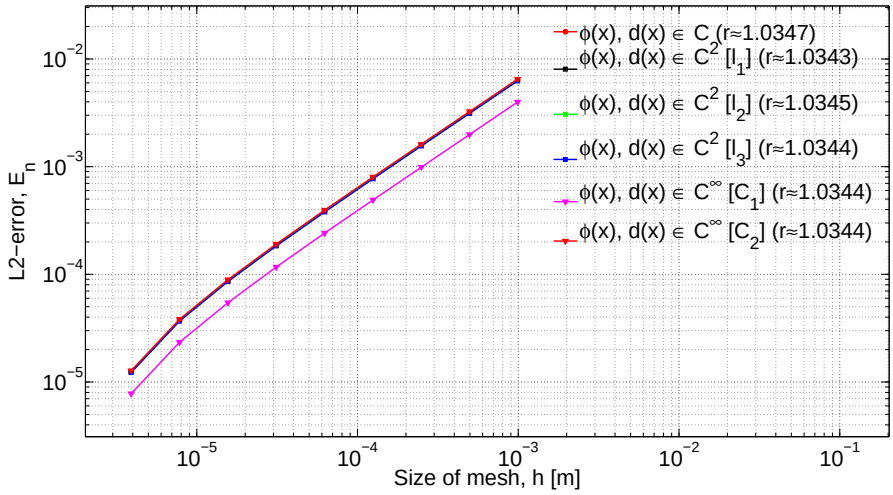

Fig. 2.11: Convergence results for model (2.9)–(2.13) with $\tau = 0\ Pa\ s$

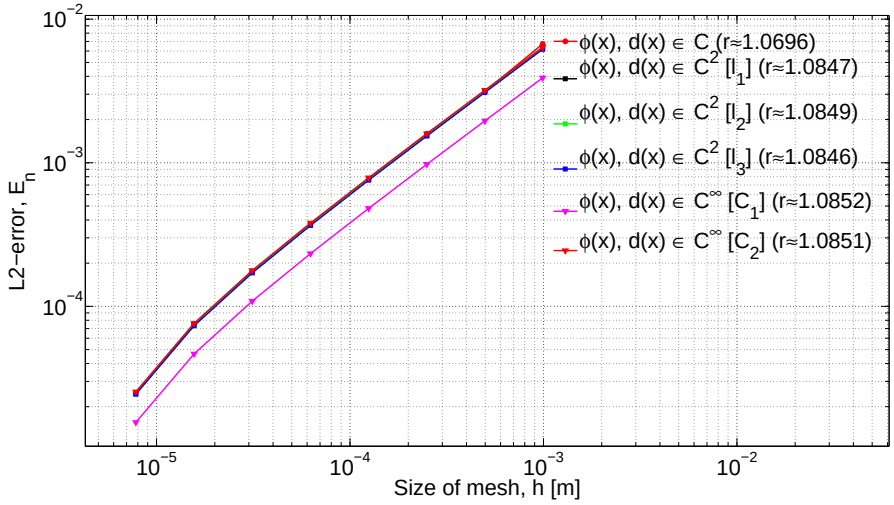

Fig. 2.12: Convergence results for model (2.9)–(2.13) with $\tau = 10\ Pa\ s$

Chapter 3

Convergence of the Discrete One-Dimensional Problem (Richards' Approach)

Richards' approach [6] is used in a lot of different applications, which deal with the water flow in porous media. We use this approach to simulate the pressing section of a paper machine. In Chapter 2 the one-dimensional model was stated and some numerical experiments were performed. Now we would like to investigate this problem from a theoretical point of view. For the one-dimensional model we are going to prove an existence and a convergence of the discrete solution to continuous one.

These theoretical studies are, in particular, motivated by a need for a better understanding of the results from our computational experiments. During the following proof, the input data is restricted minimally to have the theory applicable to real numerical experiments. All assumptions, which are made in this chapter, are satisfied by the data used in the numerical experiments in Sections 2.3, 3.1.4 and 3.2.4. Chapter 3 consists of two main parts. At first, in Section 3.1 we will be concerned with the nonlinear convection-diffusion equation, which describes the water flow within the pressing zone including the static capillary pressure model. Then, in Section 3.2 the nonlinear system of equations which takes into account the dynamic capillary effect will be investigated.

Up to the end of this chapter we consider the function p_c^{stat} to depend only on the water saturation S. It is done to simplify the representation of the following theory. In general, it should be assumed that this function also depends on the porosity: $p_c^{stat} = p_c^{stat}(S, \phi(x))$. We note that main steps of these studies remain valid for this more general case. Moreover, in this chapter we are going to keep the simplified notations introduced previously for the water pressure p, the relative

permeability of the water phase k_r, and the water viscosity μ.

3.1 Problem with static capillary pressure

A lot of theoretical studies were done for Richards' equation (see [21], [47] and references therein). Most articles consider the case of x-independent coefficients. This simplifies the system considerably since, after Kirchhoff's transformation of the problem, the elliptic operator becomes linear. In our case this condition is not satisfied and we have to consider nonlinear operator of second order.

Moreover, all these articles are concerned with the nonstationary problem, while we are interested in the stationary case. Due to complexity of the physical process our problem has a specific feature. An additional convective term appears in our model because the porous media moves with the constant velocity through the pressing rolls. This term is zero in immobile porous media. We are not aware of papers, which deal with such kind of modified steady Richards' problem.

The goal of this section is to show the existence of a solution of the discrete problem, to prove the convergence of the approximate solution to the weak solution of the modified steady Richards' equation, which describes the transport processes in the pressing section. In Section 3.1.1 we present the model which is considered. In Section 3.1.2 a numerical scheme obtained by the finite volume method is given. The main part of this section is theoretical studies, which are presented in Section 3.1.3. Section 3.1.4 develops numerical experiments. Results are discussed in Section 3.1.5.

3.1.1 Mathematical model

The one-dimensional mathematical model for the pressing section was stated in Section 2.1.2. If we set the material coefficient τ to zero the system of Eqs. (2.9), (2.10) yields to the following nonlinear equation:

$$-\frac{\partial}{\partial x}\left(d(x)\frac{k_r(S(p))}{\mu}K(\phi(x))\frac{\partial p}{\partial x}\right)+\frac{\partial}{\partial x}\left(d(x)\phi(x)V_sS(p)\right)=0,\quad x\in\Omega; \tag{3.1}$$

where $\Omega=(A,B)$. This equation describes the flow of water inside the pressing section in one-dimensional case taking into account the static capillary pressure–saturation relation.

We define $b(x)=d(x)K(\phi(x))/\mu$ and $q(x)=d(x)\phi(x)V_s$. Using a variable transformation for x, it is easy to obtain the computational domain Ω to be an interval $(0,1)$. Up to the end of this chapter using the same notations for Ω and x, we remember that they differ from ones in (3.1). Then, the nonlinear convection–diffusion problem (3.1) yields:

$$-\frac{\partial}{\partial x}\left(b(x)k_r(S(p))\frac{\partial p}{\partial x}\right)+\frac{\partial(q(x)S(p))}{\partial x}=0,\quad x\in(0,1) \tag{3.2}$$

with boundary conditions:

$$p(0) = P_0, \quad \left.\frac{\partial p}{\partial x}\right|_{x=1} = 0, \tag{3.3}$$

where $P_0 = -p_c^{stat}(C_0)$, and given constitutive relations:

$$S = S(p), \quad k_r = k_r(S). \tag{3.4}$$

Let us impose some assumptions on the input data, which do not contradict the data used for our numerical experiments.

Assumption 3.1.1.

(a) $b(x) \in C([0,1])$, $b(x) > 0$;

(b) $q(x) \in C([0,1])$, $q(x) \geq 0$;

(c) $k_r \in C([S_*, 1])$, $k_r : [S_*, 1] \to [k_*, 1]$ *is an increasing function, where* $k_* \in \mathbb{R}$ *and* $k_* > 0$;

(d) $S \in C(\mathbb{R})$, $S : \mathbb{R} \to [S_*, 1]$, *where* $S_* \in \mathbb{R}$ *and* $S_* > 0$.

Previously, in Section 2.2 we made an Assumption 2.2.1, which constrains the input function p_c^{stat}. In this section to obtain desirable theoretical results we make Assumption 3.1.1*(d)* instead. This assumption concerns only the inverse function $S(p)$ and it is less strict. We also remark that if Assumption 2.2.1 is satisfied and the function S is defined in the following way:

$$S(p) = \begin{cases} S_* & \text{for } p \leq -p_c^{stat}(S_*), \\ \left(p_c^{stat}\right)^{-1}(-p) & \text{for } p \in \left(-p_c^{stat}(S_*), -p_c^{stat}(1)\right), \\ 1 & \text{for } p \geq -p_c^{stat}(1); \end{cases}$$

where S_* is discussed in Remark 2.2.2, than Assumption 3.1.1*(d)* is satisfied automatically.

For simplicity we apply variable transformation $p = y + P_0$, then instead of (3.2), (3.3) we obtain:

$$-\frac{\partial}{\partial x}\left(b(x)k_r(S(y+P_0))\frac{\partial y}{\partial x}\right) + \frac{\partial(q(x)S(y+P_0))}{\partial x} = 0, \quad x \in (0,1), \tag{3.5}$$

$$y(0) = 0, \quad \left.\frac{\partial y}{\partial x}\right|_{x=1} = 0. \tag{3.6}$$

Let us introduce a subspace of $H^1((0,1))$ denoted by $H^1_{0-}((0,1))$ such that:

$$H^1_{0-}((0,1)) := \{ f \in H^1((0,1)) \,\big|\, f(0) = 0\}. \tag{3.7}$$

Then, the weak formulation of problem (3.5), (3.6) with $y \in H^1_{0-}((0,1))$ yields:

$$\int_0^1 b(x)k_r(S(y+P_0))\frac{\partial y}{\partial x}\frac{\partial \varphi}{\partial x}dx - \int_0^1 q(x)S(y+P_0)\frac{\partial \varphi}{\partial x}dx + q(1)S(y(1)+P_0)\varphi(1) = 0, \quad (3.8)$$

which is satisfied for all $\varphi \in C^\infty((0,1))$ such that $\varphi(0) = 0$.

3.1.2 Discretization

To obtain the finite difference scheme we introduce the mesh $\mathcal{T}^{(0,1)}$ using Definition 2.2.1. In the following, for simplicity we denote the mesh $\mathcal{T}^{(0,1)}$ as $\mathcal{T}$ and the family $\left(\mathcal{K}_i^{(0,1)}\right)_{i=\overline{0,N}}$ as $(\mathcal{K}_i)_{i=\overline{0,N}}$.

Discretizing Eq. (3.5) by finite volumes we obtain:

$$-b_{i+\frac{1}{2}}k_{r,i+\frac{1}{2}}\frac{y_{i+1}-y_i}{h} + b_{i-\frac{1}{2}}k_{r,i-\frac{1}{2}}\frac{y_i - y_{i-1}}{h} + (q_{i+\frac{1}{2}}S_{i+\frac{1}{2}} - q_{i-\frac{1}{2}}S_{i-\frac{1}{2}}) = 0, i = 1, ..., N-1. \quad (3.9)$$

Integrating Eq. (3.5) over $\mathcal{K}_N$ and using the boundary conditions (3.6), we obtain the following approximation:

$$y_0 = 0, \quad (3.10)$$

$$b_{N-\frac{1}{2}}k_{r,N-\frac{1}{2}}\frac{y_N - y_{N-1}}{h} + (q_N S_N - q_{N-\frac{1}{2}}S_{N-\frac{1}{2}}) = 0, \quad (3.11)$$

where

$$k_{r,i+\frac{1}{2}} = k_r(S_{i+\frac{1}{2}}), \quad b_{i+\frac{1}{2}} = b(x_{i+\frac{1}{2}}) \quad q_{i+\frac{1}{2}} = q(x_{i+\frac{1}{2}}) \quad (3.12)$$

and for the approximation of $S_{i+\frac{1}{2}}$ different choices are possible. For example, the ones discussed in Section 2.2.1 have the form:

$$S_{i+\frac{1}{2}} = S(y_i + P_0), \quad i = \overline{0, N-1}, \quad (3.13a)$$

$$S_{i+\frac{1}{2}} = S\left(\frac{y_i + y_{i+1}}{2} + P_0\right), \quad i = \overline{0, N-1}, \quad (3.13b)$$

$$S_N = S(y_N + P_0). \quad (3.14)$$

3.1.3 Proof of convergence

In order to obtain a convergence of the discrete solution to continuous one (see Theorem 3.1.4), we should prove an existence and a convergence of the solution of (3.9)–(3.14) for $h \to 0$ (Lemma 3.1.2 and 3.1.3). To achieve these results, at first we obtain an estimate (Lemma 3.1.1).

The following lemmas and the theorem are proven using a technique which is presented in [20] for a semilinear elliptic problem:

$$-u_{xx}(x) = f(x, u(x)), \quad x \in (0,1);$$
$$u(0) = u(1) = 0.$$

Remark 3.1.1. *Due to complexity of the presented nonlinear problem there are difficulties for obtaining uniqueness results for both continuous and discrete problems. Here we do not study this aspect of the problem.*

Lemma 3.1.1. (Estimate) (see [20], page 28, Lemma 2.3) *Let Assumption 3.1.1 be satisfied and let $\mathcal{T}$ be the mesh on $(0,1)$ (see Definition 2.2.1). If there exists $(y_0, y_1, ..., y_N) \in \mathbb{R}^{N+1}$ a solution of (3.9)–(3.14), then it satisfies:*

$$\sum_{i=0}^{N-1} \frac{(y_{i+1} - y_i)^2}{h} \le C. \tag{3.15}$$

Proof: Multiplying (3.9) by y_i and (3.11) by y_N and summing over $i = \overline{0, N}$, it yields:

$$\sum_{i=1}^{N-1} \left(-b_{i+\frac{1}{2}} k_{r,i+\frac{1}{2}} \frac{y_{i+1} - y_i}{h} + b_{i-\frac{1}{2}} k_{r,i-\frac{1}{2}} \frac{y_i - y_{i-1}}{h} \right) y_i$$
$$+ \sum_{i=1}^{N-1} (q_{i+\frac{1}{2}} S_{i+\frac{1}{2}} - q_{i-\frac{1}{2}} S_{i-\frac{1}{2}}) y_i + \left(b_{N-\frac{1}{2}} k_{r,N-\frac{1}{2}} \frac{y_N - y_{N-1}}{h} \right) y_N$$
$$+ (q_N S_N - q_{N-\frac{1}{2}} S_{N-\frac{1}{2}}) y_N = 0.$$

Reordering summation and taking into account that $y_0 = 0$, we have:

$$\sum_{i=0}^{N-1} b_{i+\frac{1}{2}} k_{r,i+\frac{1}{2}} \frac{(y_{i+1} - y_i)^2}{h} - \sum_{i=0}^{N-1} q_{i+\frac{1}{2}} S_{i+\frac{1}{2}} (y_{i+1} - y_i) + q_N S_N y_N = 0$$

and consequently:

$$\sum_{i=0}^{N-1} b_{i+\frac{1}{2}} k_{r,i+\frac{1}{2}} \frac{(y_{i+1} - y_i)^2}{h} \le \left| \sum_{i=0}^{N-1} q_{i+\frac{1}{2}} S_{i+\frac{1}{2}} (y_{i+1} - y_i) \right| + |q_N S_N y_N|. \tag{3.16}$$

According to the extreme value theorem [50] and Assumption 3.1.1, there exist b_* and b^* such that $0 < b_* \leq b(x) \leq b^*$ for all $x \in [0,1]$ and consequently $b_* \leq b_{i+\frac{1}{2}} \leq b^*$ for all $i = \overline{0, N-1}$. Similarly we obtain that there exist q_* and q^* such that $0 \leq q_* \leq q(x) \leq q^*$ for all $x \in [0,1]$ and consequently $q_* \leq q_{i+\frac{1}{2}} \leq q^*$ for all $i = \overline{0, N-1}$. Let us remark that $0 < k_* \leq k_{r,i+\frac{1}{2}} \leq 1$, for all $i = \overline{0, N-1}$. Now we consider the first term of (3.16):

$$\sum_{i=0}^{N-1} b_{i+\frac{1}{2}} k_{r,i+\frac{1}{2}} \frac{(y_{i+1}-y_i)^2}{h} \geq b_* k_* \sum_{i=0}^{N-1} \frac{(y_{i+1}-y_i)^2}{h}. \tag{3.17}$$

By the Cauchy-Schwarz inequality, for the first term on the right-hand side of (3.16) we obtain:

$$\left| \sum_{i=0}^{N-1} q_{i+\frac{1}{2}} S_{i+\frac{1}{2}} (y_{i+1}-y_i) \right| \leq \left(\sum_{i=0}^{N-1} \frac{(y_{i+1}-y_i)^2}{h} \sum_{i=0}^{N-1} (q_{i+\frac{1}{2}} S_{i+\frac{1}{2}})^2 h \right)^{\frac{1}{2}}.$$

Then, using the inequality for $q(x)$ and the facts that $S_{i+\frac{1}{2}} \in [S_*, 1]$ for all $i = \overline{0, N-1}$ and $\sum_{i=0}^{N-1} h = 1$, we have:

$$\left| \sum_{i=0}^{N-1} q_{i+\frac{1}{2}} S_{i+\frac{1}{2}} (y_{i+1}-y_i) \right| \leq q^* \left(\sum_{i=0}^{N-1} \frac{(y_{i+1}-y_i)^2}{h} \right)^{\frac{1}{2}}. \tag{3.18}$$

The second term on the right-hand side of inequality 3.16 yields:

$$|q_N S_N y_N| \leq q^* |y_N| = q^* |y_N - y_0| \leq q^* \sum_{i=0}^{N-1} |y_{i+1} - y_i| \leq q^* \left(\sum_{i=0}^{N-1} \frac{(y_{i+1}-y_i)^2}{h} \right)^{\frac{1}{2}}. \tag{3.19}$$

Then, inequalities (3.16)–(3.19) give us the estimate (3.15) with $C = \left(\frac{2q^*}{b_* k_*}\right)^2$: ■

Lemma 3.1.2. (Existence of solution) (see [20], page 28, Lemma 2.3) *Let Assumption 3.1.1 be satisfied and let $\mathcal{T}$ be the mesh on $(0,1)$ (see Definition 2.2.1). Then there exists $\mathbf{y} = (y_0, y_1, ..., y_N) \in \mathbb{R}^{N+1}$, a solution of (3.9)–(3.14).*

Proof: Let $\mathbf{v} = (v_0, v_1, ..., v_N) \in \mathbb{R}^{N+1}$ be some vector. Then, it is easy to show that there exists a unique $\mathbf{y} = (y_0, y_1, ..., y_N) \in \mathbb{R}^{N+1}$, the solution of (3.9)–(3.11) with (3.12) and instead of (3.13a), (3.14) the following is used:

$$S_{i+\frac{1}{2}} = S(v_i + P_0), \quad i = \overline{0, N-1}, \tag{3.20}$$

$$S_N = S(v_N + P_0). \tag{3.21}$$

Here we assume that (3.13a) is used for approximation of the original problem. The proof is also true if Eq. (3.13b) is used for approximation instead of (3.13a).

It means that there exists a continuous application F from $\mathbb{R}^{N+1}$ to $\mathbb{R}^{N+1}$ such that $\mathbf{y} = F(\mathbf{v})$ and $(y_0, y_1, ..., y_N)$ is a solution of (3.9)–(3.14) if and only if $\mathbf{y} = (y_0, y_1, ..., y_N)$ is a fixed point of F.

Let us introduce a discrete L_2-norm:

$$||\mathbf{v}||_{L_2((0,1))} = \left(\sum_{i=0}^{N} v_i^2 h\right)^{\frac{1}{2}} \text{ for } \mathbf{v} = (v_0, v_1, ..., v_N) \in \mathbb{R}^{N+1},\ v_0 = 0. \tag{3.22}$$

Now we are going to prove the next inequality:

$$||\mathbf{v}||_{L_2((0,1))} \leq \left(\sum_{i=0}^{N-1} \frac{(v_{i+1} - v_i)^2}{h}\right)^{\frac{1}{2}}. \tag{3.23}$$

For $|v_i|$ using the triangle inequality and the Cauchy-Schwarz inequality we have:

$$|v_i| \leq \sum_{j=0}^{i-1} |v_{j+1} - v_j| \leq \sum_{j=0}^{N-1} |v_{j+1} - v_j| \leq \left(\sum_{j=0}^{N-1} \frac{(v_{j+1} - v_j)^2}{h}\right)^{\frac{1}{2}},\ \text{for all } i = \overline{0, N};$$

then:

$$||\mathbf{v}||_{L_2((0,1))} = \left(\sum_{i=0}^{N} v_i^2 h\right)^{\frac{1}{2}} \underset{(v_0=0)}{=} \left(\sum_{i=1}^{N} v_i^2 h\right)^{\frac{1}{2}} \leq \left(\sum_{i=1}^{N} h \sum_{j=0}^{N-1} \frac{(v_{j+1} - v_j)^2}{h}\right)^{\frac{1}{2}}. \tag{3.24}$$

Thereby, (3.23) is proven.

Note, that inequality (3.15) is also true for (3.9)–(3.11) with (3.12) and (3.20). Then, (3.23) together with (3.15) gives

$$||F(\mathbf{v})||_{L_2((0,1))} = ||\mathbf{y}||_{L_2((0,1))} \leq \hat{C} \text{ for all } ||\mathbf{v}||_{L_2((0,1))} \leq \hat{C},$$

where $\hat{C} = C^{\frac{1}{2}}$. It means $F(B_{\hat{C}}) \subset B_{\hat{C}}$, where $B_{\hat{C}}$ is a closed ball of radius $\hat{C}$ and center 0 in $\mathbb{R}^{N+1}$. Then thanks to the Brouwer's fixed point theorem [15], F has a fixed point in $B_{\hat{C}}$. This fixed point is a solution of (3.9)–(3.14). Thereby, existence is proven. ■

Lemma 3.1.3. (Compactness) (see [20], page 29, Lemma 2.4) *Let Assumption 3.1.1 be satisfied and let $\mathcal{T}$ be a mesh on $(0, 1)$ (see Definition 2.2.1). Let $(y_0, y_1, ..., y_N) \in \mathbb{R}^{N+1}$ be a solution of*

(3.9)–(3.14) and let $y_{\mathcal{T}} : (0,1) \to \mathbb{R}$ by $y_{\mathcal{T}}(x) = y_i$ if $x \in \mathcal{K}_i$, $i = \overline{0,N}$. Then the set $y_{\mathcal{T}}$ for all $\mathcal{T}$ is relatively compact in $L^2((0,1))$. Furthermore, if $y_{\mathcal{T}_n} \to y$ in $L^2((0,1))$ and $h_n \to 0$, as $n \to \infty$, then, $y \in H^1_{0-}((0,1))$.

Proof: By the Kolmogorov compactness theorem (see [20], page 93, Theorem 3.9) to prove that $y_{\mathcal{T}}$ is relatively compact in $L^2((0,1))$, it is sufficient to show that:

- the set $y_{\mathcal{T}}$ is bounded in $L^2(\mathbb{R})$ for all $\mathcal{T}$,
- $||y_{\mathcal{T}}(\cdot + \nu) - y_{\mathcal{T}}||_{L^2(\mathbb{R})} \to 0$ as $\nu \to 0$ uniformly.

Step 1. Function $y_{\mathcal{T}}(x)$ can be redefined as $y_{\mathcal{T}}(x) = y_i$ if $x \in \mathcal{K}_i$, $i = \overline{0,N}$ otherwise $y_{\mathcal{T}}(x) = 0$. Using the facts that $y_0 = 0$, the Cauchy-Schwarz inequality and estimate (3.15), for all $x \in \mathbb{R}$ we have:

$$|y_{\mathcal{T}}(x)| \le \sum_{i=0}^{N-1} |y_{i+1} - y_i| \le \left(\sum_{i=0}^{N-1} \frac{(y_{i+1} - y_i)^2}{h} \right)^{\frac{1}{2}} \le \hat{C}. \tag{3.25}$$

It means that the set $y_{\mathcal{T}}(x)$ for all $\mathcal{T}$ is bounded in $L^2(\mathbb{R})$.

Step 2. Let $0 < \nu < 1$. We define $\chi_{i+\frac{1}{2}} : \mathbb{R} \to \mathbb{R}$ for $i = \overline{0, N-1}$ such that $\chi_{i+\frac{1}{2}}(x) = 1$ if $x_{i+\frac{1}{2}} \in [x, x+\nu]$ and $\chi_{i+\frac{1}{2}}(x) = 0$ if $x_{i+\frac{1}{2}} \notin [x, x+\nu]$ and $\chi_{N+\frac{1}{2}}(x) = 1$ if $x_N \in [x, x+\nu]$ and $\chi_{N+\frac{1}{2}}(x) = 0$, otherwise.

Then, for all $x \in \mathbb{R}$ we have:

$$\begin{aligned} (y_{\mathcal{T}}(x+\nu) - y_{\mathcal{T}}(x))^2 &\le \left(\sum_{i=0}^{N-1} |y_{i+1} - y_i| \chi_{i+\frac{1}{2}}(x) + y_N \chi_{N+\frac{1}{2}}(x) \right)^2 \\ &\le 2 \left(\sum_{i=0}^{N-1} \frac{(y_{i+1} - y_i)^2}{h} \chi_{i+\frac{1}{2}}(x) \right) \left(\sum_{i=0}^{N-1} h \chi_{i+\frac{1}{2}}(x) \right) + 2 y_N^2 \chi_{N+\frac{1}{2}}(x). \end{aligned} \tag{3.26}$$

Integrating (3.26) over $\mathbb{R}$, we obtain:

$$\begin{aligned} \|y_{\mathcal{T}}(\cdot + \nu) - y_{\mathcal{T}}\|^2_{L^2(\mathbb{R})} &\le 2(\nu + 2h) \int_{\mathbb{R}} \left(\sum_{i=0}^{N-1} \frac{(y_{i+1} - y_i)^2}{h} \chi_{i+\frac{1}{2}}(x) \right) dx \\ &\quad + 2\hat{C}^2 \int_{\mathbb{R}} \chi_{N+\frac{1}{2}}(x) dx \\ &= 2(\nu + 2h) \sum_{i=0}^{N-1} \frac{(y_{i+1} - y_i)^2}{h} \int_{\mathbb{R}} \chi_{i+\frac{1}{2}}(x) dx + 2C\nu \\ &\le 2C(\nu + 2h) \int_{\mathbb{R}} \chi_{i+\frac{1}{2}}(x) dx + 2C\nu = 2C\nu(\nu + 2h + 1). \end{aligned} \tag{3.27}$$

Since $h < 1$ and $\nu < 1$, we conclude:

$$\|y_{\mathcal{T}}(\cdot + \nu) - y_{\mathcal{T}}\|^2_{L^2(\mathbb{R})} \leq 8C\nu. \tag{3.28}$$

Thereby, the second condition in the Kolmogorov compactness theorem is proven.

Step 3. Let us prove that $(y_{\mathcal{T}_n}(x + h_n) - y_{\mathcal{T}_n}(x))/h_n$ converges to $\partial y/\partial x$ for all $x \in (-\infty, 1)$ in a weak sense and $h_n \to 0$, as $n \to \infty$. Let $\varphi \in C_0^\infty((-\infty, 1))$ and $\operatorname{supp}\varphi \subset (0, 1)$. The discrete function $\varphi_{\mathcal{T}}$ is defined in the following way:

$$\varphi_{\mathcal{T}}(x) = \begin{cases} \varphi_i = \varphi(x_i), & \text{if } x \in \mathcal{K}_i,\ i = \overline{0, N}; \\ 0, & \text{otherwise.} \end{cases}$$

Let us redefine the function $y_{\mathcal{T}}(x)$ such that if $x \in [x_N, x_{N+\frac{1}{2}}]$ than $y_{\mathcal{T}}(x) = y_N$ and if $x \in (x_{N+\frac{1}{2}}, x_{N+\frac{3}{2}}]$ than $y_{\mathcal{T}}(x) = y_{N+1} = y_N$, then we obtain:

$$\begin{aligned} \left(\frac{y_{\mathcal{T}_n}(\cdot + h_n) - y_{\mathcal{T}_n}}{h_n}, \varphi_{\mathcal{T}_n}\right)_{L_2((-\infty,1))} &= \int_{-\infty}^{1} \frac{y_{\mathcal{T}_n}(x + h_n) - y_{\mathcal{T}_n}(x)}{h_n} \varphi_{\mathcal{T}_n} dx \\ &= \sum_{i=0}^{N} \frac{y_{i+1} - y_i}{h_n} \varphi_i h_n \\ &= -\sum_{i=0}^{N-1} y_{i+1} \frac{\varphi_{i+1} - \varphi_i}{h_n} h_n \\ &= -\sum_{i=0}^{N} y_i \frac{\varphi_i - \varphi_{i-1}}{h_n} h_n \\ &= -\int_{-\infty}^{1} y_{\mathcal{T}_n}(x) \frac{\varphi_{\mathcal{T}_n}(x) - \varphi_{\mathcal{T}_n}(x - h_n)}{h_n} dx. \end{aligned} \tag{3.29}$$

The function $\frac{y_{\mathcal{T}_n}(\cdot+h_n)-y_{\mathcal{T}_n}}{h_n}$ is bounded in $L_2(\mathbb{R})$ (see (3.15)). Then, for any sequence of meshes $(\mathcal{T}_n)_{n\in\mathbb{N}}$ such that $h_n \to 0$, as $n \to \infty$, there exists a subsequence, still denoted by $(\mathcal{T}_n)_{n\in\mathbb{N}}$, such that function $\frac{y_{\mathcal{T}_n}(\cdot+h_n)-y_{\mathcal{T}_n}}{h_n}$ weakly converges to some function $w(x)$. We also know that $y_{\mathcal{T}_n} \to y$ in $L^2((-\infty, 1))$ and $h_n \to 0$, as $n \to \infty$.

On the other hand, thanks to the regularity of the function $\varphi(x)$ we have that $\varphi_{\mathcal{T}_n}$ strongly converges to φ and $\frac{\varphi_{\mathcal{T}_n}(x)-\varphi_{\mathcal{T}_n}(x-h_n)}{h_n}$ strongly converges to $\frac{\partial\varphi}{\partial x}$. Then, passing to the limit in (3.29), we obtain:

$$\int_{-\infty}^{1} w(x)\varphi(x)dx = -\int_{-\infty}^{1} y(x)\frac{\partial\varphi(x)}{\partial x}dx. \tag{3.30}$$

By the definition of the weak derivative (3.30) proves that $w(x) = \frac{\partial y}{\partial x}$. Using (3.15), we have:

$$\left\| \frac{\partial y}{\partial x} \right\|^2_{L_2((-\infty,1))} \leq C.$$

We also have that $\frac{\partial y}{\partial x} = 0$ if $x \in (-\infty, 0)$. Hence, the restriction of y to $(0,1)$ is in $H^1_{0-}((0,1))$. ■

Theorem 3.1.4. (Convergence) *Let Assumption 3.1.1 be satisfied. For the mesh $\mathcal{T}$ on $(0,1)$ (see Definition 2.2.1) let $(y_0, y_1, ..., y_N) \in \mathbb{R}^{N+1}$ be a solution of (3.9)–(3.14) and let $y_{\mathcal{T}} : (0,1) \to \mathbb{R}$ be $y_{\mathcal{T}}(x) = y_i$ if $x \in \mathcal{K}_i$, $i = \overline{0, N}$.*

Then, for any sequence of meshes $(\mathcal{T}_n)_{n\in\mathbb{N}}$ such that $h_n \to 0$, as $n \to \infty$, there exists a subsequence, still denoted by $(\mathcal{T}_n)_{n\in\mathbb{N}}$, such that $y_{\mathcal{T}_n} \to y$ in $L^2((0,1))$, as $n \to \infty$, where $y \in H^1_{0-}((0,1))$ is a solution of (3.8) with given functions (3.4).

Proof: Let $(\mathcal{T}_n)_{n\in\mathbb{N}}$ be a sequence of meshes on $(0,1)$ such that $h_n \to 0$, as $n \to \infty$. Lemma 3.1.2 gives us the existence of solution of the problem (3.9)–(3.14) for any mesh $\mathcal{T}_n$ from sequence $(\mathcal{T}_n)_{n\in\mathbb{N}}$. According to Lemma 3.1.3, there exists a subsequence, still denoted by $(\mathcal{T}_n)_{n\in\mathbb{N}}$, such that $y_{\mathcal{T}_n} \to y$ in $L^2((0,1))$ as $n \to \infty$. In order to conclude the proof, we show that $y \in H^1_{0-}((0,1))$ is a solution of (3.8).

Let $\varphi \in C^\infty((0,1))$ be such that $\varphi(0) = 0$. Then, the weak formulation (3.8) can be rewritten in the following way:

$$T_1 + T_2 - T_3 = 0, \tag{3.31}$$

where:

$$T_1 = \int_0^1 b(x) k_r(S(y + P_0)) \frac{\partial y}{\partial x} \frac{\partial \varphi}{\partial x} dx, \tag{3.32}$$

$$T_2 = q(1) S(y(1) + P_0) \varphi(1), \tag{3.33}$$

$$T_3 = \int_0^1 q(x) S(y + P_0) \frac{\partial \varphi}{\partial x} dx. \tag{3.34}$$

Let $\mathcal{T}_n$ be a mesh on $(0,1)$ (see Definition 2.2.1) which is one of the meshes of the extracted subsequence $(\mathcal{T}_n)_{n\in\mathbb{N}}$, and $\varphi_i = \varphi(x_i)$, $i = \overline{1, N}$ and $\varphi_0 = 0$. If $(y_0, y_1, ..., y_N)$ is a solution of (3.9)–(3.14) on the mesh $\mathcal{T}_n$, multiplying (3.9), (3.11) by φ_i and summing over $i = \overline{1, N}$ yields:

$$\sum_{i=1}^{N-1} \left(-b_{i+\frac{1}{2}} k_{r,i+\frac{1}{2}} \frac{y_{i+1} - y_i}{h_n} + b_{i-\frac{1}{2}} k_{r,i-\frac{1}{2}} \frac{y_i - y_{i-1}}{h_n} \right) \varphi_i + \sum_{i=1}^{N-1} (q_{i+\frac{1}{2}} S_{i+\frac{1}{2}} - q_{i-\frac{1}{2}} S_{i-\frac{1}{2}}) \varphi_i$$
$$+ b_{N-\frac{1}{2}} k_{r,N-\frac{1}{2}} \frac{y_N - y_{N-1}}{h_n} \varphi_N + (q_N S_N - q_{N-\frac{1}{2}} S_{N-\frac{1}{2}}) \varphi_N = 0. \tag{3.35}$$

By reordering summation in (3.35), we obtain:

$$\hat{T}_1^n + \hat{T}_2^n - \hat{T}_3^n = 0, \tag{3.36}$$

where:

$$\hat{T}_1^n = \sum_{i=0}^{N-1} b_{i+\frac{1}{2}} k_{r,i+\frac{1}{2}} \frac{y_{i+1} - y_i}{h_n} \frac{\varphi_{i+1} - \varphi_i}{h_n} h_n, \tag{3.37}$$

$$\hat{T}_2^n = q_N S_N \varphi_N, \tag{3.38}$$

$$\hat{T}_3^n = \sum_{i=0}^{N-1} q_{i+\frac{1}{2}} S_{i+\frac{1}{2}} \frac{\varphi_{i+1} - \varphi_i}{h_n} h_n. \tag{3.39}$$

Thanks to the regularity of the function φ, we notice, that:

$$\frac{\varphi_{i+1} - \varphi_i}{h_n} = \left.\frac{\partial \varphi}{\partial x}\right|_{x_{i+\frac{1}{2}}} + R_{i+\frac{1}{2}}, \text{ where } |R_{i+\frac{1}{2}}| < C_1 h_n^2, \tag{3.40}$$

with some C_1 only depending on φ. Therefore, (3.37) yields:

$$\hat{T}_1^n = \hat{T}_{1,1}^n + \hat{T}_{1,2}^n, \tag{3.41}$$

$$\hat{T}_{1,1}^n = \sum_{i=0}^{N-1} b_{i+\frac{1}{2}} k_{r,i+\frac{1}{2}} \frac{y_{i+1} - y_i}{h_n} h_n \left.\frac{\partial \varphi}{\partial x}\right|_{x_{i+\frac{1}{2}}}, \tag{3.42}$$

$$\hat{T}_{1,2}^n = \sum_{i=0}^{N-1} b_{i+\frac{1}{2}} k_{r,i+\frac{1}{2}} \frac{y_{i+1} - y_i}{h_n} R_{i+\frac{1}{2}} h_n. \tag{3.43}$$

Using inequality (3.25), we conclude that $\frac{y_{i+1}-y_i}{h}$ is bounded. Thus, we have $\hat{T}_{1,2}^n \to 0, \text{ as } n \to \infty$. Substituting (3.40) in (3.39), we obtain:

$$\hat{T}_3^n = \hat{T}_{3,1}^n + \hat{T}_{3,2}^n, \tag{3.44}$$

$$\hat{T}_{3,1}^n = \sum_{i=0}^{N-1} q_{i+\frac{1}{2}} S_{i+\frac{1}{2}} h_n \left.\frac{\partial \varphi}{\partial x}\right|_{x_{i+\frac{1}{2}}}, \tag{3.45}$$

$$\hat{T}_{3,2}^n = \sum_{i=0}^{N-1} q_{i+\frac{1}{2}} S_{i+\frac{1}{2}} R_{i+\frac{1}{2}} h_n. \tag{3.46}$$

Since the functions $q(x)$ and $S(y)$ are bounded, we have $\hat{T}_{3,2}^n \to 0, \text{ as } n \to \infty$. We also remark, that $\hat{T}_2^n \to T_2, \text{ as } n \to \infty$.

Let $\hat{T}^n_{1,1}$ and $\hat{T}^n_{3,1}$ be presented in the following way:

$$\hat{T}^n_{1,1} = \int_0^1 b_{\mathcal{T}_n} k_{r,\mathcal{T}_n} \frac{y_{\mathcal{T}_n}(x+h_n) - y_{\mathcal{T}_n}(x)}{h_n} \left(\frac{\partial \varphi}{\partial x}\right)_{\mathcal{T}_n} dx, \tag{3.47}$$

$$\hat{T}^n_{3,1} = \int_0^1 q_{\mathcal{T}_n} S_{\mathcal{T}_n} \left(\frac{\partial \varphi}{\partial x}\right)_{\mathcal{T}_n} dx, \tag{3.48}$$

where

$$k_{r,\mathcal{T}_n}(x) = k_{r,i+\frac{1}{2}}, \quad b_{\mathcal{T}_n}(x) = b_{i+\frac{1}{2}}, \quad q_{\mathcal{T}_n}(x) = q_{i+\frac{1}{2}},$$

$$\left(\frac{\partial \varphi}{\partial x}\right)_{\mathcal{T}_n} = \left.\frac{\partial \varphi}{\partial x}\right|_{x_{i+\frac{1}{2}}}, \quad S_{\mathcal{T}_n}(x) = S_{i+\frac{1}{2}},$$

if $x \in [x_i, x_{i+1}]$ for all $i = \overline{0, N-1}$.

Now let us show that $S_{\mathcal{T}_n}$ converges to S as $n \to \infty$. Let $S_{i+\frac{1}{2}}$ be approximated by (3.13a) as we used in Chapter 2, then:

$$S_{\mathcal{T}_n}(x) = S(y_{\mathcal{T}_n}(x) + P_0). \tag{3.49}$$

Since $y_{\mathcal{T}_n} \to y$ in $L^2((0,1))$ as $n \to \infty$, $S_{\mathcal{T}_n} \to S$ in $L^2((0,1))$ as $n \to \infty$. It is also clear that $k_{r,\mathcal{T}_n} \to k_r$ as $n \to \infty$, $b_{\mathcal{T}_n}(x) \to b(x)$ and $q_{\mathcal{T}_n}(x) \to q(x)$ as $n \to \infty$, $\alpha = 1, 2$. Remembering $(y(\cdot + h_n) - y)/h_n$ converges to $\partial y / \partial x$ in the weak sense of $L_2((-\infty, 1))$ as $n \to \infty$ (see proof of Lemma 3.1.3), we obtain:

$$\hat{T}^n_{1,1} \to T_1 \text{ as } n \to \infty,$$
$$\hat{T}^n_{3,1} \to T_3 \text{ as } n \to \infty.$$

Hence the theorem is proven. ■

3.1.4 Numerical experiments

To illustrate the theoretical results obtained in the previous section we carry out a numerical experiment for a test problem. We consider problem (3.2)–(3.4) with input data given in Table 3.1. Note, that these data satisfy Assumption 3.1.1. In general the problem (3.2)–(3.4) does not have an analytical solution. But in this particular case it is given by:

$$p(x) = -x^3 + 3x - 1, \quad x \in [0, 1].$$

To solve this nonlinear problem we use the Newton–iteration method. A termination criterion

Table 3.1: Experimental data for numerical experiment with the static capillary pressure

Variable	Value
$b(x)$	e^x
$q(x)$	$e^x(-3x^2+3)$
$S(p)$	$\frac{1}{2\pi}\arctan p + \frac{1}{2}$
$k_r(S)$	S
P_0	-1.0

for the iteration process is:

$$\frac{\|p^{k+1}_{\mathcal{T}_n} - p^{k}_{\mathcal{T}_n}\|_{L_2}}{\|p^{0}_{\mathcal{T}_n}\|_{L_2}} < \epsilon,$$

where k is the Newton iteration number, $\mathcal{T}_n$ is the given mesh and $\epsilon = 10^{-4}$. The saturation and pressure are shown in Figs. 3.1 and 3.2, respectively. Fig. 3.3 represents the error E_n between the discrete solution $p_{\mathcal{T}_n}$ and continuous solution p in L_2-norm. The error E_n is obtained using the following relation:

$$E_n = \frac{\|p - p_{\mathcal{T}_n}\|_{L_2}}{\|p\|_{L_2}}$$

and it converges with the rate $O(h_n)$ as $n \to \infty$.

This numerical experiment illustrates one particular example when the discrete problem has a solution as it was proven in Lemma 3.1.2 and this solution converges to the analytical one as $n \to \infty$ (see Theorem 3.1.4). In Fig. 3.3 results for the convergence of the discrete solution to continuous one are shown. The obtained rate of convergence is $O(h)$. Hence, the numerical experiment for the model with the static capillary pressure proposed in previous chapter agrees with the obtained theoretical results.

3.1.5 Results and discussions

In this section we were concerned with theoretical studies for a mathematical model with the static capillary pressure, which was developed to simulate the pressing section of a paper machine. The existence of a solution of the discrete problem was shown. We presented the proof of the weak convergence of the approximate solution to the continuous one. Let us note that the uniqueness of the solutions was not discussed since there are certain difficulties for getting these results due to complexity of the problem. As the final result the numerical experiment was performed for the test problem with a known analytical solution. Thus, we illustrated the agreement of the developed theory with the particular test case. With the help of this numerical experiment we appraised the order of the convergence, which is $O(h)$. Although, it was not possible to obtain it in our theoretical

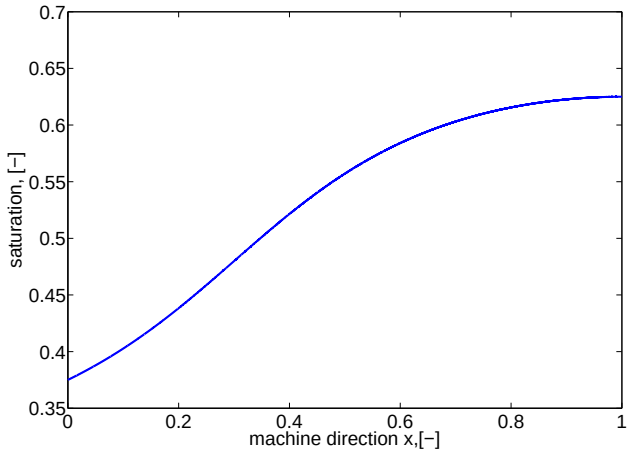

Fig. 3.1: Saturation for the test case with the static capillary pressure

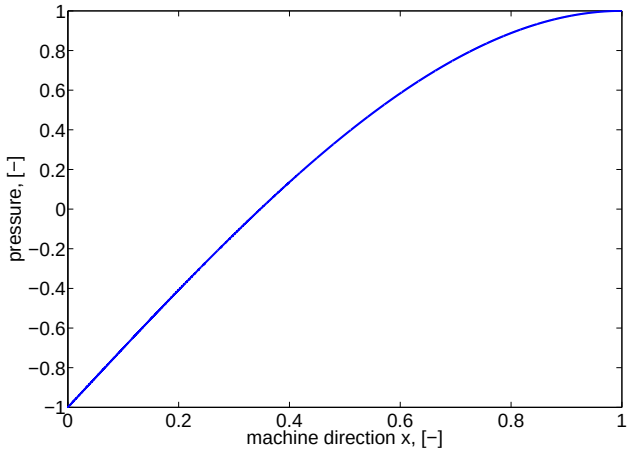

Fig. 3.2: Pressure for the test case with the static capillary pressure

studies. We would like to note that the first order of convergence was also the case in numerical experiments performed in Section 2.3

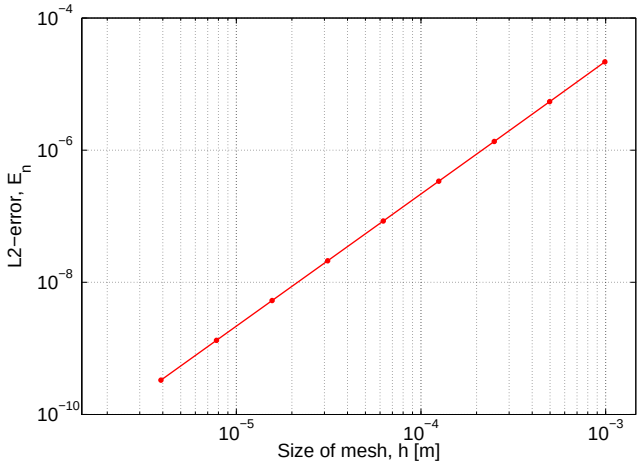

Fig. 3.3: Convergence results for the test case with the static capillary pressure (convergence rate $r = 1.0$)

3.2 Problem with dynamic capillary pressure

One of the main challenges of the pressing process modeling is the study of regimes leading to appearance of the fully saturated zones. This issue was not considered before. But in this section we start including the second flow regime, namely the fully saturated water flow. First of all, it allows us to observe how the dynamic capillary pressure behave in case of the presence of the fully saturated zone. Second of all, the second flow regime is necessary to obtain the existence and convergence results for the model with the dynamic capillary pressure, which we study in this section.

As a result of the two flow regimes, we have to deal with a free boundary problem. There exist theoretical studies which investigate the convergence of discrete solution for free boundary problems describing various applications such as fluid flow in porous media, obstacle problems and elastic problems (see [16, 32] and references therein). In this section we are concerned with a proof of convergence for the system of equations describing water flow in the pressing section. The main issue during these studies is the proof of convergence of the discrete domain with the single-phase water flow. To obtain this result we assume that the solution of continuous problem has a non-degeneracy property. This kind of assumption was used by Deckelnick and Siebert in [16] to resolve the same issue. To prove the existence and the compactness of the solution of our discrete problem we use technique from [20]. This approach uses minimal restrictions on input data to prove the convergence of the discrete problem to continuous one.

The mathematical model for the flow in the pressing section of a paper machine which is presented here includes into consideration the dynamic capillary pressure. To model this effect we choose the dynamic capillary pressure–saturation relation proposed by Hassanizadeh and Gray [23, 24, 25]. In domain with unsaturated water flow we obtain a system of two nonlinear equations, which makes the theoretical studies more complex than in case of standard (steady) capillary pressure–saturation relation. There are some theoretical studies for the flow model with the dynamic capillary effect. They deal with existence and uniqueness of the solution (see [40] and references therein). As opposed to our work, they have considered a time-dependent problem with the dynamic capillary pressure–saturation relation including partial derivative w.r.t. time. In our case, due to specificity of the pressing process we are concerned with a steady-state problem with the dynamic capillary pressure–saturation relation depending on partial derivative w.r.t. space coordinate. We are not aware of theoretical studies which deal with this kind of problems.

Here we investigate the one-dimensional model of the pressing section in machine direction. This model can be used only in case of the computational domain composed of one layer due to the dimensionality. If we want to be more close to real applications we have to consider at least a two-dimensional model, where it is possible to include the multilayer case. The technique used in

our studies is seemed to be possible to extend to two-dimensional model but only in single-layer case (see, also [20], where basic ideas and algorithms are applied for 2D and 3D problems, also). For multilayer problems discontinuities in the input data arise. Thus, absolutely different theoretical approaches have to be used in this case.

In short, the objective of this section is to study theoretically convergence of the solution of the discrete problem to the solution of the continuous problem. The one-dimensional continuous model including the dynamic capillary pressure effect, which describes water flow in the pressing section is presented in Section 3.2.1. In Section 3.2.2, the nonlinear finite difference scheme and its implementation algorithm are presented. The theoretical existence and convergence studies are presented in Section 3.2.3. Some numerical tests are developed in Section 3.2.4. Final remarks and discussions are presented in Section 3.2.5.

3.2.1 Mathematical model

When one models the pressing section of a paper machine it is important to evaluate fully saturated zones. Therefore, one has to account for two possible flow regimes inside the computational domain. Let us assume that the computational domain Ω is divided into two subdomains such that $\Omega = \Omega^1 \cup \Omega^2$ and $\Omega^1 \cap \Omega^2 = \emptyset$ (see Fig. 3.4). Ω^1 is the domain, where single-phase (water) flow takes place, and Ω^2 is the domain, where two-phase flow occurs. Then, the interface between these domains is denoted by $\Gamma = \overline{\Omega^1} \cap \overline{\Omega^2}$.

Let us shortly recall the main conditions under which we developed the model in Section 2.1. Since the aim of this work is to investigate one-dimensional model, we consider a case when the computational domain Ω is composed of one layer. We assume that this layer is transported through the press nips from the left to the right with velocity $\mathbf{V}_{s,in}$ measured in $[m/s]$ as indicated in Fig. 3.4. Remembering that a paper machine works in a non-stop regime during several days, we state the model under steady-state conditions. According to Assumption 2.1.3, the water is considered to be incompressible.

The first regime is a single-phase flow model. We describe it with the help of mass conservation equation for the water phase and Darcy's law in the case of moving porous media and neglected gravity term (for more details see [6]):

$$-\operatorname{div}\left(\frac{\mathbf{K}}{\mu}\operatorname{grad} p\right) + \operatorname{div}(\phi \mathbf{V}_s) = 0, \quad \mathbf{x} \in \Omega^1. \tag{3.50}$$

The second regime is a two-phase flow, which is simulated using Richards' assumptions, the mass conservation equation for water phase, the Darcy law and the dynamic capillary pressure-saturation relation derived by Hassanizadeh and Gray [23, 24, 25] (for more detailed explanations

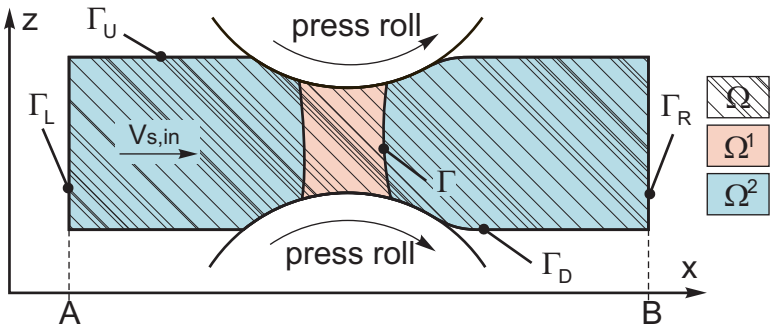

Fig. 3.4: Computational domain Ω with two flow regimes in single-layer case

see Section 2.1):

$$-\operatorname{div}\left(\frac{k_r}{\mu}\mathbf{K}\operatorname{grad} p\right)+\operatorname{div}(\phi S\mathbf{V}_s)=0,\quad \mathbf{x}\in\Omega^2, \tag{3.51}$$

$$p+p_c^{stat}(S)=\tau\mathbf{V}_s\cdot\operatorname{grad} S,\quad \mathbf{x}\in\Omega^2. \tag{3.52}$$

On the interface Γ between the domains with the different flow regimes we satisfy the continuity of the pressure and the normal fluxes. We introduce operator $[f]_\Gamma$ which indicates a jump of a function f across the interface Γ:

$$[f]_\Gamma=\lim_{t\to\Gamma+0}f(t)-\lim_{t\to\Gamma-0}f(t).$$

Then, the interfacial conditions, the continuity of the water pressure and the continuity of the normal fluxes across the interface Γ yield:

$$[p]_\Gamma=0,\quad [\mathbf{J}_w\cdot\mathbf{n}]_\Gamma=0, \tag{3.53}$$

where $\mathbf{n}$ is the unit normal vector to Γ, $\mathbf{J}_w$ is the water flux, which is defined as:

$$\mathbf{J}_w=\begin{cases}-\frac{\mathbf{K}}{\mu}\operatorname{grad} p+\phi\mathbf{V}_s & \text{for } \mathbf{x}\in\overline{\Omega^1};\\ -\frac{k_r}{\mu}\mathbf{K}\operatorname{grad} p+\phi S\mathbf{V}_s & \text{for } \mathbf{x}\in\Omega^2.\end{cases} \tag{3.54}$$

We obtain the one-dimensional model by averaging the two-dimensional model in vertical direction (for more details see Section 2.1.2 and Appendix A.1). Therefore, a thickness of the layer $d(x)$ is included into the final model:

$$-\frac{\partial}{\partial x}\left(d(x)\frac{K(\phi(x))}{\mu}\frac{\partial p}{\partial x}\right)+\frac{\partial}{\partial x}\left(d(x)\phi(x)V_s\right)=0,\quad x\in\Omega^1, \tag{3.55}$$

$$-\frac{\partial}{\partial x}\left(d(x)\frac{k_r(S)}{\mu}K(\phi(x))\frac{\partial p}{\partial x}\right)+\frac{\partial}{\partial x}\left(d(x)\phi(x)V_sS\right)=0,\quad x\in\Omega^2, \tag{3.56}$$

$$p+p_c^{stat}(S)=\tau V_s\frac{\partial S}{\partial x}\quad x\in\Omega^2. \tag{3.57}$$

In one dimension, the domains Ω^1 and Ω^2 are presented by the sets of intervals such that $\overline{\Omega^1}\cup\overline{\Omega^2}=\overline{\Omega}$ and $\Omega^1\cap\Omega^2=\emptyset$. Moreover, as in case of the theoretical studies for model with the static capillary pressure, it is assumed that the one-dimensional computational domain Ω is an interval $(0,1)$ obtained by the simple variable transformation.

We consider the paper-felt sandwich to be transported horizontally with the constant speed $\mathbf{V}_{s,in}$. Then, the x-component of the solid velocity V_s does not depend on x and it is equal to $|\mathbf{V}_{s,in}|$.

Let us define functions $b(x)=d(x)K(\phi(x))/\mu$, $q(x)=d(x)\phi(x)V_s$ and $c=\tau V_s=const$. Then, the nonlinear system of Eqs. (3.55)–(3.57) can be rewritten as:

$$-\frac{\partial}{\partial x}\left(b(x)\frac{\partial p}{\partial x}\right)+\frac{\partial q(x)}{\partial x}=0,\quad x\in\Omega^1, \tag{3.58}$$

$$-\frac{\partial}{\partial x}\left(b(x)k_r(S)\frac{\partial p}{\partial x}\right)+\frac{\partial (q(x)S)}{\partial x}=0,\quad x\in\Omega^2, \tag{3.59}$$

$$p+p_c^{stat}(S)=c\frac{\partial S}{\partial x},\quad x\in\Omega^2. \tag{3.60}$$

The boundary conditions yield:

$$p(0)=-p_c^{stat}(C_0),\qquad \left.\frac{\partial p}{\partial x}\right|_{x=1}=0,\qquad S(0)=C_0. \tag{3.61}$$

The interfacial conditions (3.53) have also to be satisfied for the one-dimensional water flux defined by:

$$J_w=\begin{cases}-b(x)\frac{\partial p}{\partial x}+\phi V_s & \text{for } x\in\overline{\Omega^1};\\ -b(x)k_r\frac{\partial p}{\partial x}+\phi SV_s & \text{for } x\in\Omega^2.\end{cases} \tag{3.62}$$

Let us impose the following assumptions on the input data:

Assumption 3.2.1.

(a) $b(x)\in C([0,1])$, $b(x)>0$*;*

(b) $q(x)\in C([0,1])$, $q(x)\geq 0$*;*

(c) $k_r\in C([S_*,1])$, $k_r:[S_*,1]\to[k_*,1]$ *is an increasing function, where* $k_*\in\mathbb{R}$ *and* $k_*>0$*;*

(d) $C_0 \in \mathbb{R}$, $C_0 \in (S_*, 1)$*;*

(e) $c \in \mathbb{R}$, $c > 0$*;*

(f) $p_c^{stat} \in C^1([S_*, 1])$, $p_c^{stat} : [S_*, 1] \leftrightarrow [p_*, p^*]$ *is a decreasing function, where* $S_* \in \mathbb{R}$ *and* $S_* > 0$.

These assumptions are physical and satisfied for the input data used in our numerical experiments. The first three statements are the same as in case of the static capillary pressure. Assumptions 2.2.1*(d), (e)* are required for the following proof. We should remark that they do not contradict the data used for our numerical experiments. Assumption 3.2.1*(f)* coincides with the Assumption 2.2.1 if, in addition, it is specified that p_c^{stat} is the one-time continuously differentiable decreasing function and S_* is defined by Remark 2.2.2. Although Assumption 3.2.1(f) is stricter than Assumption 2.2.1, it is still satisfied for the input data used for the numerical experiments.

Taking into account imposed assumptions, we can reformulate problem (3.58)–(3.60) in the following way:

$$-\frac{\partial}{\partial x}\left(b(x)k_r(S)\frac{\partial p}{\partial x}\right) + \frac{\partial (q(x)S)}{\partial x} = 0, \quad x \in \Omega, \tag{3.63}$$

$$\hat{c}(S)(p + p_c^{stat}(S)) = \frac{\partial S}{\partial x}, \quad x \in \Omega, \tag{3.64}$$

where function $\hat{c}(S)$ takes the form:

$$\hat{c}(S) = \begin{cases} 1/c & \text{for } S \in (S_*, 1); \\ 0 & \text{for } S \notin (S_*, 1). \end{cases} \tag{3.65}$$

Using Assumption 3.2.1, we notice that Eq. (3.63) coincides with Eq. (3.57) in the domain Ω^1 and with Eq. (3.58) in the domain Ω^2. Continuity of the pressure p in whole domain Ω follows from the definition of the non-linear convection–diffusion Eq. (3.63). Continuity of the normal fluxes directly follows from integration of Eq. (3.63) over a small interval which contains the interface between Ω^1 and Ω^2.

Eq. (3.64) with (3.65) transforms automatically into Eq. (3.59) in the domain Ω^2. Let us prove that in the domain Ω^1 one of the following equations are satisfied:

$$S = S_*, \quad S = 1.$$

We are going to show that solution of (3.64), (3.65) is bounded and belongs to interval $[S_*, 1]$. Integrating (3.64) over interval $(0, x)$ for some $x \in (0, 1)$ and then finding $|S(x) - S(y)|$ we can

show that solution of (3.64), (3.65), S, is a continuous function.

Let us assume that there exists $\tilde{x} \in \Omega$ such that $S(\tilde{x}) > 1$. Since the function S is continuous there exists $y \in (0, \tilde{x})$ such that $S(y) = 1$ and $S(x) > 1$ for all $x \in (y, \tilde{x}]$. Then, we have:

$$\begin{aligned} S(\tilde{x}) &= C_0 + \int_0^y \hat{c}(S)(p + p_c^{stat}(S))dt + \int_y^{\tilde{x}} \hat{c}(S)(p + p_c^{stat}(S))dt \\ &= S(y) + \int_y^{\tilde{x}} \hat{c}(S)(p + p_c^{stat}(S))dt = S(y). \end{aligned}$$

Hence, we have obtained a contradiction $S(\tilde{x}) = S(y)$, which proves that $S \leq 1$. Using the same approach it can be proven that $S \geq S_*$. Thus, system of Eqs. (3.64), (3.65) guarantees that solution S is in $[S_*, 1]$.

Remark 3.2.1. *Our model (3.63)–(3.65) contains a fictitious regime when saturation is equal to S_*. This case is included only to make the formulation of the model homogeneous for all values of saturation S. The fictitious domain method is quite popular method to solve PDEs in non-standard domains or to simulate processes described by free boundary problems. From the physical point of view instead of Eqs. (3.63)–(3.65) in this case we should formulate the following equations:*

$$p = -p^*, \quad S = S_*.$$

We will not investigate the error introduced by such fictitious domain technique, since in all our numerical experiments the single-phase air flow has never occurred.

In order to simplify notations, we apply variable transformation $p = y - p_c^{stat}(C_0)$, then we obtain the following nonlinear boundary value problem:

$$-\frac{\partial}{\partial x}\left(b(x)k_r(S)\frac{\partial y}{\partial x}\right) + \frac{\partial(q(x)S)}{\partial x} = 0, \quad x \in (0,1), \tag{3.66}$$

$$\hat{c}(S)(y + g(S)) = \frac{\partial S}{\partial x}, \quad x \in (0,1], \tag{3.67}$$

$$y(0) = 0, \tag{3.68}$$

$$\left.\frac{\partial y}{\partial x}\right|_{x=1} = 0, \tag{3.69}$$

$$S(0) = C_0, \tag{3.70}$$

where $g(S) = p_c^{stat}(S) - p_c^{stat}(C_0)$.

Let $H^1_{0-}((0,1))$ be the subspace of $H^1((0,1))$ satisfying

$$H^1_{0-}((0,1)) := \{ f \in H^1((0,1)) \big|\, f(0) = 0\}.$$

Then, we consider the weak formulation of problem (3.66)–(3.70):
find $y \in H^1_{0-}((0,1))$ and $S \in L_2((0,1))$ such that

$$\int_0^1 b(x)k_r(S)\frac{\partial y}{\partial x}\frac{\partial \varphi}{\partial x}dx - \int_0^1 q(x)S\frac{\partial \varphi}{\partial x}dx + q(1)S(1)\varphi(1) = 0, \tag{3.71}$$

$$-\int_0^1 \hat{c}(S)\left(y + g(S)\right)\varphi dx - \int_0^1 S\frac{\partial \varphi}{\partial x}dx + S(1)\varphi(1) = 0, \tag{3.72}$$

for all $\varphi \in C^\infty([0,1])$ such that $\varphi(0) = 0$.

In order to prove the main convergence theorem we will assume that the following non-degeneracy property is satisfied.

Assumption 3.2.2. *For any $\epsilon > 0$ there exists $\delta_\epsilon > 0$ such that:*

$$\mathrm{meas}\left(\{x \in \Omega : S \in (S_*, S_* + \delta_\epsilon) \cup (1 - \delta_\epsilon, 1)\}\right) \le \epsilon. \tag{3.73}$$

This kind of assumption was used by Deckelnick and Siebert in [16] to prove the convergence of the discrete domain with the free boundary to continuous one. Without this non-degeneracy property is not possible to complete the proof of convergence. We are going to to verify the admissibility of this assumption by the numerical experiments.

3.2.2 Discretization

The finite difference scheme for the one-dimensional model with the dynamic capillary pressure was stated in Section 2.2. Since in this section we investigate the proposed numerical algorithm let us recall the finite difference scheme here. Let the mesh $\mathcal{T}$ be introduced on the computational domain $\Omega = (0,1)$ (see Definition 2.2.1). The mass conservation Eq. (3.66) discretized by the finite volume method yields:

$$y_0 = 0, \tag{3.74}$$

$$\begin{aligned} -b_{i+\frac{1}{2}}k_{r,i+\frac{1}{2}}\frac{y_{i+1} - y_i}{h} + b_{i-\frac{1}{2}}k_{r,i-\frac{1}{2}}\frac{y_i - y_{i-1}}{h} \\ +(q_{i+\frac{1}{2}}S_{i+\frac{1}{2}} - q_{i-\frac{1}{2}}S_{i-\frac{1}{2}}) = 0, \quad i = \overline{1, N-1}, \end{aligned} \tag{3.75}$$

$$b_{N-\frac{1}{2}}k_{r,N-\frac{1}{2}}\frac{y_N - y_{N-1}}{h} + (q_N S_N - q_{N-\frac{1}{2}}S_{N-\frac{1}{2}}) = 0, \tag{3.76}$$

where

$$k_{r,i+\frac{1}{2}} = k_r(S_{i+\frac{1}{2}}), \qquad b_{i+\frac{1}{2}} = b(x_{i+\frac{1}{2}}), \qquad q_{i+\frac{1}{2}} = q(x_{i+\frac{1}{2}}). \tag{3.77}$$

To discretize Eq. (3.67) we have the following two-step algorithm:

$$S_0 = C_0, \tag{3.78}$$

$$\frac{1}{c}\left(y_0 + \tilde{g}(\hat{S}_{\frac{1}{2}})\right) = \frac{2}{h}(\hat{S}_{\frac{1}{2}} - S_0), \tag{3.79}$$

$$\frac{1}{c}\left(y_i + \tilde{g}(\hat{S}_{i+\frac{1}{2}})\right) = \frac{1}{h}(\hat{S}_{i+\frac{1}{2}} - S_{i-\frac{1}{2}}), \quad i = \overline{1, N-1}, \tag{3.80}$$

$$\frac{1}{c}\left(y_N + \tilde{g}(\hat{S}_N)\right) = \frac{2}{h}(\hat{S}_N - S_{N-\frac{1}{2}}), \tag{3.81}$$

where

$$\tilde{g}(S) = \begin{cases} g(S_*) & \text{for } S < S_*, \\ g(S) & \text{for } S_* \le S \le 1, \\ g(1) & \text{for } S > 1. \end{cases} \tag{3.82}$$

The second correction step has the form:

$$S_i = \begin{cases} S_* + \eta & \text{for } \hat{S}_i < S_* + \eta; \\ \hat{S}_i & \text{for } S_* + \eta \le \hat{S}_i \le 1 - \eta; \\ 1 - \eta & \text{for } \hat{S}_i > 1 - \eta; \end{cases} \tag{3.83}$$

for all $i = \{\overline{\frac{1}{2}, N - \frac{1}{2}}, N\}$. Here $\eta > 0$ is some small value which satisfies $\eta \to 0$ as $h \to 0$.

We note here, that the correction step in an implicit way defines the discrete analog of the function $\hat{c}(S)$.

3.2.3 Proof of convergence

To prove the convergence of discrete solution of (3.74)–(3.83) to continuous solution of (3.71), (3.72), first we consider Eqs. (3.74)–(3.77) separately from Eqs. (3.78)–(3.83). In the following two lemmas we prove existence of solutions of each of these problems.

Remark 3.2.2. *Due to complexity of the presented nonlinear problem there are difficulties for obtaining uniqueness results for both continuous and discrete problems. In this work we do not study this aspect of the problem.*

Let us introduce the following notation:

$$S_{-\frac{1}{2}} = S_0, \quad S_{N+\frac{1}{2}} = S_N.$$

Lemma 3.2.1. *Let Assumption 3.2.1 be satisfied and let $\mathcal{T}$ be the mesh on $(0,1)$ (see Definition 2.2.1). Let $\mathbf{S} = (S_{-\frac{1}{2}}, S_{\frac{1}{2}}, \dots, S_{N+\frac{1}{2}})^T \in \mathbb{R}^{N+2}$ be some given vector, such that $S_{i-\frac{1}{2}} \in [S_* + \eta, 1-\eta]$ for all $i = \overline{0, N+1}$. Then, there exists a unique solution of (3.74)–(3.77), $\mathbf{y} = (y_0, y_1, \dots, y_N)^T \in \mathbb{R}^{N+1}$, such that:*

$$\sum_{i=0}^{N-1} \frac{(y_{i+1} - y_i)^2}{h} \le C_1^2 = \left(\frac{2q^*}{b_* k_*}\right)^2,$$

where $q_* \le q_{i+\frac{1}{2}} \le q^*$ and $b_* \le b_{i+\frac{1}{2}} \le b^*$ for all $i = \overline{0, N-1}$.

Proof: Following the proof of Lemma 3.1.1 and 3.1.2 from Section 3.1.3 we obtain the required result. ■

For any given vector $\mathbf{v} = (v_{-\frac{1}{2}}, v_{\frac{1}{2}}, ..., v_{N+\frac{1}{2}}) \in \mathbb{R}^{N+2}$ we introduce the following seminorm:

$$\|D\mathbf{v}\|_{L_2((0,1))} = \left(\sum_{i=0}^{N} \frac{(v_{i+\frac{1}{2}} - v_{i-\frac{1}{2}})^2}{h_i}\right)^{\frac{1}{2}},$$

where $h_0 = h/2$, $h_i = h$ for all $i = \overline{1, N-1}$, $h_N = h/2$.

Lemma 3.2.2. *Let Assumption 3.2.1 be satisfied and let $\mathcal{T}$ be the mesh on $(0,1)$ (see Definition 2.2.1). Let $\mathbf{y} = (y_0, y_1, \dots, y_N)^T \in \mathbb{R}^{N+1}$ be some given vector, such that $|y_i| \le C_1$ for all $i = \overline{0, N}$. Then, there exists a solution of (3.78)–(3.83), $\mathbf{S} = (S_{-\frac{1}{2}}, S_{\frac{1}{2}}, \dots, S_{N+\frac{1}{2}})^T \in \mathbb{R}^{N+2}$, such that:*

$$S_{i-\frac{1}{2}} \in [S_* + \eta, 1-\eta], \quad i = \overline{0, N+1} \tag{3.84}$$

and

$$\|D\mathbf{S}\|_{L_2((0,1))} \le C_2 = \frac{C_1 + g^*}{c}, \tag{3.85}$$

where $g^* = p^* - p_c^{stat}(C_0)$.

Proof: The system (3.79)–(3.81) can be considered as a Cauchy problem with the initial condition (3.78). Hence, we can solve these equations sequentially. At first, let us consider Eq. (3.79) in the following form:

$$\hat{S}_{\frac{1}{2}} = S_{-\frac{1}{2}} + \frac{h}{2c}\left(y_0 + \tilde{g}(\hat{S}_{\frac{1}{2}})\right). \tag{3.86}$$

In Eq. (3.86), $S_{-\frac{1}{2}}$ is given by (3.78). We denote the right-hand side of Eq. (3.86) as $G(\hat{S}_{\frac{1}{2}})$. We notice that G is a continuous function of $\hat{S}_{\frac{1}{2}}$. It is easy to see, that:

$$|G(v)| \leq C_0 + \frac{h}{2c}(C_1 + g^*),$$

for any given v. It means $G(B_r) \subset B_r$, where $B_r \subset \mathbb{R}$ is a closed ball with radius $r = C_0 + \frac{h}{2c}(C_1 + g^*)$ and center 0. Using Brouwer's fixed point theorem we conclude that G has at least one fixed point in B_r, which is a solution of (3.86).

After the correction step (3.83) for value $S_{\frac{1}{2}}$ we have:

$$S_{\frac{1}{2}} \in [S_* + \eta, 1 - \eta]\,.$$

The same boundedness result can be obtained for every $S_{i-\frac{1}{2}}, \quad i = \overline{2, N+1}$.

It remains to prove estimate (3.85) for $\|D\mathbf{S}\|_{L_2((0,1))}$. Using Eqs. (3.80), (3.82), (3.83) we obtain:

$$\frac{\left|S_{i+\frac{1}{2}} - S_{i-\frac{1}{2}}\right|}{h} \leq \frac{\left|\hat{S}_{i+\frac{1}{2}} - S_{i-\frac{1}{2}}\right|}{h} \leq \frac{C_1 + g^*}{c}, \quad i = \overline{1, N-1}. \tag{3.87}$$

Considering Eqs. (3.79), (3.81) instead of (3.80), we obtain the same upper bound for $2\left|S_{\frac{1}{2}} - S_{-\frac{1}{2}}\right|/h$ and $2\left|S_{N+\frac{1}{2}} - S_{N-\frac{1}{2}}\right|/h$. Then, for $\|D\mathbf{S}\|^2_{L_2((0,1))}$ we have:

$$\begin{aligned}\|D\mathbf{S}\|^2_{L_2((0,1))} &\leq \left(\frac{C_1 + g^*}{c}\right)^2 \frac{h}{2} + \sum_{i=1}^{N-1} \left(\frac{C_1 + g^*}{c}\right)^2 h + \left(\frac{C_1 + g^*}{c}\right)^2 \frac{h}{2} \\ &= \left(\frac{C_1 + g^*}{c}\right)^2 h \left(\frac{1}{2} + (N-1) + \frac{1}{2}\right) = \left(\frac{C_1 + g^*}{c}\right)^2.\end{aligned}$$

■

Lemma 3.2.3. (Existence) *Let Assumption 3.2.1 be satisfied and let $\mathcal{T}$ be the mesh on $(0,1)$ (see Definition 2.2.1). Then, there exist a pair of vectors $\mathbf{y} = (y_0, y_1, \ldots, y_N)^T \in \mathbb{R}^{N+1}$ and $\mathbf{S} = (S_{-\frac{1}{2}}, S_{\frac{1}{2}}, \ldots, S_{N+\frac{1}{2}})^T \in \mathbb{R}^{N+2}$, which is solution of the system of Eqs. (3.74)–(3.83).*

Proof: Let us consider auxiliary system of equations obtained from system (3.74)–(3.77) by replacing $\mathbf{S}$ with a vector $\mathbf{v}$ and from system (3.78)–(3.83) by replacing $\mathbf{y}$ with a vector $\mathbf{u}$. The vectors $\mathbf{v}$ and $\mathbf{u}$ satisfy:

$$\mathbf{u} = (u_0, u_1, \ldots, u_N)^T \in \mathbb{R}^{N+1}, \quad |u_i| \leq C_1 \text{ for all } i = \overline{0, N}; \tag{3.88}$$

$$\mathbf{v} = (v_{-\frac{1}{2}}, v_{\frac{1}{2}}, \ldots, v_{N+\frac{1}{2}})^T \in \mathbb{R}^{N+2}, \quad v_{i-\frac{1}{2}} \in [S_* + \eta, 1 - \eta] \text{ for all } i = \overline{0, N+1}. \tag{3.89}$$

Then, it follows from Lemmas 3.2.1, 3.2.2 that there exists an operator $T : \mathbb{R}^{2N+3} \to \mathbb{R}^{2N+3}$ such that:

$$\chi = T(\theta), \tag{3.90}$$

where $\chi = (\mathbf{y}, \mathbf{S})^T \in \mathbb{R}^{2N+3}$ and $\theta = (\mathbf{u}, \mathbf{v})^T \in \mathbb{R}^{2N+3}$. Let us assume that operator T is continuous (we will prove this property later). For any given vector $\psi = (\mathbf{x}, \mathbf{z})^T \in \mathbb{R}^{2N+3}$ we define the following norm:

$$\|\psi\|_{L_2((0,1))} = \left(\sum_{i=0}^{N} x_i^2 h_i + \sum_{i=0}^{N} z_{i+\frac{1}{2}}^2 h_i \right)^{\frac{1}{2}}, \tag{3.91}$$

where $h_0 = h_N = h/2$, $h_i = h$ for all $i = \overline{1, N-1}$ and:

$$\mathbf{x} = (x_0, x_1, \ldots, x_N)^T \in \mathbb{R}^{N+1}, \quad x_0 = 0; \tag{3.92}$$

$$\mathbf{z} = (z_{-\frac{1}{2}}, z_{\frac{1}{2}}, \ldots, z_{N+\frac{1}{2}})^T \in \mathbb{R}^{N+2}, \quad z_{-\frac{1}{2}} = C_0. \tag{3.93}$$

Then, for any $\theta = (\mathbf{u}, \mathbf{v})^T$ with $\mathbf{u}$ and $\mathbf{v}$, which satisfy (3.88), (3.89), it follows that

$$\|\theta\|_{L_2((0,1))} \leq C_3 = \left(C_1^2 + 1\right)^{\frac{1}{2}}.$$

Due to the properties of the finite volume scheme (3.74)–(3.83), we also have that:

$$\|T(\theta)\|_{L_2((0,1))} = \|\chi\|_{L_2((0,1))} \leq C_3.$$

Using Brouwer's fixed point theorem, we conclude that there exists a solution of the system of Eqs. (3.74)–(3.83).

In order to apply the fixed point theorem we have to show that operator T is continuous. We notice that operator T consists of two operators. The first operator $\mathbf{y} = T_y(\mathbf{S})$ is defined by system of Eqs. (3.74)–(3.77) with some given vector $\mathbf{S}$. Continuity of this operator is a standard result from theory of finite volume schemes and it follows from the coefficient stability of elliptic operators.

The second operator $\mathbf{S} = T_S(\mathbf{y})$ is defined by (3.78)–(3.83) with some given vector $\mathbf{y}$. Let us prove that T_S is continuous, if Assumptions 3.2.1 are satisfied. Let us consider two different input vectors $\mathbf{y}$ and $\mathbf{u}$ and denote the corresponding solutions by $\mathbf{S}^y = T_S(\mathbf{y})$ and $\mathbf{S}^u = T_S(\mathbf{u})$. We want to prove that for any $\epsilon > 0$ there exists $\delta = \delta_\epsilon > 0$ such that:

$$\|\mathbf{y} - \mathbf{u}\|_{1,L_2((0,1))} < \delta_\epsilon \implies \|\mathbf{S}^y - \mathbf{S}^u\|_{2,L_2((0,1))} < \epsilon, \tag{3.94}$$

where the norms are introduced as:

$$\|\mathbf{x}\|_{1,L_2((0,1))} = \left(\sum_{i=0}^{N} x_i^2 h_i\right)^{\frac{1}{2}}, \quad \|\mathbf{z}\|_{2,L_2((0,1))} = \left(\sum_{i=0}^{N} z_{i+\frac{1}{2}}^2 h_i\right)^{\frac{1}{2}},$$

and $\mathbf{x}$, $\mathbf{z}$ satisfy conditions (3.92), (3.93). Let us write Eqs. (3.81), $i = \overline{1, N-1}$ in the following form:

$$\hat{S}^y_{i+\frac{1}{2}} - S^y_{i-\frac{1}{2}} = \frac{h}{c}\tilde{g}(\hat{S}^y_{i+\frac{1}{2}}) + \frac{h}{c}y_i, \tag{3.95}$$

$$\hat{S}^u_{i+\frac{1}{2}} - S^u_{i-\frac{1}{2}} = \frac{h}{c}\tilde{g}(\hat{S}^u_{i+\frac{1}{2}}) + \frac{h}{c}u_i. \tag{3.96}$$

Introducing vectors $\hat{e}_{i+\frac{1}{2}} = \hat{S}^y_{i+\frac{1}{2}} - \hat{S}^u_{i+\frac{1}{2}}$, $e_{i-\frac{1}{2}} = S^y_{i-\frac{1}{2}} - S^u_{i-\frac{1}{2}}$, and subtracting Eq. (3.96) from (3.95), we get:

$$\hat{e}_{i+\frac{1}{2}} - e_{i-\frac{1}{2}} = \frac{h}{c}\left(\tilde{g}(\hat{S}^y_{i+\frac{1}{2}}) - \tilde{g}(\hat{S}^u_{i+\frac{1}{2}})\right) + \frac{h}{c}(y_i - u_i). \tag{3.97}$$

Taking into account the definition of function $\tilde{g}$ in (3.82), we get the estimate:

$$\tilde{g}(\hat{S}^y_{i+\frac{1}{2}}) - \tilde{g}(\hat{S}^u_{i+\frac{1}{2}}) = g'(S^{\xi}_{i+\frac{1}{2}})\theta\hat{e}_{i+\frac{1}{2}},$$

where $S_* \le S^{\xi}_{i+\frac{1}{2}} \le 1$ and $0 \le \theta \le 1$. Since the function g is a decreasing function, then $g'(S^{\xi}_{i+\frac{1}{2}}) < 0$.

It follows from the definition of the restriction operator (3.83) that $|e_{i+\frac{1}{2}}| \le |\hat{e}_{i+\frac{1}{2}}|$. Then, using (3.97), we get:

$$\left|e_{i+\frac{1}{2}}\right| \le \left|\hat{e}_{i+\frac{1}{2}}\right| \le \left|1 - \frac{h}{c}g'(S^{\xi}_{i+\frac{1}{2}})\theta\right|\left|\hat{e}_{i+\frac{1}{2}}\right| \le \left|e_{i-\frac{1}{2}}\right| + \frac{h}{c}|y_i - u_i|. \tag{3.98}$$

Similarly from Eqs. (3.79), (3.81) we obtain:

$$\left|e_{\frac{1}{2}}\right| \le \frac{h}{2c}\left|y_0 - u_0\right|, \quad \left|e_{N+\frac{1}{2}}\right| \le \left|e_{N-\frac{1}{2}}\right| + \frac{h}{2c}\left|y_N - u_N\right|. \tag{3.99}$$

Using sequentially inequalities (3.98), (3.99) and the Cauchy–Schwartz inequality, we have:

$$\begin{aligned}\left|e_{j+\frac{1}{2}}\right| \le \sum_{i=0}^{N}\frac{h_i}{c}|y_i - u_i| &\le \frac{1}{c}\left(\sum_{i=0}^{N}(y_i - u_i)^2 h_i \sum_{i=0}^{N} h_i\right)^{\frac{1}{2}} \\ &= \frac{1}{c}\|\mathbf{y} - \mathbf{u}\|_{1,L_2((0,1))}, \quad j = 0, \ldots, N.\end{aligned} \tag{3.100}$$

From (3.100) we obtain:

$$\|\mathbf{e}\|^2_{2,L_2((0,1))} = \sum_{i=0}^{N} |e_{i+\frac{1}{2}}|^2 h_i \leq \frac{1}{c^2}\|\mathbf{y}-\mathbf{u}\|^2_{1,L_2((0,1))},$$

where h_i is defined in (3.91). Hence, statement (3.94) is proven and T is a continuous operator. ■

Lemma 3.2.4. (Compactness) *Let Assumptions 3.2.1 be satisfied and let $\mathcal{T}$ be a mesh on $(0,1)$ (see Definition 2.2.1). Let the pair of vectors $\mathbf{y} = (y_0, y_1, \ldots, y_N)^T \in \mathbb{R}^{N+1}$ and $\mathbf{S} = (S_{-\frac{1}{2}}, S_{\frac{1}{2}}, \ldots, S_{N+\frac{1}{2}})^T \in \mathbb{R}^{N+2}$ be a solution of (3.74)–(3.83). Let $y_{\mathcal{T}} : (0,1) \to \mathbb{R}$ be $y_{\mathcal{T}}(x) = y_i$ and let $S_{\mathcal{T}} : (0,1) \to [S_* + \eta, 1-\eta]$ be $S_{\mathcal{T}}(x) = S_{i+\frac{1}{2}}$ for $x \in \mathcal{K}_i$, $i = \overline{0,N}$. Then, the sets $y_{\mathcal{T}}$ and $S_{\mathcal{T}}$ are relatively compact in $L^2((0,1))$. Furthermore, if $y_{\mathcal{T}_n} \to y$ and $S_{\mathcal{T}_n} \to S$ in $L^2((0,1))$ and $h_n \to 0$ as $n \to \infty$, then, $y \in H^1_{0-}((0,1))$ and $S \in H^1((0,1))$.*

Proof: All statements for $y_{\mathcal{T}}$ were proven in Lemma 3.1.3 in Section 3.1.3. Therefore, here we are concerned only with the function $S_{\mathcal{T}}$.

Using Kolmogorov compactness theorem, it is sufficient to show that $S_{\mathcal{T}}$ is relatively compact in $L^2((0,1))$:

- the set $S_{\mathcal{T}}$ is bounded in $L^2(\mathbb{R})$ for all $\mathcal{T}$,
- $\|S_{\mathcal{T}}(\cdot+\nu) - S_{\mathcal{T}}\|_{L^2(\mathbb{R})} \to 0$ as $\nu \to 0$ uniformly.

Step 1. Function $S_{\mathcal{T}}$ can be redefined as $S_{\mathcal{T}}(x) = S_{i+\frac{1}{2}}$ if $x \in \mathcal{K}_i$, $i = \overline{0,N}$, $S_{\mathcal{T}}(x_0) = S_{-\frac{1}{2}}$, otherwise $S_{\mathcal{T}} = 0$. Then, using (3.84) it follows immediately that the set $S_{\mathcal{T}}$ for all $\mathcal{T}$ is bounded in $L^2(\mathbb{R})$.

Step 2. Let $0 < \nu < 1$. We define $\chi_i : \mathbb{R} \to \mathbb{R}$ for $i = \overline{-1, N+1}$ such that:

$$\begin{aligned}
&\chi_{-\frac{1}{2}}(x) = 1 \text{ if } x_0 \in [x, x+\nu], && \chi_{-\frac{1}{2}}(x) = 0, \text{ otherwise;}\\
&\chi_{i+\frac{1}{2}}(x) = 1, \text{ if } x_{i+\frac{1}{2}} \in [x, x+\nu], && \chi_{i+\frac{1}{2}}(x) = 0, \text{ otherwise, } i = \overline{0, N-1};\\
&\chi_{N+\frac{1}{2}}(x) = 1; \text{ if } x_N \in [x, x+\nu], && \chi_{N+\frac{1}{2}}(x) = 0, \text{ otherwise.}
\end{aligned}$$

Then, for all $x \in \mathbb{R}$ we have:

$$\begin{aligned}
(S_{\mathcal{T}}(x+\nu) - S_{\mathcal{T}}(x))^2 &\leq \left(S_{-\frac{1}{2}}\chi_{-\frac{1}{2}} + \sum_{i=0}^{N} \left| S_{i+\frac{1}{2}} - S_{i-\frac{1}{2}} \right| \chi_{i-\frac{1}{2}} + S_{N+\frac{1}{2}}\chi_{N+\frac{1}{2}} \right)^2\\
&\leq 3S^2_{-\frac{1}{2}}\chi_{-\frac{1}{2}} + 3\left(\sum_{i=0}^{N} \frac{\left(S_{i+\frac{1}{2}} - S_{i-\frac{1}{2}}\right)^2}{h_i} \chi_{i-\frac{1}{2}} \right) \left(\sum_{i=0}^{N} h_i \chi_{i-\frac{1}{2}} \right) + 3S^2_{N+\frac{1}{2}}\chi_{N+\frac{1}{2}},
\end{aligned} \tag{3.101}$$

where $h_0 = h_N = h/2$ and $h_i = h$ for all $i = \overline{1, N-1}$. Integrating (3.101) over $\mathbb{R}$ we obtain:

$$\begin{aligned}\|S_{\mathcal{T}}(\cdot+\nu) - S_{\mathcal{T}}\|^2_{L^2(\mathbb{R})} &\le 6\nu + 3(\nu+2h)\int_{\mathbb{R}}\left(\sum_{i=0}^{N}\frac{\left(S_{i+\frac{1}{2}} - S_{i-\frac{1}{2}}\right)^2}{h_i}\chi_{i-\frac{1}{2}}\right)dx \\ &\le 6\nu + 3(\nu+2h)\sum_{i=0}^{N}\frac{\left(S_{i+\frac{1}{2}} - S_{i-\frac{1}{2}}\right)^2}{h_i}\int_{\mathbb{R}}\chi_{i-\frac{1}{2}}dx \\ &\le 6\nu + 3\nu(\nu+2h)C_2^2.\end{aligned}$$

Since $\nu < 1$ and $h < 1$ we conclude that $\|S_{\mathcal{T}}(\cdot+\nu) - S_{\mathcal{T}}\|^2_{L^2(\mathbb{R})} \le \hat{C}\nu$,where $\hat{C} = const > 0$. Hence, the second condition of Kolmogorov compactness theorem is proven.

Step 3. Here we want to prove that function $S(x)$ belongs to $H^1((0,1))$. At first let us prove that $(S_{\mathcal{T}_n}(x+h_n) - S_{\mathcal{T}_n}(x))/h_n$ converges to $\partial S/\partial x$ for all $x \in (-\infty, 1)$ in a weak sense when $h_n \to 0$ as $n \to \infty$. Let $\varphi \in C_0^\infty((-\infty,1))$ and $\operatorname{supp}\varphi \subset (0,1)$. The discrete function $\varphi_{\mathcal{T}_n}$ is defined in the following way:

$$\varphi_{\mathcal{T}_n}(x) = \begin{cases}\varphi_i = \varphi(x_i) & \text{if } x \in \mathcal{K}_i, i = \overline{0,N};\\ 0, & \text{otherwise.}\end{cases}$$

Let us redefine function $S_{\mathcal{T}_n}$ such that $S_{\mathcal{T}_n} = S_{N+\frac{1}{2}}$ if $x \in [x_N, x_{N+\frac{1}{2}}]$ and $S_{\mathcal{T}_n} = S_{N+\frac{3}{2}} = S_{N+\frac{1}{2}}$ if $x \in [x_{N+\frac{1}{2}}, x_{N+\frac{3}{2}}]$. Then, we have:

$$\begin{aligned}\left(\frac{S_{\mathcal{T}_n}(\cdot+h_n) - S_{\mathcal{T}_n}}{h_n}, \varphi_{\mathcal{T}_n}\right)_{L_2((-\infty,1))} &= \int_{-\infty}^{1}\frac{S_{\mathcal{T}_n}(x+h_n) - S_{\mathcal{T}_n}(x)}{h_n}\varphi_{\mathcal{T}_n}(x)dx \\ &= \sum_{i=0}^{N}\frac{S_{i+\frac{3}{2}} - S_{i+\frac{1}{2}}}{h_n}\varphi_i h_n = -\sum_{i=1}^{N}S_{i+\frac{1}{2}}\frac{\varphi_i - \varphi_{i-1}}{h_n}h_n \\ &= -\int_{-\infty}^{1}S_{\mathcal{T}_n}(x)\frac{\varphi_{\mathcal{T}_n}(x) - \varphi_{\mathcal{T}_n}(x-h_n)}{h_n}dx \\ &= -\left(S_{\mathcal{T}_n}, \frac{\varphi_{\mathcal{T}_n} - \varphi_{\mathcal{T}_n}(\cdot-h_n)}{h_n}\right)_{L_2((-\infty,1))}.\end{aligned} \tag{3.102}$$

Functions $\varphi_{\mathcal{T}_n}$ and $(\varphi_{\mathcal{T}_n} - \varphi_{\mathcal{T}_n}(\cdot - h_n))/h_n$ strongly converge to φ and $\partial\varphi/\partial x$, respectively. We also know that $S_{\mathcal{T}_n} \to S$ in $L_2(\mathbb{R})$ as $n \to \infty$. On the other hand, function $(S_{\mathcal{T}_n}(\cdot+h_n) - S_{\mathcal{T}_n})/h_n$ is bounded in $L_2(\mathbb{R})$ (see (3.85)). Then, for any sequence of meshes $(\mathcal{T}_n)_{n\in\mathbb{N}}$ such that $h_n \to 0$ as $n \to$

∞, there exists a subsequence, still denoted by $(\mathcal{T}_n)_{n\in\mathbb{N}}$, such that function $(S_{\mathcal{T}_n}(\cdot+h_n)-S_{\mathcal{T}_n})/h_n$ weakly converges to some function. Then, passing to the limit in (2.14) and using the definition of the weak derivative we obtain that $(S_{\mathcal{T}_n}(\cdot+h_n)-S_{\mathcal{T}_n})/h_n$ converge weakly to $\partial S/\partial x$.

Using (3.85) we have:

$$\left\|\frac{\partial S}{\partial x}\right\|_{L_2((-\infty,1))} \leq C_2.$$

We also have that $\partial S/\partial x = 0$ if $x \in (-\infty, 0)$. Hence, the restriction of S to $(0,1)$ is in $H^1((0,1))$. Lemma 3.2.4 is proven. ■

In order to prove the main convergence theorem we introduce one more assumption.

Assumption 3.2.3. *The domain Ω^1, where single-phase flow occurs, consists of a finite number of simply connected subdomains.*

This assumption does not contradict physical meaning of the infiltration process.

Theorem 3.2.5. *Let Assumptions 3.2.1, 3.2.2 and 3.2.3 be satisfied. For the mesh $\mathcal{T}$ on $(0,1)$ let the pair of vectors $\mathbf{y} = (y_0, y_1, \dots, y_N)^T \in \mathbb{R}^{N+1}$ and $\mathbf{S} = (S_{-\frac{1}{2}}, S_{\frac{1}{2}}, \dots, S_{N+\frac{1}{2}})^T \in \mathbb{R}^{N+2}$ be a solution of (3.74)–(3.83) and let $y_{\mathcal{T}}$ and $S_{\mathcal{T}}$ be defined as*

$$y_{\mathcal{T}} : (0,1) \to \mathbb{R} \text{ by } y_{\mathcal{T}}(x) = y_i, \text{ if } x \in \mathcal{K}_i, \quad i = \overline{0,N};$$
$$S_{\mathcal{T}} : (0,1) \to (S_*, 1] \text{ by } S_{\mathcal{T}}(x) = S_{i+\frac{1}{2}}, \text{ if } x \in \mathcal{K}_i, \quad i = \overline{0,N}.$$

Then, for any sequence of meshes $(\mathcal{T}_n)_{n\in\mathbb{R}}$ such that $h_n \to 0$, as $n \to \infty$, there exists a subsequence, still denoted by $(\mathcal{T}_n)_{n\in\mathbb{R}}$, such that $y_{\mathcal{T}_n} \to y$ and $S_{\mathcal{T}_n} \to S$ in $L_2((0,1))$, as $n \to \infty$, where $y \in H^1_{0-}((0,1))$ and $S \in H^1((0,1))$ are solutions to the system (3.71), (3.72).

Proof: Let $(\mathcal{T}_n)_{n\in\mathbb{N}}$ be a sequence of meshes on $(0,1)$ such that $h_n \to 0$, as $n \to \infty$. Lemma 3.2.3 gives us the existence of solution of the problem (3.74)–(3.83) for any mesh $\mathcal{T}_n$ from sequence $(\mathcal{T}_n)_{n\in\mathbb{N}}$. Lemma 3.2.4 guarantees that there exists a subsequence, still denoted by $(\mathcal{T}_n)_{n\in\mathbb{N}}$, such that $y_{\mathcal{T}_n} \to y$ and $S_{\mathcal{T}_n} \to S$ in $L_2((0,1))$ as $n \to \infty$ and that $y \in H^1_{0-}((0,1))$ and $S \in H^1((0,1))$.

Following the proof of Theorem 3.1.4 from Section 3.1.3 we obtain that $y \in H^1_{0-}$ is a solution to (3.71) for a any given $S \in L_2((0,1))$. In order to conclude the proof we have to show that $S \in L_2((0,1))$ is a solution of (3.72) for any given $y \in H^1_{0-}$.

Let $\varphi \in C^\infty([0,1])$ such that $\varphi(0) = 0$. Then the weak formulation (3.72) can be written in the following way:

$$-T_1 - T_2 + T_3 = 0,$$

where:

$$T_1 = \int_{\Omega^2} \frac{1}{c}\left(y + g(S)\right)\varphi dx, \quad T_2 = \int_0^1 S\frac{\partial\varphi}{\partial x}dx, \quad T_3 = S(1)\varphi(1),$$

where domain Ω^2 is defined in the following way:

$$\Omega^2 = \{x \in (0,1) : S(x) \in (S_*, 1)\}. \tag{3.103}$$

Taking into account two-step algorithm (3.78)–(3.83) we notice that solution $S_{i-\frac{1}{2}}$ for $i = \overline{0, N+1}$ satisfies:

$$S_{-\frac{1}{2}} = C_0, \tag{3.104}$$

$$\frac{1}{c}\left(y_i + g(S_{i+\frac{1}{2}})\right) = \frac{1}{h_i^n}(S_{i+\frac{1}{2}} - S_{i-\frac{1}{2}}), \quad i \in U, \tag{3.105}$$

$$S_{i+\frac{1}{2}} - S_* - \eta_n = 0, \quad i \in F_*, \tag{3.106}$$

$$S_{i+\frac{1}{2}} - 1 + \eta_n = 0, \quad i \in F^*; \tag{3.107}$$

where η_n corresponds to mesh $\mathcal{T}_n$, $U \cup F_* \cup F^* = \overline{0, N}$ and:

$$U = \{i : S_* + \eta_n < \hat{S}_{i+\frac{1}{2}} < 1 - \eta_n\}, \tag{3.108}$$

$$F_* = \{i : \hat{S}_{i+\frac{1}{2}} \le S_* + \eta_n\}, \tag{3.109}$$

$$F^* = \{i : \hat{S}_{i+\frac{1}{2}} \ge 1 - \eta_n\}. \tag{3.110}$$

We rewrite Eqs. (3.106), (3.107) in the following way:

$$\frac{1}{h_i^n}\left(S_{i+\frac{1}{2}} - S_{i-\frac{1}{2}}\right) + \frac{1}{h_i^n}\left(S_{i-\frac{1}{2}} - S_* - \eta_n\right) = 0, \quad i \in F_*, \tag{3.111}$$

$$\frac{1}{h_i^n}\left(S_{i+\frac{1}{2}} - S_{i-\frac{1}{2}}\right) + \frac{1}{h_i^n}\left(S_{i-\frac{1}{2}} - 1 + \eta_n\right) = 0, \quad i \in F^*. \tag{3.112}$$

Let $\mathcal{T}_n$ be the mesh on $[0,1]$ (see Definition 2.2.1), which is one of the meshes of the subsequence $(\mathcal{T}_n)_{n\in\mathbb{N}}$ and $\varphi_i = \varphi(x_i)$, $i = \overline{0, N}$. If $\mathbf{S} = \left(S_{-\frac{1}{2}}, S_{\frac{1}{2}}, \ldots, S_{N+\frac{1}{2}}\right)^T$ is a solution of (3.104)–(3.107) for some given $\mathbf{y} = (y_0, y_1, \ldots, y_N)^T$ on the mesh $\mathcal{T}_n$, multiplying (3.105), (3.111), (3.112) by $\varphi_i h_i^n$ for all $i = \overline{0, N}$ and summing over $i = \overline{0, N}$ we get

$$\begin{aligned} &-\sum_{i\in U}\frac{1}{c}\left[y_i + g(S_{i+\frac{1}{2}})\right]\varphi_i h_i^n + \sum_{i=0}^{N}\frac{1}{h_i^n}\left(S_{i+\frac{1}{2}} - S_{i-\frac{1}{2}}\right)\varphi_i h_i^n \\ &+\sum_{i\in F_*}\frac{1}{h_i^n}\left(S_{i-\frac{1}{2}} - S_* - \eta_n\right)\varphi_i h_i^n + \sum_{i\in F^*}\frac{1}{h_i^n}\left(S_{i-\frac{1}{2}} - 1 + \eta_n\right)\varphi_i h_i^n = 0. \end{aligned} \tag{3.113}$$

Reordering summation in the second term of (3.113), we obtain:

$$-\hat{T}_1^n - \hat{T}_2^n + \hat{T}_3^n + \hat{T}_4^n = 0, \tag{3.114}$$

$$\hat{T}_1^n = \sum_{i\in U} \frac{1}{c}\left[y_i + g(S_{i+\frac{1}{2}})\right]\varphi_i h_i^n, \tag{3.115}$$

$$\hat{T}_2^n = \sum_{i=0}^{N-1} S_{i+\frac{1}{2}} \frac{\varphi_{i+1}-\varphi_i}{h_i^n} h_i^n, \tag{3.116}$$

$$\hat{T}_3^n = S_{N+\frac{1}{2}}\varphi_N, \tag{3.117}$$

$$\hat{T}_4^n = \sum_{i\in F_*} \frac{S_{i-\frac{1}{2}} - S_* - \eta_n}{h_i^n}\varphi_i h_i^n + \sum_{i\in F^*} \frac{S_{i-\frac{1}{2}} - 1 + \eta_n}{h_i^n}\varphi_i h_i^n. \tag{3.118}$$

Let us consider the terms in Eq. (3.114) separately. Term $\hat{T}_1^n$ can be written down in the following integral formulation:

$$\hat{T}_1^n = \int_{\Omega^{n,2}} \frac{1}{c}\left(y_{\mathcal{T}_n} + g(S_{\mathcal{T}_n})\right)\varphi_{\mathcal{T}_n} dx,$$

where $\varphi_{\mathcal{T}_n} = \varphi_i$ if $x \in \mathcal{K}_i$, $i = \overline{0,N}$, domain $\Omega^{n,2} = \cup_{i\in U}\mathcal{K}_i$. Using (3.108), the domain $\Omega^{n,2}$ can be represented in the following form:

$$\begin{aligned}\Omega^{n,2} &= \{\mathcal{K}_i, i : \hat{S}_{i+\frac{1}{2}} \in (S_* + \eta_n, 1-\eta_n)\}\\ &\overset{(3.83)}{=} \{\mathcal{K}_i, i : S_{i+\frac{1}{2}} \in (S_* + \eta_n, 1-\eta_n)\}\\ &= \{x \in \Omega : S_{\mathcal{T}_n}(x) \in (S_* + \eta_n, 1-\eta_n)\}.\end{aligned} \tag{3.119}$$

Let us now consider the difference $\left|T_1 - \hat{T}_1^n\right|$:

$$\begin{aligned}\left|T_1 - \hat{T}_1^n\right| &= \left|\int_{\Omega^2}\frac{1}{c}\left(y + g(S)\right)\varphi dx - \int_{\Omega^{n,2}}\frac{1}{c}\left(y_{\mathcal{T}_n} + g(S_{\mathcal{T}_n})\right)\varphi_{\mathcal{T}_n} dx\right|\\ &< \left|\int_{\Omega^2}\frac{1}{c}\left(y + g(S)\right)\varphi dx - \int_{\Omega^{n,2}}\frac{1}{c}\left(y + g(S)\right)\varphi dx\right|\\ &+ \int_{\Omega^{n,2}}\left|\frac{1}{c}\left(\left(y_{\mathcal{T}_n} + g(S_{\mathcal{T}_n})\right)\varphi_{\mathcal{T}_n} - \left(y + g(S)\right)\varphi\right)\right| dx\\ &\le \left|\int_{\Omega^2\oplus\Omega^{n,2}}\frac{1}{c}\left(y + g(S)\right)\varphi dx\right|\\ &+ \int_{\Omega}\left|\frac{1}{c}\left(\left(y_{\mathcal{T}_n} + g(S_{\mathcal{T}_n})\right)\varphi_{\mathcal{T}_n} - \left(y + g(S)\right)\varphi\right)\right| dx.\end{aligned} \tag{3.120}$$

The second term on the right-hand side in inequality (3.120) converges to zero as $n \to \infty$. To prove that the first term on the right-hand side also converges to zero as $n \to \infty$ we have to show that for any $\varepsilon > 0$ there exists $N^\varepsilon \in \mathbb{N}$ such that:

$$\int_{\Omega^2 \oplus \Omega^{n,2}} dx < \varepsilon \text{ for all } n \geq N^\varepsilon. \tag{3.121}$$

This condition is sufficient, since all functions under the integral in (3.120) are bounded.

It was shown in Lemma 3.2.4 that $S_{\mathcal{T}_n} \to S$ in $L_2((0,1))$, which means that it also converges in measure. Then, for any $\delta > 0$ and $\epsilon > 0$ there exists $N \in \mathbb{N}$ such that:

$$\text{meas}\left(\{x \in \Omega : |S_{\mathcal{T}_n}(x) - S(x)| > \delta\}\right) < \epsilon, \text{ for all } n \geq N,$$

where $\Omega = (0,1)$. To simplify the notations we suppose that $\delta = \epsilon$ then definition of convergence in measure yields for any $\delta > 0$ there exists $N = N(\delta) \in \mathbb{N}$ such that:

$$\text{meas}\left(\{x \in \Omega : |S_{\mathcal{T}_n}(x) - S(x)| > \delta\}\right) < \delta, \text{ for all } n \geq N. \tag{3.122}$$

Using (3.122) we define two subsets of Ω in the following way:

$$\Omega^\delta = \{x \in \Omega : |S_{\mathcal{T}_n}(x) - S(x)| \leq \delta\}, \tag{3.123}$$

$$\tilde{\Omega}^\delta = \Omega \setminus \Omega^\delta = \{x \in \Omega : |S_{\mathcal{T}_n}(x) - S(x)| > \delta\}. \tag{3.124}$$

Next we consider the integral (3.121). Using an indicator function, namely $\mathbf{1}_A(x) = 1$, if $x \in A$, and $\mathbf{1}_A(x) = 0$, if $x \notin A$, we obtain:

$$\int_{\Omega^2 \oplus \Omega^{n,2}} dx = \int_\Omega \mathbf{1}_{\Omega^2 \oplus \Omega^{n,2}} dx = \int_\Omega \mathbf{1}_{\Omega^2 \setminus \Omega^{n,2}} dx + \int_\Omega \mathbf{1}_{\Omega^{n,2} \setminus \Omega^2} dx. \tag{3.125}$$

Using sets Ω^δ and $\tilde{\Omega}^\delta$, defined in (3.123), (3.124), we split integrals on the right hand side of (3.125) into four integrals:

$$\int_{\Omega^2 \oplus \Omega^{n,2}} dx = I_1 + I_2 + I_3 + I_4, \tag{3.126}$$

$$I_1 = \int_\Omega \mathbf{1}_{\left(\Omega^2 \cap \Omega^\delta\right) \setminus \left(\Omega^{n,2} \cap \Omega^\delta\right)} dx, \tag{3.127}$$

$$I_2 = \int_\Omega \mathbf{1}_{(\Omega^2 \setminus \Omega^{n,2}) \cap \tilde{\Omega}^\delta} dx, \tag{3.128}$$

$$I_3 = \int_\Omega \mathbf{1}_{\left(\Omega^{n,2} \cap \Omega^\delta\right) \setminus \left(\Omega^2 \cap \Omega^\delta\right)} dx, \tag{3.129}$$

$$I_4 = \int_\Omega \mathbf{1}_{(\Omega^{n,2} \setminus \Omega^2) \cap \tilde{\Omega}^\delta} dx. \tag{3.130}$$

Summing integrals I_2 and I_4 we have:

$$I_2 + I_4 = \int_\Omega \mathbf{1}_{(\Omega^2 \oplus \Omega^{n,2}) \cap \tilde{\Omega}^\delta} dx < \int_\Omega \mathbf{1}_{\tilde{\Omega}^\delta} < \delta.$$

Let us now consider the integral I_1. Introducing a set:

$$\tilde{\Omega}^2 = \left\{ x \in \Omega : S(x) \in (S_* + \delta + \eta_n, 1 - \delta - \eta_n) \right\},$$

it is easy to show that $\left(\tilde{\Omega}^2 \cap \Omega^\delta\right) \subseteq \left(\Omega^{n,2} \cap \Omega^\delta\right)$. Then, we notice that:

$$I_1 \leq \int_\Omega \mathbf{1}_{\left(\Omega^2 \cap \Omega^\delta\right) \setminus \left(\tilde{\Omega}^2 \cap \Omega^\delta\right)} dx = \int_\Omega \mathbf{1}_{\left(\Omega^2 \setminus \tilde{\Omega}^2\right) \cap \Omega^\delta} dx,$$

This integral is the measure of the domain where $|S_{\mathcal{T}_n}(x) - S(x)| \leq \delta$ and:

$$S \in (S_*, S_* + \delta + \eta_n] \cup [1 - \delta - \eta_n, 1). \tag{3.131}$$

Using Assumption 3.2.2 for small enough δ and η_n we notice that $I_1 \to 0$ as $n \to \infty$.

Concerning I_3, we choose δ such that $\delta < \eta_n$. Then, we have:

$$\left(\Omega^{n,2} \cap \Omega^\delta\right) \subseteq \left(\Omega^2 \cap \Omega^\delta\right)$$

and it follows that $I_3 = 0$.

Now we consider the term $\hat{T}_2^n$. Thanks to the regularity of the function φ, from Eq. (3.116) we may obtain:

$$\begin{aligned} \hat{T}_2^n &= \sum_{i=0}^{N-1} S_{i+\frac{1}{2}} \left.\frac{\partial \varphi}{\partial x}\right|_{x_i} h_n + \sum_{i=0}^{N-1} S_{i+\frac{1}{2}} R_i h_n \\ &= \int_0^{1-h_n/2} S_{\mathcal{T}_n} \left(\frac{\partial \varphi}{\partial x}\right)_{\mathcal{T}_n} dx + \sum_{i=0}^{N-1} S_{i+\frac{1}{2}} R_i h_n, \end{aligned} \tag{3.132}$$

where R_i is an error between the continuous derivative of φ and the discrete one at the point x_i. The function $\left(\frac{\partial \varphi}{\partial x}\right)_{\mathcal{T}_n}$ is equal to $\left.\frac{\partial \varphi}{\partial x}\right|_{x_i}$, if $x \in \mathcal{K}_i$, $i = \overline{0, N-1}$. Since all values $S_{i+\frac{1}{2}}$ are bounded the last term in (3.132) converges to zero as $n \to \infty$. Thus, we have $\hat{T}_2^n \to T_2$ as $n \to \infty$.

Using (3.117) we remark, that:

$$\hat{T}_3^n \to T_3 \text{ as } n \to \infty,$$

Now let us consider $\hat{T}_4^n$ defined by (3.118). We notice that sets F_* and F^* can be divided into the following subsets:

- $F_{*,U\to F_*} = \{i \in F_* : S_* + \eta_n < \hat{S}_{i-\frac{1}{2}} < 1 - \eta_n\}$,
- $F_{*,F^*\to F_*} = \{i \in F_* : \hat{S}_{i-\frac{1}{2}} \geq 1 - \eta_n\}$,
- $F_{*,internal} = \{i \in F_* : \hat{S}_{i-\frac{1}{2}} \leq S_* + \eta_n\}$,
- $F^*_{U\to F^*} = \{i \in F^* : S_* + \eta_n < \hat{S}_{i-\frac{1}{2}} < 1 - \eta_n\}$,
- $F^*_{F_*\to F^*} = \{i \in F^* : \hat{S}_{i-\frac{1}{2}} \leq S_* + \eta_n\}$,
- $F^*_{internal} = \{i \in F^* : \hat{S}_{i-\frac{1}{2}} \geq 1 - \eta_n\}$.

Then, term $\hat{T}_4^n$ yields:

$$\hat{T}_4^n = \sum_{i\in F_1} \frac{S_{i-\frac{1}{2}} - S_* - \eta_n}{h_i^n}\varphi_i h_i^n + \sum_{i\in F_2} \frac{S_{i-\frac{1}{2}} - 1 + \eta_n}{h_i^n}\varphi_i h_i^n,$$

$$F_1 = F_{*,U\to F_*} \cup F_{*,F^*\to F_*}, \quad F_2 = F^*_{U\to F^*} \cup F^*_{F_*\to F^*},$$

since for all $i \in F_{*,internal}$ saturation $S_{i-\frac{1}{2}}$ is equal to constant S_* and for all $i \in F^*_{internal}$ saturation $S_{i-\frac{1}{2}}$ is equal to constant 1.

Using inequalities (3.87) for $\hat{T}_4^n$ we have:

$$\left|\hat{T}_4^n\right| \leq \sum_{i\in F_1\cup F_2} \frac{\left|S_{i-\frac{1}{2}} - \hat{S}_{i+\frac{1}{2}}\right|}{h_i^n}|\varphi_i|h_i^n \leq \frac{C_1 + g^*}{c}\varphi^* h_n \sum_{i\in F_1\cup F_2} 1,$$

where function φ is bounded by constant $\varphi^* > 0$ since it is a continuous function on $[0, 1]$.

Since domain Ω^1 consists of a finite number of simply connected subdomains and each subdomain corresponds to one element of set $F_1 \cup F_2$, the number of elements of set $F_1 \cup F_2$ does not depend on discretization. Then, we obtain:

$$\left|\hat{T}_4^n\right| \to 0 \text{ as } n \to \infty. \tag{3.133}$$

Hence, the theorem is proven. ■

3.2.4 Numerical experiments

The goal of this section is to investigate numerically some typical examples. We are going to estimate the rate of convergence of the proposed numerical scheme (3.74)–(3.83) and verify Assumption 3.2.2. The test problems are selected such that fully saturated regions appear.

For the numerical experiments we consider three different cases of parameters which are typical for a paper layer during a production process. All information on input data is presented in Table 3.2 and in Figs. 3.5 and 3.6. Note that the input data satisfy Assumption 3.2.1. Obtained distributions of saturation and pressure are presented in Figs. 3.7 and 3.8, respectively.

Table 3.2: Experimental data for numerical experiment with the dynamic capillary pressure

Variable	Dimension	Test Case 1	Test Case 2	Test Case 3
C_0	$[\%]$	50	60	55
c	$[Pa\ m]$	16.7	200	125
k_r	$[-]$	$S^{3.5}$		
S_*	$[\%]$	10		
S_r	$[\%]$	$S_* - 1e-3$		
p_c^{stat}	$[Pa]$	$a(\phi-1)\left(\frac{1}{S-S_r}-\frac{1}{1-S_r}\right)^{1/2}$		
a	$[Pa]$	$\frac{P_0}{1-\phi_0}\left(\frac{1}{C_0-S_r}-\frac{1}{1-S_r}\right)^{-1/2}$		
P_0	$[Pa]$	-5000		
ϕ_0	$[\%]$	87.5		
Ω	$[m]$	$(-0.05, 0.05)$		

Exact solutions of the presented problems are unknown. To obtain the convergence rate, the reference solutions, by which the errors are measured, has been calculated on a very fine mesh $\mathcal{T}_*$. Corresponding distributions of saturation and pressure are denoted by $S_{\mathcal{T}_*}$ and $p_{\mathcal{T}_*}$. Then we define the relative error E_n between the discrete solution $S_{\mathcal{T}_n}$, $p_{\mathcal{T}_n}$ and the reference solution $S_{\mathcal{T}_*}$, $p_{\mathcal{T}_*}$ as:

$$E_n = \left(\frac{\|S_{\mathcal{T}_*} - S_{\mathcal{T}_n}\|^2_{L_2(\Omega)}}{\|S_{\mathcal{T}_*}\|^2_{L_2(\Omega)}} + \frac{\|p_{\mathcal{T}_*} - p_{\mathcal{T}_n}\|^2_{L_2(\Omega)}}{\|p_{\mathcal{T}_*}\|^2_{L_2(\Omega)}} \right)^{\frac{1}{2}}.$$

For each test case we consider three different values of $\eta_{\mathcal{T},i}$:

$$\eta_{\mathcal{T},i} = \frac{C_i h}{\operatorname{meas}\Omega}, \quad i = 1, 2, 3,$$

where $C_1 = 1$, $C_2 = 2$ and $C_3 = 10$. The results are given in Fig. 3.9. For all three cases and

different values of $\eta_{\mathcal{T},i}$ we observe a first-order convergence (the estimated order r is defined as:

$$r = \frac{1}{N_e - 2} \sum_{n=2}^{N_e-1} \frac{\log |E_{n+1}/E_n|}{\log |E_n/E_{n-1}|},$$

where N_e is the number of experiments).

In the proof of Theorem 3.2.5 we have obtained that the parameter η can not be too small, because the convergence of the measure of the domain with single-phase flow regime depends on it. So we carry out numerical experiments to estimate the behavior of the domain measure convergence for different values of η. The reference domain with single-phase water flow is denoted by $\Omega^{*,1}$. Then, error M_n between the measure of the reference domain $\Omega^{*,1}$ and the measure of the domain for a current mesh $\Omega^{n,1}$ is computed as:

$$M_n = \frac{|\operatorname{meas}(\Omega^{*,1}) - \operatorname{meas}(\Omega^{n,1})|}{\operatorname{meas}(\Omega^{*,1})}.$$

Results are presented in Fig. 3.10. As it follows from the proof of Theorem 3.2.5 the optimal value of parameter η is unknown in advance. The results of numerical experiments show that the convergence of the solution is not sensitive to the value of η (see Fig. 3.9). But here we should take into account that increasing η we also increase the solution error. On the other hand, convergence of measure of the single-phase flow domain shows stronger behavior for bigger values of η (see Fig. 3.10).

The last goal of the numerical experiments is to verify Assumption 3.2.2, which states that the non-degeneracy property for the solution S is satisfied. Since the exact solution is unknown and validity of this assumption can not be shown in advance, we use the reference solution $S_{\mathcal{T}_*}$ and plot in Fig. 3.11 the dependence of δ_ϵ on ϵ from condition (3.73). It follows from the presented results that Assumption 3.2.2 is satisfied for the given numerical examples.

3.2.5 Results and discussions

The objective of these studies is to show the convergence of the numerical solution to the continuous one in one-dimensional case for the system of equations describing the pressing section of a paper machine including the dynamic capillary effect. One of the challenges of this problem is an evaluation of the fully saturated regions. Solving this problem we have to keep in mind that in the computational domain the region with single-phase water flow may appear. At first, we state two mathematical models for the both flow regimes with a free boundary. Then, we combine them into one model in the whole computational domain. For the discretized system we propose a numerical

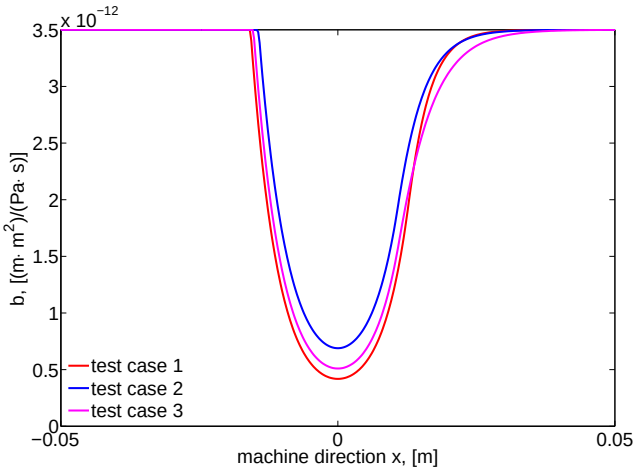

Fig. 3.5: Input function $b(x)$ for the test case with the dynamic capillary pressure

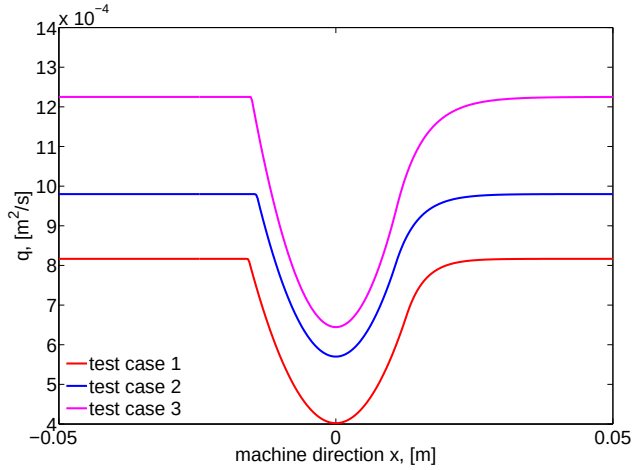

Fig. 3.6: Input function $q(x)$ for the test case with the dynamic capillary pressure

algorithm, which implicitly takes into account the two flow regimes.

The theoretical part of this work contains the proof of existence of solution of the discrete system, compactness and the convergence theorem. The main idea of the theoretical studies is to prove the convergence for the input data which is typical for real numerical experiments. Since we can not imply too strong assumptions we do not get precise estimates on the convergence order and we are not concerned with the proof of uniqueness.

Some assumptions for solution, which are made during the theoretical studies, are verified by the numerical experiments. We also have estimated numerically the rate of convergence of solution

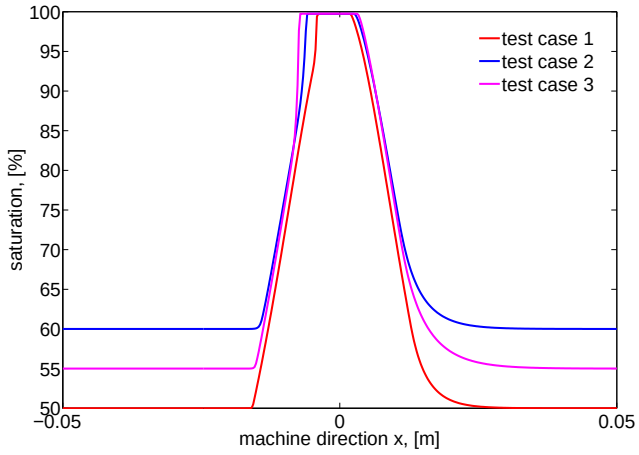

Fig. 3.7: Saturation for the test case with the dynamic capillary pressure

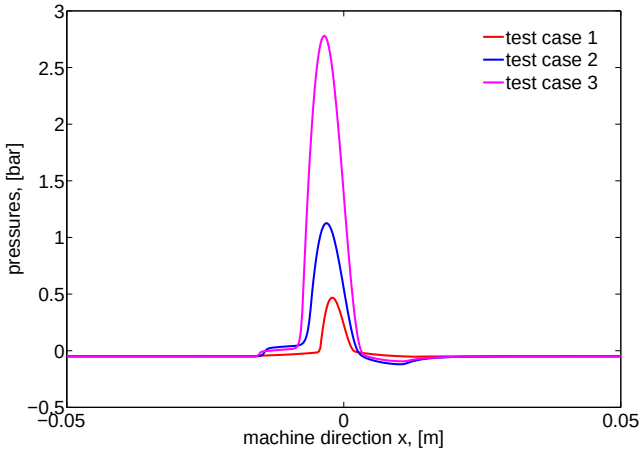

Fig. 3.8: Pressure for the test case with the dynamic capillary pressure

and measure of the fully saturated region.

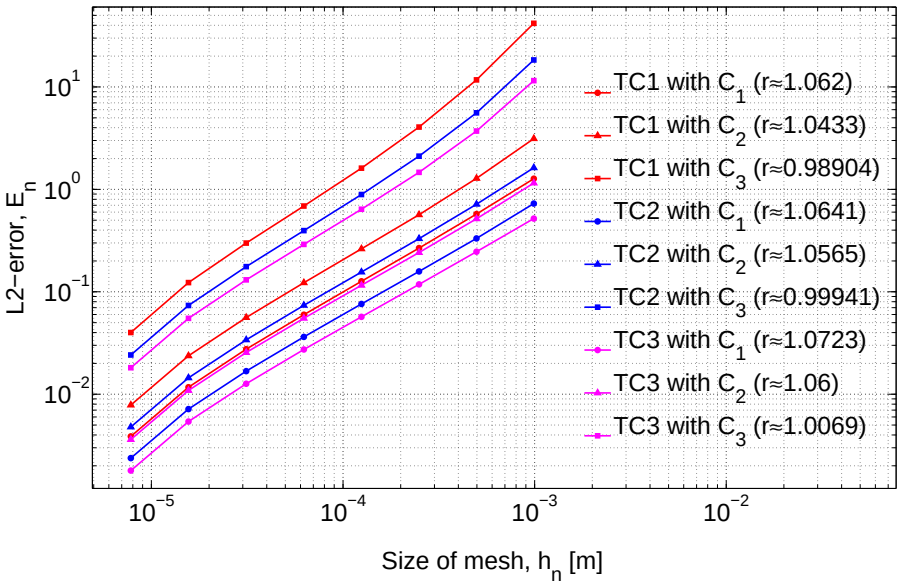

Fig. 3.9: Convergence of the solution for the test case with the dynamic capillary pressure (TC is an abbreviation for ”test case”)

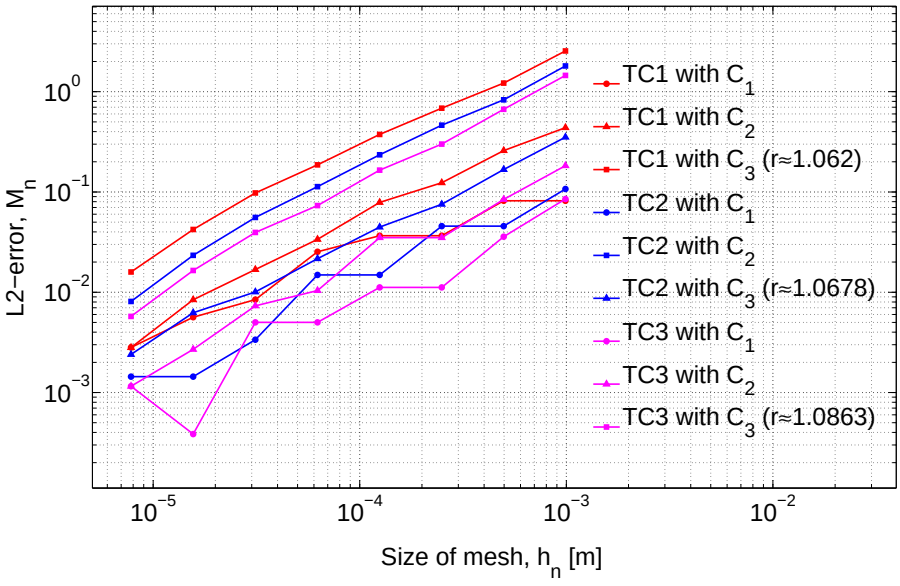

Fig. 3.10: Convergence of the domain measure for the test case with the dynamic capillary pressure (TC is an abbreviation for ”test case”)

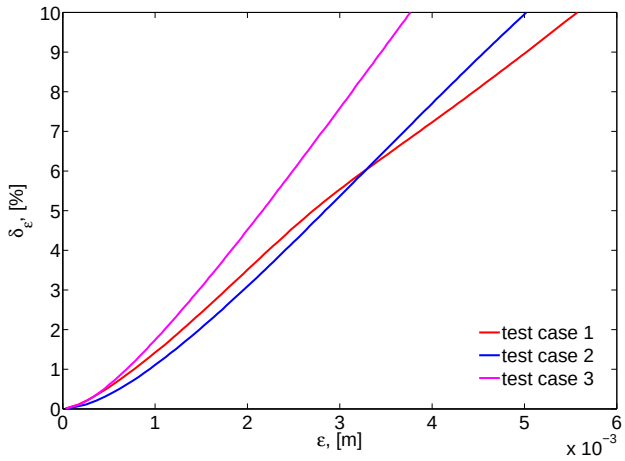

Fig. 3.11: Verification of Assumption 3.2.2 using the reference solution of the test case with the dynamic capillary pressure

Chapter 4

Two-Dimensional Model (Richards' Approach)

In the pressing section of a paper machine dewatering of the paper layer is performed by pressing it against special felts with the help of pressing nips. Width of the paper layer as well as width of the flat pressing nips may reach up to $12\ m$, which is much larger than the pressing zone. Thus, a two-dimensional mathematical model in vertical and machine directions is sufficient for understanding the infiltration processes occurring within the pressing zone. The aim of this chapter is to develop an accurate two-dimensional model for the pressing section which takes into account the dynamic capillary effects.

The mathematical model is developed in the way that the real industrial processes can be simulated. The one-dimensional model developed in Chapter 2 is extended to the two dimensions. Now, instead of the single-layer computational domain, the multilayer paper-felt sandwich is taken into account. Chosen mathematical model and discretization technique allow us to satisfy the continuity of the fluid pressure and the normal fluxes across interfaces of the different layers. Moreover, a formation of fully saturated zones during the pressing process is included by accounting for two possible flow regimes, saturated and unsaturated water flow.

The Richards' approach accompanied by the dynamic capillary pressure is used to describe the water flow within the pressing zone. The two-dimensional mathematical model takes into account the dynamic capillary pressure–saturation relation proposed by Hassanizadeh and co-workers in [24] (see Section 1.2). The goal of this chapter is to develop and to numerically investigate the proposed model. In short, Chapter 4 is constructed in the following way. In Section 4.1 we present the mathematical model, which take into account all the issues discussed above. Advanced discretization is performed by the MPFA-O method in Section 4.2. In Section 4.3 some numerical

experiments are performed. To conclude this chapter we draw some conclusions in Section 4.4.

4.1 Mathematical model

In this section we present the two-dimensional model for the pressing section of a paper machine. At first, we recall the model which was stated in Section 3.2.1 for the single-layer case. Then, the model is extended by the inclusion of the layers and by the formulation of the boundary conditions in Section 4.1.1. To close the mathematical model, in Section 4.1.2 we recall the elasticity model stated in [43, 44].

4.1.1 Two-dimensional flow model in multilayer case

As a starting point, we consider the mathematical model for the two flow regimes: saturated and unsaturated water flow in single-layer case stated in Section 3.2.1. In Fig. 4.1 we remind the main notations introduced earlier for our problem (the direction of the paper–felt transportation, the computational domain Ω, the subdomains Ω^1 and Ω^2 with the saturated and unsaturated water flow, respectively, the boundaries of Ω and the interface Γ between Ω^1 and Ω^2).

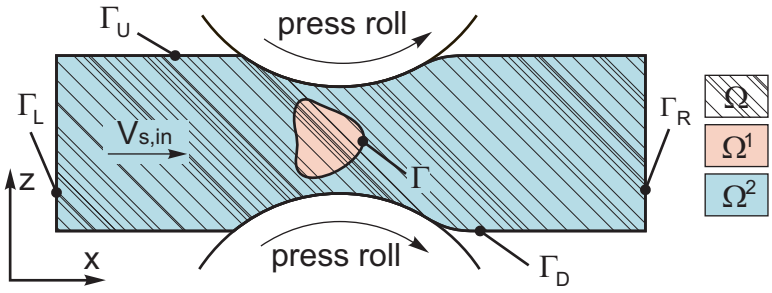

Fig. 4.1: Computational domain Ω with two flow regimes for multilayer case

Remark 4.1.1. *As opposed to Fig. 3.4, we show in Fig. 4.1 that the fully saturated zone is located inside Ω and that the interface Γ may not have common points with the boundary $\partial\Omega$. The reason is that in Section 3.2.1 we aimed to present the one-dimensional model, which after the averaging procedure in vertical direction gives us a fully saturated zone. It is satisfied in case of the domain presented in Fig. 3.4, but not in case of the domain shown in Fig. 4.1. In this section we would like to state a two-dimensional model in multilayer case, which may contain the fully saturated zone inside the computational domain as it is indicated in Fig. 4.1.*

The two-dimensional model for the one-layer case and the two flow regimes in two dimensions was stated in Section 3.2.1 by Eqs. (3.50)–(3.54). Summarizing the two flow models, we reformulate the problem (3.50)–(3.54) in a more suitable way for further developments. Let Assumption 3.1.1*(c)* (or 3.2.1*(c)*) be satisfied. Then, we rewrite Eqs. (3.50)–(3.52) in the following form:

$$-\operatorname{div}\left(\frac{k_{rw}}{\mu_w}\mathbf{K}\operatorname{grad} p_w\right)+\operatorname{div}(\phi S\mathbf{V}_s)=0,\quad \mathbf{x}\in\Omega, \tag{4.1}$$

$$S=1,\quad \mathbf{x}\in\Omega^1, \tag{4.2}$$

$$p_w+p_c^{stat}=\tau\mathbf{V}_s\cdot\operatorname{grad} S,\quad \mathbf{x}\in\Omega^2; \tag{4.3}$$

where we assume that $k_{rw}=k_{rw}(S)$, $\mathbf{K}=\mathbf{K}(\mathbf{x})$, $\phi=\phi(\mathbf{x})$, $\mathbf{V}_s=\mathbf{V}_s(\mathbf{x})$, $p_c^{stat}=p_c^{stat}(S,\phi)$, $\tau=\tau(\mathbf{x})$.

We notice that Eq. (4.1) coincides with (3.50) in Ω^1 and with (3.51) in Ω^2. We also have to make sure that continuity conditions (3.53), (3.54) are satisfied in this case. Continuity of the water pressure p_w follows from the definition of the nonlinear convection–diffusion Eq. (4.1). Continuity of the normal fluxes follows directly from integration of Eq. (4.1) over a small neighborhood of the interface Γ.

Layered computational domain

In general, the computational domain Ω consists of several layers (see Fig. 4.2). Therefore, it is divided into nonoverlapping subdomains $\Omega_1, \Omega_2, \ldots, \Omega_L$, where L is the total number of layers. Interfaces between the subdomains are denoted by $\Gamma_l=\overline{\Omega}_l\cap\overline{\Omega}_{l+1}$ for all $l=\overline{1,L-1}$.

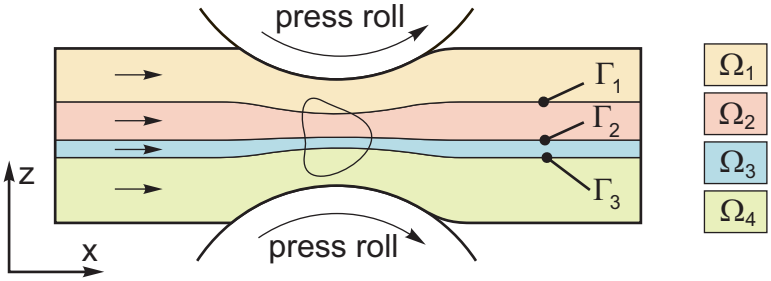

Fig. 4.2: Computational domain Ω with indicated layers

Then, the system of Eqs. (4.1)–(4.3) has to be satisfied together with the continuity of the fluid pressure and the continuity of the normal fluxes on the interfaces:

$$[p_w]_{\Gamma_l}=0,\quad [\mathbf{J}_w\cdot\mathbf{n}]_{\Gamma_l}=0,\quad l=\overline{1,L-1}; \tag{4.4}$$

where we remember that each layer has its own properties, therefore, functions $k_{rw} = k_{rw}(S, \mathbf{x})$, $\mathbf{K} = \mathbf{K}(\mathbf{x})$, $\phi = \phi(\mathbf{x})$, $p_c^{stat} = p_c^{stat}(S, \phi, \mathbf{x})$, $\tau = \tau(\mathbf{x})$ may have jumps over the layer interfaces.

Boundary conditions

To close the system of Eqs. (4.1)–(4.4) we impose boundary conditions. Let Assumption 2.1.4 be satisfied. On the left boundary Γ_L the distributions of the saturation and the pressure are known. This case is typical for the production process. Then, Dirichlet boundary conditions are imposed on Γ_L. Let Assumption 2.1.4 be satisfied. It means that water remains at equilibrium w.r.t. the solid skeleton on Γ_L and the dynamic effect is absent there. Therefore, for the pressure we use the dependence p_c^{stat} on initial values of saturation. Since the right boundary Γ_R is also far from the pressing zone, it is assumed that the water reaches the equilibrium state w.r.t. the solid skeleton on Γ_R. Therefore, we apply no-flow boundary conditions on Γ_R. On the upper and lower boundaries Γ_U and Γ_D we assume that there is no escape of water and also impose zero-Neumann boundary conditions. Hence, we have:

$$S|_{\Gamma_L} = C_0(\mathbf{x}), \quad p_w|_{\Gamma_L} = -p_c^{stat}(C_0), \quad \mathbf{x} \in \Gamma_L; \tag{4.5}$$

$$\left(-\frac{k_{rw}}{\mu_w}\mathbf{K}\operatorname{grad} p_w\right)\cdot \mathbf{n}_s\Big|_{\Gamma_R} = 0; \tag{4.6}$$

$$\left(-\frac{k_{rw}}{\mu_w}\mathbf{K}\operatorname{grad} p_w\right)\cdot \mathbf{n}\Big|_{\Gamma_U,\Gamma_D} = 0; \tag{4.7}$$

where $\mathbf{n}_s$ is the unit vector collinear to $\mathbf{V}_s$. We remark that the second term of water flux related to convection in (4.7) is equal to zero since $\mathbf{V}_s \cdot \mathbf{n} = 0$ for the outer unit normal vector $\mathbf{n}$ to Γ_U or Γ_D.

According to the production process, sometimes layers of the paper and felt in the paper–felt sandwich are separated as shown in Fig. 1.2, 1.3 (see Section 1.1). To take it into account we also provide a possibility to impose no-flow boundary conditions on some parts of the interfaces between layers.

4.1.2 Elasticity model in multilayer case

We supplement our flow model with the elasticity model stated in [43, 44], which accounts for the solid deformations. In Section 2.1.3 we recalled this model in the single-layer case. Let us now shortly state this elasticity model for the multilayer computational domain. More detailed discussions on this elasticity model, its discretization and solution can be found in [43, 44].

The main reason of the solid deformations is the pressing forces which are about $100\ kN/m$ in the roll press and about $1000\ kN/m$ in the shoe press. Thus, we assume that the water acting on the

solid skeleton can be neglected in a first approximation. According to Assumption 2.1.3, the solid phase is incompressible. Therefore, the porous medium gets deformed by a rearrangement of the solid skeleton in vertical direction. Assuming that the felt and the paper behave viscoelastically (see [49, 31]), we can state the Kelvin-Voigt model for L layers:

$$\mathrm{t}(x) = E_1(\varepsilon_1(x)) + \Lambda_1 \left|\mathbf{V}_{s,in}\right| \frac{d}{dx} E_1(\varepsilon_1(x)) - k\mathrm{t}_{max}(x), \tag{4.8}$$

$$\mathrm{t}(x) = E_i(\varepsilon_i(x)) + \Lambda_i \left|\mathbf{V}_{s,in}\right| \frac{d}{dx} E_i(\varepsilon_i(x)), \quad i = \overline{2, L}; \tag{4.9}$$

where t is the stress measured in $[Pa]$. The dimensionless strain is defined by

$$\varepsilon_i(x) = \frac{l_{0,i} - l_i(x)}{l_{0,i}} \text{ for each layer } i = \overline{1, L}, \tag{4.10}$$

with undeformed and deformed thicknesses of the layer i at coordinate x denoted by $l_{0,i}(x)$ and $l_i(x)$, respectively. In general, E_i is some nonlinear function related to the elastic part of the stress and the strains. Λ_i ($[s]$) is the viscoelastic time constant, which determines the speed of relaxation.

Eqs. (4.9) correspond to the felts. Eq. (4.8) corresponds to the paper layer and has an additional third term on the right hand side. This term is introduced to model the permanent compression, which appears due to plasticity of the paper. We assume that the value of the permanent deformation depends linearly on the maximum stress to which the paper has been exposed multiplied by some constant k:

$$\mathrm{t}_{max}(x_0) = \max_{x \le x_0} \mathrm{t}(x). \tag{4.11}$$

To close the system of Eqs. (4.8),(4.9) we also use the following relation:

$$\sum_{i=1}^{L} \varepsilon_i(x) l_{0,i} = l_0 - f(x), \tag{4.12}$$

where $l_0 = \sum_{i=1}^{L} l_{0,i}$ is the total thickness of the undeformed paper–felt sandwich. Due to the fact that the thickness of the paper–felt sandwich will never exceed l_0, the function $f(x)$ has the form:

$$f(x) = \min\{l_0, \text{distance between press profiles at position } x\}. \tag{4.13}$$

To resolve the system of Eqs. (4.8),(4.9),(4.12) one more input parameter has to be provided. The first possibility is to provide the minimum distance between press profiles, which defines the position of the pressing nips and the geometry of the computational domain Ω. Another possibility which is more convenient for the industrial applications is to define the pressing force, which is

equal to the integral of the stress profile over the length of the computational domain. Having one of these parameters, the system of equations can be solved.

After we find the distribution of the stress and the strains, it is possible to compute the necessary input data for the flow solver. Since the thickness of the layers is small we consider that the porosity changes only in horizontal direction. Then, the porosity for each layer can be found as:

$$\phi_i(x) = \frac{\varepsilon_i(x) + \phi_{0,i}}{\varepsilon_i(x) + 1} \text{ for all } i = \overline{1, L}, \tag{4.14}$$

where $\phi_{0,i}$ is the porosity of the ith undeformed layer. Using the computed strains, the flow mesh can be obtained immediately as well as the distribution of the solid velocity $\mathbf{V}_s(\mathbf{x})$ (for more details see [43, 44]).

Remark 4.1.2. *As it was mentioned in Chapter 1, we also consider the second type of the press nips, so-called shoe press. In this case the paper–felt sandwich is not transported strictly in horizontal direction (see Fig. 1.2). But since the thickness of the pressing zone is very small compared to its length the angle between the paper–felt sandwich and machine direction is small. Therefore, the assumption on the horizontal transportation is still a very good approximation, and we use the same elasticity model for the shoe press.*

4.2 Discretization

Let us now discuss the discretization on a quadrilateral unstructured grid of the flow model stated in the previous section. We use the finite volume method namely the MPFA-O method. For an introduction to the discretization method see Section 1.3 and [1, 2, 19].

At first, the two-dimensional mesh is introduced.

Definition 4.2.1. *Let Ω be an open bounded polygonal subset of $\mathbb{R}^2$ with boundary $\partial\Omega$. The discretization of Ω is defined as $\mathcal{D} = (\mathcal{T}, \mathcal{E}, \mathcal{X})$, where the following holds.*

- *$\mathcal{T}$ is the finite set of nonoverlapping quadrilateral cells $\mathcal{K}$ ('control volumes') such that $\overline{\Omega} = \cup_{\mathcal{K}\in\mathcal{T}}\overline{\mathcal{K}}$. The boundary of each control volume is denoted by $\partial\mathcal{K} = \overline{\mathcal{K}} \setminus \mathcal{K}$.*
- *$\mathcal{E}$ is the finite set of one-dimensional edges of all control volumes. For any control volume $\mathcal{K} \in \mathcal{T}$ there exists a subset $\mathcal{E}_\mathcal{K}$ of $\mathcal{E}$ such that $\partial K = \cup_{\sigma\in\mathcal{E}_\mathcal{K}}\overline{\sigma}$. Furthermore, $\mathcal{E} = \cup_{\mathcal{K}\in\mathcal{T}}\mathcal{E}_\mathcal{K}$. For any $\mathcal{K}$, $\mathcal{L}$ from $\mathcal{T}$ with $\mathcal{K} \neq \mathcal{L}$, either $\overline{\mathcal{K}} \cap \overline{\mathcal{L}} = \emptyset$ or $\overline{\mathcal{K}} \cap \overline{\mathcal{L}} = \overline{\sigma}$ for some $\sigma \in \mathcal{E}$, which then will be denoted by index $\mathcal{K}|\mathcal{L}$.*
- *$\mathcal{X} = (\mathbf{x}_\mathcal{K})_{\mathcal{K}\in\mathcal{T}}$ is the finite set of points of Ω ('cell centers') such that $\mathbf{x}_\mathcal{K} \in \mathcal{K}$ for all $\mathcal{K} \in \mathcal{T}$.*

Remark 4.2.1. *In the previous section the computational domain Ω was used. In Definition 4.2.1 the polygonal set still denoted by Ω is an approximation of the original computational domain.*

Definition 4.2.1 introduces some general notations for the mesh which is used for discretization. The mesh which is constructed for our computational domain has constant step size h_x in x-direction (see Fig. 4.3). In z-direction at the left and right boundaries where no deformations occur the mesh has also constant step size h_z. If the cell contains an interface between two layers the step size h_z is divided into two parts to resolve the interface. In general, the mesh has varying step size in z-direction which is proportional to the solid deformations. Cell center $\mathbf{x}_\mathcal{K}$ is defined as the intersection point of intervals connecting midpoints of the opposed edges of the control volume $\mathcal{K}$.

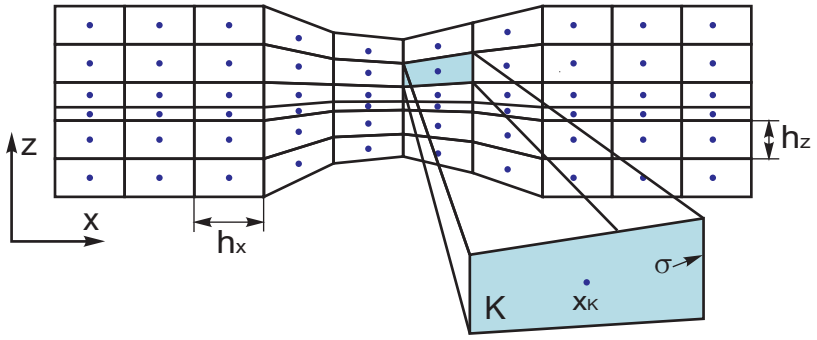

Fig. 4.3: Discretization of the computational domain Ω

The system of Eqs. (4.1)–(4.3) together with interfacial conditions (4.4) and boundary conditions (4.5)–(4.7) is discretized with the help of the finite volume method (see e.g. [20]). To simplify the notations we omit the index 'w' in the variables p_w, k_{rw} and μ_w.

Now let us introduce some notations. If $\sigma = \sigma_{\mathcal{K}|\mathcal{L}}$ is the common edge of cells $\mathcal{K}$ and $\mathcal{L}$ then we denote:

$$S_\sigma = \frac{1}{2}(S_\mathcal{K} + S_\mathcal{L}); \tag{4.15}$$

$$S_{\sigma,+} = \begin{cases} S_\mathcal{K}, & \text{if } \mathbf{V}_s \cdot \mathbf{n}_\sigma \geq 0; \\ S_\mathcal{L}, & \text{if } \mathbf{V}_s \cdot \mathbf{n}_\sigma < 0; \end{cases} \tag{4.16}$$

where $S_\mathcal{K}$ is the approximated value of S at $\mathbf{x}_\mathcal{K}$, $\mathbf{n}_\sigma$ is the normal unit vector to σ outward to $\mathcal{K}$.

Integrating (4.1) over the control volume $\mathcal{K}$, we obtain:

$$-\sum_{\sigma\in\mathcal{E}_\mathcal{K}} \frac{k_r(S_\sigma)}{\mu} F_{\mathcal{K},\sigma} + \sum_{\sigma\in\mathcal{E}_\mathcal{K}} m_\sigma \phi_\sigma S_{\sigma,+} \mathbf{V}_s \cdot \mathbf{n}_\sigma = 0, \quad \mathcal{K} \in \mathcal{T}; \tag{4.17}$$

where m_σ is the one-dimensional measure of the boundary σ, ϕ_σ is the porosity at σ. The general form of $F_{\mathcal{K},\sigma}$ is:

$$F_{\mathcal{K},\sigma} = \sum_{\mathcal{L}\in\mathcal{N}_{\mathcal{K},\sigma}} t^{\mathcal{L}}_{\mathcal{K},\sigma} p_{\mathcal{L}}; \tag{4.18}$$

with transmissibility coefficients $t^{\mathcal{L}}_{\mathcal{K},\sigma}$ and the subset $\mathcal{N}_{\mathcal{K},\sigma}$ of all control volumes such that:

$$\mathcal{N}_{\mathcal{K},\sigma} = \{\mathcal{L}\in\mathcal{T}: \quad \sigma\in\mathcal{E}_{\mathcal{K}}, \quad \overline{\sigma}\cap\overline{\mathcal{L}}\neq\emptyset\}. \tag{4.19}$$

For the quadrilateral grid the set $\mathcal{N}_{\mathcal{K},\sigma}$ consists of six control volumes as shown in Fig. 4.4.

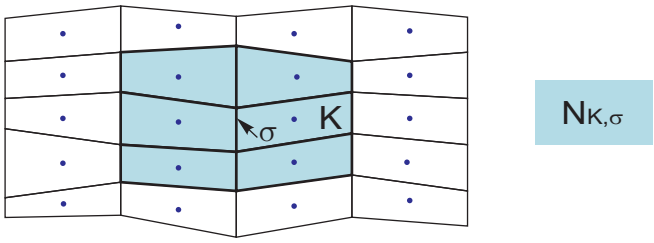

Fig. 4.4: Set $\mathcal{N}_{\mathcal{K},\sigma}$ for quadrilateral grid

The discrete flux $F_{\mathcal{K},\sigma}$ is an approximation of the integral $\int_\sigma (\mathbf{n}_\sigma \cdot \mathbf{K}\,\mathrm{grad}\,p)\,ds$. The main idea of the MPFA method is to obtain the transmissibility coefficients by carrying out some preprocessing calculations, which depend only on the input data. The approximation is carried out by the multi-point flux approximation O-method (see [1, 2, 19]). Coefficients $t^{\mathcal{L}}_{\mathcal{K},\sigma}$ are so-called transmissibility coefficients, which satisfy:

$$\sum_{\mathcal{L}\in\mathcal{N}_{\mathcal{K},\sigma}} t^{\mathcal{L}}_{\mathcal{K},\sigma} = 0.$$

Finite volume schemes for Eqs. (4.2) and (4.3) yield:

$$S_{\mathcal{K}} = 1, \quad \mathcal{K}\in\mathcal{T}_1, \tag{4.20}$$

$$m_{\mathcal{K}}\left(p_{\mathcal{K}} + p_c^{stat}(S_{\mathcal{K}})\right) = \tau \sum_{\sigma\in\mathcal{E}_{\mathcal{K}}} m_\sigma (S_{\sigma,+} - S_{\mathcal{K}})\mathbf{V}_s\cdot\mathbf{n}_\sigma, \quad \mathcal{K}\in\mathcal{T}_2, \tag{4.21}$$

where $m_{\mathcal{K}}$ is the two-dimensional measure of the control volume $\mathcal{K}$. $\mathcal{T}_1$ and $\mathcal{T}_2$ are the sets of the control volumes which approximate the domains Ω^1 and Ω^2, respectively. These sets satisfy $\mathcal{T}_1\cap\mathcal{T}_2=\emptyset$ and $\mathcal{T}_1\cup\mathcal{T}_2=\mathcal{T}$.

Let us now take into account the boundary conditions (4.5)–(4.7). Let the set $\mathcal{E}$ be divided into

five subsets:

$$\mathcal{E}_{int} = \{\sigma \in \mathcal{E} : \sigma \cap \partial\Omega = \emptyset\}, \tag{4.22}$$

$$\mathcal{E}_{ext,\alpha} = \{\sigma \in \mathcal{E} : \sigma \cap \Gamma_\alpha \neq \emptyset\}, \quad \alpha = \{L, U, R, D\}. \tag{4.23}$$

In Eqs. (4.17) and (4.21) the following relations are used:

- if $\sigma \in \mathcal{E}_\mathcal{K} \cap \mathcal{E}_{ext,L}$ than

$$S_{\sigma,+} = \begin{cases} S_\mathcal{K}, & \text{if } \mathbf{V}_s \cdot \mathbf{n}_\sigma \geq 0; \\ C_{0,\sigma}, & \text{if } \mathbf{V}_s \cdot \mathbf{n}_\sigma < 0; \end{cases}, \quad S_\sigma = \frac{1}{2}(S_\mathcal{K} + C_{0,\sigma}), \tag{4.24}$$

  where $C_{0,\sigma}$ is the value of C_0 at σ;

- if $\sigma \in \mathcal{E}_\mathcal{K} \cap \mathcal{E}_{ext,R}$ than

$$S_{\sigma,+} = S_\mathcal{K}, \quad S_\sigma = S_\mathcal{K}. \tag{4.25}$$

We also remark that if $\sigma \in \mathcal{E}_\mathcal{K} \cap (\mathcal{E}_{ext,U} \cup \mathcal{E}_{ext,D})$ than $\mathbf{n}_\sigma \cdot \mathbf{V}_s = 0$ and $F_{\mathcal{K},\sigma} = 0$. So we do not need to define S_σ and $S_{\sigma,+}$ there. The boundary conditions (4.5)–(4.7) also have to be taken into account while computing transmissibility coefficients $t^\mathcal{L}_{\mathcal{K},\sigma}$ (for more details see [1, 2]).

To solve the nonlinear system of Eqs. (4.17), (4.20) and (4.21) the Newton's method is used (see [17, 36]). Remembering that the static capillary pressure–saturation relation depends also on the porosity, initial guesses for pressure and saturation are chosen as:

$$p^0_\mathcal{K} = -p_c^{stat}(C_0(\mathbf{x}_{\mathcal{K},\Gamma_L}), \phi(\mathbf{x}_{\mathcal{K},\Gamma_L})), \quad S^0_\mathcal{K} = (p_c^{stat})^{-1}(p^0_\mathcal{K}, \phi(\mathbf{x}_\mathcal{K})), \tag{4.26}$$

where upper indices correspond to Newton's iterations. $\mathbf{x}_{\mathcal{K},\Gamma_L}$ is the point which corresponds to $\mathbf{x}_\mathcal{K}$ on the left boundary Γ_L taking into account deformations. In other words, the initial guess of the pressure remains constant along streamlines of the solid deformations.

The initial guess of the saturation satisfies $S^0_\mathcal{K} \in (S_*, 1)$ for all $\mathcal{K} \in \mathcal{T}$. Thus, the initial guess $\mathcal{T}^0_1$ is an empty set and the initial guess $\mathcal{T}^0_2$ is equal to $\mathcal{T}$. After each Newton's iteration k for Eqs. (4.17), (4.20) and (4.21), when correction values for pressure $\Delta p^{k+1}_\mathcal{K}$ and saturation $\Delta S^{k+1}_\mathcal{K}$ are computed, we define $p^{k+1}_\mathcal{K}$ as:

$$p^{k+1}_\mathcal{K} = p^k_\mathcal{K} + \Delta p^{k+1}_\mathcal{K} \text{ for all } \mathcal{K} \in \mathcal{T} \tag{4.27}$$

and the simple restriction operator is applied to define $S^{k+1}_\mathcal{K}$:

$$S_{\mathcal{K}}^{k+1} = \begin{cases} S_*, & \text{if } S_{\mathcal{K}}^k + \Delta S_{\mathcal{K}}^{k+1} \leq S_*; \\ S_{\mathcal{K}}^k + \Delta S_{\mathcal{K}}^{k+1}, & \text{if } S_{\mathcal{K}}^k + \Delta S_{\mathcal{K}}^{k+1} \in (S_*, 1); \\ 1, & \text{if } S_{\mathcal{K}}^k + \Delta S_{\mathcal{K}}^{k+1} \geq 1; \end{cases} \tag{4.28}$$

for all $\mathcal{K} \in \mathcal{T}$, where S_* is discussed in Remark 2.2.2. Then, the sets $\mathcal{T}_1^{k+1}$ and $\mathcal{T}_2^{k+1}$ are defined as:

$$\mathcal{T}_1^{k+1} = \{\mathcal{K} \in \mathcal{T} : S_{\mathcal{K}}^{k+1} = 1\}, \tag{4.29}$$

$$\mathcal{T}_2^{k+1} = \{\mathcal{K} \in \mathcal{T} : S_{\mathcal{K}}^{k+1} \in (S_*, 1)\}, \tag{4.30}$$

$$\mathcal{T}_3^{k+1} = \{\mathcal{K} \in \mathcal{T} : S_{\mathcal{K}}^{k+1} = S_*\}. \tag{4.31}$$

Remark 4.2.2. *The proposed numerical procedure (4.27)–(4.30) may cause an appearance of some unphysical domains $\mathcal{T}_3^{k+1}$ with the water saturation being equal to S_*. This domain is required for the completeness of the numerical approach. From a physical point of view, in the domain where this regime appears the following equations have to be satisfied:*

$$p_{\mathcal{K}} = -p_c^{stat}(S_*), \quad S_{\mathcal{K}} = S_*. \tag{4.32}$$

In practice, we do not observe numerical experiments where single-phase air flow appears.

If after kth Newton's iteration the set $\mathcal{T}_3^{k+1}$ is not empty any more then on the next Newton's iteration $(k+1)$ one more equation has to be added to the system of equations (4.17), (4.20), (4.21):

$$S_{\mathcal{K}} = S_*, \quad \mathcal{K} \in \mathcal{T}_3.$$

4.3 Numerical experiments

This section presents numerical experiments for the pressing section of a paper machine. At first, single-layer test cases are considered to evaluate the behavior of the solution in presence of the dynamic capillary effect and to compare the results with the laboratory experiments presented in [8]. Then, we study how the dynamic capillarity acts in the multilayer case. Since in this work we suggested to use the MPFA-O FV scheme for discretizing the governing equations at the end of this section we compare numerical results with the results earlier obtained in [43] using the FE scheme with the static capillary pressure.

All tests are performed with realistic sets of parameters provided by our industrial partner Voith

Table 4.1: Experimental data for all two-dimensional test cases

Variable	Dimension	Value
k_r	$[-]$	$S^{3.5}$
$\mathbf{K}$	$[m^2]$	$\mathbf{K}_0 \frac{\phi^3}{(1-\phi)^2}$
μ	$[Pa\ s]$	0.0008
p_c^{stat}	$[Pa]$	$a(\phi-1)\left(\frac{1}{S-S_r}-\frac{1}{1-S_r}\right)^{1/2}$
a	$[Pa]$	$\frac{P_0}{1-\phi_0}\left(\frac{1}{C_0-S_r}-\frac{1}{1-S_r}\right)^{-1/2}$
S_*	$[\%]$	10
S_r	$[\%]$	$S_* - 1e-3$
P_0	$[Pa]$	-5000

Paper Fabric and Roll Systems GmbH at Heidenheim. More detailed description of the parameter evaluation can be found in [44].

4.3.1 Numerical experiments for evaluation of the dynamic capillary effect: single-layer case

Simulation results for three different test cases with single layer configuration are presented. Sets of parameters correspond to two types of felts and a paper. For the dynamic capillary pressure model we consider the material coefficient τ equal to 0, 10 and $100\ Pa\ s$. The case $\tau = 0$ corresponds to the static capillary pressure. Our studies of a one-dimensional model in [29] indicated that values of τ of order 10 and $100\,Pa\,s$ are realistic for the process studied in this paper. Further on, we consider cases with different velocities $\mathbf{V}_{s,in}$ and with different initial saturation C_0.

The input data is presented in Tables 4.1, 4.2 (see [44]). We give the input data only for the flow model. For the typical parameters for the elasticity model we refer to [44]. As it was mentioned in Section 4.1.2, the elasticity model is used to obtain the geometry of the computational domain Ω, the distributions of the porosity $\phi(\mathbf{x})$, and the solid velocity $\mathbf{V}_s(\mathbf{x})$. As an example, the typical distributions of these parameters are shown for the first test case "Felt 1" with $|\mathbf{V}_{s,in}| = 100m/min$ in Fig. 4.5, where in Fig. 4.5A the porosity ϕ is presented. In Figs. 4.5B and 4.5C the x and z-components of the solid velocity $\mathbf{V}_s$ are shown, respectively.

The obtained distributions of the water saturation and the water pressure in the single-layer case show a homogeneous behavior in the vertical direction. Therefore, all numerical results in this subsection are shown as one-dimensional graphs, representing vertical averages of two-dimensional values. Simulation results for "Felt 1", "Felt 2" and "Paper" are shown in Figs. 4.6, 4.7, Figs. 4.8, 4.9 and Figs. 4.10, 4.11, respectively. Figs. 4.6, 4.8, 4.10 correspond to $|\mathbf{V}_{s,in}| = 100m/min$, while

Table 4.2: Experimental data for two-dimensional single-layer test cases

Variable	Dimension	Felt 1	Felt 2	Paper
$\mathbf{K}_{0,xx}$	$[m^2]$	$2.95e-11$	$1.57e-11$	$5.00e-12$
$\mathbf{K}_{0,xy}$	$[m^2]$	$-6.66e-14$	$-1.43e-13$	0
$\mathbf{K}_{0,yy}$	$[m^2]$	$1.82e-11$	$2.96e-11$	$1.00e-13$
$\phi\|_{\Gamma_L}$	$[\%]$	45	34	88
$d\|_{\Gamma_L}$	$[mm]$	0.80	1.20	0.56
C_0	$[\%]$	$25, 35$	$30, 50$	$40, 60$
Γ_L	$[m]$		-0.05	
Γ_R	$[m]$		0.05	
$\|\mathbf{V}_{s,in}\|$	$[m/min]$		$100, 300$	

Figs. 4.7, 4.9, 4.11 correspond to $|\mathbf{V}_{s,in}| = 300\, m/min$. Figs. 4.6A–4.11A illustrate the computed saturation, while in Figs. 4.6B–4.11B the computed fluid pressure is shown. Further on, Figs. 4.6C–4.11C represent different magnification of part of the data, aiming at better visualization. These figures represent only part of the results, namely those which can not be well seen in Figs. 4.6B–4.11B. For every test case we vary the initial saturation to see the influence of the dynamic capillary pressure model in case of the unsaturated and saturated water flow. For "Felt 1" we consider two values of C_0, which are 25% and 35%, for "Felt 2" the initial saturation is equal to 30% and 50%, and for "Paper" C_0 is equal to 40% and 60%. In Figs. 4.6–4.11 the data which corresponds to the same initial saturation is shown with the same type of markers. The data corresponding to the same value of τ we present with the same color.

In general, we see that the two-dimensional model in the single-layer case shows the same kind of behavior of the pressure and the saturation in presence of the dynamic capillary effect as the one-dimensional model considered in Chapter 2. With the increase of the material coefficient τ we observe a decrease of the maximum value of the saturation or a reduction of the fully saturated zone. Regarding the distribution of the fluid pressure, with the increase of τ the maximum value of the pressure decreases a little bit in case when saturated flow is present and it shifts to the left in case of the unsaturated flow. For both flow regimes we observe a decrease of the pressure below the initial value behind the center of the pressing zone. These effects are well seen in the test cases "Felt 1" and "Felt 2". The fluid pressure in the test case "Paper" behave similarly but less evidently. The behavior of the pressure profiles obtained by the model with the dynamic capillary pressure–saturation relation was also observed in laboratory experiments carried out by Beck [8].

In Fig. 4.12A the dependence of the fluid pressure peak on the initial saturation is shown for all test cases with different material coefficients τ and fixed $|\mathbf{V}_{s,in}| = 100\, m/min$. This numerical experiment shows that for small initial saturation the dynamic capillary pressure model significantly

influences the fluid pressure peak. But when the initial saturation becomes larger, the pressure peak increases and does not differ much for the static and dynamic capillary pressure models. We also observe that the values of C_0 after which pressure peak increases depends on the test case.

For better understanding of the behavior of the fluid pressure let us introduce the following quantity Q_{in}:

$$Q_{in} = C_0 \frac{\phi(x_L)d(x_L)}{\phi(x_*)d(x_*)}, \tag{4.33}$$

where d is the one-dimensional function of the x-coordinate which expresses the thickness of the layer, x_L is the x-coordinate of the left boundary Γ_L, x_* is the x-coordinate where the layer reaches the minimum thickness or the maximum value of the porosity during pressing. In other words, the quantity Q_{in} expresses the ratio of incoming water volume to void volume at the center of the nip. In Fig. 4.12B we show the dependence of the fluid pressure peak on Q_{in}. When Q_{in} become greater than one, a fully saturated zone appears and the fluid pressure rises dramatically. In [8] a similar dependence is presented. They observe the same behavior of the fluid pressure for $Q_{in} < 1.3$. But when Q_{in} exceeds 1.3, the pressure reaches a metastable state and does not increase much with increase of the initial saturation due to the water escape through the entrance of the nip. In our model water rearranges within the computational domain but it is not allowed to escape from the computational domain. So we do not observe this stabilization of the fluid pressure peak due to the model limitations. Enrichment of the model with the boundary conditions which allow escape of the water through the upper and lower boundaries is planned as the next step of our future studies.

4.3.2 Numerical experiments for evaluation of the dynamic capillary effect: multi-layer case

Now we consider the multilayer cases which may be investigated numerically only with the help of the two-dimensional model. The input data from Table 4.1 is used in all numerical experiments.

The first test case is developed for the roll press with eleven layers (see Table 4.3), where Layer 6 presents the paper. The paper–felt sandwich is transported with the speed $|\mathbf{V}_{s,in}| = 100\ m/min$. The boundaries of the computational domain are considered to be $\Gamma_L = \{x = -0.1\ m\}$, $\Gamma_R = \{x = 0.1\ m\}$. Remembering that τ equal to zero corresponds to the static capillary pressure model, we show the numerical results for the first test case in Figs. 4.13–4.16. Figs. 4.13A, B, C show the distribution of the water saturation for τ equal to 0, 10, and $100\ Pa\ s$, respectively. In Figs. 4.14A, B, C the location of the fully saturated zone and in Figs. 4.15A, B, C the distribution of the fluid pressure are shown for τ equal to 0, 10, and $100\ Pa\ s$. Fig. 4.16 presents the dry solid content of the paper layer for the different values of τ. As we can see from the obtained numerical results, the behavior of the solution of the multilayer test problem is quite similar to the single-layer tests. The

Table 4.3: Experimental data for two-dimensional multilayer test case 1

	$\mathbf{K}_{0,xx}$, $[m^2]$	$\mathbf{K}_{0,xy}$, $[m^2]$	$\mathbf{K}_{0,yy}$, $[m^2]$	$\phi\|_{\Gamma_L}$, $[\%]$	$d\|_{\Gamma_L}$, $[mm]$	C_0, $[\%]$
Layer 1	$1.00e-09$	0	$1.00e-09$	20	2.50	26
Layer 2	$1.89e-11$	$-1.89e-13$	$5.91e-11$	40	0.28	38
Layer 3	$1.57e-11$	$-1.43e-13$	$2.96e-11$	34	0.60	44
Layer 4	$6.72e-12$	$-6.51e-14$	$2.42e-11$	31	0.52	45
Layer 5	$8.34e-11$	$-1.05e-13$	$2.46e-11$	52	0.60	42
Layer 6	$5.00e-12$	0	$1.00e-13$	88	0.28	90
Layer 7	$2.95e-11$	$-6.66e-14$	$1.82e-11$	45	0.40	44
Layer 8	$2.93e-12$	$-5.22e-14$	$1.59e-11$	25	0.42	45
Layer 9	$8.36e-12$	$-8.88e-14$	$1.36e-11$	29	0.65	44
Layer 10	$1.11e-11$	$-1.13e-13$	$3.02e-11$	31	0.28	48
Layer 11	$8.17e-11$	$-1.05e-13$	$6.48e-11$	53	0.23	49

fully saturated zone decreases and the fluid pressure takes the characteristic shape with increase of the material coefficient τ. We also notice that the dry solid content of the paper is not influenced much by the dynamic capillary effect. It changes the shape with the increase of τ but the final value remains the same.

The second numerical test is performed for the roll press with parameters presented in Table 4.4 and $|\mathbf{V}_{s,in}| = 500m/min$. The boundaries of the computational domain are $\Gamma_L = \{x = -0.15m\}$, $\Gamma_R = \{x = 0.15\ m\}$. The numerical results are presented in Figs. 4.17–4.20. The saturation for τ equal to 0, 10, and $100\ Pa\ s$ is shown in Figs. 4.17A, B, and C, respectively. The location of the fully saturated zone and the distribution of the pressure are presented in Figs. 4.18A, B, C and 4.19A, B, C for the different values of the material coefficient, respectively. Here we observe a significant decrease of the fully saturated zone with increase of the dynamic component. The fluid pressure shows the same behavior as before. With increase of τ we observe after the pressure peak an appearance of the region with the pressure below the initial value. As opposed to the previous example, the dry solid content of the paper is influenced by the dynamic capillarity. Its value increases after the pressing with increasing τ.

For the third numerical test we consider the shoe press with $|\mathbf{V}_{s,in}| = 1000\ m/min$ and $\Gamma_L = \{x = -0.30\ m\}$, $\Gamma_R = \{x = 0.40\ m\}$. We use the input data for the layers as in test case 1 from Table 4.3 except the initial saturation which is presented in Table 4.5. Numerical results are presented in Figs. 4.21–4.24. The difference in the water saturation for the considered values of τ can not be seen. Thus, we show only one distribution of the water saturation in Fig. 4.21, where Figs. 4.21(A) and (B) show the water saturation in the undeformed and standard computational domains, respectively. Figs. 4.22A, 4.23A correspond to the static capillary pressure model. In

Table 4.4: Experimental data for two-dimensional multilayer test case 2

	$\mathbf{K}_{0,xx}$, $[m^2]$	$\mathbf{K}_{0,xy}$, $[m^2]$	$\mathbf{K}_{0,yy}$, $[m^2]$	$\phi\vert_{\Gamma_L}$, $[\%]$	$d\vert_{\Gamma_L}$, $[mm]$	C_0, $[\%]$
Layer 1	$5.00e-12$	0	$1.00e-13$	88	0.24	91
Layer 2	$1.51e-10$	$1.64e-12$	$1.15e-10$	53	0.51	51
Layer 3	$1.45e-10$	$2.34e-12$	$1.60e-10$	53	0.81	51
Layer 4	$3.46e-10$	$-5.60e-13$	$2.05e-10$	57	2.65	51
Layer 5	$9.75e-10$	$-2.88e-12$	$4.93e-10$	80	0.65	51
Layer 6	$1.00e-08$	0	$1.00e-08$	35	5.00	17

Table 4.5: Experimental data for two-dimensional multilayer test case 3

	C_0, $[\%]$
Layer 1	12
Layer 2	38
Layer 3	44
Layer 4	45
Layer 5	42
Layer 6	99
Layer 7	44
Layer 8	45
Layer 9	44
Layer 10	48
Layer 11	49

Figs. 4.22B, 4.23B and Figs. 4.22C, 4.23C the material coefficient τ is equal to 10 and $100\ Pa\ s$, respectively. The location of the fully saturated zone are shown in Fig. 4.22. Fig. 4.23 represents the distribution of the fluid pressure. The dry solid content of the paper layer is shown in Fig. 4.24 for different τ. All numerical results are presented for the undeformed geometry except the saturation for $\tau = 100\ Pa\ s$. The fluid pressure shows the same behavior as in the previous test cases. But in saturation we observe an increase of the fully saturated zone with increasing τ. It may be caused by the different geometries of the computational domain. The curve of the dry solid content changes its shape but the final value remains the same for the cases with the dynamic and static capillary pressure.

4.3.3 Numerical experiments for the discretization technique

For the model with the static capillary pressure we have the possibility to compare the numerical solution with results obtained in [43], where the model was discretized with the finite element

method. This opportunity is used to investigate the quality of the discretization technique used in this study. Typically, the difference in solutions can be well seen in the distribution of the water velocity. For the first and third test cases we show distributions of the water velocities in Figs. 4.25, 4.26. In these figures we do not show the whole range of the water velocity in order to see better regions with nonphysical values. We cut the water velocities by some value which is shown in each figure on the color bar (see Figs. 4.25, 4.26). Figs. 4.25A and 4.26A represent the distribution of the water velocity obtained with the help of our model. The results obtained with the help of the model proposed by Rief are shown in Figs. 4.25B and 4.26B. In Figs. 4.25C, 4.26C we show magnified regions which are indicated in Figs. 4.25B, 4.26B with the help of black boxes. The last figures show that the solution obtained with the help of discretization used by Rief gives nonsmooth and sometimes oscillatory solution at the same time as our solution is smooth. Such nonphysical oscillations of the finite element solution are typical for convection-diffusion equations, if no stabilization technique (e.g. streamwise diffusion) is used.

In most of the test cases it was observed that the numerical algorithm proposed in this study converges faster than the algorithm from [43]. The MPFA-O method is also very well applicable to the specific boundary conditions which we have to preserve between layers.

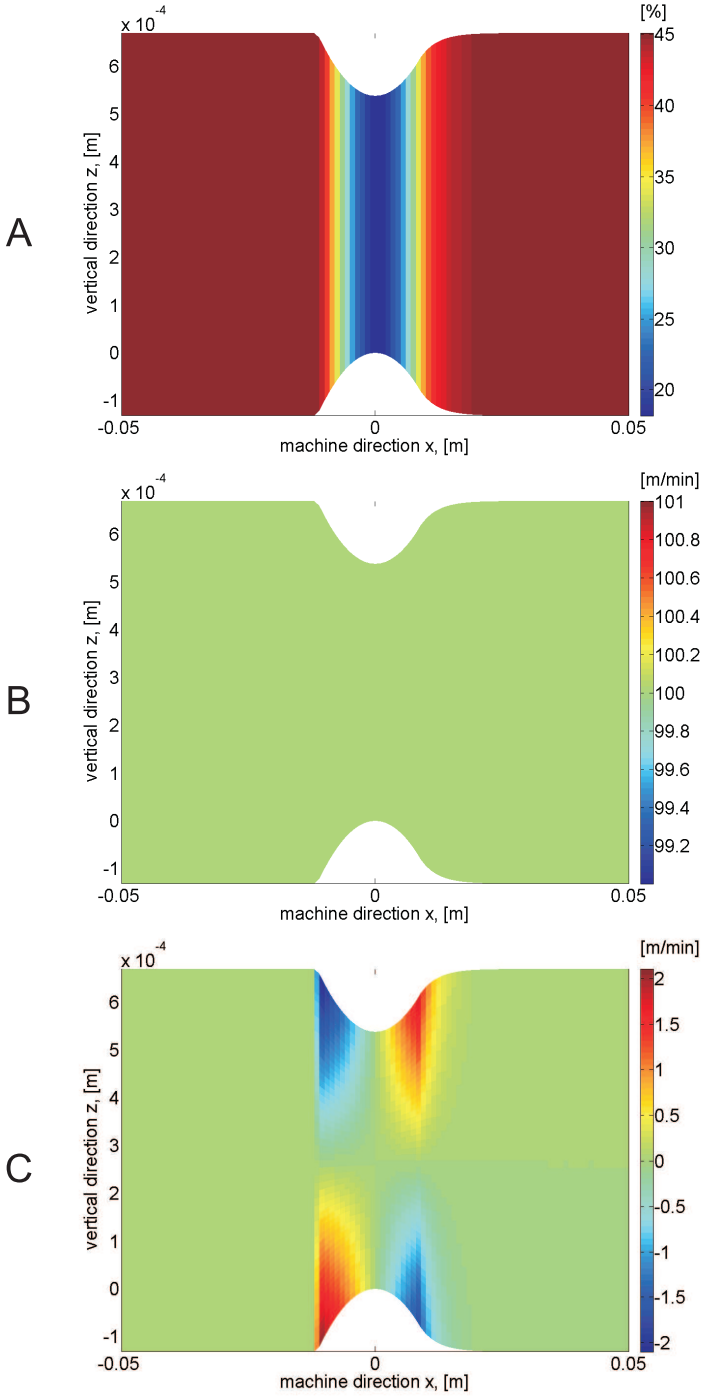

Fig. 4.5: Input data for the flow solver for "Felt 1" with $|\mathbf{V}_{s,in}| = 100\ m/min$: porosity ϕ (A), x-component of solid velocity $\mathbf{V}_s$ (B), z-component of solid velocity $\mathbf{V}_s$ (C)

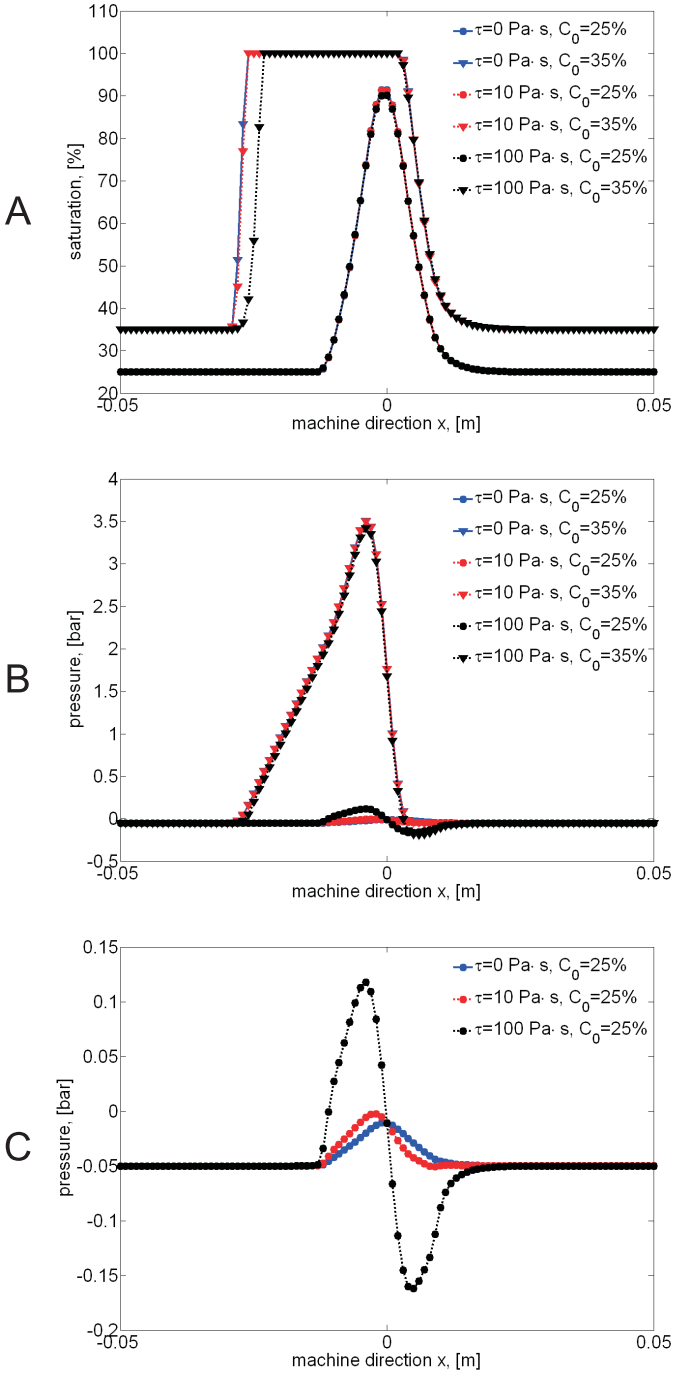

Fig. 4.6: Saturation (A) and pressure (B, C) for "Felt 1" with $|\mathbf{V}_{s,in}| = 100\, m/min$

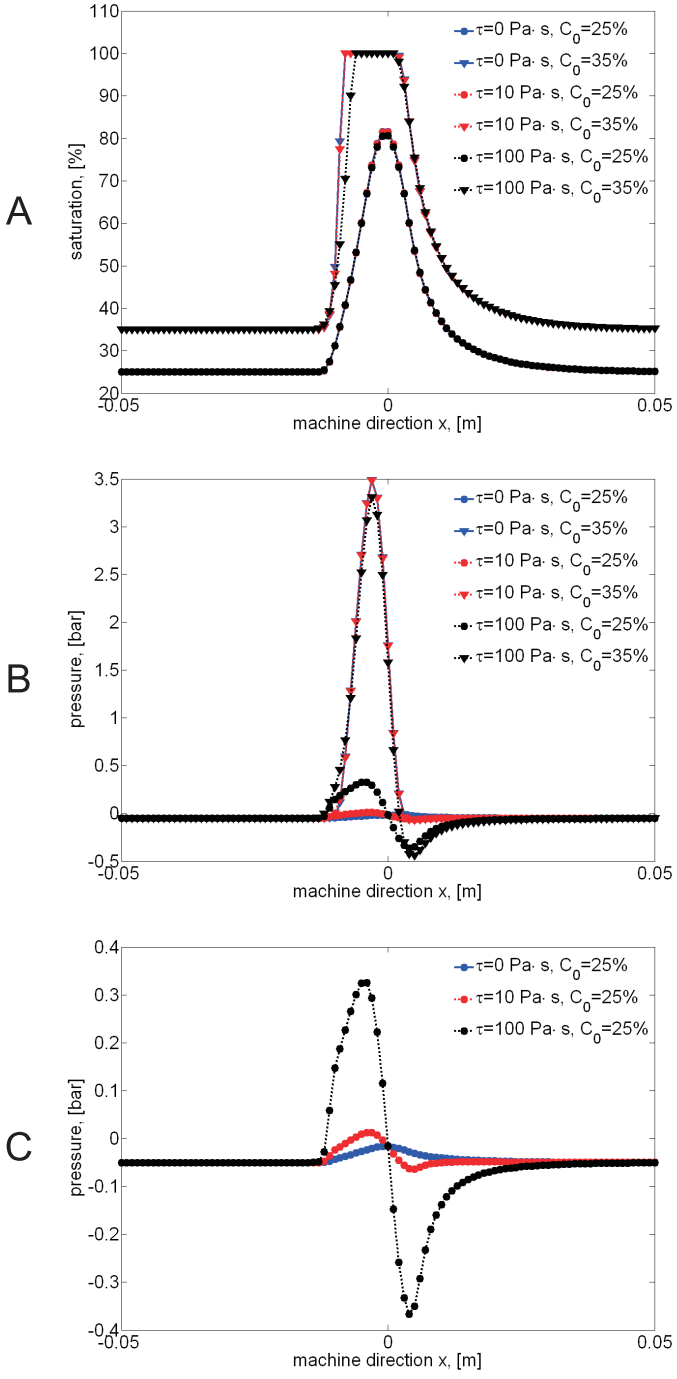

Fig. 4.7: Saturation (A) and pressure (B, C) for ”Felt 1” with $|\mathbf{V}_{s,in}| = 300\ m/min$

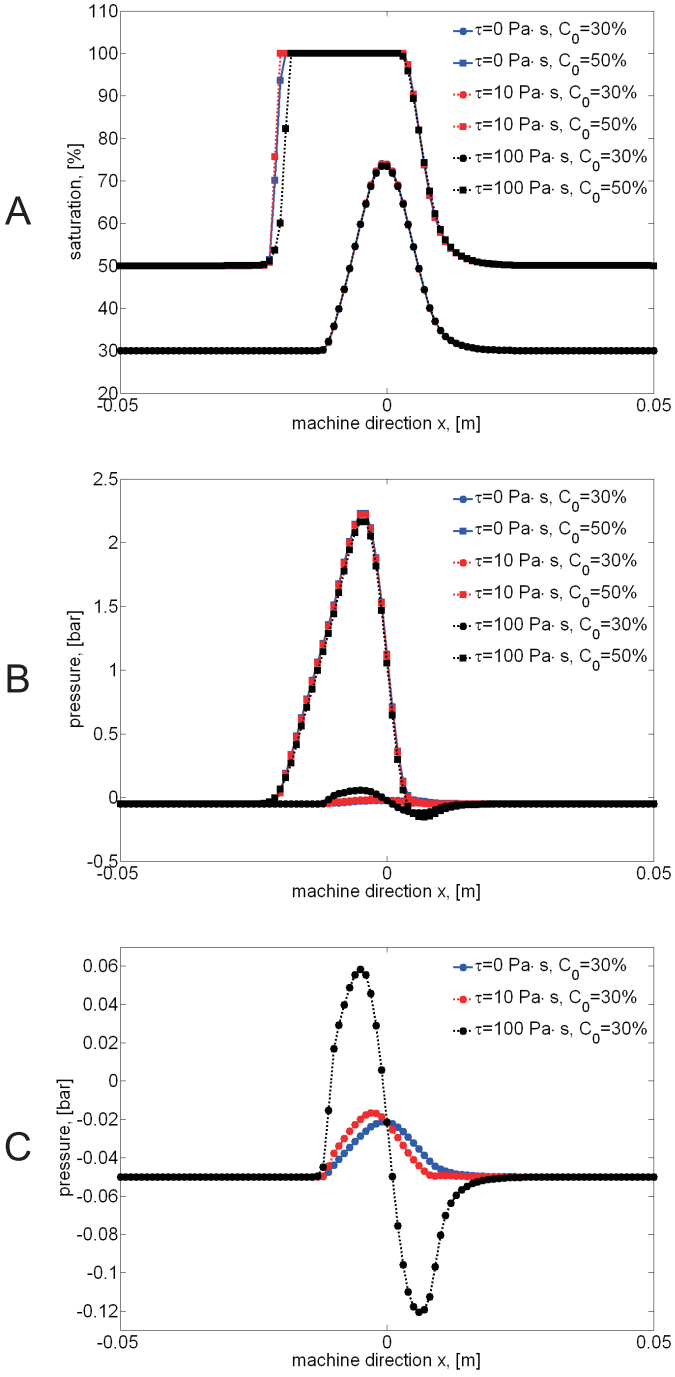

Fig. 4.8: Saturation (A) and pressure (B, C) for "Felt 2" with $|\mathbf{V}_{s,in}| = 100\, m/min$

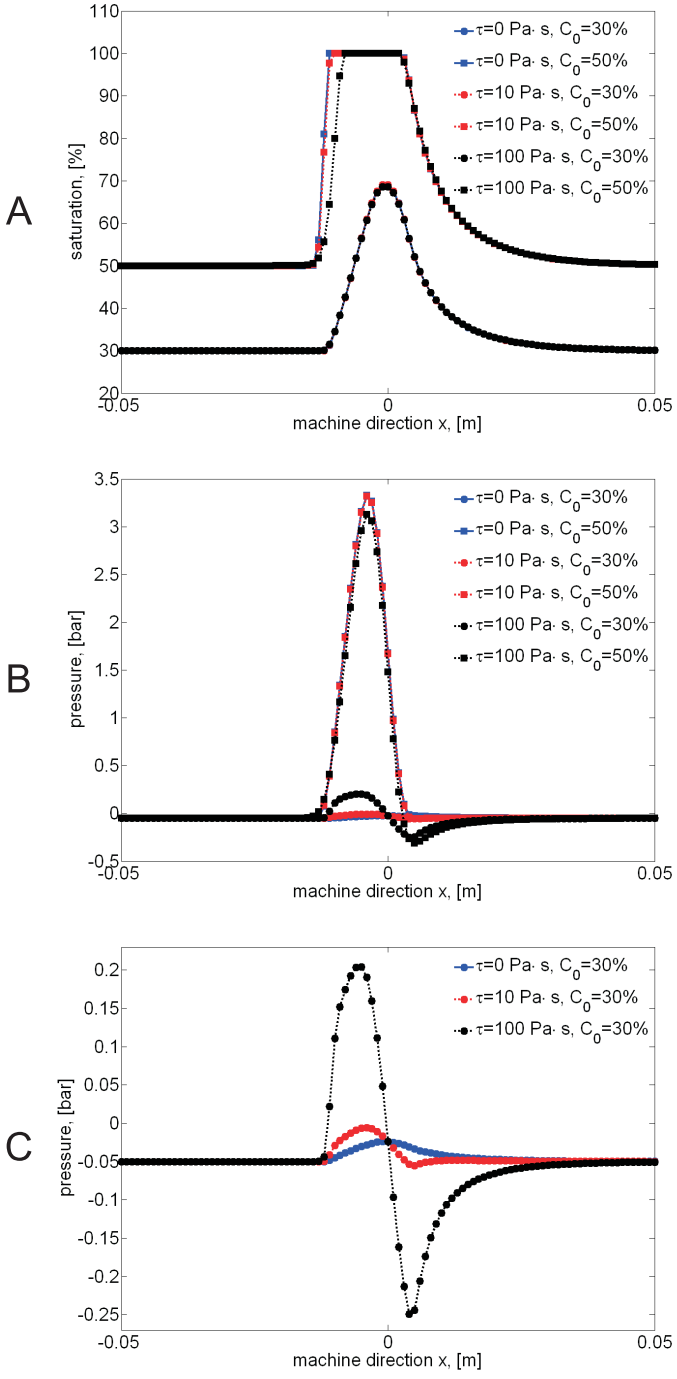

Fig. 4.9: Saturation (A) and pressure (B, C) for "Felt 2" with $|\mathbf{V}_{s,in}| = 300\ m/min$

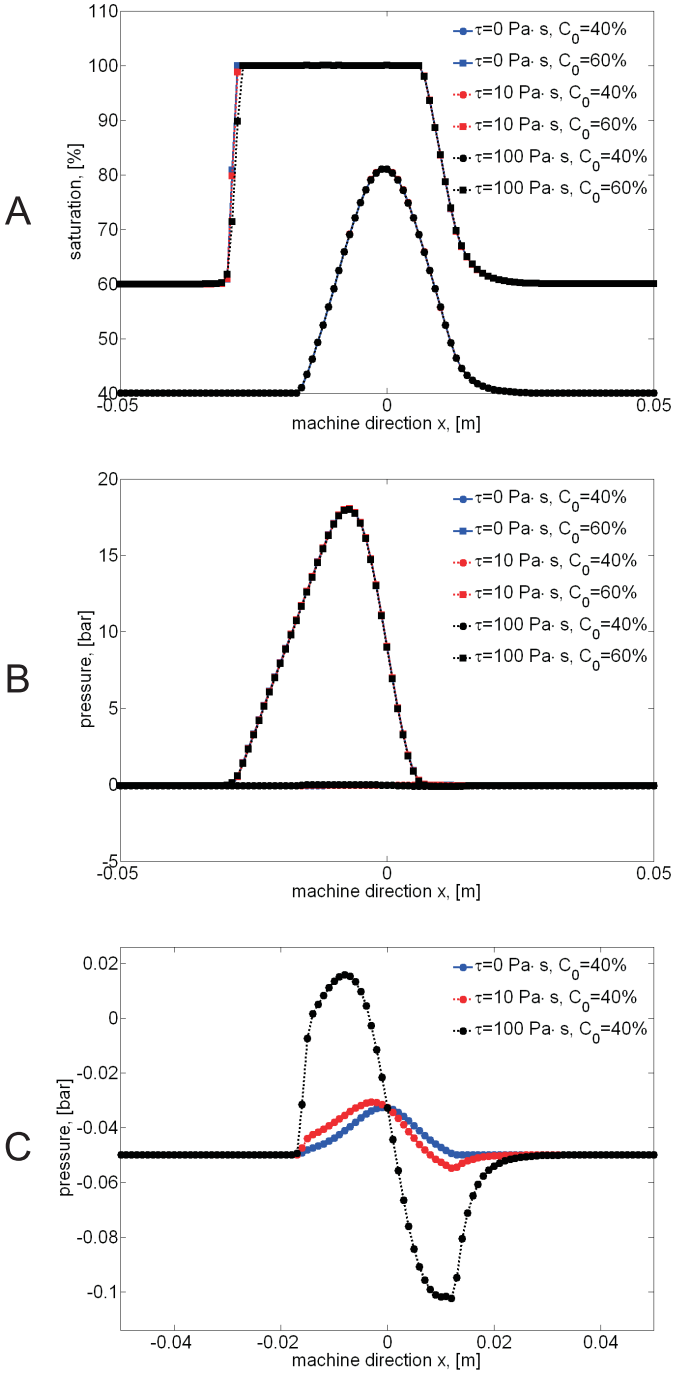

Fig. 4.10: Saturation (A) and pressure (B, C) for "Paper" with $|\mathbf{V}_{s,in}| = 100\ m/min$

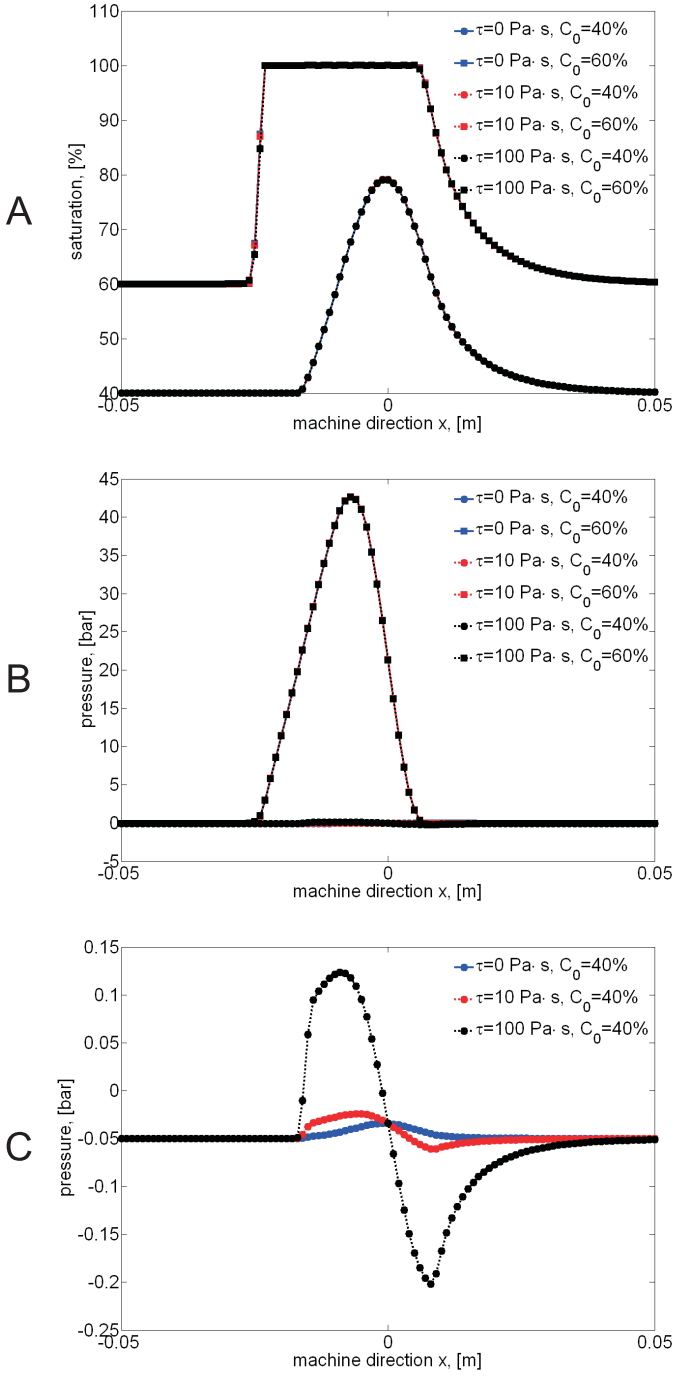

Fig. 4.11: Saturation (A) and pressure (B, C) for "Paper" with $|\mathbf{V}_{s,in}| = 300\, m/min$

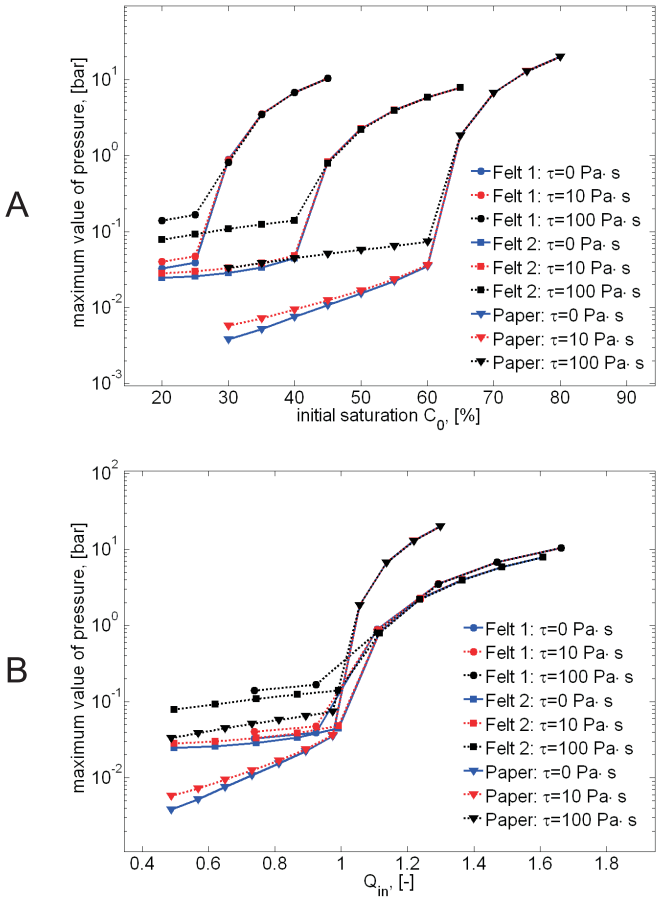

Fig. 4.12: Fluid pressure peak as a function of the initial saturation C_0 (A) and Q_{in} (B) for $|\mathbf{V}_{s,in}| = 100\ m/min$

4.4 Results and discussions

In this chapter a two-dimensional model was developed for the pressing section of a paper machine. This model adopted the dynamic capillary pressure effects described earlier by Hassanizadeh and Gray. At first, the mathematical model was discussed together with its discretization technique. Then, some numerical results were obtained. Single-layer test cases were carried out to compare the two-dimensional solutions with the laboratory experiments and to obtain the main behavior of the water saturation and the water pressure in presence of the dynamic capillary effects. The behavior of the pressure for the model with the dynamic capillary pressure is similar to the behavior of the pressure obtained in the laboratory experiments by [8]. We also observed the same kind of dependence of the pressure peak on the initial saturation as Beck.

Multilayer simulations showed that the behavior of the fluid pressure is the same as in the single-layer case. Regarding the distribution of the saturation, we notice that the behavior of the fully saturated regions for the static and dynamic capillary pressure models may differ for different geometries of the computational domain. So we observed a decrease of the fully saturated area with increasing τ for the roll nips and otherwise for the shoe press. For the dry solid content of the paper layer it was not possible to evaluate a general behavior for all test cases. We observed dependence of the dry solid content on particular test cases. In general, the numerical experiments showed that the material coefficient τ of order 10 and $100\ Pa\ s$ significantly influences the distributions of the fluid pressure and the saturation. On the other hand the distribution of the dry solid content of the paper layer does not change much when τ changes in this range.

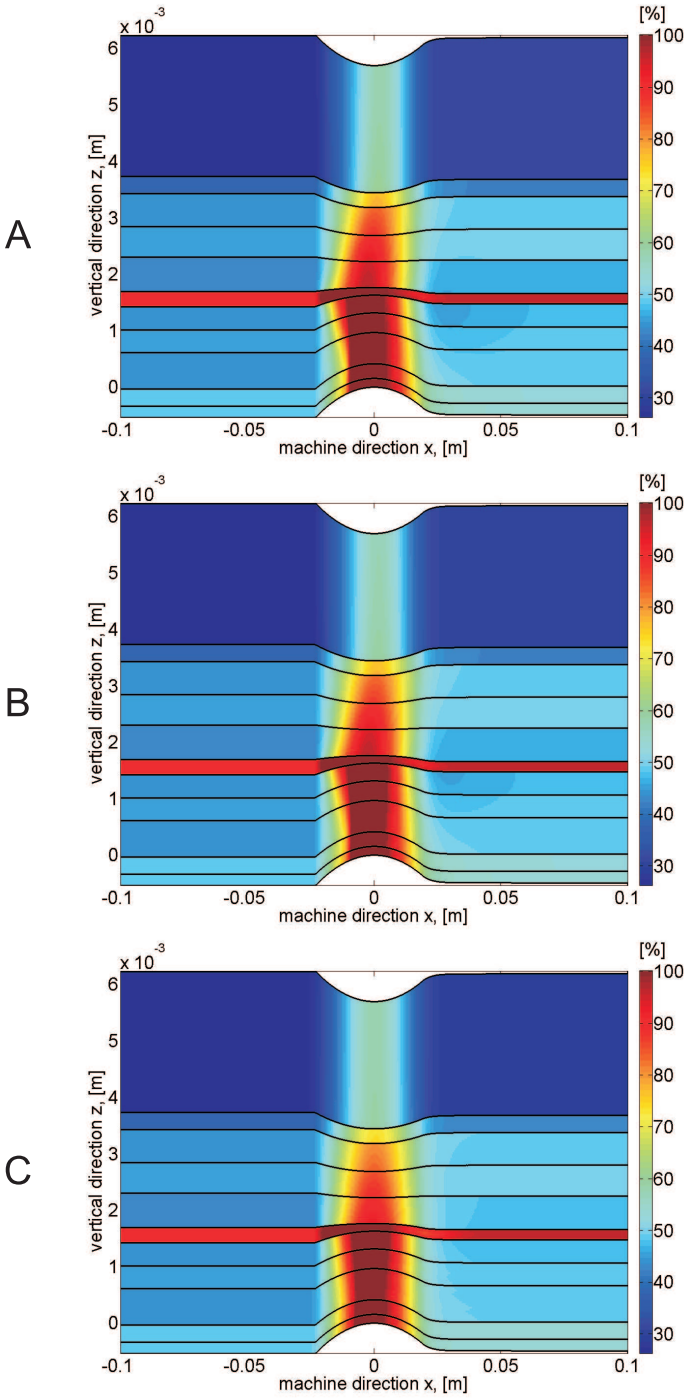

Fig. 4.13: Saturation for the test case 1 with τ equal to 0 (A), 10 (B) and 100 $Pa\ s$ (C)

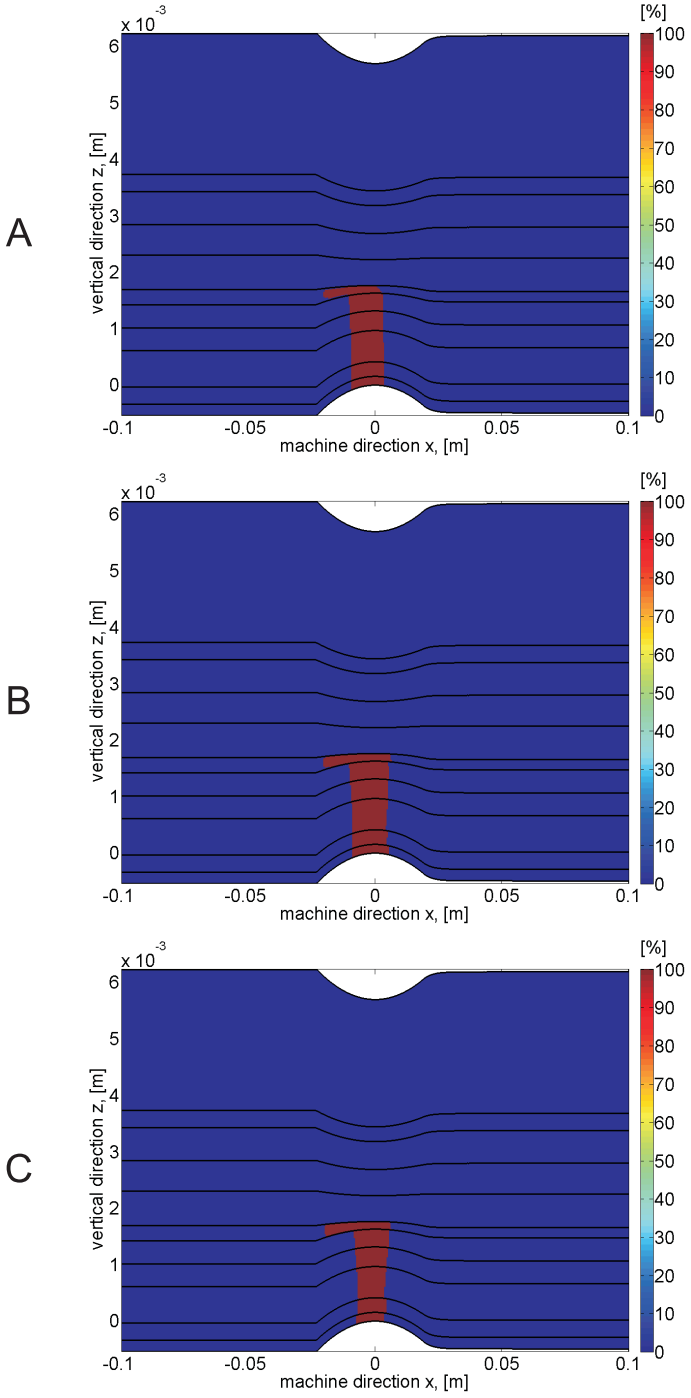

Fig. 4.14: Fully saturated zone for the test case 1 with τ equal to 0 (A), 10 (B) and 100 $Pa\ s$ (C)

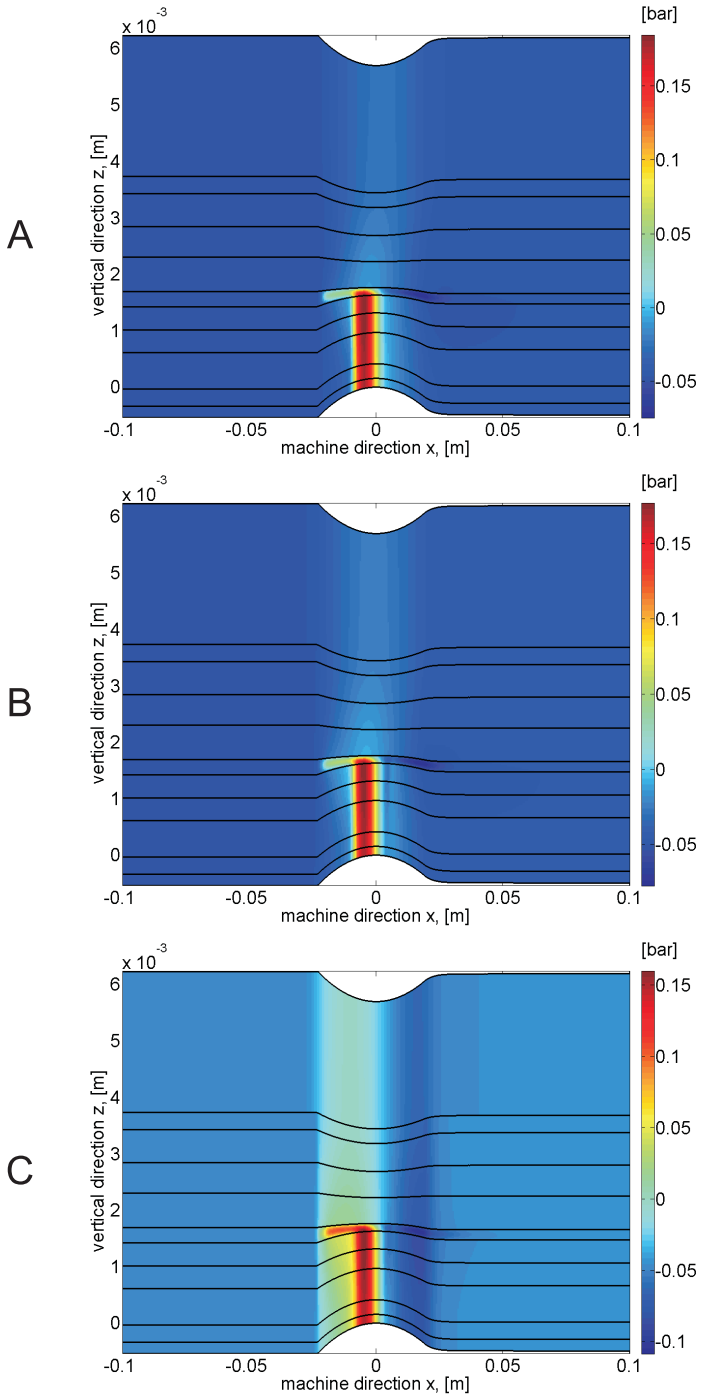

Fig. 4.15: Pressure for the test case 1 with τ equal to 0 (A), 10 (B) and 100 $Pa\ s$ (C)

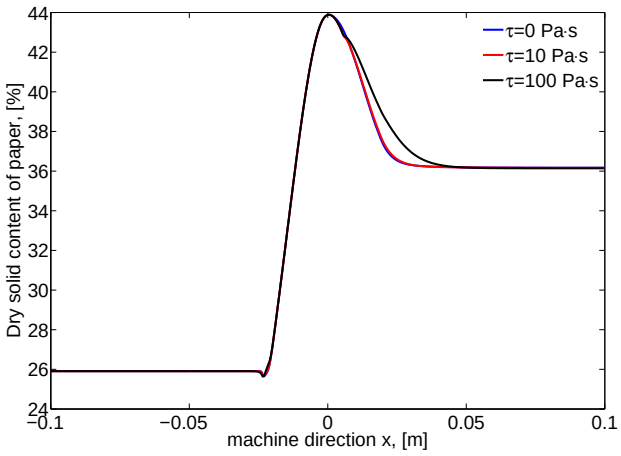

Fig. 4.16: Dry solid content of the paper for the test case 1 for different values of τ

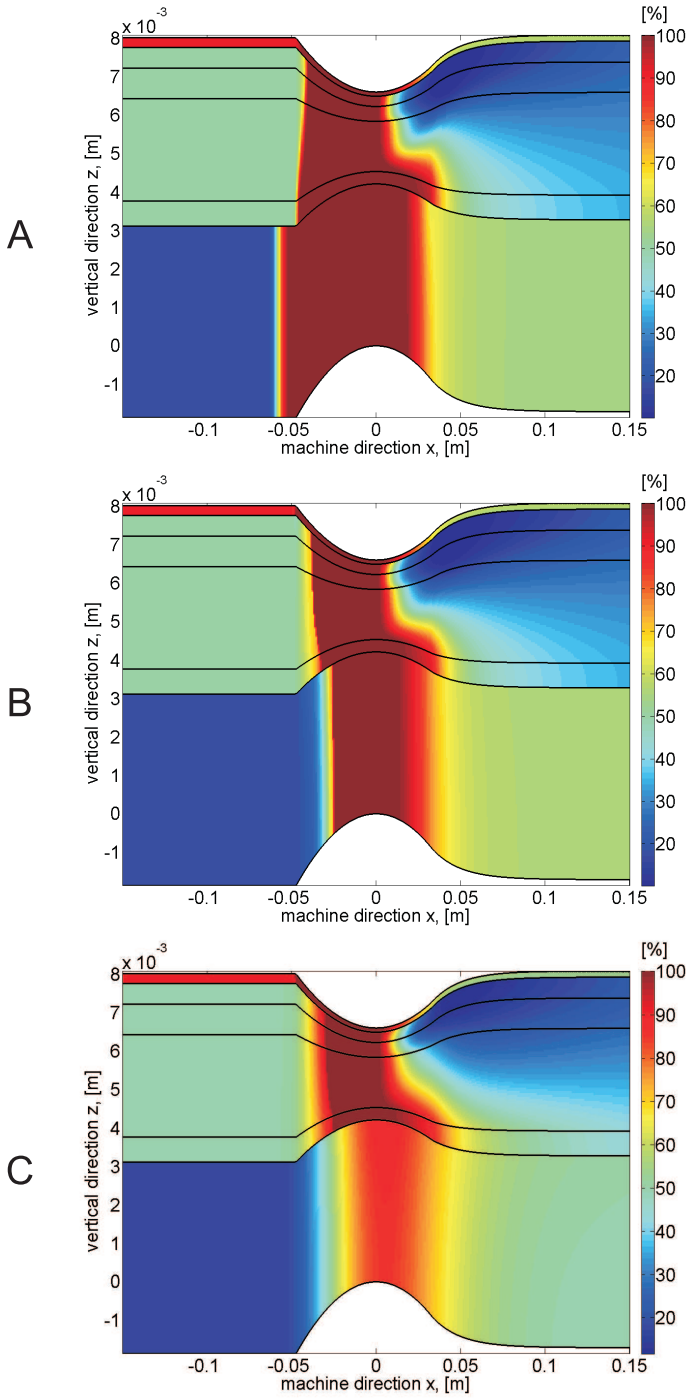

Fig. 4.17: Saturation for the test case 2 with τ equal to 0 (A), 10 (B) and 100 $Pa\ s$ (C)

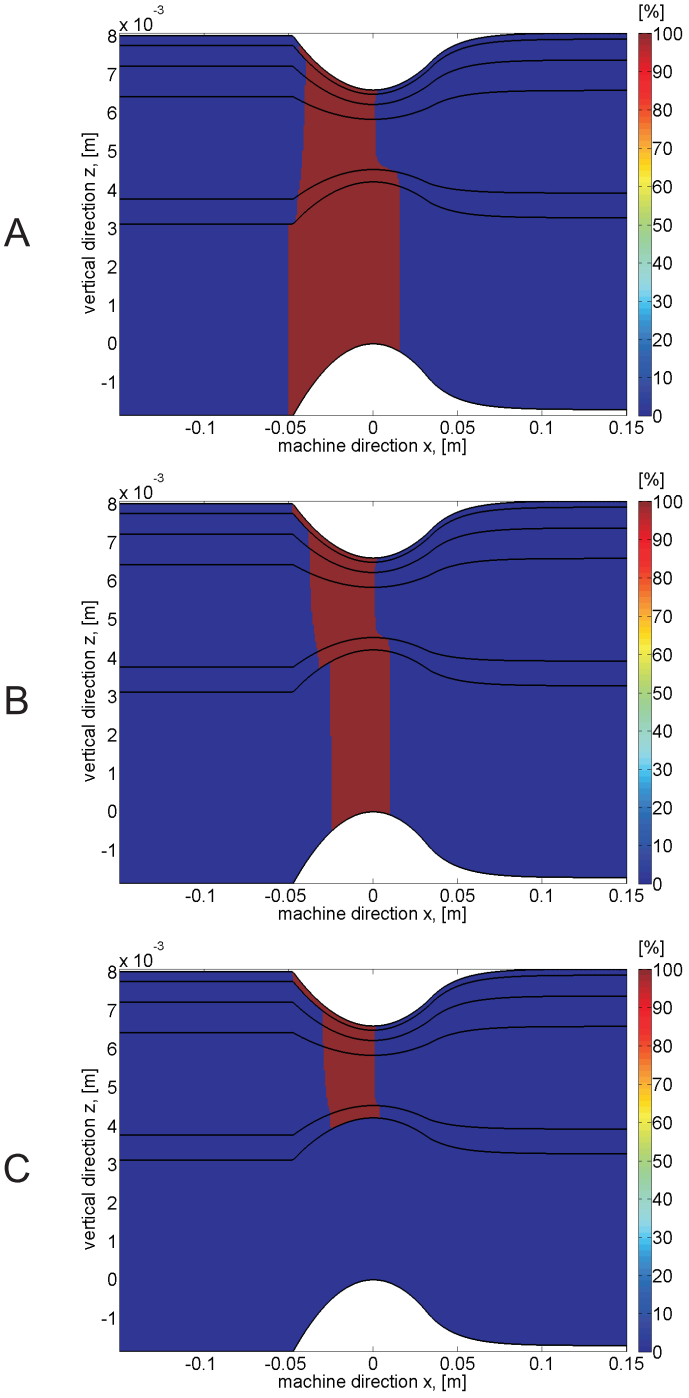

Fig. 4.18: Fully saturated zone for the test case 2 with τ equal to 0 (A), 10 (B) and 100 $Pa\ s$ (C)

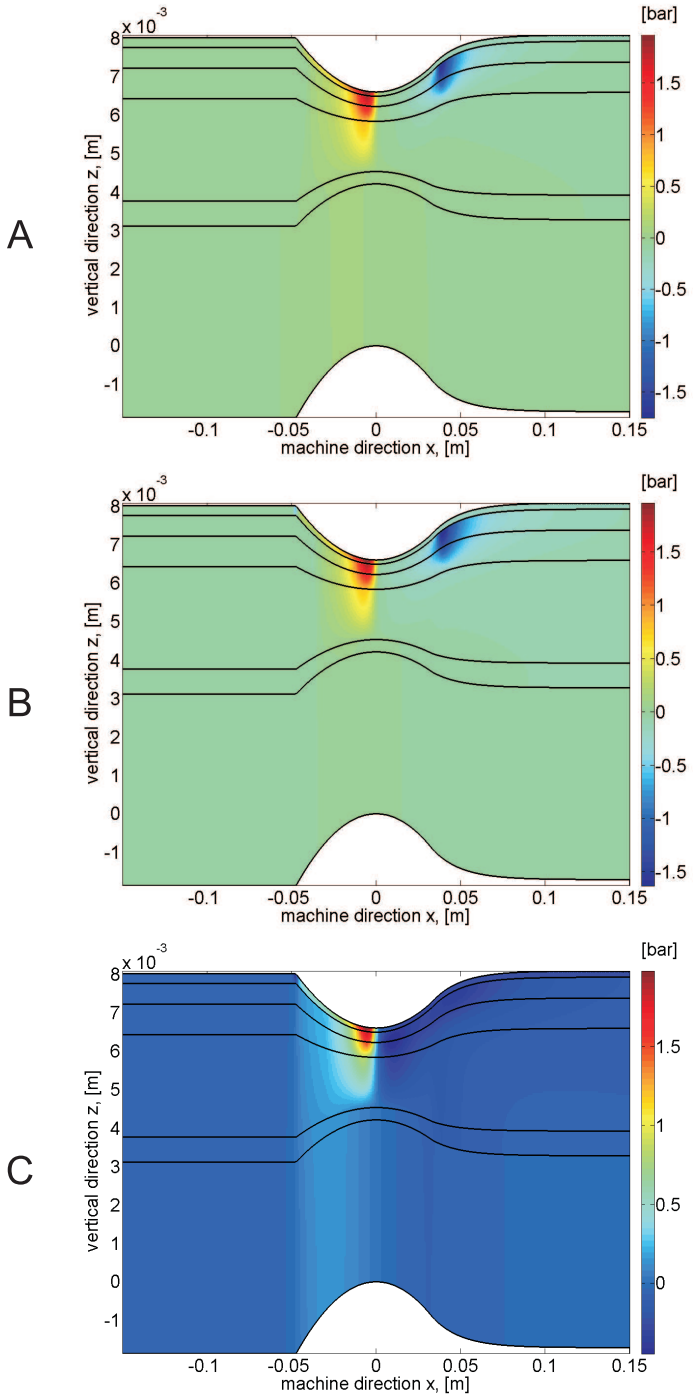

Fig. 4.19: Pressure for the test case 2 with τ equal to 0 (A), 10 (B) and 100 $Pa\ s$ (C)

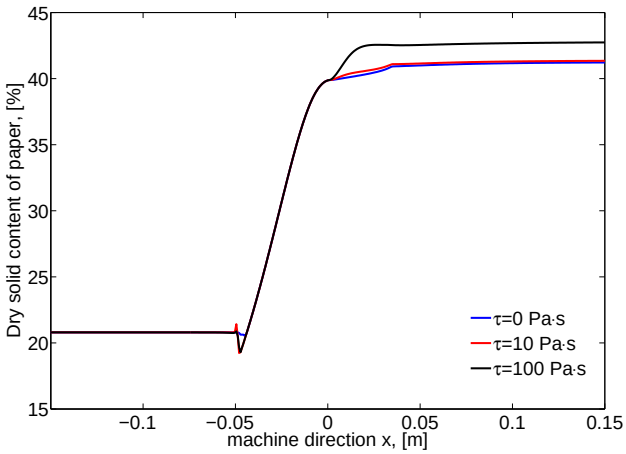

Fig. 4.20: Dry solid content of the paper for the test case 2 for different values of τ

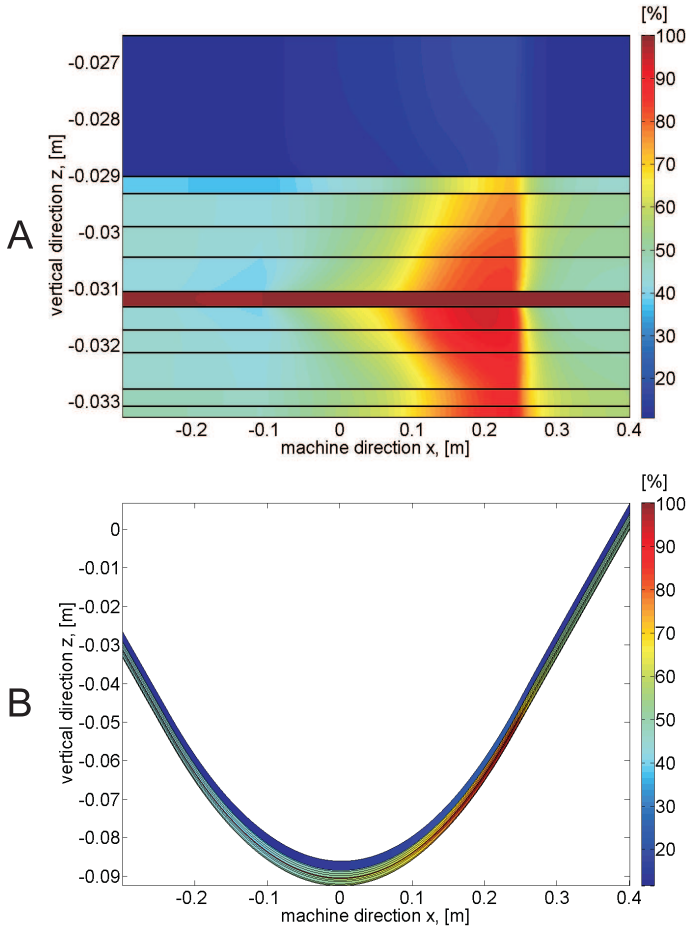

Fig. 4.21: Saturation for the test case 3 for different values of τ for the undeformed (A) and standard (B) computational domains

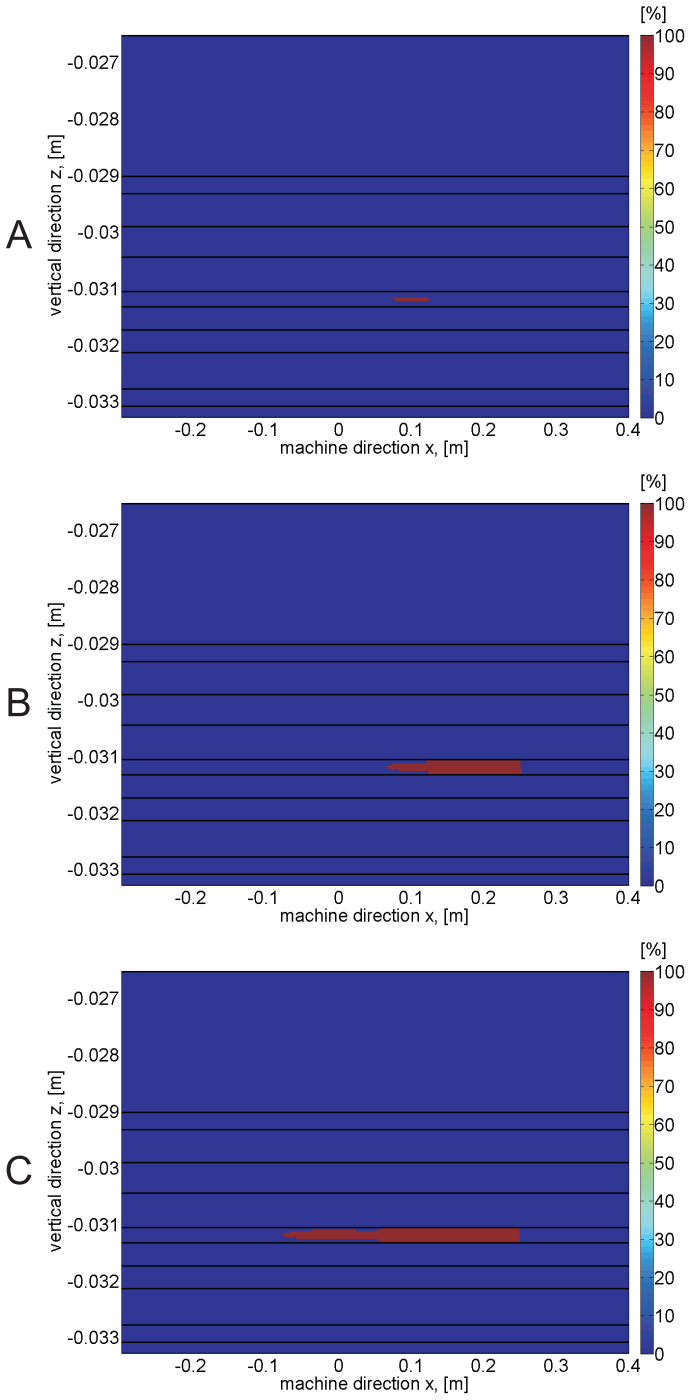

Fig. 4.22: Fully saturated zone for the test case 3 with τ equal to 0 (A), 10 (B) and 100 $Pa\ s$ (C)

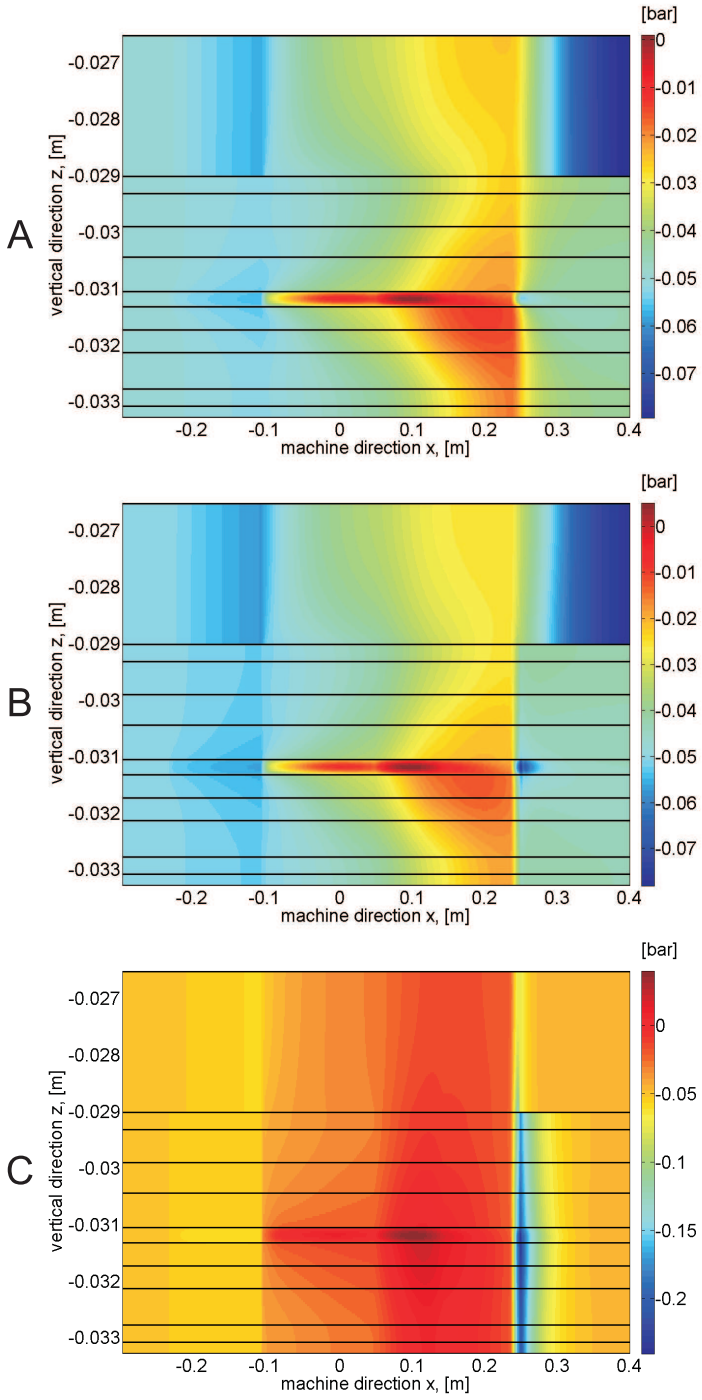

Fig. 4.23: Pressure for the test case 3 with τ equal to 0 (A), 10 (B) and 100 $Pa\ s$ (C)

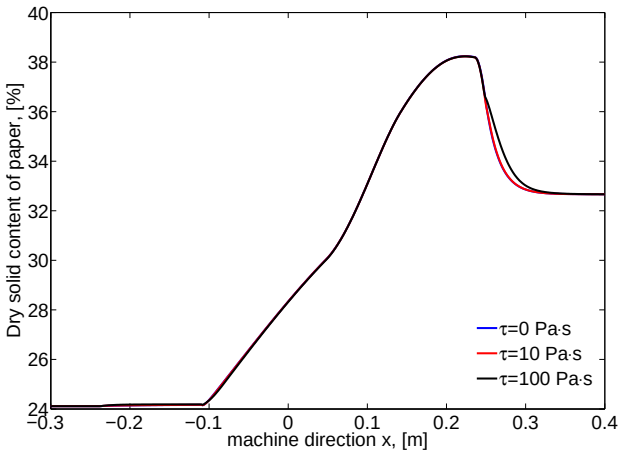

Fig. 4.24: Dry solid content for the test case 3 for different values of τ

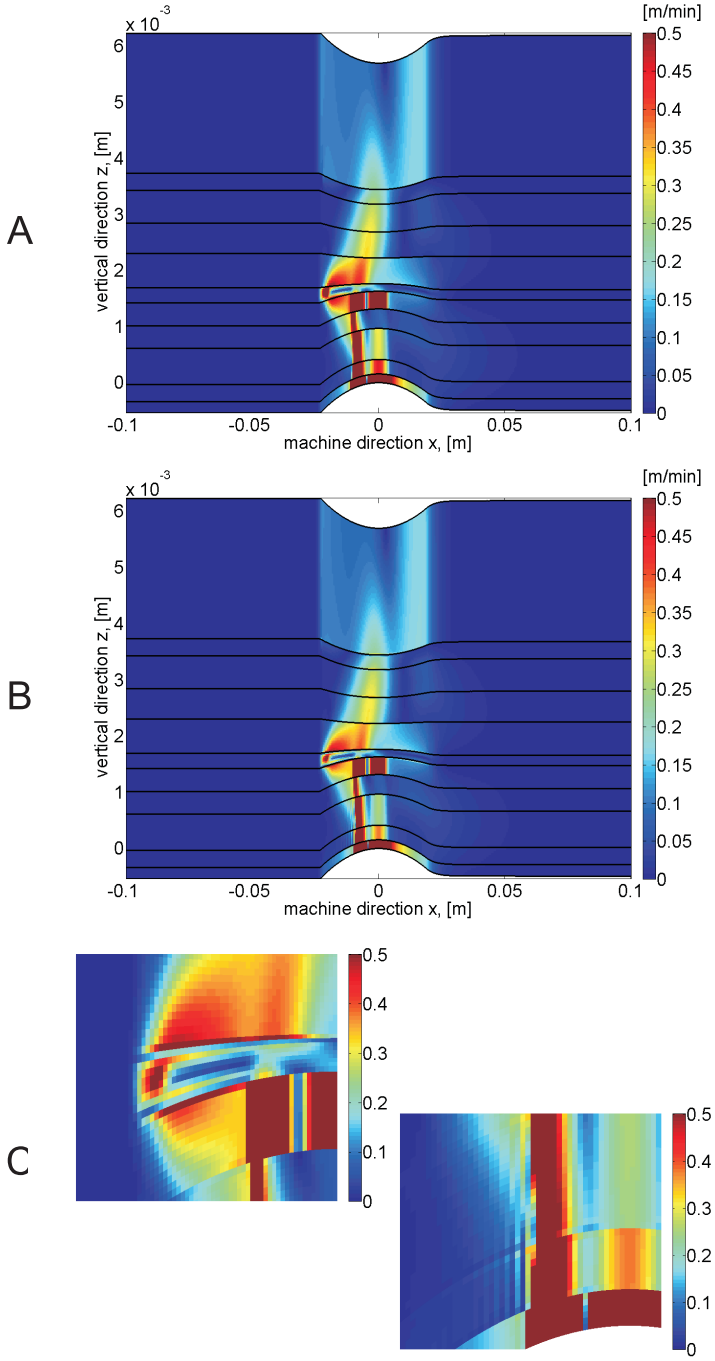

Fig. 4.25: Water velocity for the test case 1 with the static capillary pressure model obtained by the MPFA-O method (A) and by the FE method (B,C)

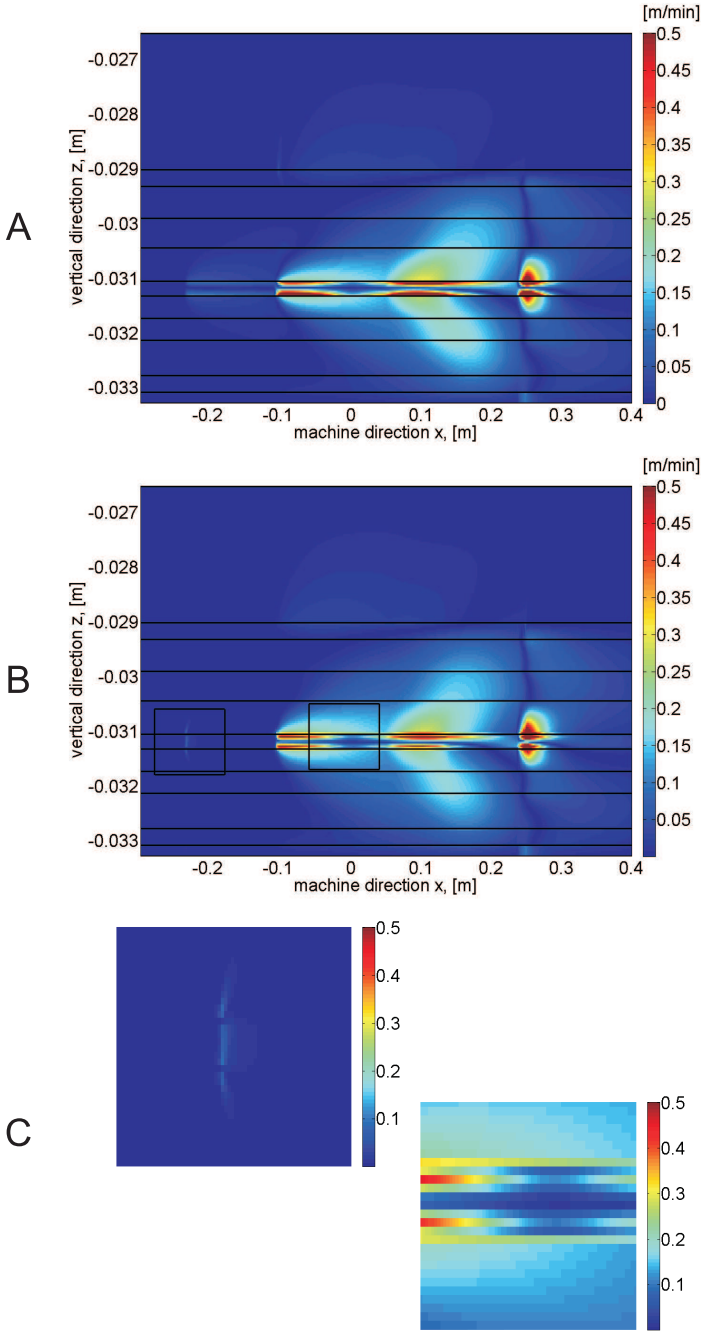

Fig. 4.26: Water velocity for the test case 3 with the static capillary pressure model obtained by the MPFA-O method (A) and by the FE method (B,C)

Chapter 5

Two-Dimensional Model (Two-Phase Flow)

Developing the mathematical model of the pressing section of a paper machine, up to now we have assumed that the air phase has a constant pressure within the computational domain. It simplifies the mathematical model significantly since we consider instead of two nonlinear mass conservation equations in the flow model only one for the water phase. But when we make Assumption 2.1.1 in Section 2.1.1 we remark that its admissibility has to be shown. Thus, now we are going to develop a model for the pressing section using a two-phase flow model without the Richards' assumption.

The previously stated mathematical model takes into consideration the dynamic capillary pressure–saturation relation, which allows us to obtain the behavior of the fluid pressure similar to one obtained in the laboratory experiments carried out by Beck [8]. As the first step we are going to investigate the admissibility of Assumption 2.1.1 for the model without the dynamic capillary effects. We will check if accounting for the real dynamics of the air phase allows us to recover effects which we encountered under the Richards' assumption for the air phase, but with dynamic capillary pressure. The model accounting for the both phases and the dynamic capillary pressure is going to be a subject for our future work.

In this chapter the pressing section of a paper machine is simulated with the help of the two-phase flow approach. The two-dimensional model accounts for the filtration of the water and the air within the computational domain taking into consideration the static capillary pressure–saturation relation. At first, in Section 5.1 we extend the previous flow model by inclusion of the mass conservation equation for the air phase. Moreover, the mathematical model is improved by allowing for more complex boundary conditions which allow water to escape through of the upper and lower boundaries. This issue was not accounted for before. The finite difference scheme obtained by the

MPFA-O method and the numerical algorithm are discussed in Section 5.2. Numerical experiments checking range of applicability of the Richards' approach for the mathematical modeling of the pressing section are performed in Section 5.3. Finally, we draw some conclusions in Section 5.4.

5.1 Mathematical model

As in the previous chapter, we consider the computational domain Ω indicated in Fig. 5.1. We assume that the paper-felt sandwich is transported in horizontal direction from the left to the right with the constant speed $\mathbf{V}_{s,in}$. We also consider that the two flow regimes may be present in Ω. Ω^1 and Ω^2 denote the domains with the single-phase water flow and the two-phase air-water flow, respectively. The interface between these domains is denoted by Γ.

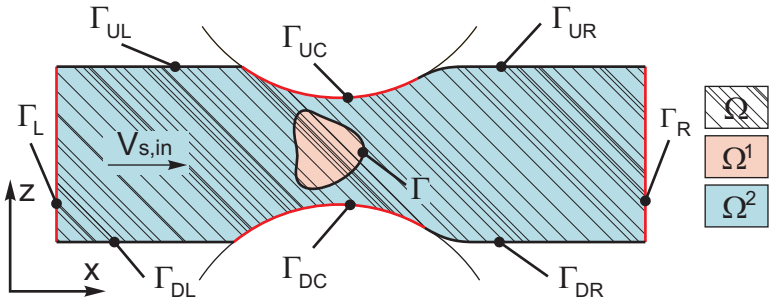

Fig. 5.1: Computational domain Ω with two flow regimes and new partitioning of $\partial\Omega$

Let Assumptions 2.1.2 and 2.1.3 be satisfied. Let the function p_c^{stat} be defined by Assumption 2.2.1. Then, the function S is defined in the following way:

$$S(p_c) = \begin{cases} S_* & \text{for } p_c \geq p_c^{stat}(S_*), \\ \left(p_c^{stat}\right)^{-1}(p_c) & \text{for } p_c \in (p_c^{stat}(1), p_c^{stat}(S_*)), \\ 1 & \text{for } p_c \leq p_c^{stat}(1); \end{cases} \tag{5.1}$$

where S_* is discussed in Remark 2.2.2. Then, the saturated water flow obeys the following mass conservation equation:

$$-\operatorname{div}\left(\frac{\mathbf{K}}{\mu_w}\operatorname{grad} p_w\right) + \operatorname{div}\left(\phi \mathbf{V}_s\right) = 0, \quad \mathbf{x} \in \Omega^1. \tag{5.2}$$

The two-phase air-water flow is described by the mass conservation equations for the air and water

phases:

$$-\operatorname{div}\left(\frac{k_{rw}}{\mu_w}\mathbf{K}\operatorname{grad} p_w\right)+\operatorname{div}\left(\phi S\mathbf{V}_s\right)=0,\quad \mathbf{x}\in\Omega^2; \tag{5.3}$$

$$-\operatorname{div}\left(\frac{k_{ra}}{\mu_a}\mathbf{K}\operatorname{grad} p_a\right)+\operatorname{div}\left(\phi(1-S)\mathbf{V}_s\right)=0,\quad \mathbf{x}\in\Omega^2; \tag{5.4}$$

where k_{ra} ($[-]$) is the relative permeability of the air phase, μ_a is the air viscosity measured in $[Pa\ s]$, the water saturation S is a function of the capillary pressure $p_c = p_a - p_w$, the saturation of the air phase is equal to $(1-S)$.

Now we are concerned with the conditions which have to be satisfied at the interfaces between the domains with the different flow regimes and between the layers. As it was introduced in Section 4.1.1 the interfaces between domains $\Omega_1, \Omega_2, \ldots, \Omega_L$, which indicate different layers, are denoted by $\Gamma_l = \overline{\Omega}_l \cap \overline{\Omega}_{l+1}$ for all $l = \overline{1, L-1}$, where L is the total number of layers (see Fig. 4.2). The water flux $\mathbf{J}_w$ within Ω is defined as:

$$\mathbf{J}_w = \begin{cases} -\frac{\mathbf{K}}{\mu_w}\operatorname{grad} p_w + \phi\mathbf{V}_s & \text{for } \mathbf{x}\in\overline{\Omega^1};\\ -\frac{k_{rw}}{\mu_w}\mathbf{K}\operatorname{grad} p_w + \phi S\mathbf{V}_s & \text{for } \mathbf{x}\in\Omega^2. \end{cases} \tag{5.5}$$

For the air flux $\mathbf{J}_a$ within Ω we have:

$$\mathbf{J}_a = \begin{cases} 0 & \text{for } \mathbf{x}\in\overline{\Omega^1};\\ -\frac{k_{ra}}{\mu_a}\mathbf{K}\operatorname{grad} p_a + \phi(1-S)\mathbf{V}_s & \text{for } \mathbf{x}\in\Omega^2. \end{cases} \tag{5.6}$$

Then, the continuity of the pressures and the continuity of the normal fluxes across the interfaces have to be satisfied in the following form:

$$[p_w]_\Gamma = 0,\quad [\mathbf{J}_w\cdot\mathbf{n}]_\Gamma = 0, \tag{5.7}$$

$$[p_w]_{\Gamma_l} = 0,\quad [\mathbf{J}_w\cdot\mathbf{n}]_{\Gamma_l} = 0,\ l = \overline{1, L-1}, \tag{5.8}$$

$$[\mathbf{J}_a\cdot\mathbf{n}]_\Gamma = 0, \tag{5.9}$$

$$[p_a]_{\Gamma_l} = 0,\quad [\mathbf{J}_a\cdot\mathbf{n}]_{\Gamma_l} = 0,\ l = \overline{1, L-1}. \tag{5.10}$$

Now let the function k_{rw} satisfy Assumption 3.1.1(c) and the function k_{ra} satisfy the following assumption.

Assumption 5.1.1. *$k_{ra} \in C([S_*, 1])$, $k_{ra} : [S_*, 1] \to [0, 1]$ is a decreasing function.*

In the fully saturated region Ω^1 the water saturation satisfies $S \equiv 1$ and p_a is undefined. To have

a unique model for both saturated and unsaturated flows we define a prolongation of p_a in Ω^1 with the help of Eq. (5.12). Then, the system of equations (5.2)–(5.10) yields:

$$-\operatorname{div}\left(\frac{k_{rw}(S)}{\mu_w}\mathbf{K}\operatorname{grad} p_w\right)+\operatorname{div}(\phi S\mathbf{V}_s)=0,\quad \mathbf{x}\in\Omega; \tag{5.11}$$

$$p_a-p_w-p_c^{stat}(1)=0,\quad \mathbf{x}\in\Omega^1; \tag{5.12}$$

$$-\operatorname{div}\left(\frac{k_{ra}(S)}{\mu_a}\mathbf{K}\operatorname{grad} p_a\right)+\operatorname{div}(\phi(1-S)\mathbf{V}_s)=0,\quad \mathbf{x}\in\Omega^2; \tag{5.13}$$

together with the continuity of the pressures and the normal fluxes (5.8) and (5.10) on Γ_l, $l=\overline{1,L-1}$. We remark that thanks to the assumptions on the functions k_{rw} and k_{ra} the interfacial conditions (5.7) and (5.9) across Γ are satisfied automatically. We remark that the air pressure p_a extended to Ω by (5.12) also satisfies continuity condition across Γ: $[p_a]_\Gamma=0$.

Specification of the boundary conditions is important for the development of a mathematical model. Often the simulated process is too complex to precisely define the boundary conditions which have to be specified. In Section 4.1.1 we used the no-flow conditions for the water phase on the upper and lower boundaries. But as it was observed during the numerical experiments carried out in Section 4.3.1 the no-flow boundary conditions for the water phase in some test cases are too artificial. Thus, in this model we are going to improve this issue by allowing the water to escape from the upper and lower boundaries of the computational domain where there is no contact with the pressing rolls.

Since the boundary conditions for the water phase become more complex and the boundary conditions for the air phase have to be introduced the boundaries Γ_U and Γ_D have to be divided into some parts as shown in Fig. 5.1:

$$\Gamma_\alpha=\Gamma_{\alpha L}\cup\Gamma_{\alpha C}\cup\Gamma_{\alpha R},\quad \alpha=\{U,D\}.$$

As before we want Assumption 2.1.4 to be satisfied. Then, for the water phase we have the same Dirichlet and no-flow boundary conditions on Γ_L and Γ_R, respectively (for more details see Section 4.1.1). On the parts of the upper and lower boundaries Γ_{UC} and Γ_{DC} where the computational domain is in contact with the pressing rolls we preserve the zero-Neumann boundary conditions since the water can not escape there. On the rest of the boundaries we would like to allow the escape of water if the fluid pressure is greater than the atmospheric pressure. Here the atmospheric pressure is chosen as the first approximation. Although, we note that in reality the pressure outside the boundary where water escapes is nonconstant and greater than atmospheric. Thus, on Γ_{UL}, Γ_{UR}, Γ_{DL} and Γ_{DR} we specify Robin conditions. The boundary conditions for the water pressure

yield:

$$p_w|_{\Gamma_L} = -p_c^{stat}(C_0(\mathbf{x})), \quad \mathbf{x} \in \Gamma_L; \tag{5.14}$$

$$\left(-\frac{k_{rw}}{\mu_w}\mathbf{K}\,\mathrm{grad}\,p_w\right)\cdot\mathbf{n}_s\Big|_{\Gamma_R} = 0; \tag{5.15}$$

$$\left(-\frac{k_{rw}}{\mu_w}\mathbf{K}\,\mathrm{grad}\,p_w\right)\cdot\mathbf{n}\Big|_{\Gamma_{\alpha C}} = 0, \quad \alpha = \{U, D\}; \tag{5.16}$$

$$\left(-\frac{k_{rw}}{\mu_w}\mathbf{K}\,\mathrm{grad}\,p_w\right)\cdot\mathbf{n}\Big|_{\Gamma_{\alpha L},\Gamma_{\alpha R}} = \hat{\gamma}(p_w)(p_w - p^{atm})\big|_{\Gamma_{\alpha L},\Gamma_{\alpha R}}, \quad \alpha = \{U, D\}; \tag{5.17}$$

where γ is the parameter which defines how much water is allowed to escape, p^{atm} is the atmospheric pressure in $[Pa]$. We define the function $\hat{\gamma}$ as:

$$\hat{\gamma}(p_w) = \begin{cases} \gamma & \text{if } p_w \geq p^{atm}; \\ 0 & \text{if } p_w < p^{atm}; \end{cases} \tag{5.18}$$

where $\gamma = const > 0 \in \mathbb{R}$.

Now let us discuss the boundary conditions for the air phase. Since the boundaries Γ_L and Γ_R are far away from the pressing zone (see Assumption 2.1.4) we assume that the air remains at the atmospheric pressure there. On the rest of the boundaries where the computational domain is not in contact with the pressing rolls Dirichlet boundary conditions are applied. On Γ_{UC} and Γ_{DC} the zero-Neumann boundary conditions are preserved since air as well as water can not escape through these parts of the boundaries. Thus, the boundary conditions for the air phase yield:

$$p_a|_{\Gamma_\alpha} = p^{atm}, \quad \alpha = \{L, UL, UR, R, DR, DL\}; \tag{5.19}$$

$$\left(-\frac{k_{ra}}{\mu_a}\mathbf{K}\,\mathrm{grad}\,p_a\right)\cdot\mathbf{n}\Big|_{\Gamma_{\alpha C}} = 0, \quad \alpha = \{U, D\}. \tag{5.20}$$

The elasticity model by which the flow model is supplemented was discussed in Section 4.1.2.

5.2 Discretization

Now we are going to discuss the discretization of the flow model (5.11)–(5.13) by the finite volume method on the quadrilateral unstructured grid. Let the two-dimensional mesh $\mathcal{D}$ be introduced by Definition 4.2.1 as shown in Fig. 4.3 and discussed in Section 4.2.

Then, for Eq. (5.11) we have the following finite volume scheme:

$$-\sum_{\sigma\in\mathcal{E}_{\mathcal{K}}}\frac{k_{rw}(S_\sigma)}{\mu_w}F^w_{\mathcal{K},\sigma}+\sum_{\sigma\in\mathcal{E}_{\mathcal{K}}}m_\sigma\phi_\sigma S_{\sigma,+}\mathbf{V}_s\cdot\mathbf{n}_\sigma=0,\quad \mathcal{K}\in\mathcal{T};\tag{5.21}$$

where S_σ and $S_{\sigma,+}$ are defined by Eqs. (4.15) and (4.16), respectively. We remember that $\mathcal{T}_1$ and $\mathcal{T}_2$ are the sets of the control volumes which approximate the domains Ω^1 and Ω^2, respectively. Using properties of the function S, the finite difference scheme for Eq. (5.12) yields:

$$p_{a,\mathcal{K}}-p_{w,\mathcal{K}}=p_c^{stat}(1),\quad \mathcal{K}\in\mathcal{T}_1.\tag{5.22}$$

For Eq. (5.13) we have:

$$-\sum_{\sigma\in\mathcal{E}_{\mathcal{K}}}\frac{k_{ra}(S_\sigma)}{\mu_a}F^a_{\mathcal{K},\sigma}+\sum_{\sigma\in\mathcal{E}_{\mathcal{K}}}m_\sigma\phi_\sigma(1-S_{\sigma,+})\mathbf{V}_s\cdot\mathbf{n}_\sigma=0,\quad \mathcal{K}\in\mathcal{T}_2.\tag{5.23}$$

The general form of $F^\alpha_{\mathcal{K},\sigma}$, $\alpha=\{w,a\}$ yields:

$$F^\alpha_{\mathcal{K},\sigma}=\sum_{\mathcal{L}\in\mathcal{N}_{\mathcal{K},\sigma}}t^{\alpha,\mathcal{L}}_{\mathcal{K},\sigma}p_{\alpha,\mathcal{L}};\tag{5.24}$$

where $t^{\alpha,\mathcal{L}}_{\mathcal{K},\sigma}$ are the transmissibility coefficients and $\mathcal{N}_{\mathcal{K},\sigma}$ is defined by (4.19).

The boundary conditions (5.14)–(5.20) and the interfacial conditions (5.8), (5.10) are considered during accounting for the transmissibility coefficients $t^{\alpha,\mathcal{L}}_{\mathcal{K},\sigma}$ by the MPFA-O method (for more details see [1, 2]). In case if the control volume $\mathcal{K}$ contains an edge common with the boundary $\partial\Omega$, values S_σ and $S_{\sigma,+}$ are defined by (4.24), (4.25) (see Section 4.2). Remembering that on the upper and lower boundaries the Robin boundary conditions for the water phase and the Dirichlet boundary conditions for the air phase may be specified, in addition we have:

- if $\sigma\in\mathcal{E}_{\mathcal{K}}\cap(\mathcal{E}_{ext,U}\cup\mathcal{E}_{ext,D})$ than $S_\sigma=S_{\mathcal{K}}$ and $S_{+,\sigma}$ do not need to be defined since $\mathbf{n}_\sigma\cdot\mathbf{V}_s=0$.

To solve the system of equations (5.21)–(5.24) the Newton's method is used. Initial guesses for the fluid pressure p_w and the air pressure p_a are chosen as:

$$\begin{aligned}p^0_{w,\mathcal{K}}&=p^{atm}-p_c^{stat}\left(C_0(\mathbf{x}_{\mathcal{K},\Gamma_L}),\phi(\mathbf{x}_{\mathcal{K},\Gamma_L})\right);\\ p^0_{a,\mathcal{K}}&=p^{atm};\end{aligned}$$

where the upper index corresponds to the number of the Newton's iteration. The initial guesses are chosen in a way that the pressures remain constant along the solid streamlines. Initial guess for the

water saturation $C_0(\mathbf{x})$ satisfies $C_0(\mathbf{x}) \in (S_*, 1)$. Thus, the set $\mathcal{T}_1^0$ is empty and $\mathcal{T}_2^0$ is equal to $\mathcal{T}$. After every Newton's iteration k for the system of equations (5.21)–(5.23) we obtain the correction values $\Delta p_{w,\mathcal{K}}^{k+1}$ and $\Delta p_{a,\mathcal{K}}^{k+1}$. New approximations of the fluid and air pressures are obtained as:

$$p_{w,\mathcal{K}}^{k+1} = p_{w,\mathcal{K}}^{k} + \Delta p_{w,\mathcal{K}}^{k+1}, \quad \mathcal{K} \in \mathcal{T};$$
$$p_{a,\mathcal{K}}^{k+1} = p_{a,\mathcal{K}}^{k} + \Delta p_{a,\mathcal{K}}^{k+1}, \quad \mathcal{K} \in \mathcal{T}.$$

Using Eq. (5.1), the water saturation can be defined. The sets $\mathcal{T}_1^{k+1}$ and $\mathcal{T}_2^{k+1}$ are obtained in the following form:

$$\mathcal{T}_1^{k+1} = \{\mathcal{K} \in \mathcal{T} : S\left(p_{a,\mathcal{K}}^{k+1} - p_{w,\mathcal{K}}^{k+1}\right) = 1\};$$
$$\mathcal{T}_2^{k+1} = \{\mathcal{K} \in \mathcal{T} : S\left(p_{a,\mathcal{K}}^{k+1} - p_{w,\mathcal{K}}^{k+1}\right) \in (S_*, 1)\};$$
$$\mathcal{T}_3^{k+1} = \{\mathcal{K} \in \mathcal{T} : S\left(p_{a,\mathcal{K}}^{k+1} - p_{w,\mathcal{K}}^{k+1}\right) = S_*\}.$$

Remark 5.2.1. *We use the fictitious domain method like in previous chapters. The proposed numerical approach may cause an appearance of some fictitious domains $\mathcal{T}_3^{k+1}$ with $S = S_*$. It is done to make sure that the formulation of the model is homogeneous for all values of the water saturation S. From the physical point of view, in this domain the mathematical model for the single-phase air flow has to be stated. Since in our numerical experiments the single-phase air flow has never occurred in this work we are not concerned with this flow regime.*

If after the kth Newton's iteration the set $\mathcal{T}_3^{k+1}$ is not empty any more, then on the next Newton's iteration $(k+1)$ one more equation has to be added to the system of equations (5.21)–(5.23):

$$S_{\mathcal{K}} = S_*, \quad \mathcal{K} \in \mathcal{T}_3.$$

5.3 Numerical experiments

Using the mathematical model developed in Section 5.1 and discretized in Section 5.2, which accounts for the water and air phases, we are going to perform some numerical experiments. This section aims at investigating the admissibility of Assumption 2.1.1, which states that the air phase remains at a constant pressure within the computational domain. We are going to use the same sets of parameters as in the numerical experiments performed in Section 4.3 and compare the results with the results obtained under Richards' assumption. Thus, some single-layer and multilayer test cases will be carried out sequentially.

As we discussed before, these numerical experiments will be performed only for the model

Table 5.1: Experimental data for the two-phase flow model

Variable	Dimension	Value
k_{ra}	$[-]$	$(1-S_e)^2(1-S_e^{1.5})$
S_e	$[-]$	$(S-S_*)/(1-S_*)$
μ_a	$[Pa\ s]$	$1.862e-5$
γ	$[mm^3 s/kg]$	$5.00e-9$
p^{atm}	$[Pa]$	0

with the static capillary pressure–saturation relation. The dynamic capillary effects in case of the two-phase flow model are going to be investigated in our future work.

5.3.1 Numerical experiments for the Richards' assumption: single-layer case

The input data for the single-layer test case is presented in Tables 4.1, 4.2. Some additional data required for the two-phase flow model is presented in Table 5.1. As a result of several numerical experiments, the parameter γ for the boundary condition (5.17) is chosen to be $5.00e-9\, mm^3 s/kg$. The atmospheric pressure p^{atm}, which is used in the boundary conditions for the water phase (5.17) and for the air phase (5.19) is chosen to be $0\ Pa$ (see Table 5.1). Since we are interested in values of pressure up to some constant, we have chosen zero for simplicity.

The numerical results for "Felt 1" are presented in Figs. 5.2–5.10. Figs. 5.2–5.7 show two-dimensional distributions of the water saturation, the water pressure, and the water velocities for the different initial saturations C_0 and the velocities $\mathbf{V}_{s,in}$. The water saturation S is shown in Figs. 5.2A–5.7A. Figs. 5.2B–5.7B and Figs. 5.2C–5.7C present the water pressure and the water velocity, respectively. The initial saturation C_0 is equal to 25% and 35% for the numerical tests presented in Figs. 5.2, 5.4, 5.6 and Figs. 5.3, 5.5, 5.7, respectively. The velocity $\mathbf{V}_{s,in}$ is considered to be equal to 100, 300, and 900 m/min and it is presented in Figs. 5.2, 5.3, Figs. 5.4, 5.5, and Figs. 5.6, 5.7, respectively.

The obtained results show that accounting for the real dynamics of the air phase causes some visible differences in distribution of the water phase. At first, let us remark that in the results presented in Figs. 5.2–5.7 we observe that the behavior of the water pressure has changed in comparison to the behavior obtained by the model under the Richards' assumption with static capillary pressure. The water pressure has the maximum value shifted to the left with respect to the center of the nip. Moreover, for small velocities $\mathbf{V}_{s,in}$ (100 and 300 m/min) we observe a decrease of the water pressure below the initial value behind the center of the press nip. The same kind of the water pressure behavior was obtained for the Richards' model with the dynamic capillary pressure–saturation relation and it is in agreement with the laboratory experiments carried out by Beck in

[8]. Secondly, we would like to pay attention to the water velocities $\mathbf{V}_w$ for the test cases with the large initial saturation C_0 and the large velocity $\mathbf{V}_{s,in}$ (see Fig. 5.3C, 5.5C–5.7C). Thanks to the extended boundary conditions, we observe a water escape from the computational domain when the water pressure is large near the boundary where the layer is not in contact with the roll surface.

Now we would like to have a better impression on how significant the difference between the two-phase flow model and the model using the Richards' approach is. Thereto, we average the results obtained with the help of the two-phase flow model in the vertical direction and show them on the same figure with the averaged results obtained with the help of the model from Chapter 4 (see Figs. 5.8–5.10). In Figs. 5.8–5.10 abbreviations "2PF" and "Rich" indicate the two-phase flow model and the Richards' model, respectively. Figs. 5.8A–5.10A show the water saturation for the different velocities $\mathbf{V}_{s,in}$, when Figs. 5.8B,C–5.10B,C show the water pressure.

The one-dimensional representation of the water saturation (see Figs. 5.8A–5.10A) allows us to see that a decrease of the maximum value of the water saturation is observed for the two-phase flow model in comparison to the flow model obtained under Richards' assumption. Let us now discuss it in more details. The comparison of the water saturation for the two-phase model and the Richards' model can be made in three steps. When the maximum value of the water saturation is small (see Fig. 5.10A with $C_0 = 25\%$), these two mathematical approaches give almost the same water saturation. The second case is when the maximum saturation reaches higher values around 80% and 90% but still not big enough to form a fully saturated zone in case of the Richards' model (see Figs. 5.8A, 5.9A with $C_0 = 25\%$, and Fig. 5.10 with $C_0 = 35\%$). Here, the decrease of the maximum value becomes visible. But the water saturation differs only for the big values and for smaller values results coincides with the results obtained by the Richards' model. This type of the water saturation behavior was also obtained by the Richards' model with the dynamic capillary effect (see Section 4.3). But the decrease of the maximum value of the saturation was much less than we observe for the two-phase flow model. The third case is when a fully saturated zone is formed for the Richards' approach in Figs. 5.8A, 5.9A with $C_0 = 35\%$. We observe that the air does not escape from the computational domain completely. The water saturation reaches some high value but it is not equal to one. Let us remark the remaining air is not due to the residual saturation of the air phase since it is considered to be equal to zero. We observe it due to the fact that the air velocity can not be infinite as in the case of the Richards' assumption. In this third case the distribution of the water saturation differs completely for whole range of the saturation values from the results obtained by the previous model.

In Figs. 5.8A and 5.9A with $C_0 = 35\%$ we can also observe an influence of the Robin boundary conditions included in this model to allow the water escape through the upper and lower boundaries. It effects the water saturation value on the right boundary. Since the amount of water within the

computational domain is not constant any more, the value of the water saturation after the pressing decreases in comparison with the saturation, when all water remains inside the paper-felt sandwich.

Regarding the water pressure, the one-dimensional profiles (see Figs. 5.8B,C–5.10B,C) show the behavior which we described previously discussing the two-dimensional representation of the obtained results. The maximum value of the water pressure occurs before the center of the nip for all performed test cases. The decrease of the water pressure below the initial value is observed in the cases when the velocities $\mathbf{V}_{s,in}$ are equal to 100 and 300 m/min. But it was not the case for the larger velocity ($|\mathbf{V}_{s,in}| = 900\, m/min$). According to the laboratory experiments carried out for the pressing section by Beck in [8], the decrease of the water pressure below the initial value was observed for the velocity $|\mathbf{V}_{s,in}| = 381\ m/min$. Thus, we can conclude that the pressure profiles obtained by the two-phase flow model for small $\mathbf{V}_{s,in}$ correspond to the reality and in case of large $\mathbf{V}_{s,in}$ more laboratory experiments are required. Analyzing the one-dimensional pressure profiles presented in Figs. 5.8B,C–5.10B,C, we also note that in most of the numerical tests for "Felt 1" the maximum value of the water pressure significantly rises in comparison to the test cases with the Richards' assumption.

The second and third single-layer test cases are performed for the felt and the paper with parameters presented in Tables 4.1, 4.2, and 5.1. The results are shown in Figs. 5.11–5.19 for "Felt 2" and in Figs. 5.20–5.28 for "Paper". Figs. 5.11–5.16, 5.20–5.25 show the obtained results in two dimensions. In Figs. 5.17–5.19, 5.26–5.28 the comparison of the results presented as one-dimensional variables and obtained by the averaging procedure in the vertical direction is presented. The behavior of the obtained results is similar to the behavior discussed in detail for the first test case "Felt 1". The water pressure profiles have the typical shape with the maximum value shifted to the left and the decrease after the center of the pressing nip. The maximum value of the water pressure rises significantly in the two-phase model in comparison to the model under the Richards' assumption. The water saturation also shows behavior similar to the test case "Felt 1". For the averaged one-dimensional profiles of the water saturation (see Figs. 5.17A–5.19A for "Felt 2" and Figs. 5.26A–5.28A for "Paper") the behavior of the water saturation can be divided into the following groups:

- if the water saturation values are less than 70%, the two-phase model gives almost the same results as the Richards' model (see Figs. 5.18A, 5.19A with $C_0 = 30\%$ and Figs. 5.28A with $C_0 = 40\%$);
- if the water saturation has the maximum value around 80% and 90%, the decrease of the maximum value of the water saturation is observed for the two-phase model in comparison to the saturation profiles obtained by the Richards' model (see Fig. 5.17A with $C_0 = 30\%$, Fig. 5.19A with $C_0 = 50\%$, Figs. 5.26A, 5.27 with $C_0 = 40\%$);

- if the Richards' model has a fully saturated region, the behavior of the one-dimensional profiles of the water saturation is completely different for the two-phase flow model and the Richards' model (see Figs. 5.17A, 5.18A with $C_0 = 50\%$, Figs. 5.26A–5.28A with $C_0 = 60\%$).

The influence of the new boundary conditions, which allow the escape of water through the upper and lower boundaries we can observe in Figs. 5.12C, 5.14C–5.16C for "Felt 2" and in Figs. 5.21C, 5.23C–5.25C for "Paper", where the water velocity is shown, and in Figs. 5.17A, 5.18A for "Felt 2" and in Figs. 5.26A–5.28A for "Paper", where the averaged water saturation is shown.

We remark that as opposed to the Richards' model in the two-phase flow model we observe two-dimensional effects, namely the water saturation and the water pressure vary in the vertical direction. This effect can be well seen in the test case "Paper" in the figures presenting the two-dimensional results (see Figs. 5.21–5.25) and also in some figures for "Felt 1" and "Felt 2", namely with the high initial saturation C_0 (see Figs. 5.3, 5.5, 5.7 and Figs. 5.12, 5.14, 5.16).

In Fig. 5.29 the water pressure peak is presented as a function of the initial saturation C_0 (see Fig. 5.29A) and Q_{in} (see Fig. 5.29B), where the quantity Q_{in} is defined by (4.33). Here we compare results obtained with the help of the two-phase flow model and the Richards' model for all the single-layer test cases. As it was also remarked before, we observe that the fluid pressure significantly rises in the case when the air phase is taken into account. Thanks to the Robin boundary conditions, which have been introduced in this chapter, we observe that the pressure peak profile is smoother for the two-phase flow model. Moreover, the fluid pressure does not rise much for $Q_{in} > 1.3$. This effect was also observed in the laboratory experiments performed by Beck in [8]. Thus, we may conclude that the new boundary conditions have improved the mathematical model.

5.3.2 Numerical experiments for the Richards' assumption: multilayer case

In this section we are going to carry out numerical experiments for the multilayer test cases using the input data from Section 4.3.2. The data presented in Tables 4.1, 4.3, and 5.1 is used to carry out the first numerical experiment. The velocity $\mathbf{V}_{s,in}$ is chosen to be $100\, m/min$. The boundaries of the computational domain are considered to be $\Gamma_L = \{x = -0.1\, m\}$, $\Gamma_R = \{x = 0.1\, m\}$. Results for the test case 1 are shown in Figs 5.30–5.32, where the water saturation, the water pressure, and the dry solid content of the paper layer are presented, respectively. In Figs. 5.30A and 5.31A the results obtained with the help of the two-phase flow model are shown. Figs. 5.30B and 5.31B present the results obtained with the help of the Richards' model. The dry solid content of the paper layer is shown for both flow models as well.

The numerical results for test case 1 show the similar behavior earlier discussed for the single-layer test cases. With the new mathematical model, the distribution of the water saturation changes

significantly (see Fig. 5.30). The fully saturated zone is not observed in case of the two-phase flow model while the same test case using the Richards' assumption shows the region with the single-phase water flow. As it can be seen in Fig. 5.31, the maximum pressure value rises and it is shifted to the left for the two-phase flow model in comparison with the Richards' model. Moreover, as well as for the single-layer test cases the decrease of the water pressure below the initial value is observed after the maximum pressure value. The dry solid content of the paper layer (see Fig. 5.32) has also changed. The profile for the two-phase flow model with bigger value on the right boundary of the computational domain differ from the profile for the Richards' model.

For the second test cases we use data presented in Tables 4.1, 4.4, and 5.1. The paper-felt sandwich is considered to be transported through the roll press with the velocity $|\mathbf{V}_{s,in}| = 500\, m/min$. The boundaries of the computational domain are fixed at $\Gamma_L = \{x = -0.15\ m\}$ and $\Gamma_R = \{x = 0.15\ m\}$. In the third test case we use the paper-felt sandwich with parameters presented in Tables 4.1, 4.3, 5.1, and the initial saturation defined in Table 4.5. The velocity $\mathbf{V}_{s,in}$ is chosen to be equal to $100 m/min$. The boundaries of the computational domain are set to $\Gamma_L = \{x = -0.30 m\}$, $\Gamma_R = \{x = 0.40\ m\}$. In Figs. 5.33–5.35 and Figs. 5.36–5.38 the results for the test case 2 and 3 are shown, respectively. In Figs. 5.33 and 5.36 the water saturation is shown. The water pressure and the dry solid content of the paper layer are presented in Figs. 5.34, 5.37 and Figs. 5.35, 5.38, respectively. In Figs. 5.33A, 5.34A, 5.36A, and 5.37A results obtained with the help of the two-phase flow model are shown, while Figs. 5.33B, 5.34B, 5.36B, and 5.37B present the results obtained by the Richards' model. The distribution of water significantly differs for the two-phase flow model from the model with the Richards' assumption. The water saturation and the water pressure show the behavior discussed in the first test case. The dry solid content profiles have completely different shapes for these two mathematical models in the test case 2 (see Fig. 5.35). The value on the right boundary for the two-phase flow model is significantly lower than the value obtained under the Richards' assumption. In the test case 3 (see Fig. 5.38) the dry solid content profiles have similar shape but the values for the two-phase flow model are greater in the whole computational domain.

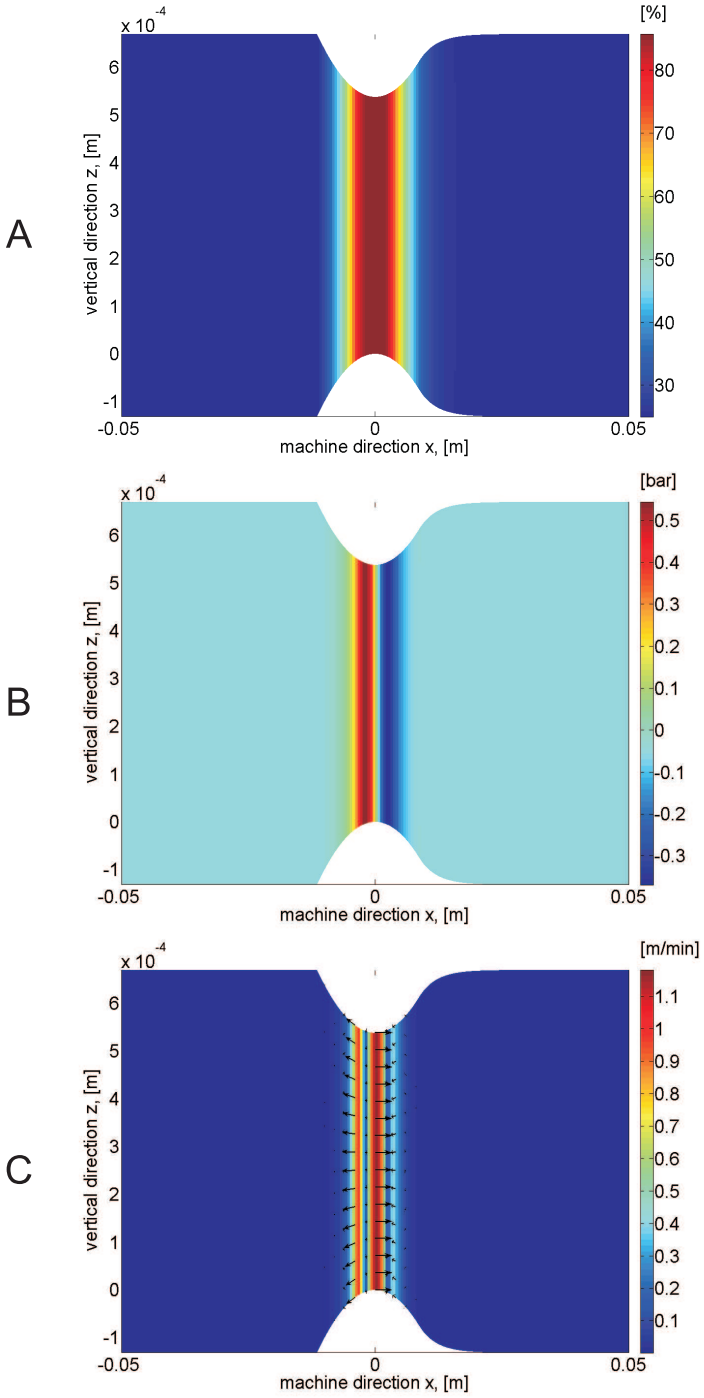

Fig. 5.2: Saturation S (A), pressure p_w (B) and velocity $\mathbf{V}_w$ (C) for "Felt 1" with $|\mathbf{V}_{s,in}| = 100\, m/min$ and $C_0 = 25\%$

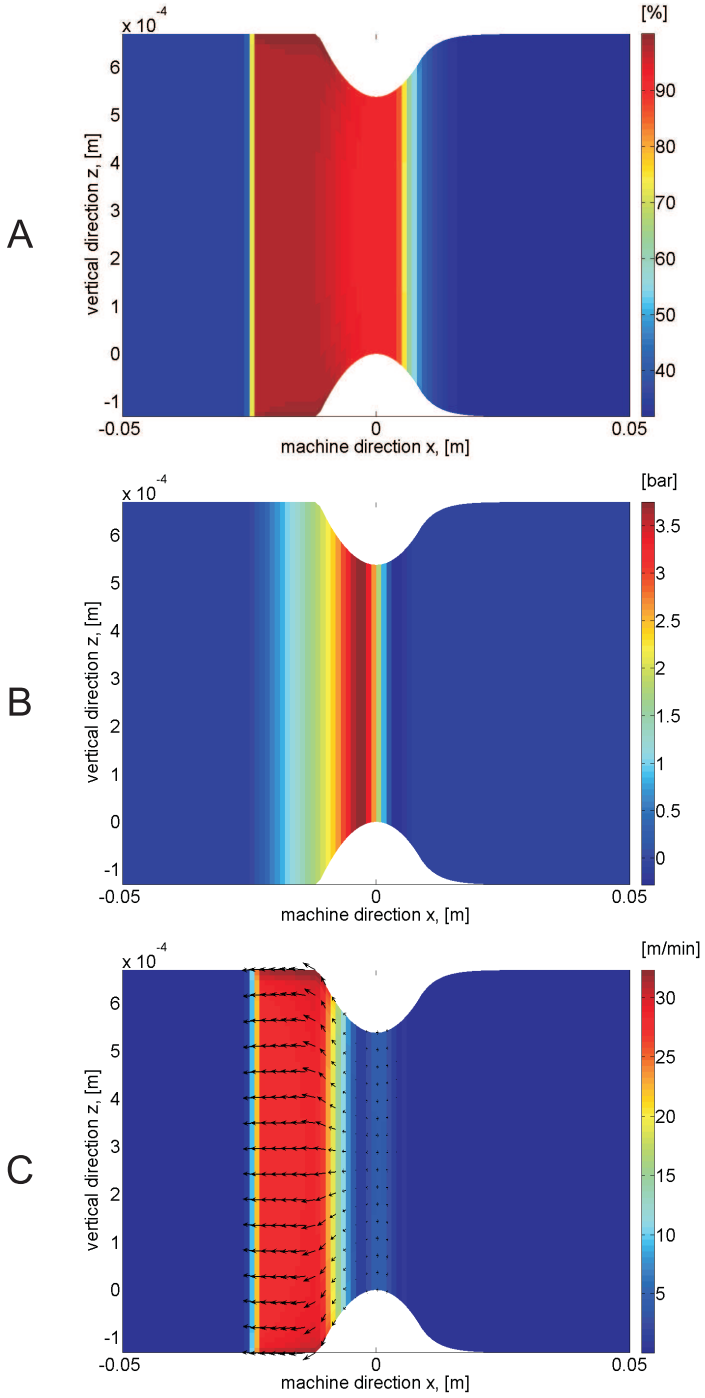

Fig. 5.3: Saturation S (A), pressure p_w (B) and velocity $\mathbf{V}_w$ (C) for "Felt 1" with $|\mathbf{V}_{s,in}| = 100\,m/min$ and $C_0 = 35\%$

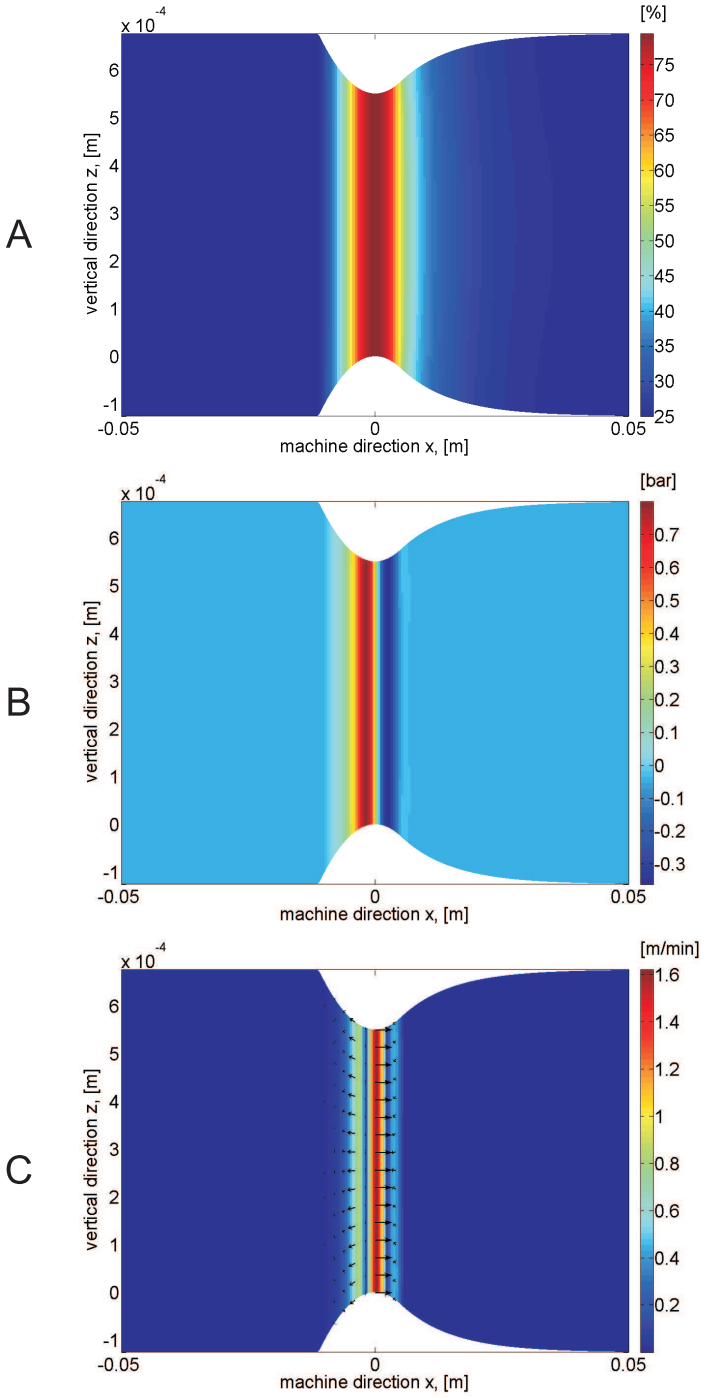

Fig. 5.4: Saturation S (A), pressure p_w (B) and velocity $\mathbf{V}_w$ (C) for "Felt 1" with $|\mathbf{V}_{s,in}| = 300\, m/min$ and $C_0 = 25\%$

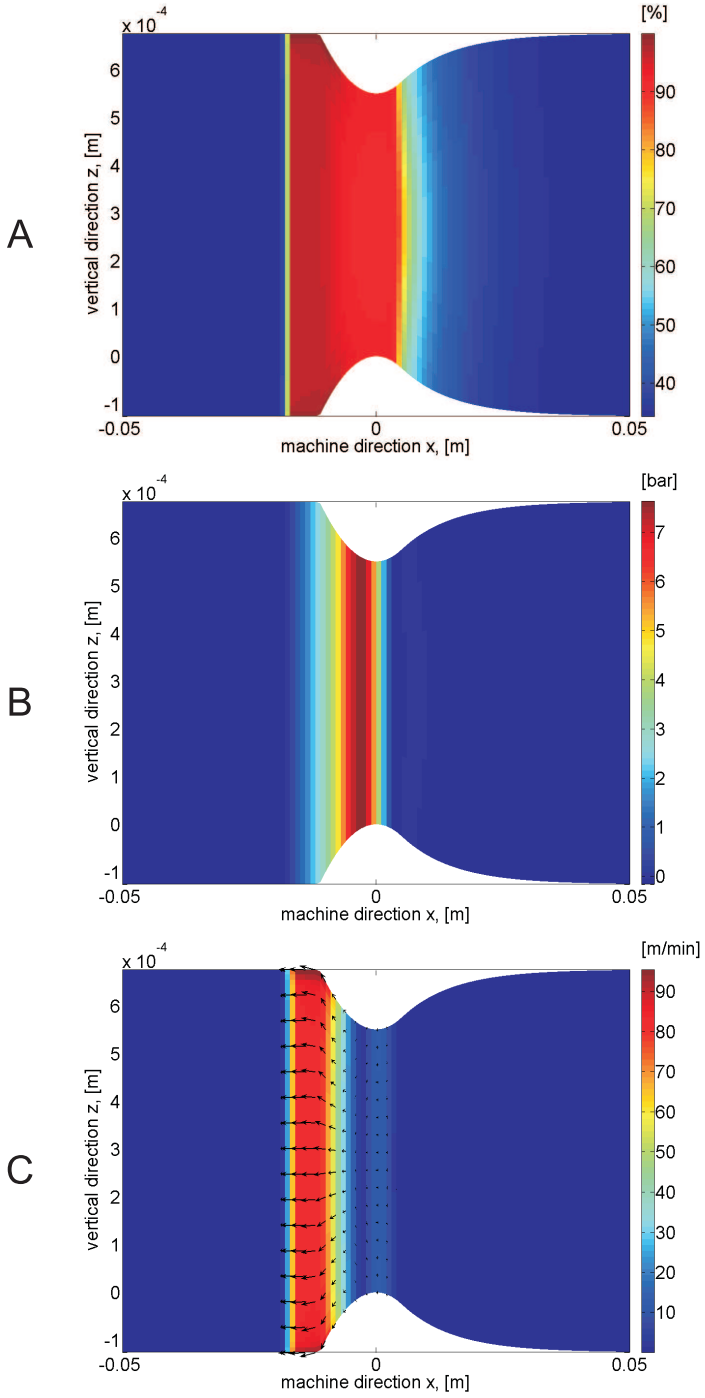

Fig. 5.5: Saturation S (A), pressure p_w (B) and velocity $\mathbf{V}_w$ (C) for "Felt 1" with $|\mathbf{V}_{s,in}| = 300\,m/min$ and $C_0 = 35\%$

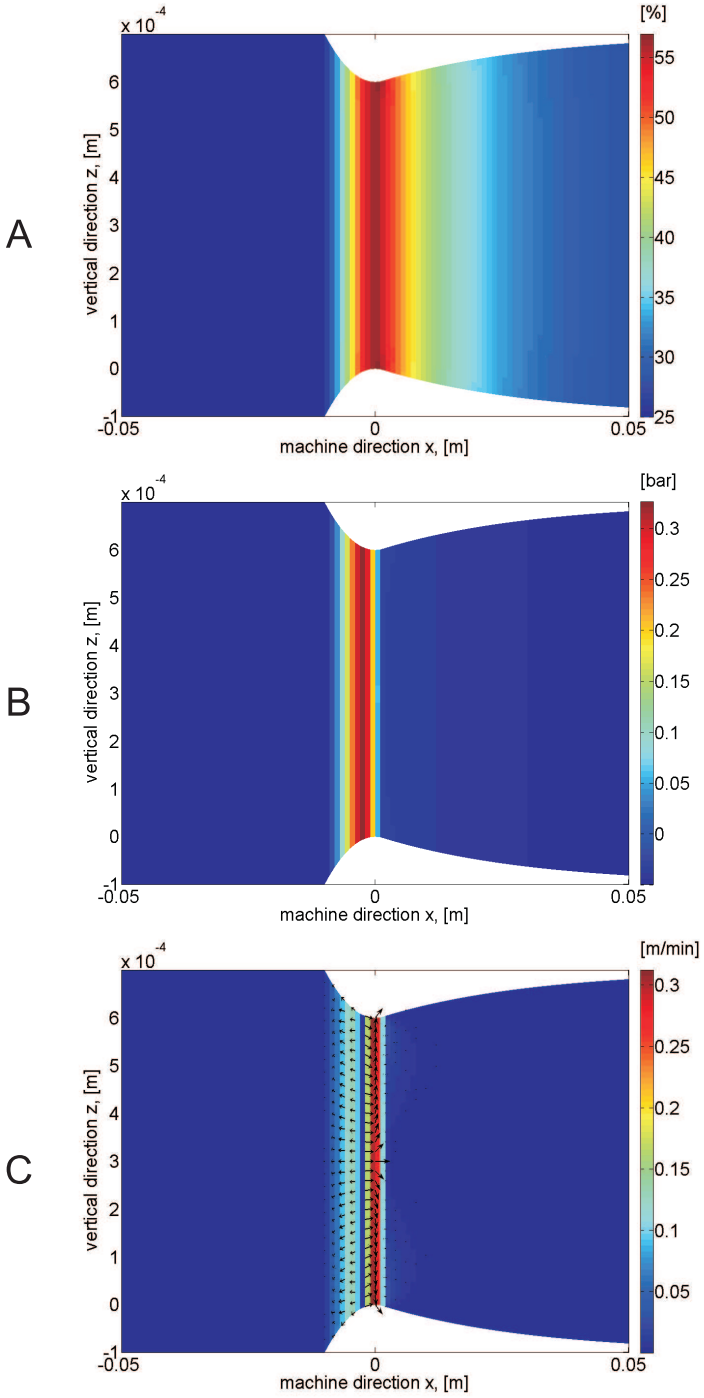

Fig. 5.6: Saturation S (A), pressure p_w (B) and velocity $\mathbf{V}_w$ (C) for "Felt 1" with $|\mathbf{V}_{s,in}| = 900\, m/min$ and $C_0 = 25\%$

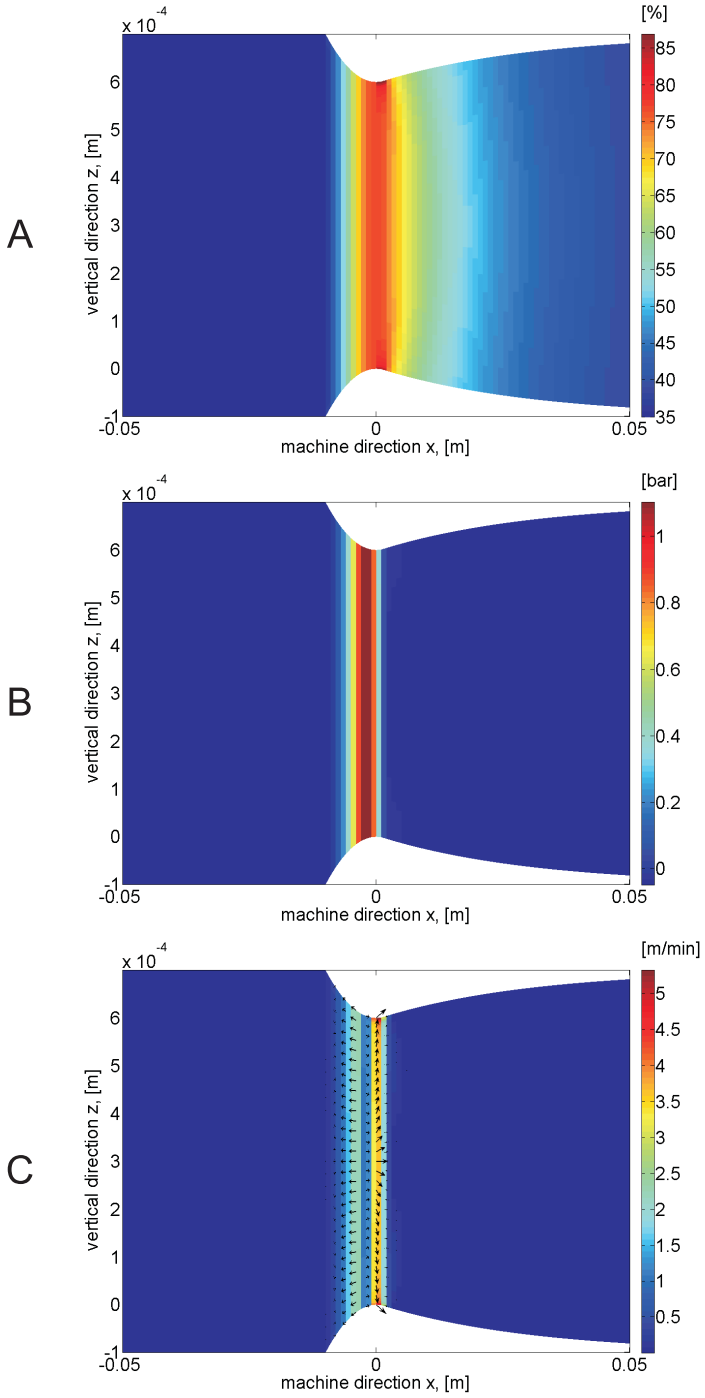

Fig. 5.7: Saturation S (A), pressure p_w (B) and velocity $\mathbf{V}_w$ (C) for "Felt 1" with $|\mathbf{V}_{s,in}| = 900\,m/min$ and $C_0 = 35\%$

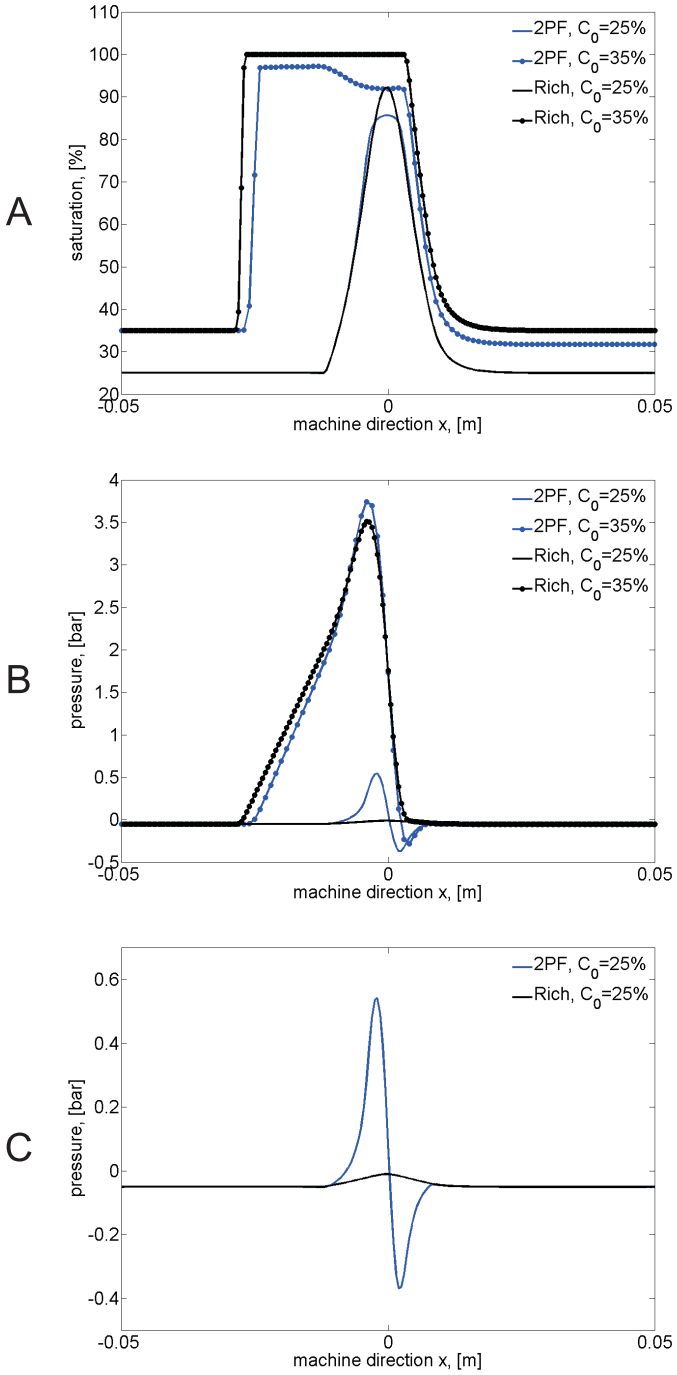

Fig. 5.8: Saturation S (A), pressure p_w (B,C) for "Felt 1" with $|\mathbf{V}_{s,in}| = 100\ m/min$ for the two-phase flow model and for the Richards' model

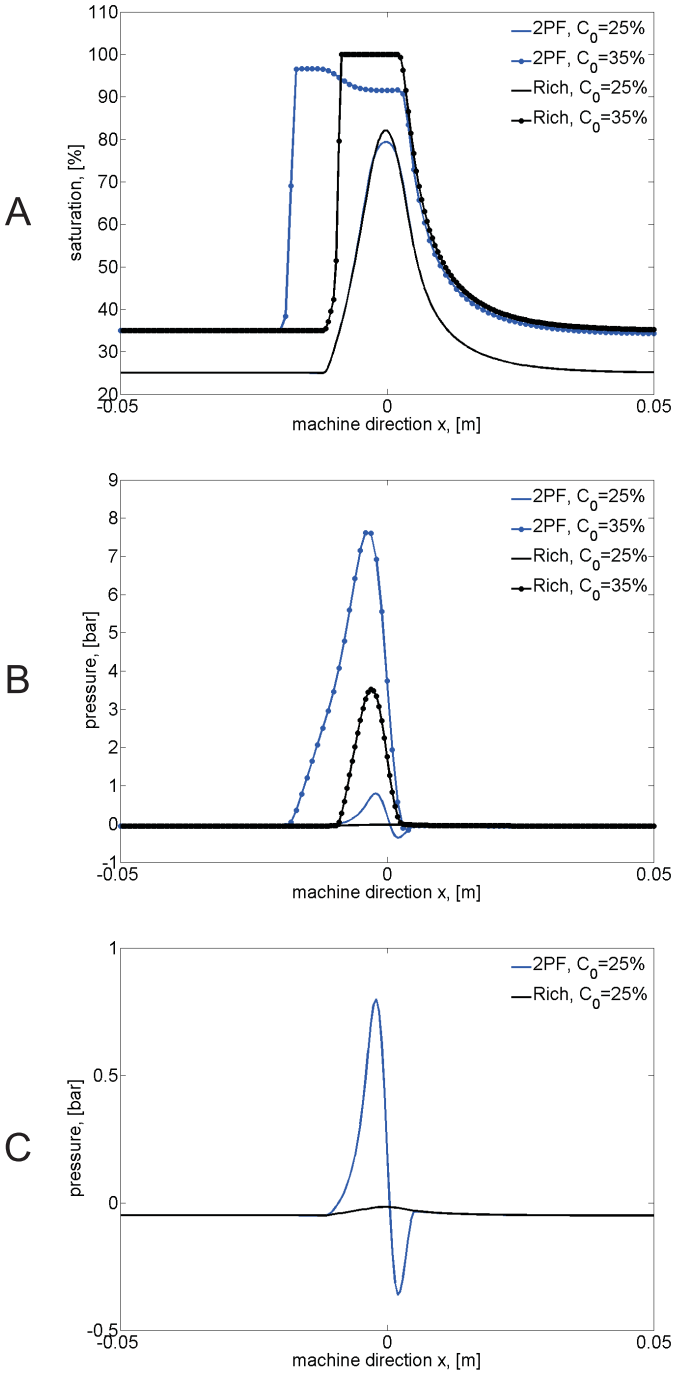

Fig. 5.9: Saturation S (A), pressure p_w (B,C) for "Felt 1" with $|\mathbf{V}_{s,in}| = 300\ m/min$ for the two-phase flow model and the Richards' model

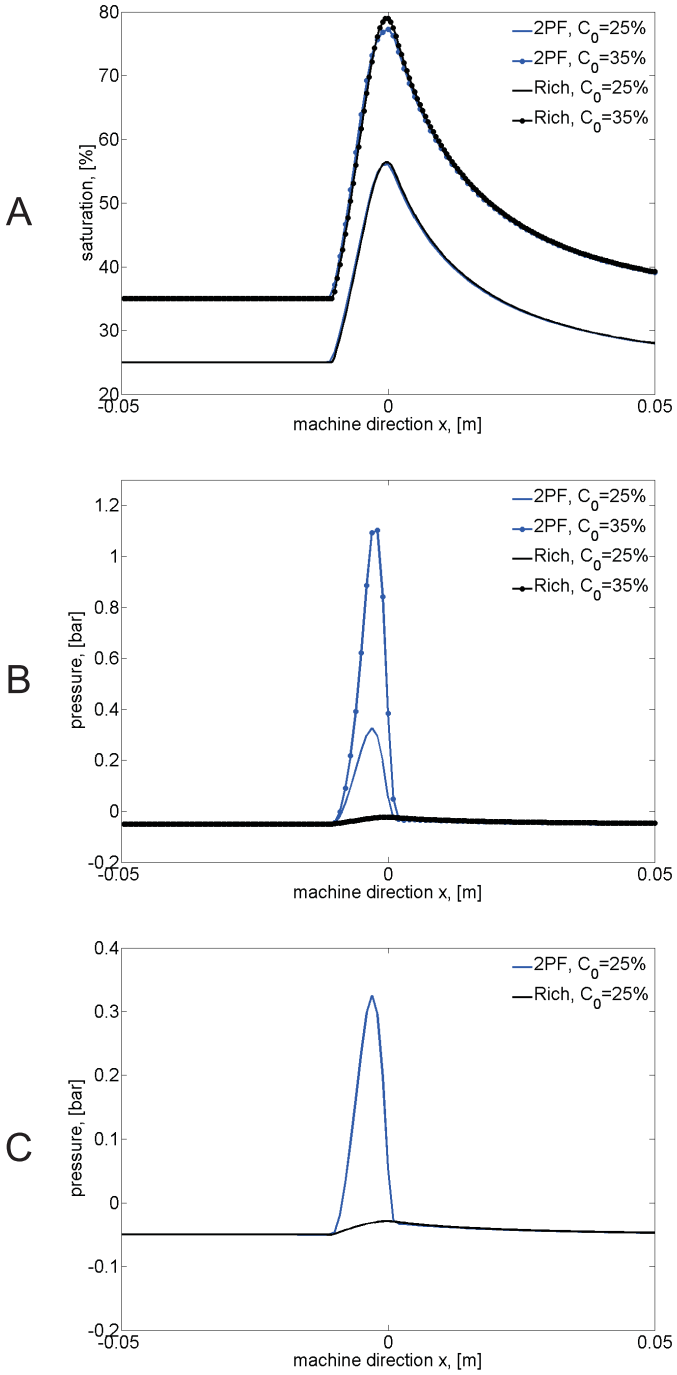

Fig. 5.10: Saturation S (A), pressure p_w (B,C) for "Felt 1" with $|\mathbf{V}_{s,in}| = 900\ m/min$ for the two-phase flow model and for the Richards' model

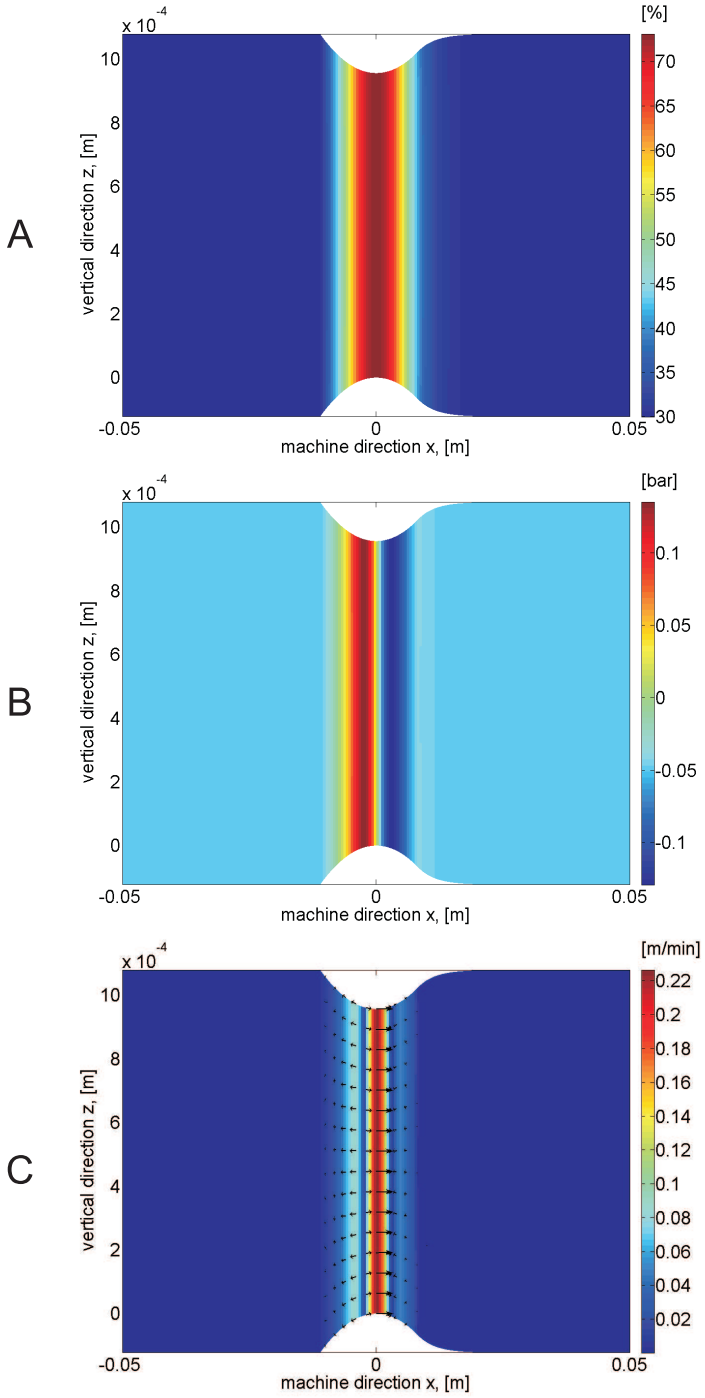

Fig. 5.11: Saturation S (A), pressure p_w (B) and velocity $\mathbf{V}_w$ (C) for "Felt 2" with $|\mathbf{V}_{s,in}| = 100\,m/min$ and $C_0 = 25\%$

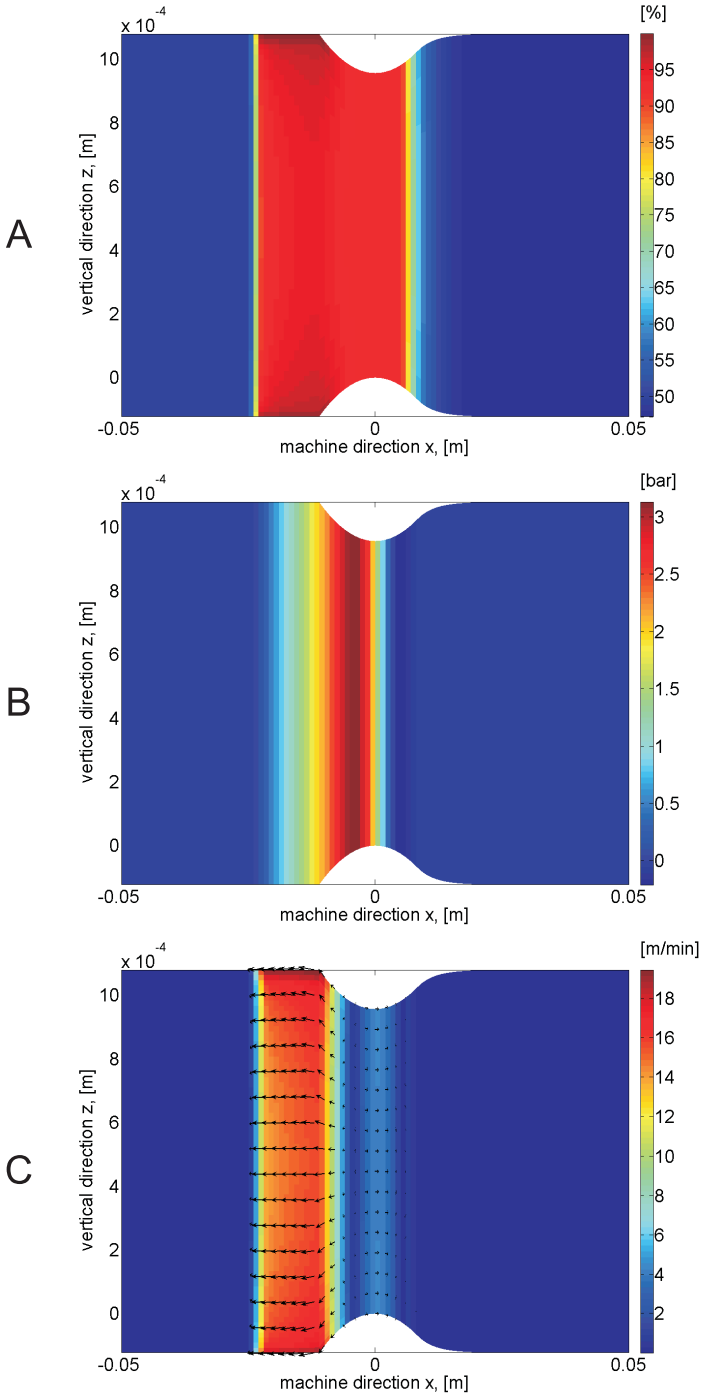

Fig. 5.12: Saturation S (A), pressure p_w (B) and velocity $\mathbf{V}_w$ (C) for "Felt 2" with $|\mathbf{V}_{s,in}| = 100\, m/min$ and $C_0 = 35\%$

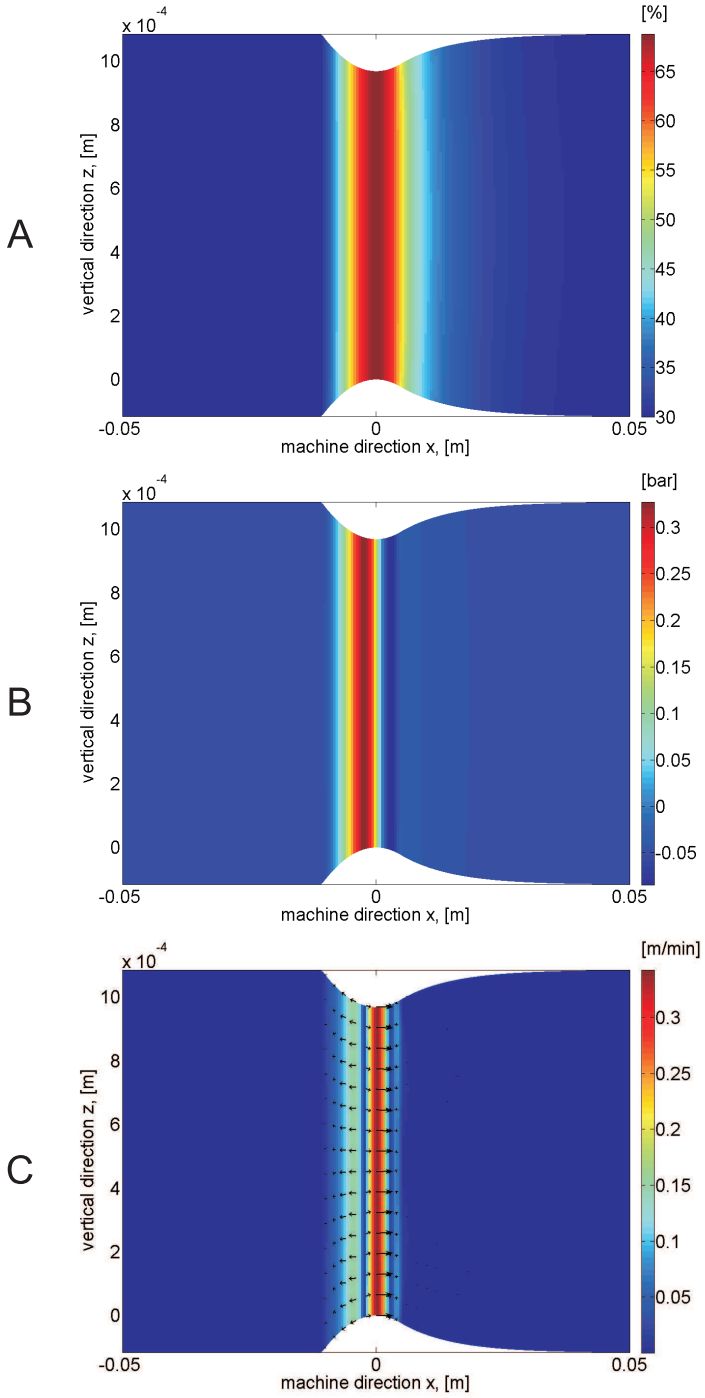

Fig. 5.13: Saturation S (A), pressure p_w (B) and velocity $\mathbf{V}_w$ (C) for "Felt 2" with $|\mathbf{V}_{s,in}| = 300\,m/min$ and $C_0 = 25\%$

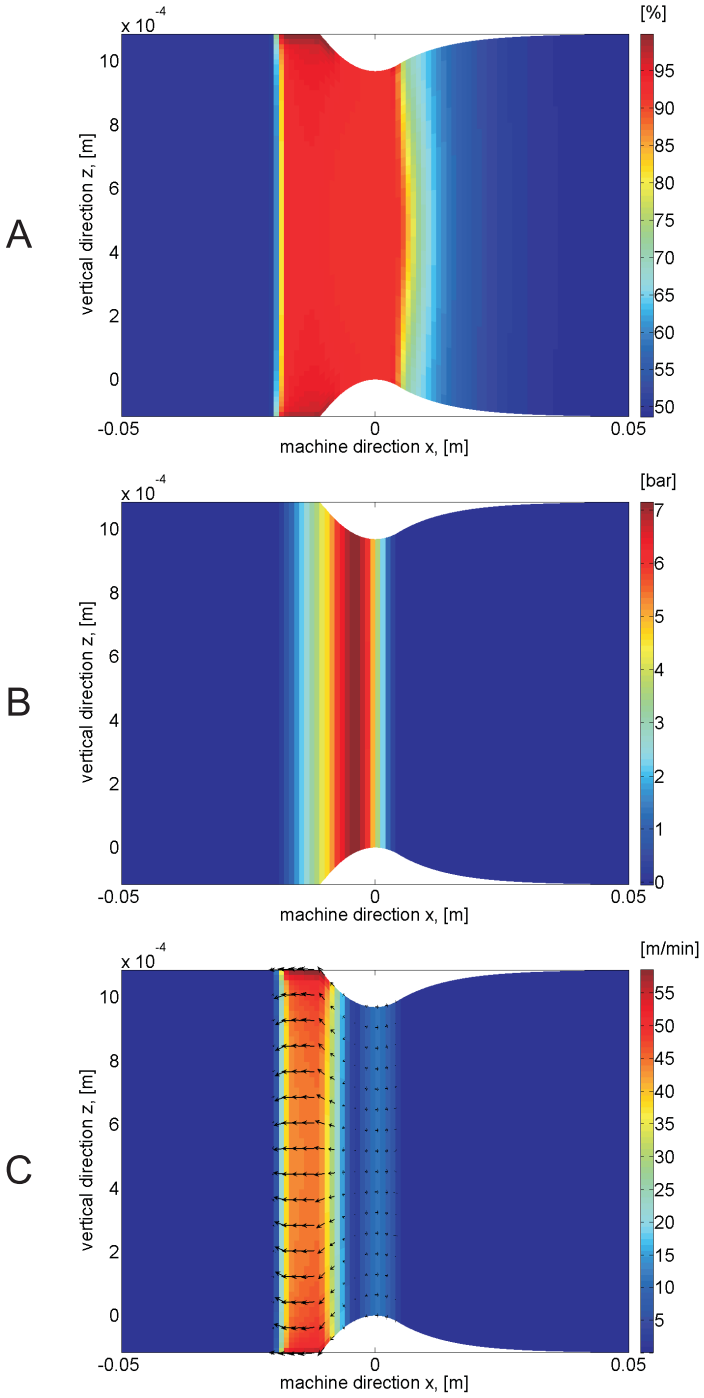

Fig. 5.14: Saturation S (A), pressure p_w (B) and velocity $\mathbf{V}_w$ (C) for "Felt 2" with $|\mathbf{V}_{s,in}| = 300\, m/min$ and $C_0 = 35\%$

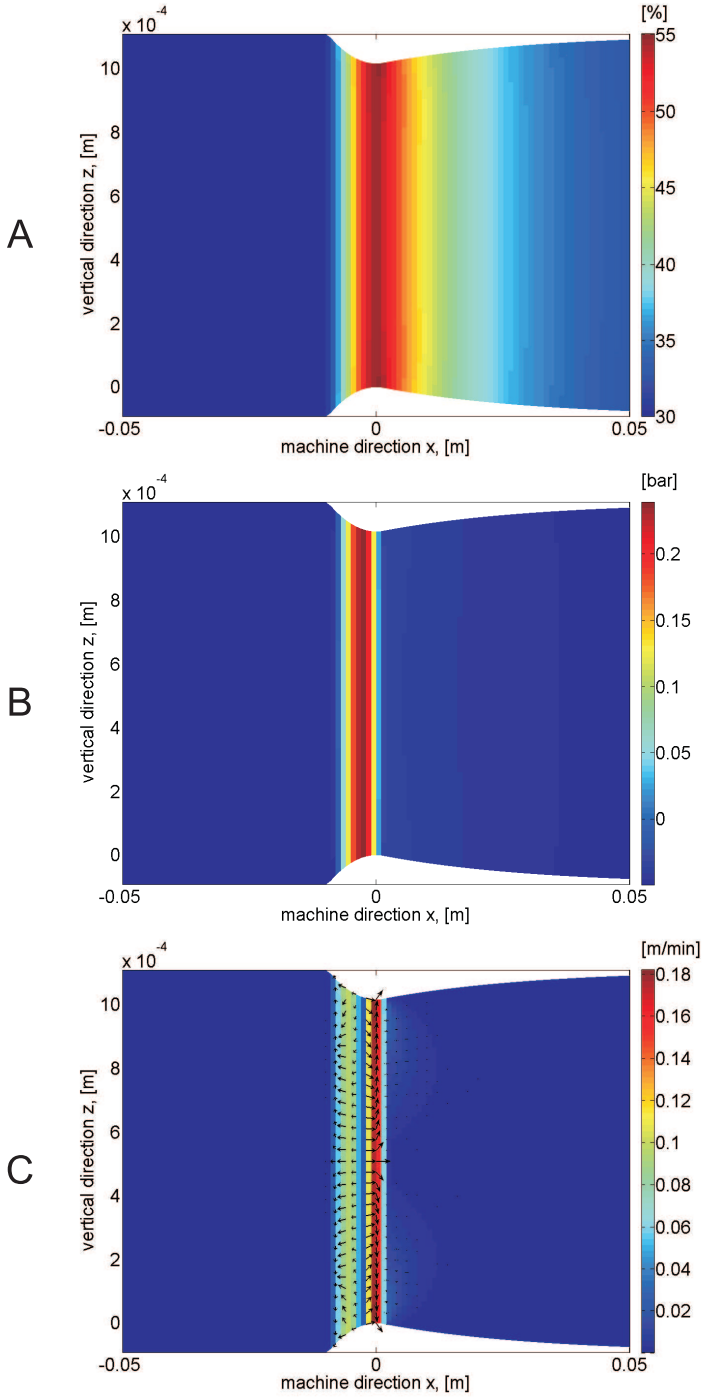

Fig. 5.15: Saturation S (A), pressure p_w (B) and velocity $\mathbf{V}_w$ (C) for "Felt 2" with $|\mathbf{V}_{s,in}| = 900\,m/min$ and $C_0 = 25\%$

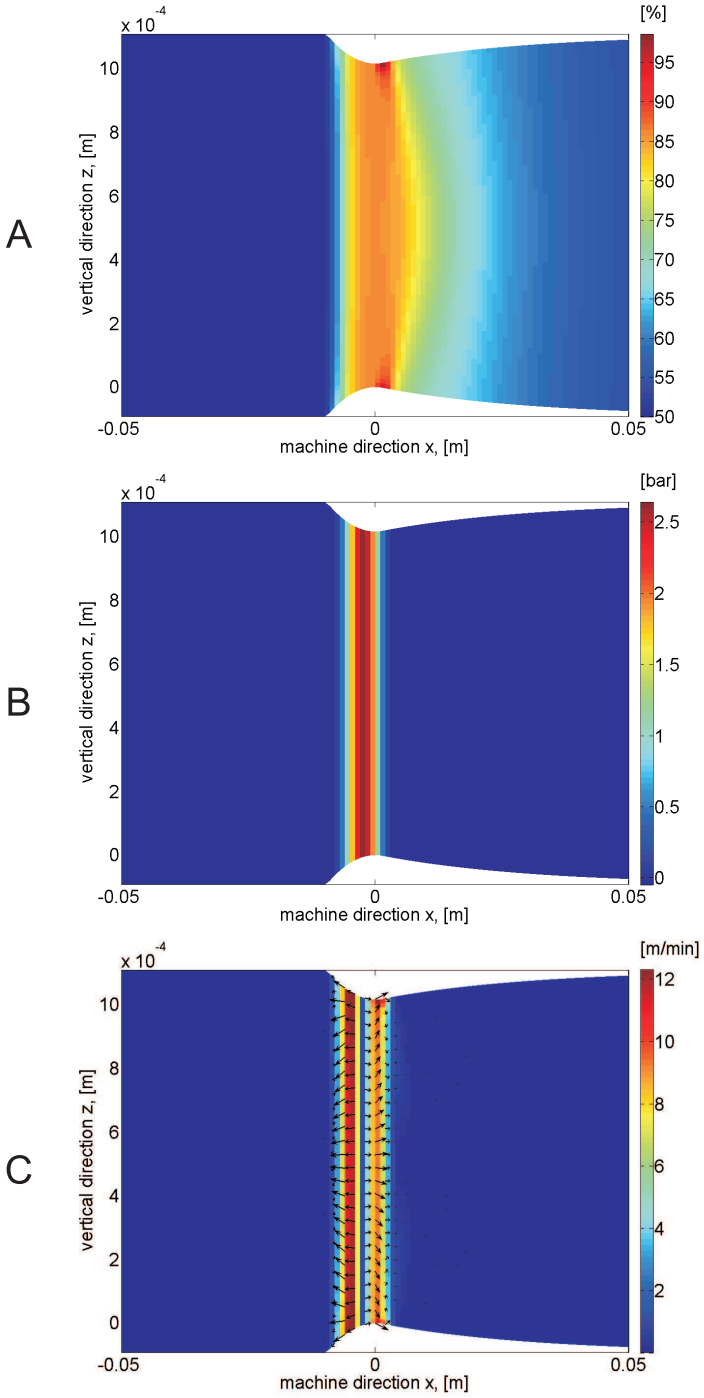

Fig. 5.16: Saturation S (A), pressure p_w (B) and velocity $\mathbf{V}_w$ (C) for "Felt 2" with $|\mathbf{V}_{s,in}| = 900\, m/min$ and $C_0 = 35\%$

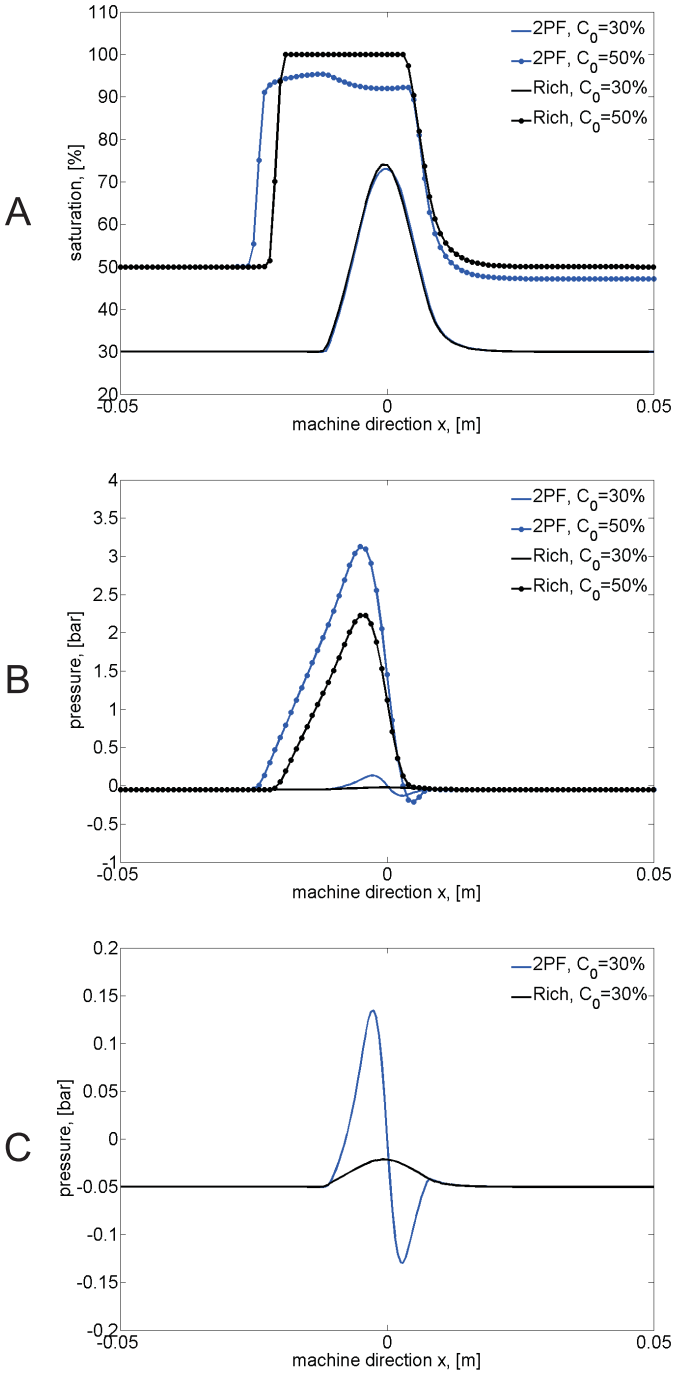

Fig. 5.17: Saturation S (A), pressure p_w (B,C) for "Felt 2" with $|\mathbf{V}_{s,in}| = 100\ m/min$ for the two-phase flow model and for the Richards' model

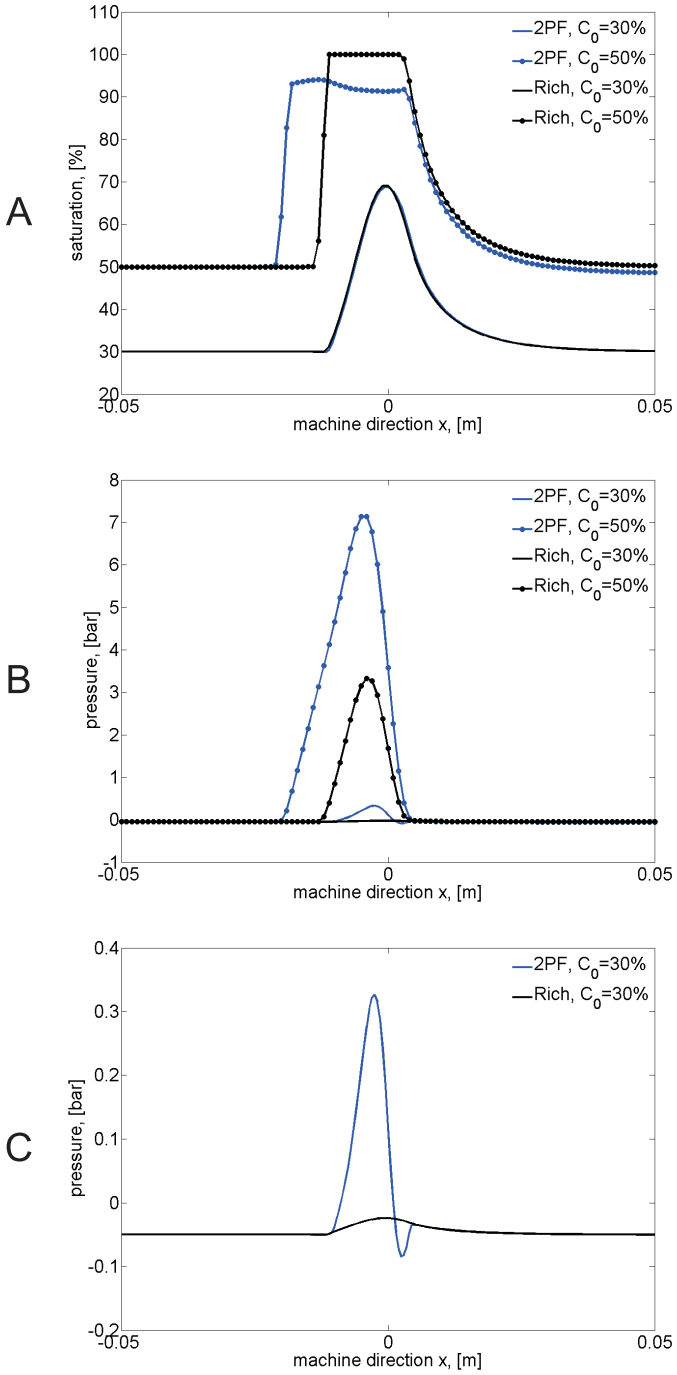

Fig. 5.18: Saturation S (A), pressure p_w (B,C) for "Felt 2" with $|\mathbf{V}_{s,in}| = 300\ m/min$ for the two-phase flow model and for the Richards' model

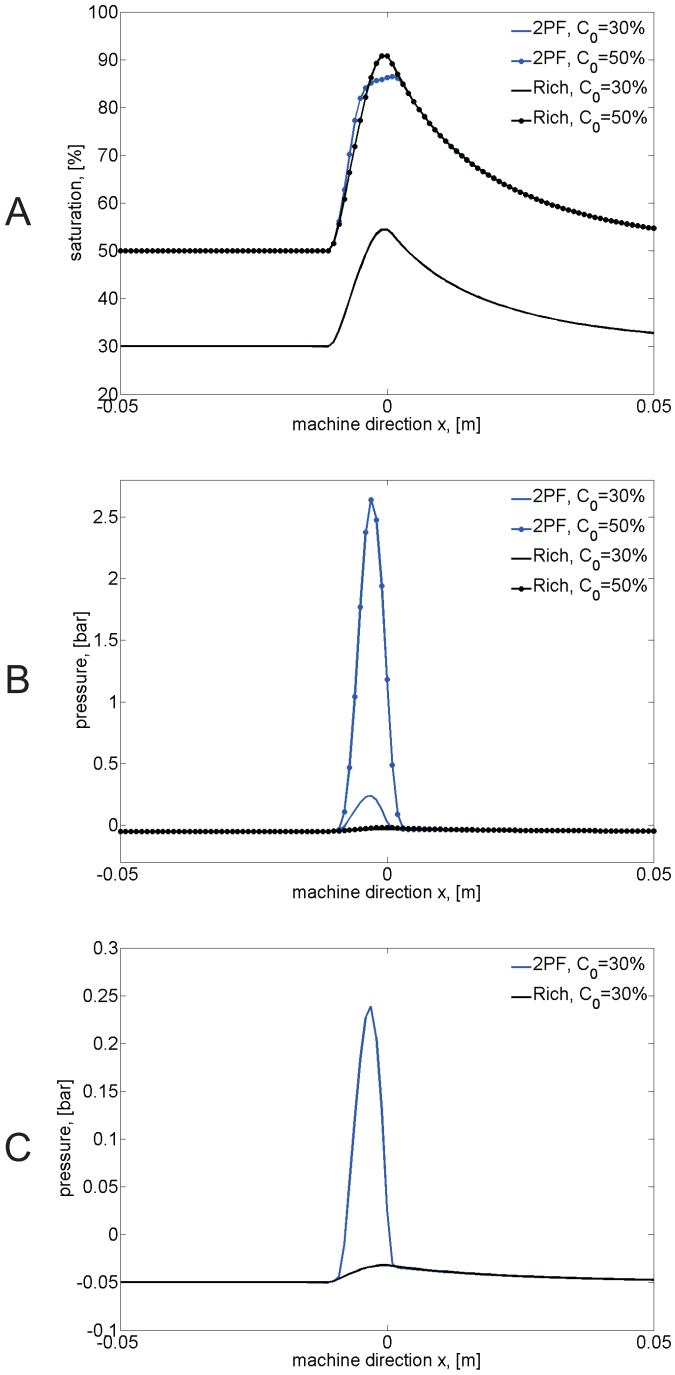

Fig. 5.19: Saturation S (A), pressure p_w (B,C) for "Felt 2" with $|\mathbf{V}_{s,in}| = 900\ m/min$ for the two-phase flow model and for the Richards' model

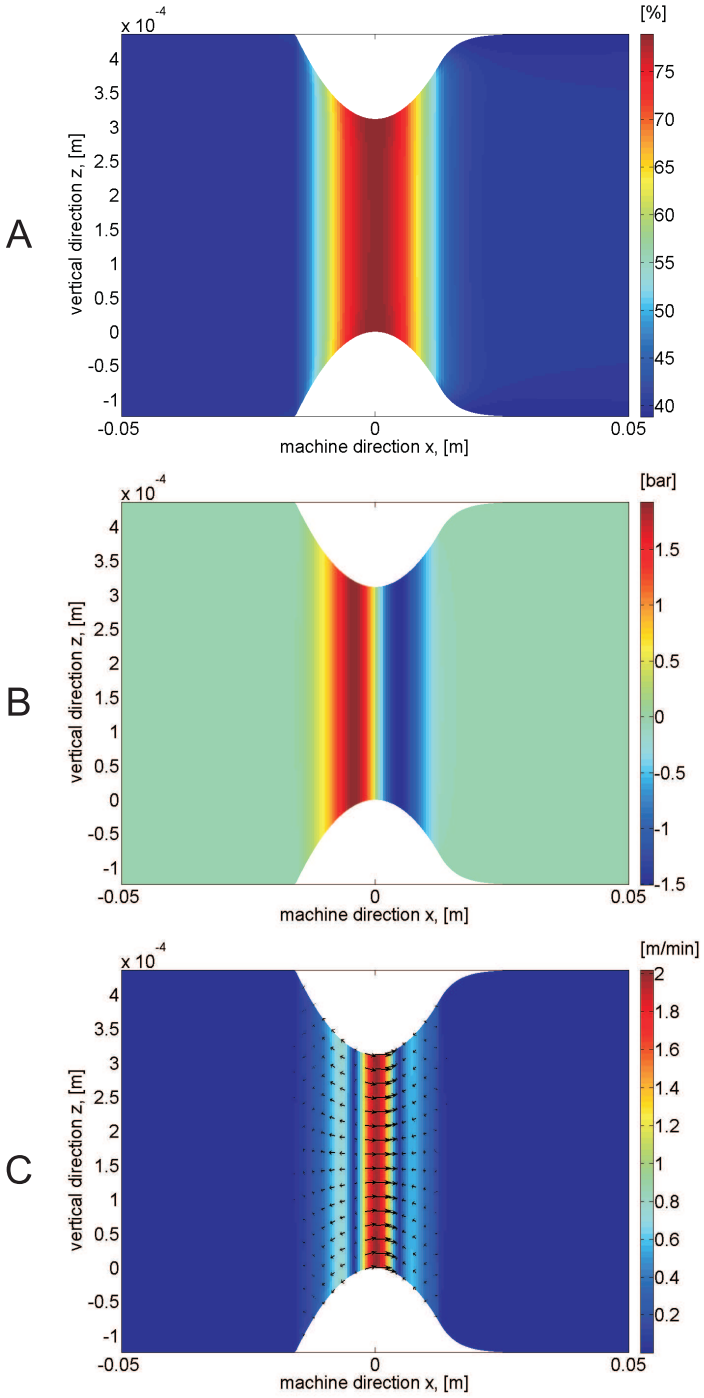

Fig. 5.20: Saturation S (A), pressure p_w (B) and velocity $\mathbf{V}_w$ (C) for "Paper" with $|\mathbf{V}_{s,in}| = 100\, m/min$ and $C_0 = 25\%$

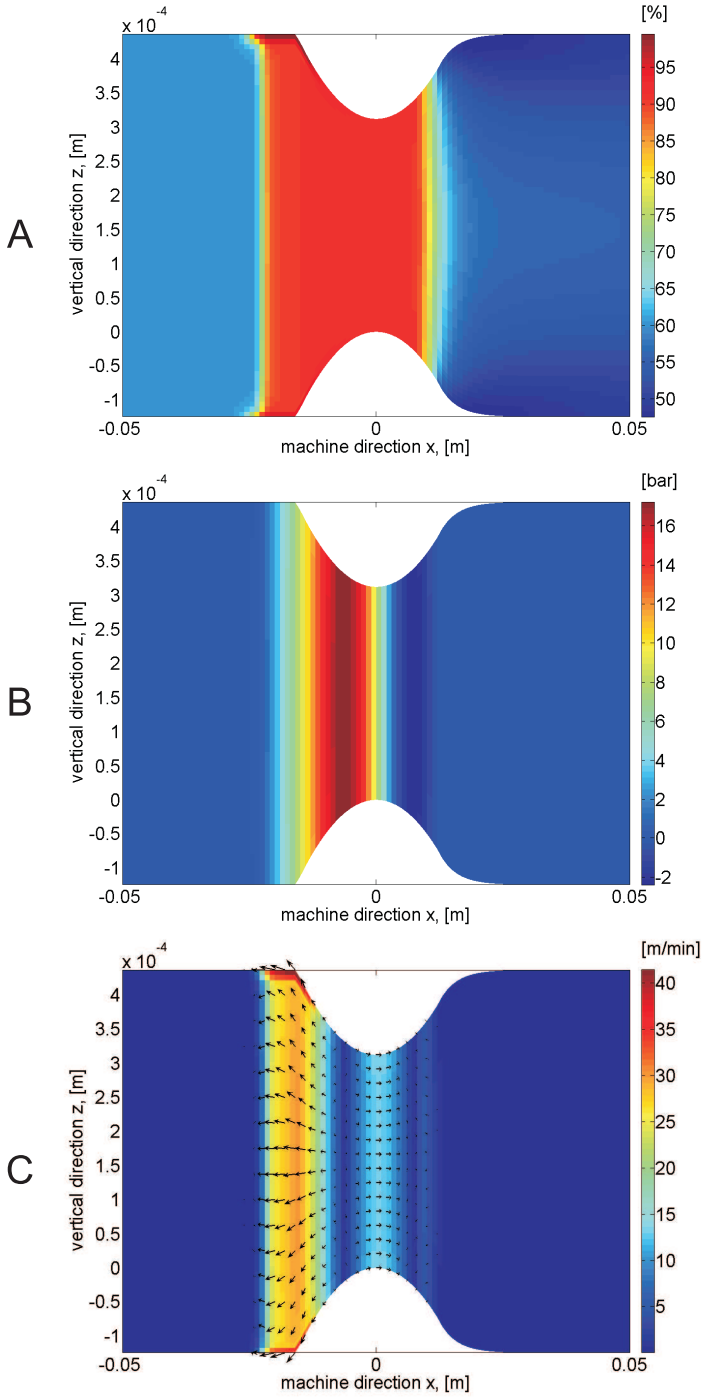

Fig. 5.21: Saturation S (A), pressure p_w (B) and velocity $\mathbf{V}_w$ (C) for "Paper" with $|\mathbf{V}_{s,in}| = 100\,m/min$ and $C_0 = 35\%$

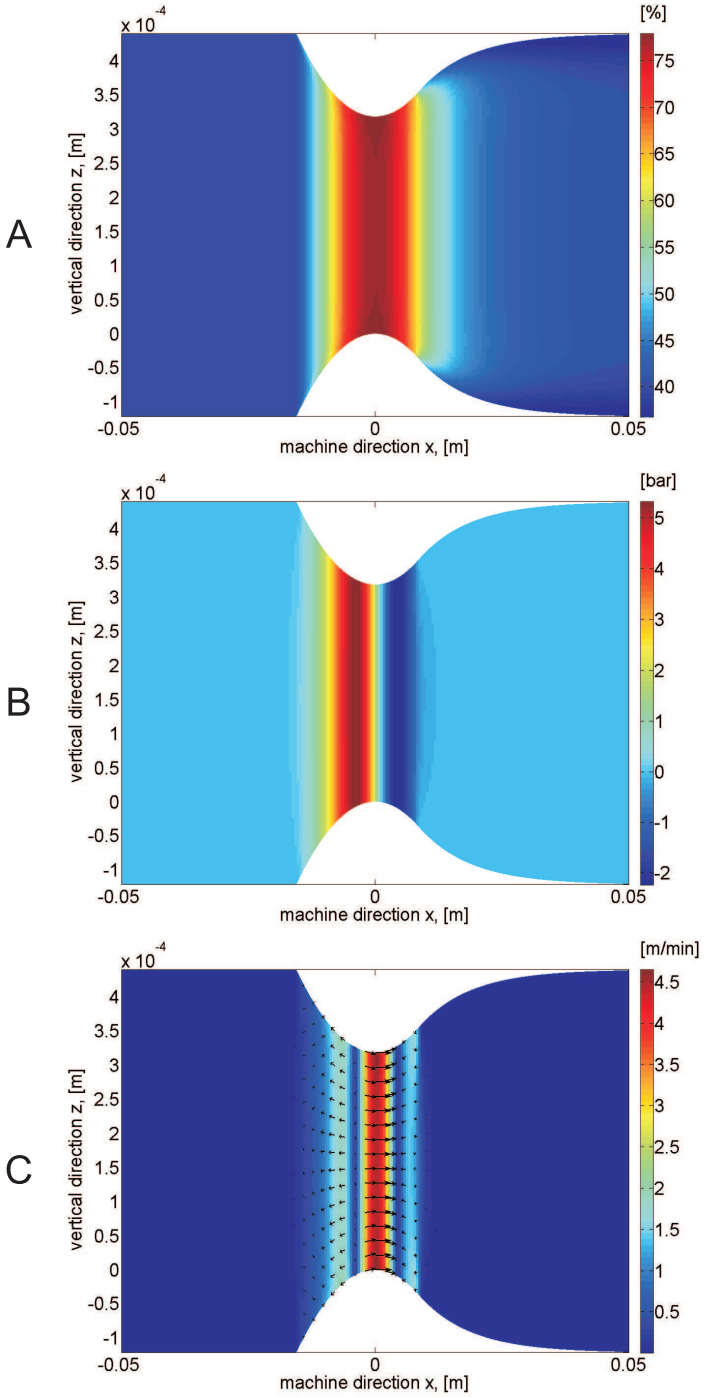

Fig. 5.22: Saturation S (A), pressure p_w (B) and velocity $\mathbf{V}_w$ (C) for "Paper" with $|\mathbf{V}_{s,in}| = 300\, m/min$ and $C_0 = 25\%$

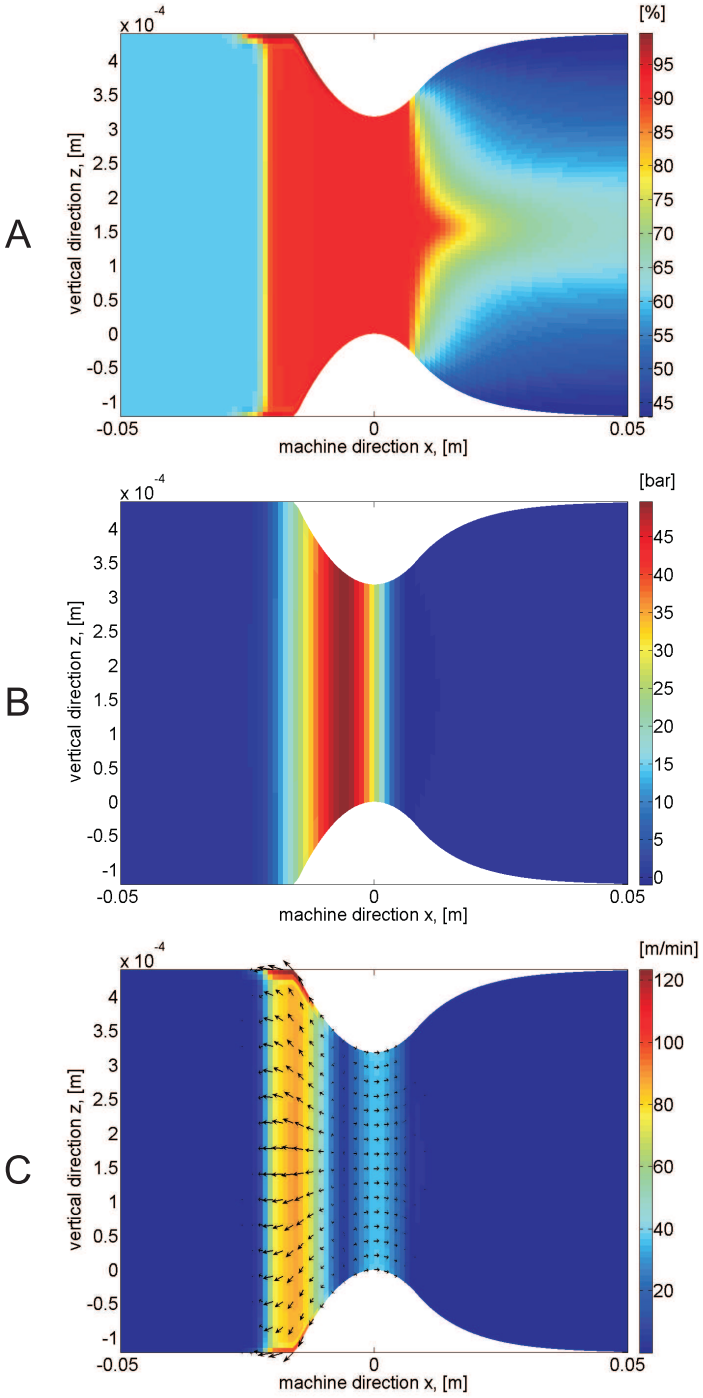

Fig. 5.23: Saturation S (A), pressure p_w (B) and velocity $\mathbf{V}_w$ (C) for "Paper" with $|\mathbf{V}_{s,in}| = 300\,m/min$ and $C_0 = 35\%$

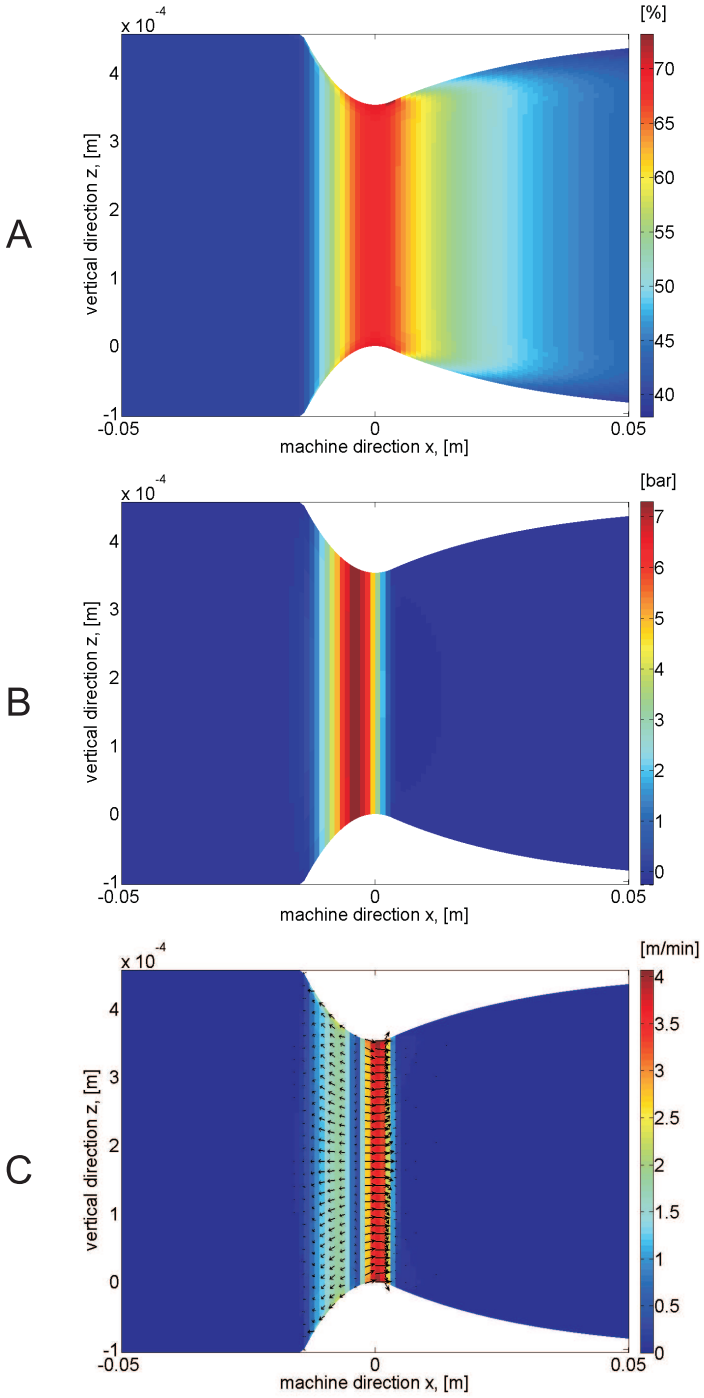

Fig. 5.24: Saturation S (A), pressure p_w (B) and velocity $\mathbf{V}_w$ (C) for "Paper" with $|\mathbf{V}_{s,in}| = 900\, m/min$ and $C_0 = 25\%$

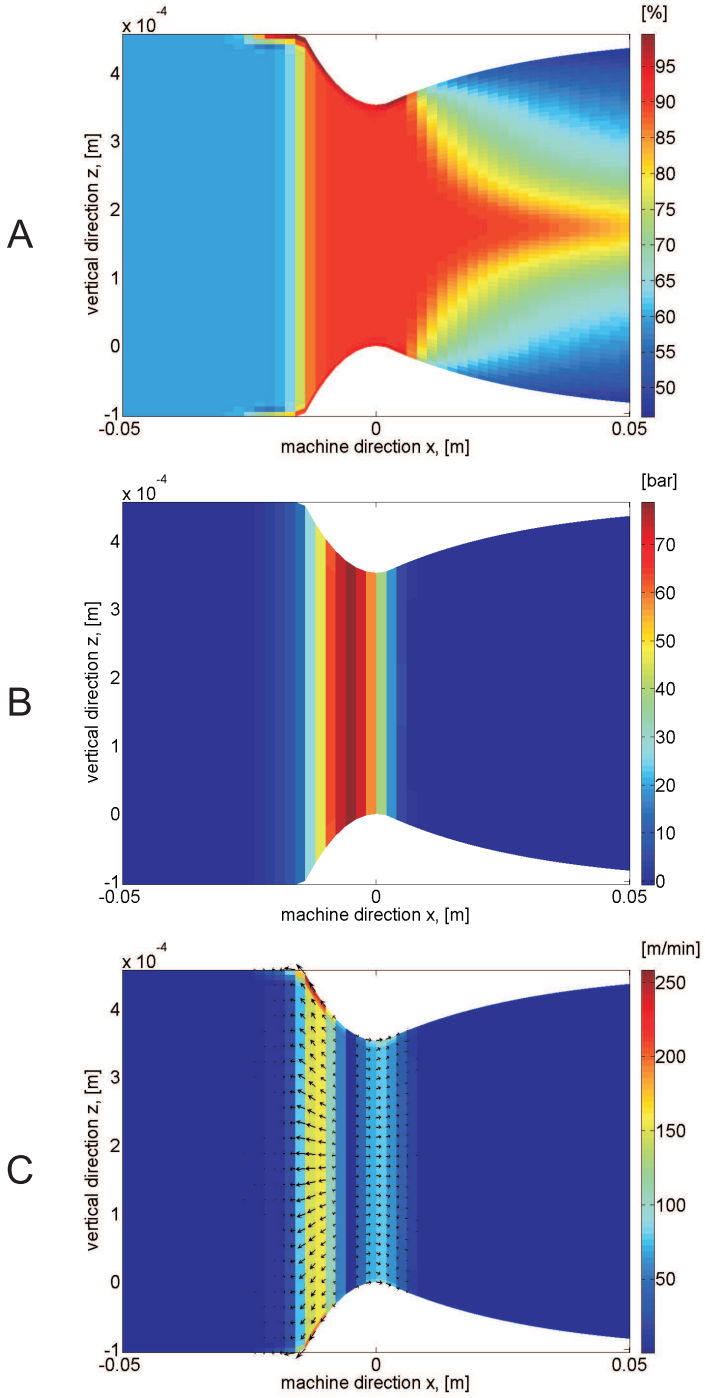

Fig. 5.25: Saturation S (A), pressure p_w (B) and velocity $\mathbf{V}_w$ (C) for "Paper" with $|\mathbf{V}_{s,in}| = 900\, m/min$ and $C_0 = 35\%$

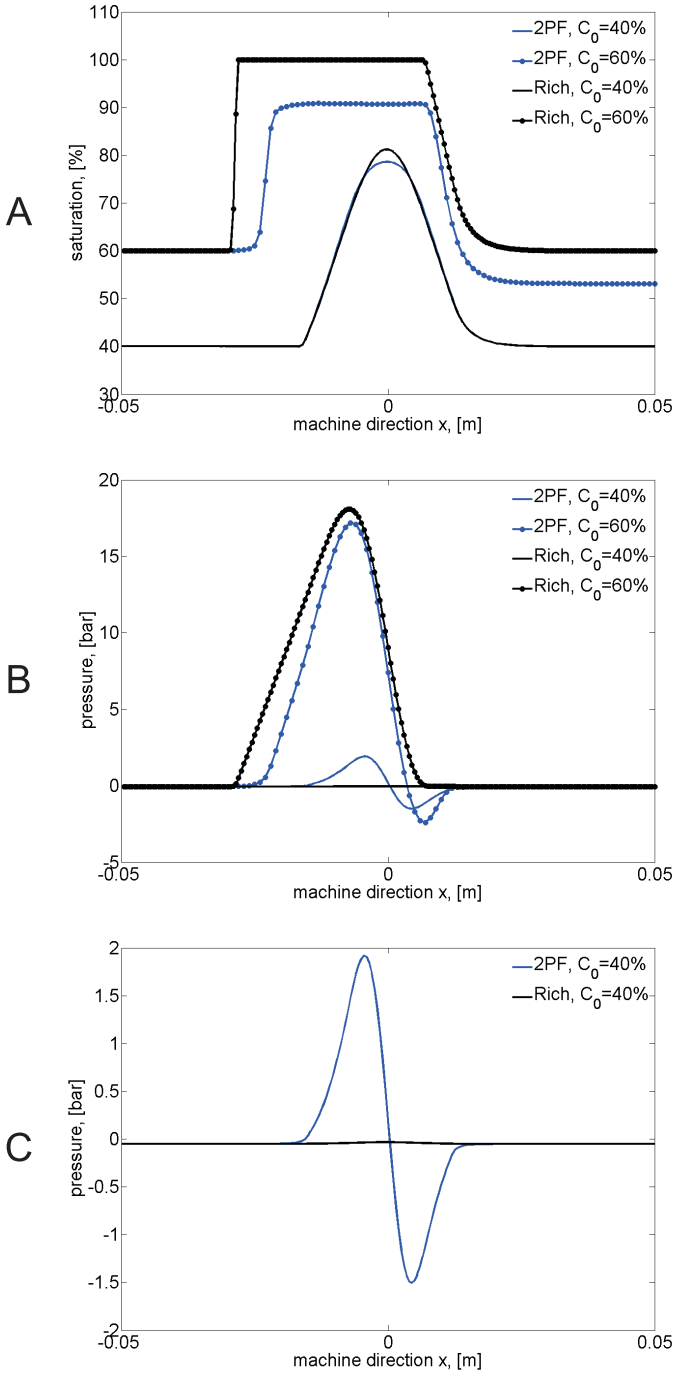

Fig. 5.26: Saturation S (A), pressure p_w (B,C) for "Paper" with $|\mathbf{V}_{s,in}| = 100\ m/min$ for the two-phase flow model and for the Richards' model

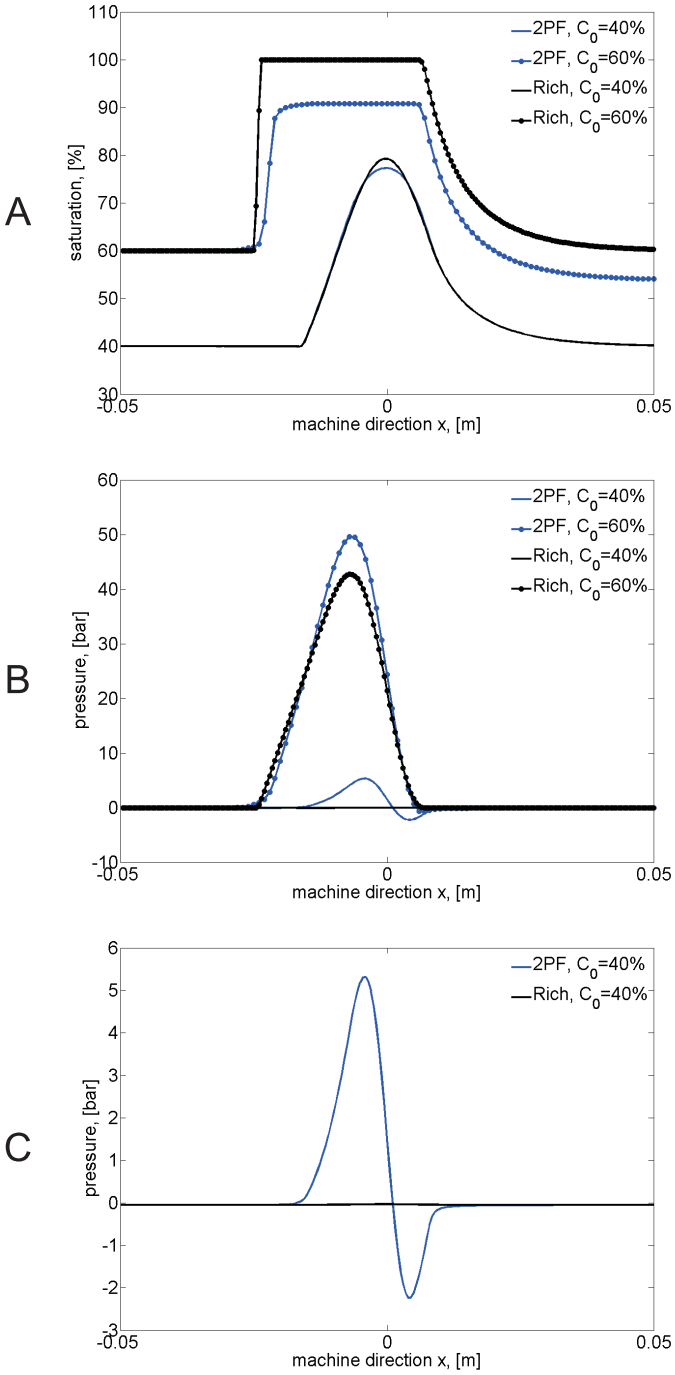

Fig. 5.27: Saturation S (A), pressure p_w (B,C) for "Paper" with $|\mathbf{V}_{s,in}| = 300\ m/min$ for the two-phase flow model and for the Richards' model

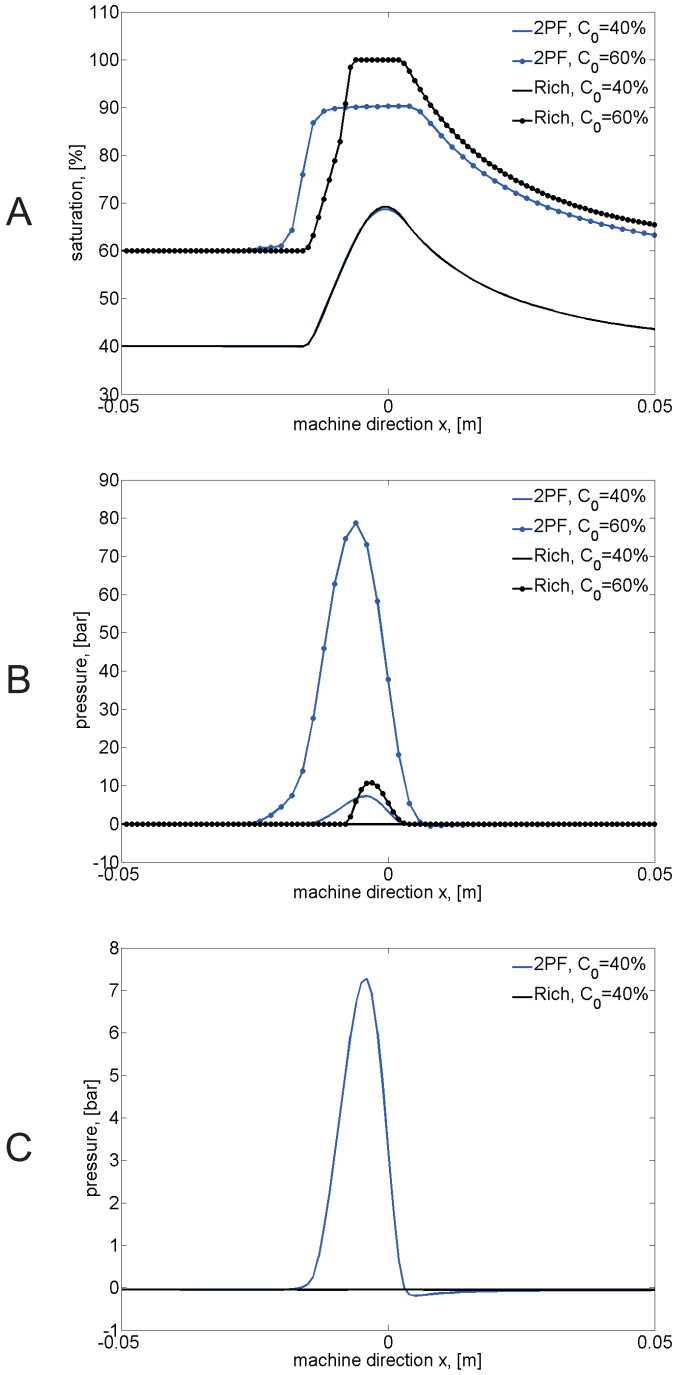

Fig. 5.28: Saturation S (A), pressure p_w (B,C) for "Paper" with $|\mathbf{V}_{s,in}| = 900\ m/min$ for the two-phase flow model and for the Richards' model

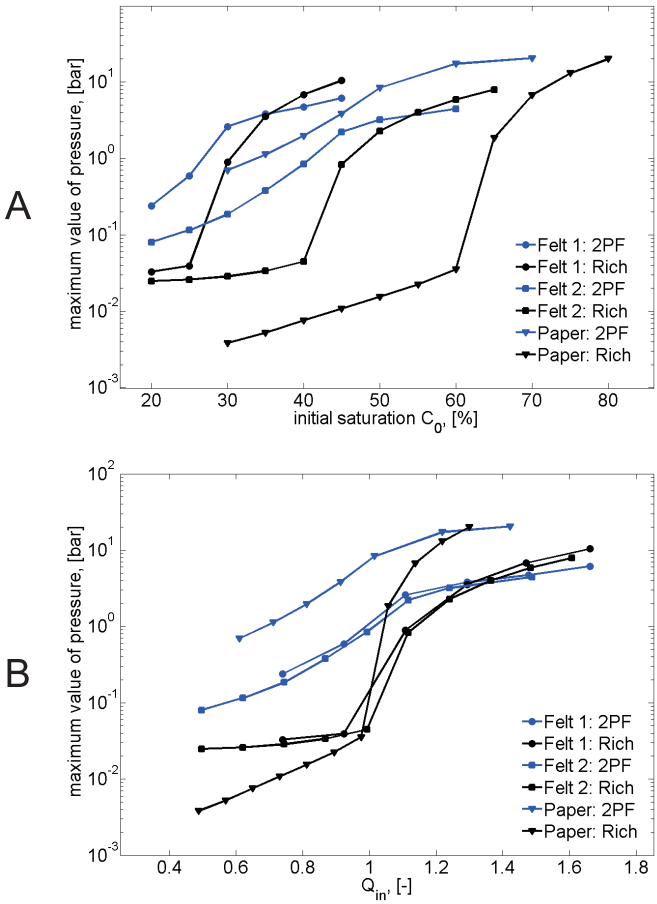

Fig. 5.29: Fluid pressure peak as a function of the initial saturation C_0 (A) and Q_{in} (B) for $|\mathbf{V}_{s,in}| = 100\ m/min$

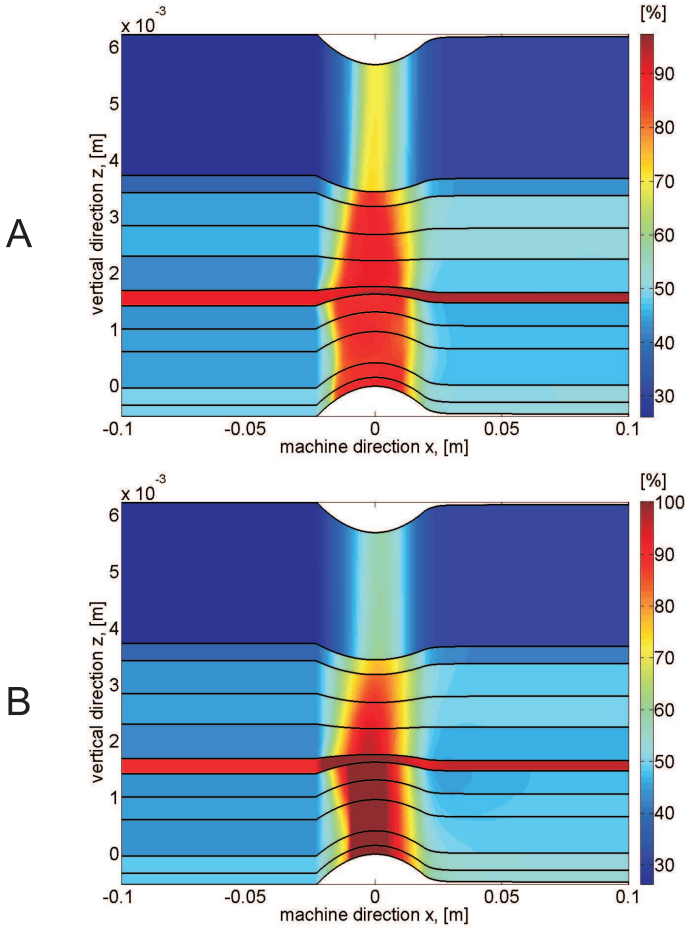

Fig. 5.30: Saturation for the test case 1 using the two-phase flow model (A) and the Richards' model (B)

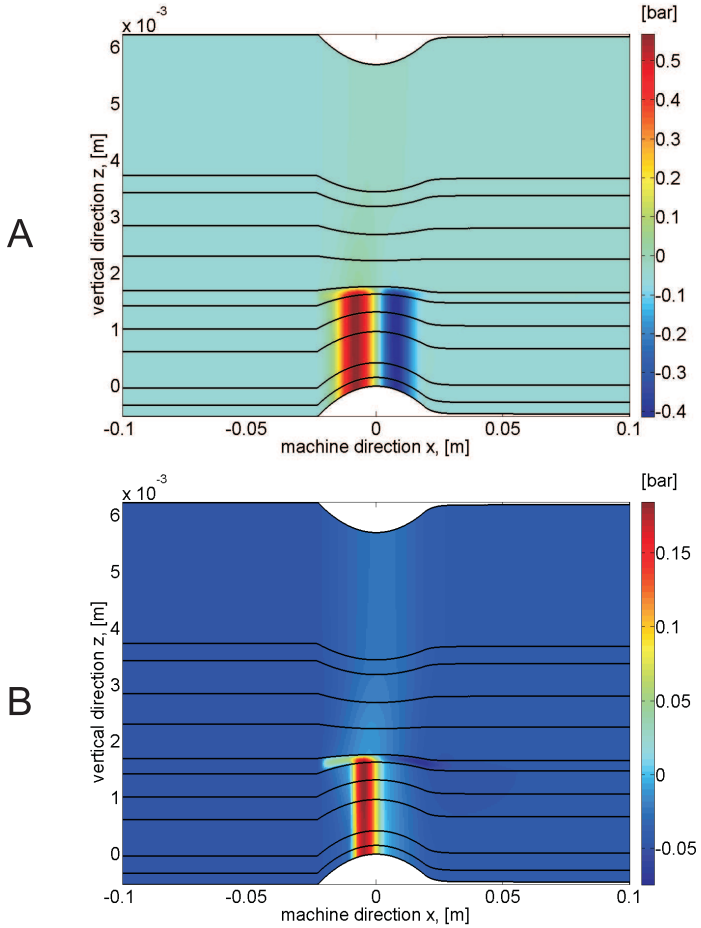

Fig. 5.31: Pressure for the test case 1 using the two-phase flow model (A) and the Richards' model (B)

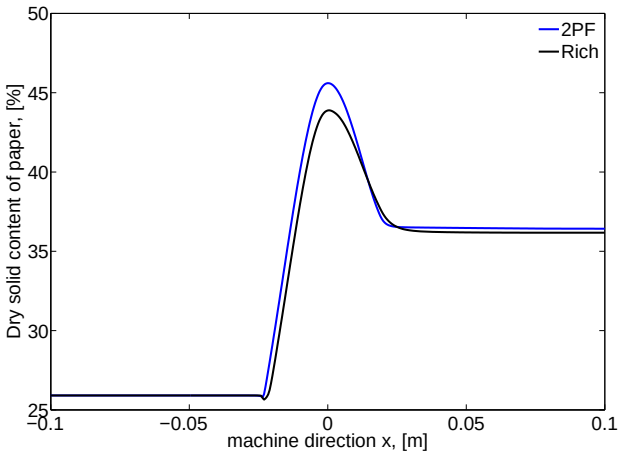

Fig. 5.32: Dry solid content of the paper for the test case 1 using the two-phase flow model and the Richards' model

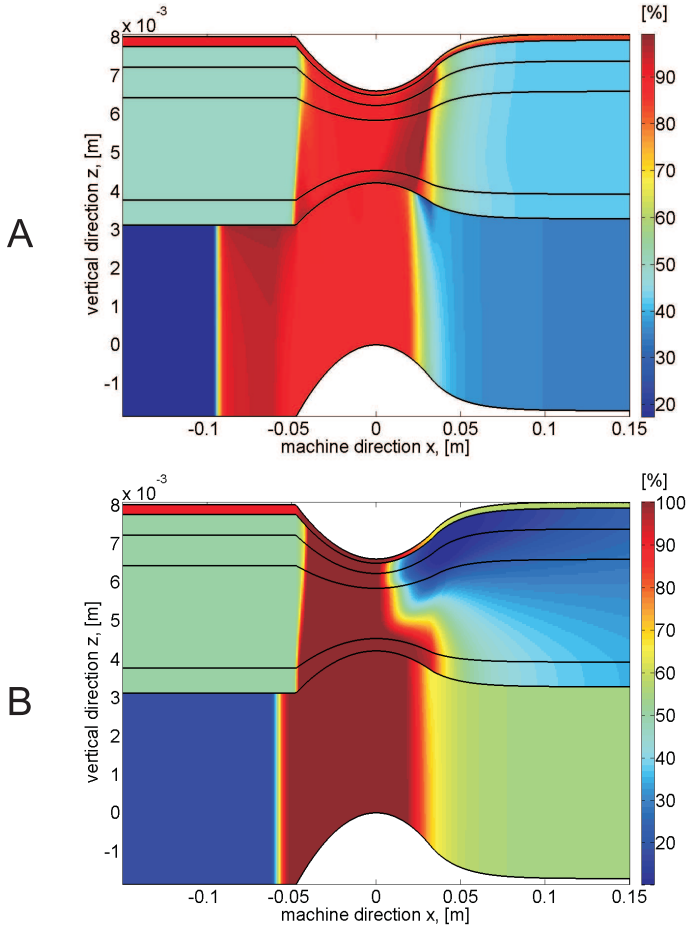

Fig. 5.33: Saturation for the test case 2 using the two-phase flow model (A) and the Richards' model (B)

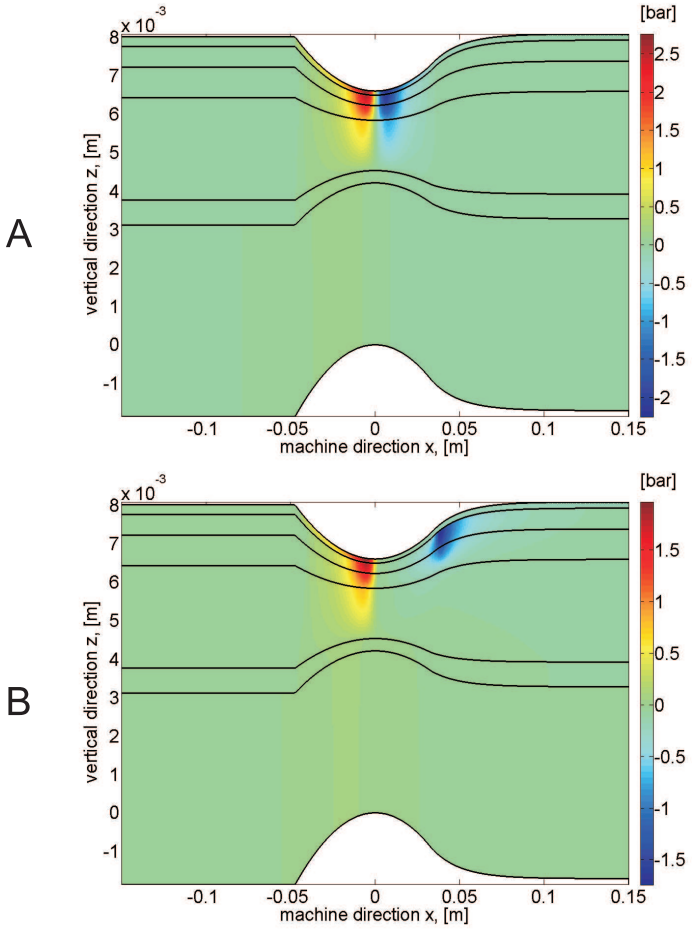

Fig. 5.34: Pressure for the test case 2 using the two-phase flow model (A) and the Richards' model (B)

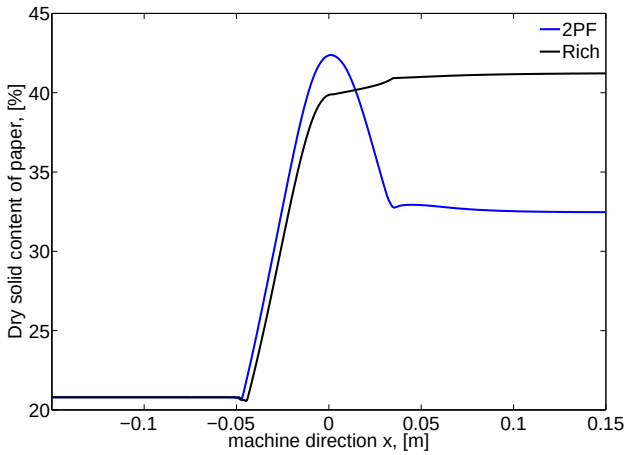

Fig. 5.35: Dry solid content of the paper for the test case 2 using the two-phase flow model and the Richards' model

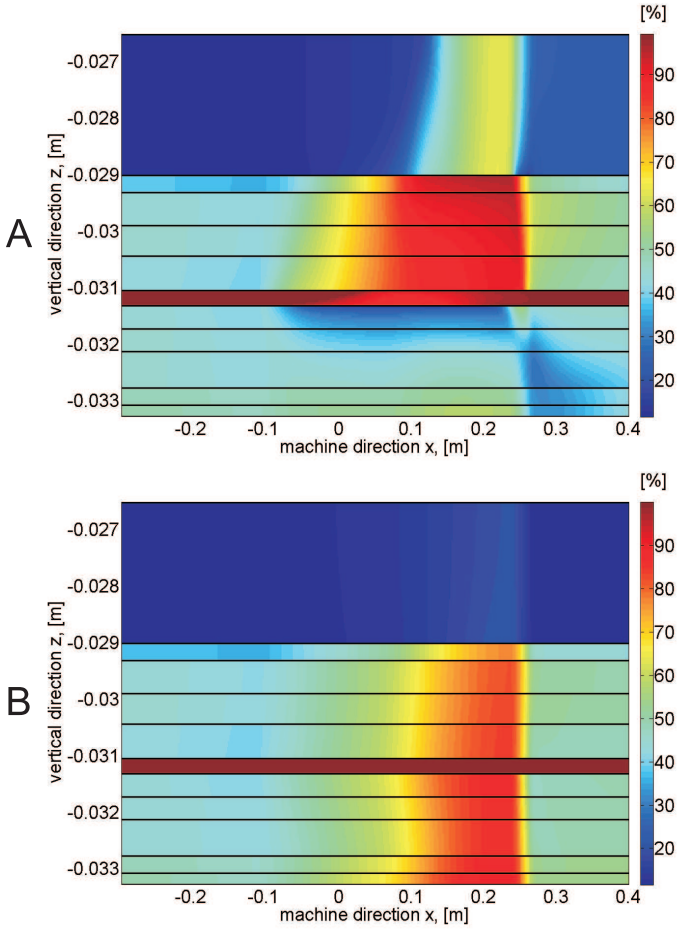

Fig. 5.36: Saturation for the test case 3 using the two-phase flow model (A) and the Richards' model (B)

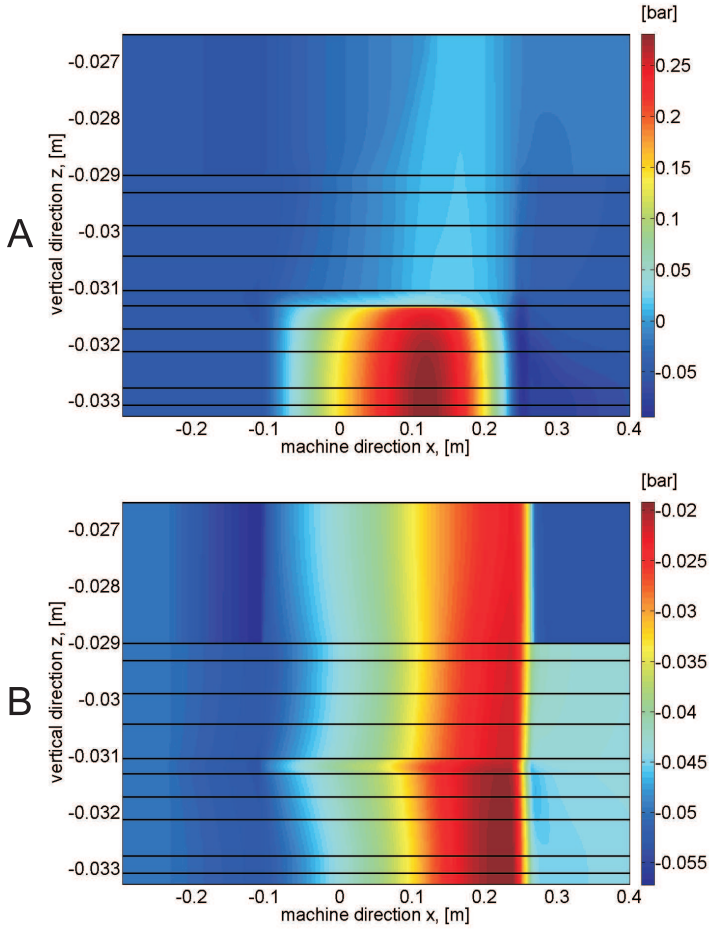

Fig. 5.37: Pressure for the test case 3 using the two-phase flow model (A) and the Richards' model (B)

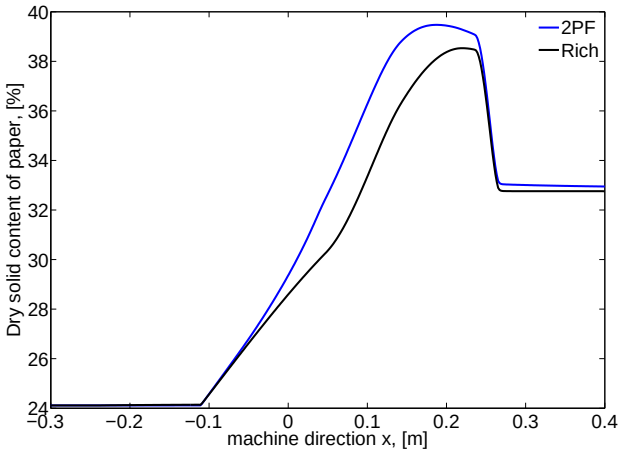

Fig. 5.38: Dry solid content of the paper for the test case 3 using the two-phase flow model and the Richards' model

5.4 Results and discussions

In this chapter a two-dimensional mathematical model for the pressing section of a paper machine was developed. The model uses the two-phase flow approach to simulate the infiltration processes in the pressing zone. We aimed to check the validity range of the Richards' assumption, which had been used in all previous chapters for the pressing section modeling. As the first step we developed the mathematical model using the static capillary pressure saturation relation. The model with the included dynamic capillary effects is planned to be investigated in our future work.

The numerical experiments have shown that the new mathematical model has a significant influence on the distribution of the water. We have observed that the water saturation has changed in comparison to the Richards' model especially in the areas where it reaches high values. Moreover, we have not obtained the fully saturated zones in case of the two-phase flow model. One of the possible reasons is that in this model the air phase has a finite velocity and it is not able to escape completely. It may also happen because of the Robin boundary conditions introduced in this chapter, which allow the escape of water through the upper and lower boundaries. The water pressure has shown behavior similar to the behavior obtained by the Richards' model with the dynamic capillary pressure–saturation relation (see Chapter 4). We observed the maximum pressure value shifted to the left and the decrease of the pressure below the initial value after this maximum. But the two-phase flow model has also shown a significant increase of the maximum value of the pressure in comparison to the Richards' model. The dry solid content of the paper layer is also influenced a lot

by the two-phase flow model. The way it changes depends on the particular test case.

The new boundary conditions, which allow the water escape from the computational domain, were used. The numerical experiments showed that it improved the mathematical model.

To conclude this chapter, we notice that the mathematical modeling of the pressing section should take into consideration both the air and water phases. It will also be very interesting to see how the dynamic capillary effects influence the two-phase flow model.

Summary

The current studies have been intended to develop a mathematical model for the pressing section of a paper machine. As a starting point a one-dimensional model was introduced. The Richards' type equation together with the dynamic capillary pressure–saturation relation was used to simulate the pressing section in Chapter 2. The obtained behavior of the water pressure appeared to be in agreement with laboratory experiments.

In Chapter 3 the stated mathematical model was investigated from the theoretical point of view. The convergence of the discrete solution to the continuous one was proven together with the existence and the compactness of the solution to the discrete problem. In the first part of this chapter, we considered the one-dimensional mathematical model with the static capillary pressure–saturation relation. In the second part, the model including the dynamic capillary effects was investigated. The theoretical studies were developed under minimal restrictions on the input data which were satisfied by the data used in our numerical experiments.

Since the one-dimensional model can not provide a complete image of the infiltration processes within the pressing zone, in Chapter 4 we extended the mathematical model to two dimensions. There we considered a two-phase flow model under Richards' assumption with a possible formation of the fully saturated zones in a multilayer computational domain. The MPFA-O method was applied to discretize the obtained mathematical model on a nonorthogonal quadrilateral grid resolving the layer interfaces. To conclude this chapter, we carried out a number of numerical experiments with realistic sets of parameters.

The last chapter aimed to validate the admissibility of the Richards' assumption used for developing the mathematical model in all previous chapters. Simulations for the pressing section have been performed accounting for the water phase as well as for the air phase. Moreover, the boundary conditions have been improved by allowing a water phase escape from the computational domain where there is no contact with the surface of the pressing roll. In Chapter 5, we have considered the flow model with the static capillary pressure–saturation relation. The dynamic capillary effects are planned to be included into the flow model in our future studies.

The performed simulations have allowed us to better understand the infiltration process occurring within the pressing zone. Moreover, using the developed model we are able to test the various felts and the different press configurations, which may lead to further improvements of the pressing section.

Appendix A

Averaging Procedure

A.1 Averaging procedure for the mass conservation equation

Let us consider the integral form of the mass conservation equation for the domain $\hat{\Omega} \subset \mathbb{R}^2$ (see Figure A.1) in the case of no sources and no sinks and impermeable upper and lower boundaries:

$$\int_{\hat{\Omega}} \operatorname{div}\left(\phi S \mathbf{V}_w\right) d\sigma = 0,$$

where $\hat{\Omega} = \{(\hat{x}, \hat{z}) : \ \hat{x} \in [x, x + \Delta x], \ \hat{z} \in [f_l(\hat{x}), f_u(\hat{x})]\}$, $x \in [A, B]$, $\Delta x > 0, \ \Delta x \in \mathbb{R}_+$ is a fixed value, such that $x + \Delta x \in [A, B]$. Using Green's theorem, one obtains the following integral

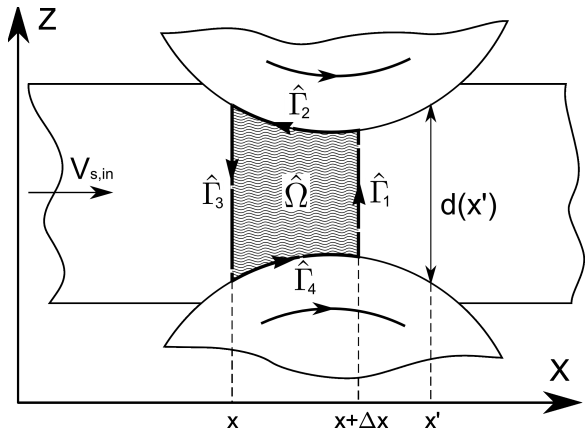

Fig. A.1: Computational domain $\hat{\Omega}$ for the averaging procedure

over the boundary $\partial\hat{\Omega}$ with integration in the counterclockwise direction:

$$\oint_{\partial\hat{\Omega}} \phi S \mathbf{V}_w \cdot \mathbf{n} ds = 0, \tag{A.1}$$

where $\mathbf{n}$ is the outward unit normal of the boundary $\partial\hat{\Omega}$. The boundary $\partial\hat{\Omega}$ can be represented as (see Figure A.1):

$$\partial\hat{\Omega} = \hat{\Gamma}_1 \cup \hat{\Gamma}_2 \cup \hat{\Gamma}_3 \cup \hat{\Gamma}_4,$$

where $\hat{\Gamma}_i \cap \hat{\Gamma}_j = \emptyset$ for all $i \neq j$. Let vector $\mathbf{V}_w$ have the following components $\mathbf{V}_w = \left(V_w^1, V_w^2\right)$. Then (A.1) yields:

$$\begin{aligned} 0 = \oint_{\partial\hat{\Omega}} \phi S \mathbf{V}_w \cdot \mathbf{n} ds &= \int_{\hat{\Gamma}_1} \phi S \mathbf{V}_w \cdot \mathbf{n}_1 ds + \int_{\hat{\Gamma}_2} \phi S \mathbf{V}_w \cdot \mathbf{n}_2 ds \\ &+ \int_{\hat{\Gamma}_3} \phi S \mathbf{V}_w \cdot \mathbf{n}_3 ds + \int_{\hat{\Gamma}_4} \phi S \mathbf{V}_w \cdot \mathbf{n}_4 ds \\ &= \int_{\mathcal{E}_{x+\Delta x}} \phi S V_w^1 ds - \int_{\mathcal{E}_x} \phi S V_w^1 ds, \end{aligned} \tag{A.2}$$

where $\mathcal{E}_x = \{(x,z) : z \in [f_l(x), f_u(x)]\}$ and the integrals over the boundaries $\hat{\Gamma}_2$ and $\hat{\Gamma}_4$ are equal to zero since in the two-dimensional case we imposed no-flow conditions for these boundaries ($\mathbf{V}_w \cdot \mathbf{n}|_{\hat{\Gamma}_2, \hat{\Gamma}_4} = 0$). We introduce vertically averaged horizontal quantities $\hat{\phi}(x)$, $\hat{S}(x)$ and $\hat{V}_w^1(x)$ in the following way:

$$\begin{aligned} \hat{\phi}(x) &= \frac{1}{d(x)} \int_{\mathcal{E}_x} \phi(x,z) dz, \\ \hat{S}(x) &= \frac{1}{d(x)\hat{\phi}(x)} \int_{\mathcal{E}_x} \phi(x,z) S(x,z) dz, \\ \hat{V}_w^1(x) &= \frac{1}{d(x)\hat{\phi}(x)\hat{S}(x)} \int_{\mathcal{E}_x} \phi(x,z) S(x,z) V_w^1(x,z) dz, \end{aligned}$$

where $A \leq x < x + \Delta x \leq B$, $d(x) = f_u(x) - f_l(x) > 0$ is the thickness of the layer.

Remembering that $\hat{\Gamma}_1 = \mathcal{E}_x$ and $\hat{\Gamma}_2 = \mathcal{E}_{x+\Delta x}$, equation (A.2) yields:

$$-\hat{\phi}(x)\hat{S}(x)\hat{V}_w^1(x)d(x) + \hat{\phi}(x+\Delta x)\hat{S}(x+\Delta x)\hat{V}_w^1(x+\Delta x)d(x+\Delta x) = 0. \tag{A.3}$$

Dividing (A.3) by Δx and passing to the limit $\Delta x \to 0$, one obtains:

$$\frac{\partial}{\partial x}\left(\hat{S}(x)\hat{\phi}(x)\hat{V}_w^1(x)d(x)\right) = 0, \quad x \in \Omega. \tag{A.4}$$

Note, that x (see Figure A.1) was chosen arbitrarily, therefore, equation (A.4) is satisfied for any $x \in [A, B]$.

A.2 Averaging procedure for dynamic capillary pressure–saturation relation

Now, we are concerned with the dynamic capillary pressure–saturation relation (2.7). For our problem, we consider p_c^{stat} as a function of the saturation and the porosity: $p_c^{stat} = p_c^{stat}(S, \phi)$. Integration of the left hand side of (2.7) over $\hat{\Omega}$ yields:

$$\int_{\hat{\Omega}} p + p_c^{stat}(S, \phi) d\sigma \approx \left(\hat{p}_{\hat{\Omega}} + p_c^{stat}\left(\hat{S}_{\hat{\Omega}}, \hat{\phi}_{\hat{\Omega}} \right) \right) m(\hat{\Omega}), \tag{A.5}$$

where $\hat{u}_{\hat{\Omega}}$ is the averaged over domain $\hat{\Omega}$ quantity defined by:

$$\hat{u}_{\hat{\Omega}} = \frac{1}{m\left(\hat{\Omega}\right)} \int_{\hat{\Omega}} u d\sigma, \quad \lim_{\Delta x \to 0} \hat{u}_{\hat{\Omega}} = \hat{u}, \tag{A.6}$$

under assumption that $\hat{u}$ is a continuous function.

Let us integrate the right hand side of (2.7) over $\hat{\Omega}$:

$$\begin{aligned} \int_{\hat{\Omega}} \tau \mathbf{V}_s \cdot \operatorname{grad} S d\sigma &= \int_{\hat{\Omega}} \operatorname{div}\left(\tau S \mathbf{V}_s\right) d\sigma - \int_{\hat{\Omega}} S \operatorname{div}\left(\tau \mathbf{V}_s\right) d\sigma \\ &\approx \oint_{\partial\hat{\Omega}} \tau S \mathbf{V}_s \cdot \mathbf{n} ds - \hat{S}_{\hat{\Omega}} \oint_{\partial\hat{\Omega}} \tau \mathbf{V}_s \cdot \mathbf{n} ds, \end{aligned}$$

where $\hat{S}_{\hat{\Omega}}$ is defined by (A.6). Remembering that V_s is the x-component of the vector $\mathbf{V}_s$ and that $\mathbf{V}_s \cdot \mathbf{n}|_{\hat{\Gamma_2}, \hat{\Gamma_4}} = 0$, we have:

$$\begin{aligned} \int_{\hat{\Omega}} \tau \mathbf{V}_s \cdot \operatorname{grad} S d\sigma &\approx \int_{\hat{\Gamma_1}} \tau S \mathbf{V}_s \cdot \mathbf{n}_1 ds + \int_{\hat{\Gamma}_3} \tau S \mathbf{V}_s \cdot \mathbf{n}_3 ds \\ &\quad - \hat{S}_{\hat{\Omega}} \left(\int_{\hat{\Gamma_1}} \tau \mathbf{V}_s \cdot \mathbf{n}_1 ds + \int_{\hat{\Gamma}_3} \tau \mathbf{V}_s \cdot \mathbf{n}_3 ds \right) \\ &= \int_{\mathcal{E}_{x+\Delta x}} \tau S V_s ds - \int_{\mathcal{E}_x} \tau S V_s ds \\ &\quad - \hat{S}_{\hat{\Omega}} \left(\int_{\mathcal{E}_{x+\Delta x}} \tau V_s ds - \int_{\mathcal{E}_x} \tau V_s ds \right). \end{aligned} \tag{A.7}$$

Defining functions $\hat{\tau}(x)$ and $\hat{S}(x)$ in the following way:

$$\hat{\tau}(x) = \frac{1}{d(x)} \int_{\mathcal{E}_x} \tau(x,z) dz,$$
$$\hat{S}(x) = \frac{1}{d(x)\hat{\tau}(x)} \int_{\mathcal{E}_x} \tau(x,z) S(x,z) dz.$$

Then, equation (A.7) yields:

$$\begin{aligned} \int_{\hat{\Omega}} \tau \mathbf{V}_s \cdot \operatorname{grad} S d\sigma \approx & \hat{\tau}(x+\Delta x)\hat{S}(x+\Delta x)V_s d(x+\Delta x) \\ & - \hat{\tau}(x)\hat{S}(x)V_s d(x) \\ & - \hat{S}_{\hat{\Omega}}\hat{\tau}(x+\Delta x)V_s d(x+\Delta x) \\ & + \hat{S}_{\hat{\Omega}}\hat{\tau}(x)V_s d(x). \end{aligned} \tag{A.8}$$

Dividing the right hand sides of equations (A.5) and (A.8) by Δx and passing to the limit $\Delta x \to 0$, one obtains:

$$\begin{aligned} & d(x)\left(\hat{p}(x) + p_c^{stat}\left(\hat{S}(x), \hat{\phi}(x)\right)\right) \\ & \qquad = \frac{\partial}{\partial x}\left(\hat{\tau}(x)\hat{S}(x)V_s d(x)\right) - \hat{S}(x)\frac{\partial}{\partial x}\left(\hat{\tau}(x)V_s d(x)\right). \end{aligned} \tag{A.9}$$

Transforming equation (A.9) we obtain:

$$p = \tau V_s \frac{\partial S}{\partial x} - p_c^{stat}(S,\phi), \quad x \in \Omega,$$

where the hats over the functions are omitted.

Bibliography

[1] I. Aavatsmark. An introduction to multipoint flux approximations for quadrilateral grids. *Comput. Geosci.*, 6:405–432, 2002.

[2] I. Aavatsmark. Multipoint flux approximation methods for quadrilateral grids. In *9th International Forum on Reservoir Simulation, Abu Dhabi*, 2007.

[3] G.I. Barenblatt and A.A. Gilman. Nonequilibrium counterflow capillary impregnation. *J. of Eng. Phys.*, 52:335–339, 1987.

[4] G.I. Barenblatt, T.W. Patzek, and D.B. Silin. The mathematical model of non-equilibrium effects in water–oil displacement. In *In:SPE/DOE 13th Symposium on Improved Oil Recovery, SPE 75169, Tusla, USA*, 2002.

[5] J. Bear. *Dynamics of fluids in porous media*. American Elsevier Pub. Co., 1972.

[6] J. Bear and Y. Bachmat. *Introduction to modeling of transport phenomena in porous media*. Kluwer, Dordrecht, 1990.

[7] J. Bear and A. Verruijt. *Modeling groundwater flow and pollution*. Reidel, Dordrecht, the Netherlands, 1987.

[8] D. Beck. Fluid pressure in a press nip: measurements and conclusions. In *Engineering Conference Proceedings, TAPPI, Atlanta, GA*, pages 475–487, 1983.

[9] C. Bermond. Establishing the scientific base for energy efficiency in emerging pressing and drying technologies. *Applied Thermal Engineering*, 17:901–910, 1997.

[10] D. Bezanovic, C.J. van Duijn, and E.F. Kaasschieter. Analysis of paper pressing: the saturated one-dimensional case. *J. Appl. Math. Mech.*, 86:18–36, 2006.

[11] D. Bezanovic, C.J. van Duijn, and E.F. Kaasschieter. Analysis of wet pressing of paper: the three-phase model. part 2: compressible air case. *Transp. Porous Med.*, 67:171–187, 2007.

[12] D. Bezanovic, C.J. van Duijn, and E.F. Kaasschieter. Analysis of wet pressing of paper: the three-phase model. part 1: constant air density. Technical Report CASA 05–16, the Department of Mathematics and Computer Science, Eindhoven, University of Technology, 2007a.

[13] M. Bourgeat, A.and Panfilov. Effective two-phase flow through highly heterogeneous porous media: Capillary nonequilibrium effects. *Computational Geosciences*, 2:191–215, 1998.

[14] R.H. Broocks and A.T. Corey. Hydraulic properties of porous media. Technical Report Hydrol. Pap., vol. 3, Fort Collins, Colorado State University, 1964.

[15] J.B. Conway. *A course in functional analysis*. Springer-Verlag, New-York, 2 edition, 1990.

[16] K. Deckelnick and K.G. Siebert. $w^{1,\infty}$-convergence of the discrete free boundary for obstacle problems. *IMA Journal of Numerical Analysis*, 20:481–498, 2000.

[17] P. Deuflhard. *Newton Methods for Nonlinear Problems. Affine invariance and adaptive algorithms*. Computational Mathematics.35, Springer, 2004.

[18] M.G. Edwards. Unstructured, control-volume distributed, full-tensor finite-volume schemes with flow based grids. *Comput. Geosci.*, 2:433–452, 2002.

[19] G.T. Eigestad and R.A. Klausen. On the convergence of the multi-point flux approximation o-method: Numerical experiments for discontinuous permeability. Technical Report An Update of the Preprint no 97–19 du LATP, UMR 6632, Wiley Interscience, 2005.

[20] R. Eymard, T. Gallouet, and R. Herbin. Finite volume methods. Technical Report An Update of the Preprint no 97–19 du LATP, UMR 6632, Marseille, Sept 1997, 2006.

[21] R. Eymard, M. Gutnic, and D. Hilhorst. The finite volume method for Richards' equation. *Comput. Geosci.*, 3:259–294, 1999.

[22] R. Eymard and G. Printsypar. A proof of convergence of a finite volume scheme for modified steady Richards' equation describing transport processes in the pressing section of a paper machine. Technical Report 184, Fraunhofer ITWM, 2010.

[23] S.M. Hassanizadeh, M.A. Celia, and H.K. Dahle. Dynamic effect in the capillary pressure–saturation relationship and its impacts on unsaturated flow. *Vadose Zone Journal*, 1:38–57, 2002.

[24] S.M. Hassanizadeh and W.G. Gray. Mechanics and thermodynamics of multiphase flow in porous media including interphase boundaries. *Adv. Water Resour.*, 13:169–186, 1990.

[25] S.M. Hassanizadeh and W.G. Gray. Thermodynamic basis of capillary pressure in porous media. *Water Resour. Res.*, 29:3389–3405, 1993a.

[26] R. Helmig. *Multiphase flow and Transport Processes in the Subsurface*. Springer (Environmental Engineering), Berlin, 1997.

[27] R. Herbin and F. Hubert. Benchmark on discretization schemes for anisotropic diffusion problems on general grids for anisotropic heterogeneous diffusion problems, in finite volumes for complex applications V, R. Eymard and J.–M. Hérard. *eds., Wiley, Hoboken, NJ*, page 659692, 2008.

[28] K. Hiltunen. *Mathematical and Numerical Modelling of Consolidation Processes in Paper Machines*. PhD thesis, University of Jyväskylä, Finland, 1995.

[29] O. Iliev, G. Printsypar, and S. Rief. On mathematical modeling and simulation of the pressing section of a paper machine including dynamic capillary effects: One-dimensional model. *Transp. Porous Med.*, 92(1):41–59, 2012, (extended version of the paper available as Technical Report 206, Fraunhofer ITWM, 2011).

[30] O. Iliev, G. Printsypar, and S. Rief. A two-dimensional model of the pressing section of a paper machine including dynamic capillary effects. *Submitted*, (extended version of the paper available as Technical Report 211, Fraunhofer ITWM, 2012).

[31] K. Jewett, W. Ceckler, L. Busker, and A. Co. Computer model of a transversal flow nip. In *AIChE Symposium Series 76 (200), New York*, pages 59–70, 1980.

[32] B. Jiang. Convergence analysis of p_1 finite element method for free boundary problems on non-overlapping subdomains. *omput. Methods Appl. Mech. Engrg.*, 196:371–378, 2006.

[33] V. Joekar-Niasar and S.M. Hassanizadeh. Effect of fluids properties on non-equilibrium capillarity effects: Dynamic pore-network modeling. *International Journal of Multiphase Flow*, 37:198–214, 2010.

[34] F. Kalaydjian. Dynamic capillary pressure curve for water/oil displacement in porous media: Theory vs. experiment. In *Society of Petroleum Engineers*, pages SPE 24813:491–506, 1992.

[35] M. Kataja, K. Hiltunen, and J. Timonen. Flow of water and air in a compressible porous medium. a model of wet pressing of paper. *J. Phys. D: Appl. Phys.*, 25:1053–1063, 1992.

[36] C. T. Kelley. *Iterative Methods for Linear and Nonlinear Equations*. SIAM, Philadelphia, 1995.

[37] M.C. Leverett. Capillary behavior in porous solids. *Transactions of the AIME*, 142:152–169, 1941.

[38] S. Manthey. *Two-phase flow processes with dynamic effects in porous media – parameter estimation and simulation*. PhD thesis, Institute of Hydraulic Engineering of Stuttgart, Germany, 2006.

[39] Metso Corporation. http://www.metso.com/pulpandpaper.

[40] A. Mikelić. A global existence result for the equations describing unsaturated flow in porous media with dynamic capillary pressure. *J. Differential Equations*, 248:1561–1577, 2010.

[41] Paper academy. http://www.paperacademy.net/855/paper-papermaking-manufacturing/paper-machine-press-section/.

[42] G. Printsypar and R. Ciegis. On convergence of a discrete problem describing transport processes in the pressing section of a paper machine including dynamic capillary effects: one-dimensional case. *J. Comp. Appl. Math.*, 236:3409–3425, 2012 (extended version of the paper available as Technical Report 210, Fraunhofer ITWM, 2011).

[43] S. Rief. *Nonlinear Flow in Porous Media*. PhD thesis, University of Kaiserslautern, Germany, 2005.

[44] S. Rief. Modeling and simulation of the pressing section of a paper machine. Technical Report 113, Fraunhofer ITWM, 2007.

[45] P.J. Ross and K.R.J. Smettem. A simple treatment of physical nonequilibrium water flow in soils. *Soil Sci. Soc. Am. J.*, 64:1926–1930, 2000.

[46] A.A. Samarskij. *Introduction to Theory of Difference Schemes*. Moscow, Nauka, in Russian, 1971.

[47] B. Schweizer. Regularization of outflow problems in unsaturated porous media with dry regions. *Differential Equations*, 237:278–306, 2007.

[48] M.T. Van Genuchten. A closed-form equation for predicting the hydraulic conductivity of unsaturated soils. *Soil Sci. Soc. Am. J.*, 44:892–898, 1980.

[49] K. Velten and W. Best. Rolling of unsaturated porous materials: Evolution of a fully saturated zone. *Physical Review E*, 62:3891–3899, 2000.

[50] E.W. Weisstein. *CRC Concise Encyclopedia of Mathematics*. CRC Press LLC, 1999.

Wissenschaftlicher Werdegang

Galina Printsypar

09/1993–05/2003	Schulausbildung
09/2003–06/2007	Bachelor in Applied Mathematics and Computer Science, Taganrog Technological Institute of Southern Federal University, Russland
07/2007–06/2008	The specialist degree in Applied Mathematics and Computer Science, Taganrog Technological Institute of Southern Federal University, Russland
10/2008–03/2009	ProSat Programm, Technische Universität Kaiserslautern, Deutschland
seit 04/2009	Doktorand der Mathematik, Technische Universität Kaiserslautern, Deutschland

Education and Working Experience

Galina Printsypar

09/1993–05/2003	School education
09/2003–06/2007	Bachelor in Applied Mathematics and Computer Science, Taganrog Technological Institute of Southern Federal University, Russia
07/2007–06/2008	The specialist degree in Applied Mathematics and Computer Science, Taganrog Technological Institute of Southern Federal University, Russia
10/2008–03/2009	ProSat Program, Technical University Kaiserslautern, Germany
since 04/2009	PhD student, Technical University Kaiserslautern, Germany